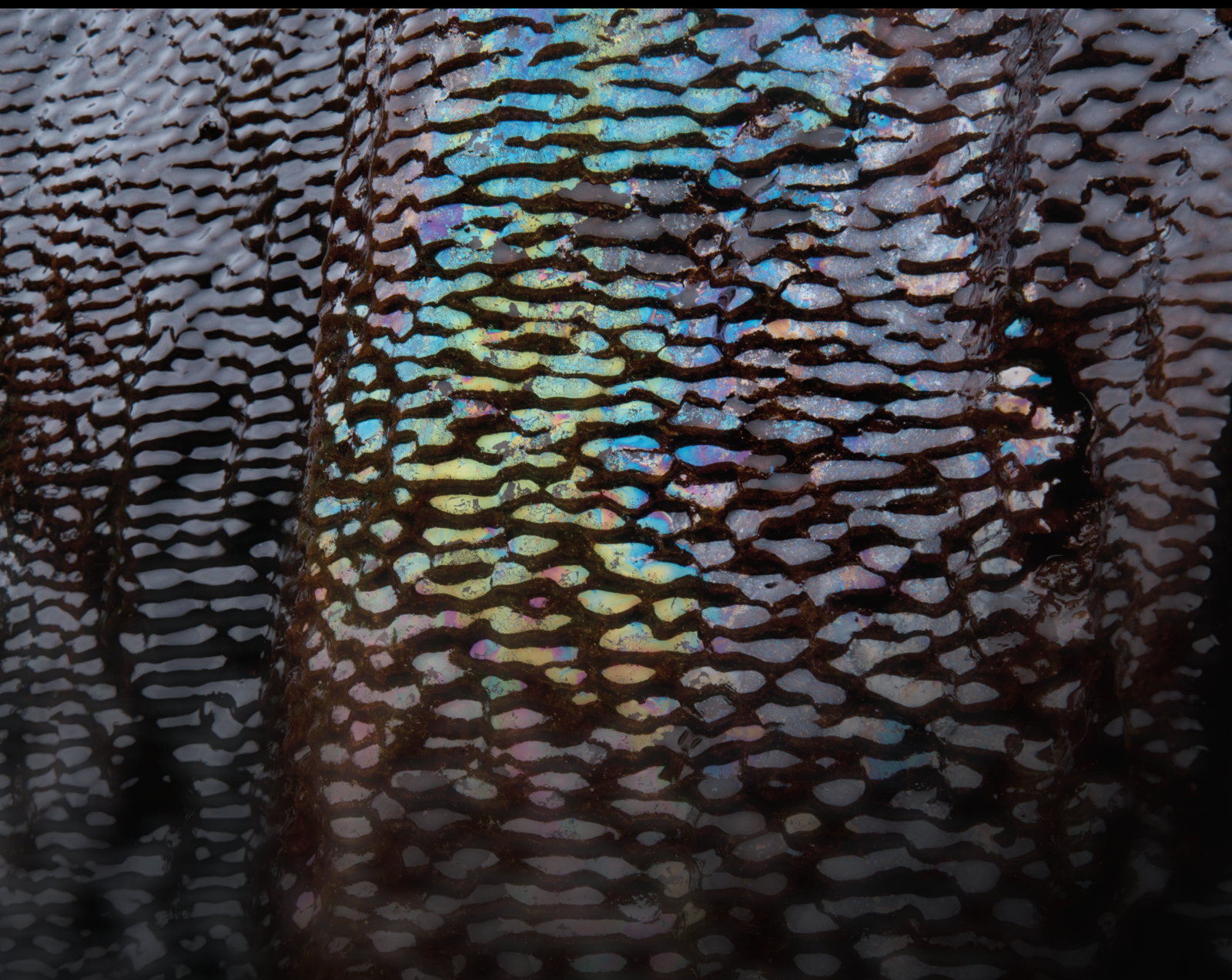# Multiscale Hydro-Mechanical Response of Gas/Water Migration in Geomaterials

Lead Guest Editor: Jiangfeng Liu
Guest Editors: Long Xu and Xiangjian Dong

Multiscale Hydro-Mechanical Response of Gas/Water Migration in Geomaterials

Multiscale Hydro-Mechanical Response of Gas/Water Migration in Geomaterials

Lead Guest Editor: Jiangfeng Liu
Guest Editors: Long Xu and Xiangjian Dong

Bisheng Wu [iD], China
Da-yang Xuan [iD], China
Yi Xue [iD], China
HE YONGLIANG, China
Fan Yang [iD], China
Zhenyuan Yin [iD], China
Sohrab Zendehboudi, Canada
Zhixiong Zeng [iD], Hong Kong
Yuanyuan Zha [iD], China
Keni Zhang, China
Mingjie Zhang [iD], China
Rongqing Zhang, China
Xianwei Zhang [iD], China
Ye Zhang [iD], USA
Zetian Zhang [iD], China
Ling-Li Zhou [iD], Ireland
Yingfang Zhou [iD], United Kingdom
Daoyi Zhu [iD], China
Quanle Zou, China
Martina Zucchi, Italy

Contents

WILEY | Hindawi

Research Article

Applicability of the Time Fractional Derivative Model on Fickian and Non-Fickian Transport in the Single Fracture: An Experimental Investigation

Haoming Zhang ,[1] Jiazhong Qian ,[1] Yong Liu ,[2] Yi Xu,[3] Hongguang Sun,[3] Xuequn Chen,[4] and Fulin Li [4]

[1]*School of Resources and Environmental Engineering, Hefei University of Technology, Hefei 230009, China*
[2]*School of Food Science and Engineering, Hefei University of Technology, Hefei 230009, China*
[3]*State Key Laboratory of Hydrology-Water Resources and Hydraulic Engineering, College of Mechanics and Materials, Hohai University, Nanjing 210098, China*
[4]*Water Conservancy Research Institute of Shandong Province, Jinan 250013, China*

Correspondence should be addressed to Yong Liu; liuyong@hfut.edu.cn and Fulin Li; fulinli@126.com

The understanding of solute transport in rock fractures is of great importance in many engineering fields. In this study, two groups of experiments on artificial and natural single fractures with different fracture apertures and roughness were conducted to investigate the changes of solute transport regimes. The time fractional advection–dispersion equation (tFADE) as a promising model was applied to describe the anomalous transport. The performance of the classical advection-dispersion equation (ADE) and tFADE was compared according to the fitting precision of breakthrough curves (BTCs). The responses of the fitting parameters in the tFADE to the experimental conditions were also discussed. The results indicated that the non-Fickian transport more likely occurred in the short distance transport, and the larger Peclet number (Pe) led to the increase of the exponent of the power-law function in the phase of concentration decline. The tFADE was superior to ADE in capturing the non-Fickian transport especially the tailing behavior. The fractional order of time α in the tFADE was the key parameter to describe the anomalous transport process, and its responding mechanisms of were revealed: the best-fit α decreased with the increase of flow velocity and the decrease of the fracture aperture. The roughness of the single fracture which leads to a complex flow field had a significant effect on the best-fit α. The findings of this study can help for better understanding the effectiveness and physical significance of the tFADE.

1. Introduction

Solute transport in fractured rocks is of great significance to the underground engineering such as tunnel excavation, shale gas development, and CO_2 geological storage. Due to the variable geometry and hydraulic conditions in the geological environment, the accurate quantitative prediction of solute transport in the fracture is an important research with great challenges [1, 2].

In order to predict the solute transport process in fractured media, mathematical models have been developed and applied in the laboratory investigation and numerical simulation [3–5]. The acknowledged advection–dispersion equation (ADE), derived from Fick's law, has been used to describe solute transport in fractures for years [6]. However, many laboratory researches claimed that medium heterogeneity deeply affects the transport of solute in the fracture, resulting in the limitation of the ADE model in describing the early arrival or tailing behavior which is typical non-Fickian behavior [7–9]. In single fractures, the geometry structure of walls and inertial effects of flow are mainly considered as the causes of

the non-Fickian phenomena [10, 11]. That is, the rougher fracture and higher velocity of the flow lead to the differentiation of the main flow paths and recirculation zones which affect the transport process deeply and cause the failures of the ADE (Figure 1) [12, 13]. Moreover, non-Fickian phenomena are common in nature [14]. Thus, quantitative capture of non-Fickian phenomenon at a laboratory scale contributes to the study of solute transport in a natural scale [15].

To improve the precision accuracy of pollutant transport and capture the non-Fickian transport, several mathematical approaches have been developed [16, 17]. Based on a transition rate approach, continuous time random walk (CTRW) which includes the Fokker-Panck equation with a memory equation has been widely used to capture solute transport in both the fracture system and heterogeneous porous media [18, 19]. Nowamooz et al. [20] interpreted the tracer transport in the original fractures with the equivalent-stratified model and the continuous time random walk (CTRW) and analyzed the advantages and disadvantages of the two models. Though CTRW can capture the transport process well, the physical relationship between the transport velocity and the average fluid velocity is not clear enough and the parameters of CTRW are relatively more than those of other models which result in the difficulty in simulation. Improved on the ADE, several mathematical approaches can also capture the solute transport process with a certain degree of accuracy like the mobile-immobile (MIM) model and fractional advection-dispersion equation (FADE) [21, 22]. Qian et al. [23] used the single-rate MIM model, ADE, and advection–dispersion equation with retardation (ADE-R) to fit the sodium chloride transport in the filled fracture and test the precision of the MIM. The results showed that MIM can capture the anomalous transport process well including early arrival and tailing behaviors. The equivalent-stratified method can quantify the degree of fracture heterogeneity, but the goodness of fit for the solute transport process of short-distance transportation is low. By adding a fractional-order operator to time in the traditional ADE, the time fractional advection-dispersion equation (tFADE) can describe the solute remaining in an immobile domain [24, 25]. Hence, the tFADE has the potential to describe the tailing behavior caused by the geometry structure of the single fracture. On the other hand, the spatial fractional advection-dispersion equation (sFADE) has been used in describing solute transport for many years which can describe the solute transport at different transport distances [3, 4, 9]. Benson et al. [26] regarded FADE as a predictive tool with certain precision by fitting the transport in a relatively homogeneous sandbox. Huang et al. [27] simulated the atrazine transport in a sand column by numerical approach and found that the FADE can capture well the non-Fickian transport especially the tailing behaviors. Hence, the FADE is a promising approach to describe the solute transport process in the fracture system with a complex interference factor. However, the physical significance of the fractional order is still unclear.

In summary, the capture of non-Fickian transport still remains to be further researched. The effectiveness of the FADE to the simulated solute transport process under different conditions at the laboratory scale needs to be proved. Researches on the physical significance and influence factors of the parameters in the FADE are necessary. Hence, systematical studies of the FADE for describing the solute transport in a single fracture are still a requisite [28]. It can provide strong theoretical support for the wider application of the FADE.

This study is aimed at analyzing the cause of the non-Fickian transport process in single fractures, testing the fitting precision of the tFADE under different experimental conditions, and investigating the effect of the flow rate, fracture aperture, and roughness in granite fractures and plexiglass fractures on the parameters of the tFADE.

The research steps are organized as follows. First, the theoretical background of solute transport is introduced in Section 2. Then, 2 groups of solute transport experiments are performed in Section 3. Third, the experimental results and fitting results with ADE and tFADE are described, as well as the comparison of the fitting of the two models and discussion of the influence of experimental conditions on the fitting accuracy and the parameters of the tFADE. Finally, the conclusion and limitation of this study are summarized in Section 5.

2. Theoretical Background of Solute Transport

The fractional operator has been developed in many fields for years [29]. Mehdinejadiani and Fathi [30] simulated water table profiles using the space fractional Boussinesq equation. Jafari et al. [31] developed a fractional Glover-Dumm equation to simulate the groundwater flow under heterogeneous unconfined aquifers. The fractional-derivative operator of the FADE can be used to describe anomalous diffusion for its nonlocality [32]. Many studies have shown that the FADE can describe the abnormal transport of particles [4, 33, 34]. The time fractional advection-dispersion equation (tFADE) is an upgrade based on the ADE by replacing a fractional derivative from 0 to 1 to the first time derivative, arising from the power law of the time distribution of particles [35, 36]. The basic form of the tFADE is as follow:

$$\frac{\partial^{\alpha} C(x,t)}{\partial t^{\alpha}} = -V \frac{\partial C(x,t)}{\partial x} + D \frac{\partial^2 C(x,t)}{\partial x^2}, \qquad (1)$$

where C is the concentration of the solute (mol/L), D is the dispersion coefficient (m^2/s), V is the advective velocity (m/s), t is the time (s), x is the spatial coordinate of the solute along the direction of flow (m), and α (dimensionless) is the order of fractional differentiation. The smaller value of α explains the more remarkable solute retention in the fracture. In addition, when the α value is 1, the tFADE recedes to the ADE. The dispersion coefficient D in the tFADE is different from that in the ADE, because the fractional operator describes the partially local velocity rather than the mean velocity.
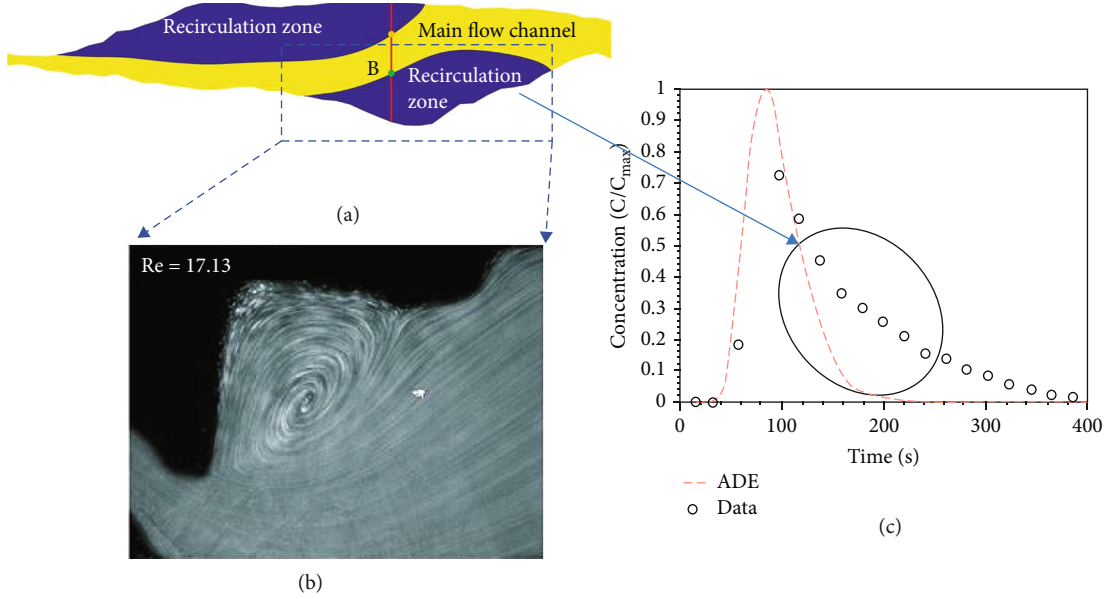
FIGURE 1: Schematic of the tailing behavior caused by roughness of single fractures. (a) A partition chart for the flow in the single fracture [12]. (b) A microscopic picture of particle flow in the fracture [13]. (c) A breakthrough curved in which the tailing behavior can be noticed and ADE fails to capture the transport process.

The numerical solutions of equation (2) are obtained by finite difference approximation, and the initial and the boundary conditions of solute transport are shown as follows:

$$C(x, t)|_{t=0} = 0 \; x > 0,$$

$$C(x, t)|_{x=0} = \begin{cases} C_0 (0 \le t \le t_0), \\ 0 (t_0 \le t \le +\infty), \end{cases}$$

$$\lim_{x \longrightarrow +\infty} C(x, t) = 0,$$

(2)

where t_0 represents the duration of solution injection and C_0 represents the injected concentration and, in this study, C_0 is set to 1 for the normalized concentration.

To evaluate the fitting accuracy of the tFADE, the coefficient of determination (r^2) and root mean square error (RMSE) were calculated. The coefficient of determination r^2 can express the goodness of fit by calculating the proportion of variability in the dependent variable that can be explained in the FADE, and the range of r^2 is from 0 to 1. RMSE is a non-negative number which reflects the measure of dispersion of an observation [37]. It should be mentioned that the normalized concentration is used in this study, so both parameters are dimensionless. In the experiments, the closer r^2 near to 1 and the smaller RMSE represent the better fitting result. The mathematical expressions of r^2 and RMSE are as follows:

$$r^2 = 1 - \frac{\sum_{i=1}^N (C_{io} - C_{ie})^2}{\sum_{i=1}^N (C_{io} - \bar{C}_{io})^2},$$

$$\text{RMSE} = \sqrt{\frac{1}{n} \sum_{i=1}^N (C_{io} - C_{ie})^2},$$

(3)

in which C_{io} is the observed concentration, $\bar{C}_{io}$ is the average value of the observed concentration, and C_{ie} is the simulated concentration.

In this study, two important dimensionless numbers are used. The Reynolds number (Re) is a classic quantity to describe the ratio of inertial effect to viscous effects on the field flow, and the Peclet number (Pe) is defined as the ratio of the convection, and the diffusion can be used to describe the importance of convective flux. The larger Pe indicates the more significant convective transport [38]. The computational expressions are shown as follows:

$$\text{Re} = \frac{\rho v d}{\mu},$$

(4)

$$\text{Pe} = \frac{v d}{D_m},$$

(5)

where ρ is the fluid density ($1 \times 10^3 \, \text{kg/m}^3$), v is the average flow velocity, d is the apparent fracture aperture, μ is the dynamic fluid viscosity ($1.01 \times 10^{-3} \, \text{Pa·s}$), and D_m is the molecular diffusion coefficient.

The residence-time distributions (RTDs), effective metric for evaluate the features of non-Fickian transport, are developed by the nonlocal dispersion theory [39, 40]. In this study, RTDs were calculated for the solute transport in the granite fracture and plexiglass fracture to examine the features of tailing behavior. RTDs were derived from the time derivative of BTCs of the step injection for its resident concentration time series, and the residence time distribution can be expressed as follows [41]:

$$R(t) = \frac{dc_s}{dt'},$$

(6)
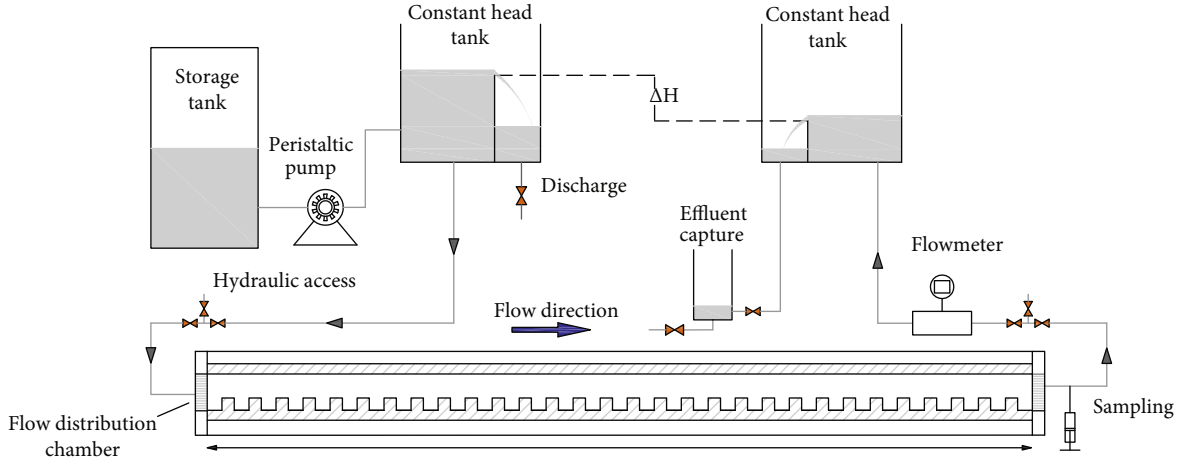
FIGURE 2: Experimental setup for the BBF transport in a single plexiglass fracture.

TABLE 1: Summary of experimental parameters.

Experiment	Pattern	Width (cm)	Length (cm)	Mechanical aperture (mm)	Relative roughness
Group 1	Pattern 1	12	59	1.71	0.09
				1.71	0.09
				1.71	0.09
				2.60	0.1
				2.60	0.1
				2.60	0.1
	Pattern 2	13	69	2	0.34
				2	0.34
				2	0.34
				3	0.23
				3	0.23
				3	0.23
Group 2	Pattern 1	60	15	4	1
				5	0.8
				6	0.67
				4	1
				5	0.8
				6	0.67
	Pattern 2			2	0
				3	0
				4	0
				2	0
				3	0
				4	0

$$t' = \frac{Qt}{V_f}, \qquad (7)$$

where t' is a dimensionless time called pore volume, Q is the flow rat e(cm^3/s), and V_f is the volume of the fracture (cm^3). It should be noted that a single instantaneous injection was simulated in our study and the BTCs can be converted from the single instantaneous injection to the step injection [42].

$$\frac{dC_s}{dt'} = C_p, \qquad (8)$$

where the C_s and C_p represent the concentration obtained in response to the step injection and pulse injection, respectively. According to equation (8), equation (9) can be transformed into
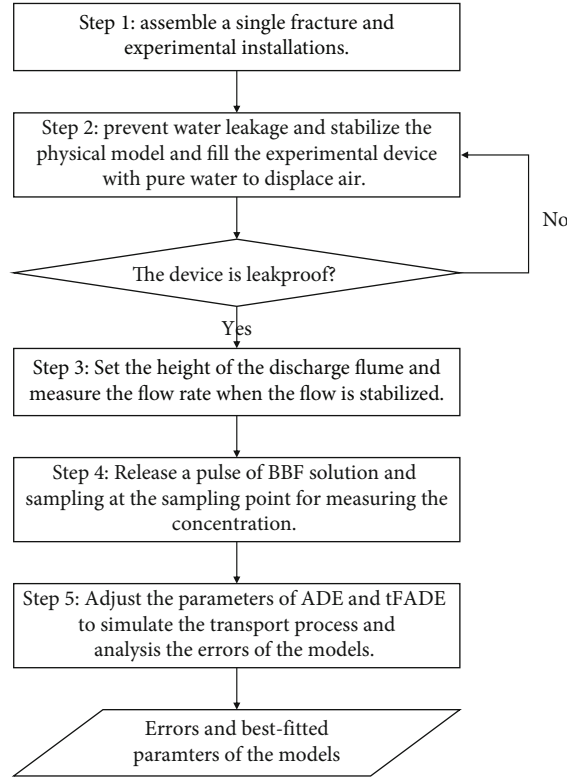
FIGURE 3: Flowchart for measuring errors and best-fit parameters of ADE and tFADE.

$$\frac{dC_s}{dt} = \frac{Q}{V_{\mathrm{f}}} C_p. \tag{9}$$

3. Experimental Apparatus and Procedure

3.1. Experimental Apparatus. In this study, two groups of experiments in a single fracture under different experimental conditions were conducted and each group involved two patterns.

The schematic diagram of the laboratory setup are shown in Figure 2. Three main parts including a recharge flume, a discharge flume, and a single fracture are assembled in group 1. Both the recharge flume and the discharge flume consist of a water pipe for the control device and an overflow launder. Three hydraulic gradients for each pattern in group 1 are designed by adjusting the height of the recharge flume with the constant position of the discharge flume. The steady flow rates are calculated by a chronograph and a measuring cylinder after the water head is stable. Sampling analyses are taken at certain intervals to monitor the change of solute concentration. Each experiment was repeated three times.

Brilliant blue FCF (BBF), an ionic molecule, was used in several solute transport experiments as a conservative tracer recently for its nontoxicity, mobility, and low adsorption [43–45]. To measure the concentration of BBF in the fracture, the standard curve is calculated by configuring a series of concentrations of BBF solutions and measuring the absorbance. The value of absorbance of the sample is measured at 630 nm by a spectrophotometer SP-754 (Shanghai Precision and Scientific Instrument) in group 1 and 752 N (Shanghai Precision & Scientific Instrument Co. Ltd., China) in group 2.

Two patterns of fractures were contained in group 1. The natural and rough fracture was made up of two granite plates 59 cm long and 12 cm wide. The average aperture of the natural fracture is calculated by measuring the width of 110 points with a vernier caliper because of unobvious depressions, and projections are present on the granite plate, and the apertures of 1.71 and 2.60 mm are set. Another pattern is made up of two parallel plexiglass plates, which were 69 cm long, 13 cm wide, and 1 cm thick. 1 of which is smooth, and the other is rough, evenly inlaid with 1 cm × 1 cm × 0.3 cm blockages spaced 1 cm apart to improve roughness. The fracture aperture was adjustable, and three sets of planes were made to obtain different fracture apertures with 2 and 3 mm. The sampling point was set at the end of the fracture.

Group 2 consists of a peristaltic pump, a single fracture, and a discharge flume. A flow distribution device was provided at the entrance of the fracture. A peristaltic pump was set as 55 and 100 rpm before each experiment of group 2. The hydraulic gradient was made constant by the overflow flume in every single experimental process. The sampling point was set at the center point of the fracture. The cross-section of the fracture was narrow, and the ratio of the length to the width of the fractures was large both in groups 1 and 2. Hence, vertical flow can be neglected and the one-dimensional transport was considered in this study.

Table 2: Values of the Re and Pe versus Darcy's velocity (V) with different fracture patterns.

Experiment	Pattern	Number	Q (ml/s)	V (mm/s)	Re	Pe
Group 1	Pattern 1	1	0.6	2.924	5.0	8333
		2	1	4.873	8.3	13888
		3	1.4	6.823	11.6	19446
		4	0.6	1.923	5.0	8333
		5	1	3.205	8.3	13888
		6	1.4	4.487	11.6	19444
	Pattern 2	1	0.6	2.308	4.6	7693
		2	1	3.846	7.6	12820
		3	1.4	5.385	10.7	17950
		4	0.6	1.538	4.6	7690
		5	1	2.564	7.6	12820
		6	1.4	3.590	10.7	17950
Group 2	Pattern 1	1	0.825	1.375	5.5	9167
		2	0.825	1.1	5.5	9167
		3	0.825	0.917	5.5	9170
		4	1.5	2.5	10	16667
		5	1.5	2	10	16667
		6	1.5	1.67	10	16700
	Pattern 2	1	0.825	2.75	5.5	9167
		2	0.825	1.83	5.49	9150
		3	0.825	1.375	5.5	9167
		4	1.5	5	10	16667
		5	1.5	3.33	10	16650
		6	1.5	2.5	10	16667

Three smooth fractures with average apertures of 2, 3, and 4 mm were prepared by mounting two plexiglass plates horizontally. Each plate was set to be 60 cm long, 15 cm wide, and 1 cm thick. The single rough fracture was composed of a smooth plate and a rough plate formed by cutting a slot with 4 mm wide and 4 mm deep spaced every 4 mm on the side of the plexiglass plate. The space between the two plates is the same as that of the smooth fracture but the average apertures of rough fractures were 4, 5, and 6 mm.

In group 1, pattern 1 represents the granite fracture and pattern 2 represents the plexiglass fracture. And in group 2, pattern 1 represents the rough fracture and pattern 2 represents the fracture with a smooth surface. The summary of experimental models parameters can be seen in Table 1.

3.2. Experimental Procedure. The tracer experiments and simulations included the following steps which can also be seen briefly in Figure 3. The experimental apparatus was installed to ensure a watertight seal according to the design. The glass cement was used to prevent water leakage and stabilize the physical model. Water was continuously pumped into the fracture, and ensure that the air was expelled completely. The height of the recharge flume was adjusted by maintaining the height of the discharge flume to control the hydraulic head before injecting the BBF solution in group 1. When the flow rate stabilized,

the BBF solution was injected through the injection syringe in an instant pulse while the chronograph begins to count. 5 ml of BBF solution with the concentration of 0.1 g/l was injected every single experiment. In group 2, the speed of the peristaltic pump was adjusted before adding the BBF solution and the dosage and concentration of the BBF solution were 2 ml and 0.15 g/l every time. Samples were taken at sampling points regularly till the BBF solution passed through the device completely. Each sampling volume was 3 ml to minimize quality loss effect, and the absorbance was determined to obtain the concentration. After each test, the plates were detached from the fracture and rinsed thoroughly with water. ADE and tFADE were conducted to simulate the transport process by adjusting the parameters of the models till the accuracy could not be improved.

4. Results and Discussion

4.1. Flow Fields and Transport Processes in the Single Fractures. The flow fields can deeply affect advection and mechanical dispersion. To quantify the flow regime and transport pattern, Re and Pe are calculated by equations (4) and (5) and listed in Table 2. Noted that the D_m for BBF is set as 6×10^{-6} cm^2/s according to Kone et al. [46]. The flow regime in this study is considered as the laminar flow because Re ranged from 5.0 to 11.6 which

(a)

(b)
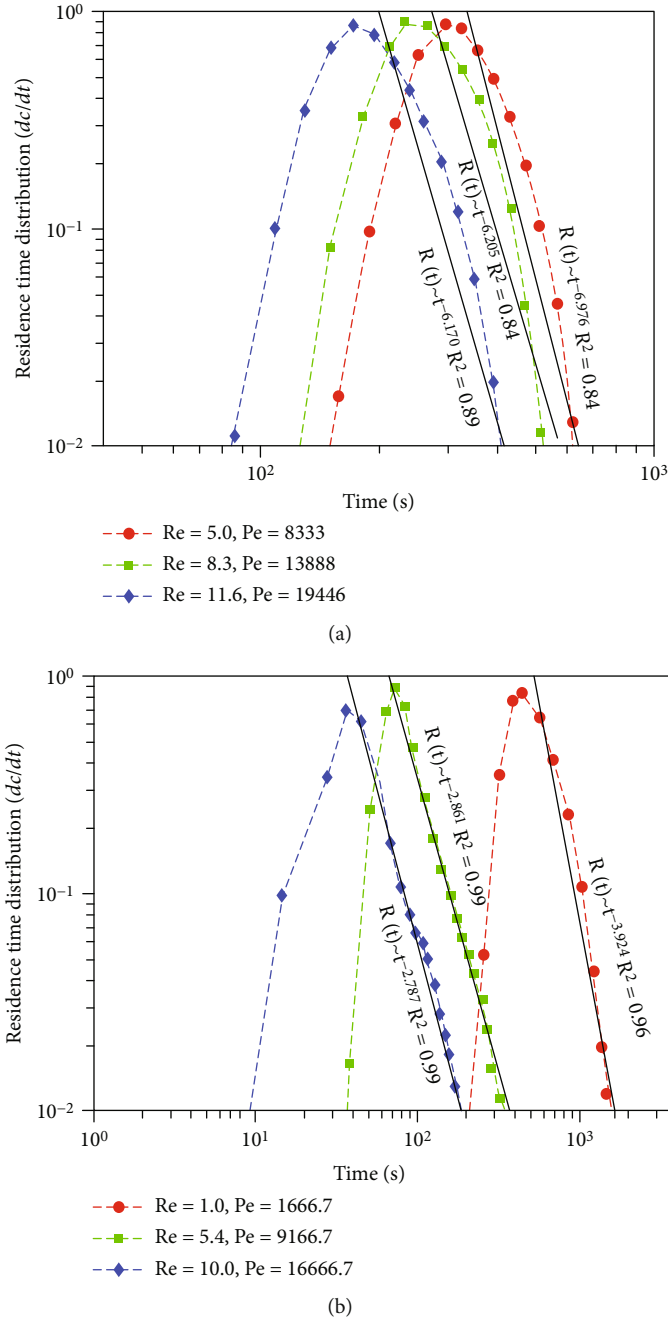
Figure 4: The corresponding RTDs for the single fracture in pattern 1 of group 1 (a) and pattern 1 of group 2 (b) with different Pe.

is obviously less than 100 [47]. The Pe for the experiments ranges from 7693 to 19446 which are over 4000, indicating that molecular diffusion and transverse dispersion in the laboratory experiments can be negligible, and advection and mechanical dispersion in the flow direction made the main contribution [18, 48, 49].

To analyze the transport processes of the solute, the RTDs are calculated under different Pe as equation (6). Figure 4 shows the RTDs for BBF transport in the granite fracture with the aperture of 1.71 mm (Figure 4(a)) and the RTDs for that in the smooth fracture with the aperture of 2 mm (Figure 4(b)).

When the solute transport follows Fick's law, the BTC should present Gaussian distribution and the corresponding RTD will tend to be symmetric as shown in Figure 4(a). On the contrary, the tailing behaviors can be observed as the power-law drop in the RTDs if the non-Fickian transport occurs as shown in Figure 4(b).

If the solute transport process follows Fick's law, the value of RTD after the peak will drop sharply rather than following the power law. To evaluate the degree of tailing behavior, the RTD value after the peak is fitted with power function of time and the r^2 is calculated. As seen in Figure 4(a), the three RTDs all present nearly inverted
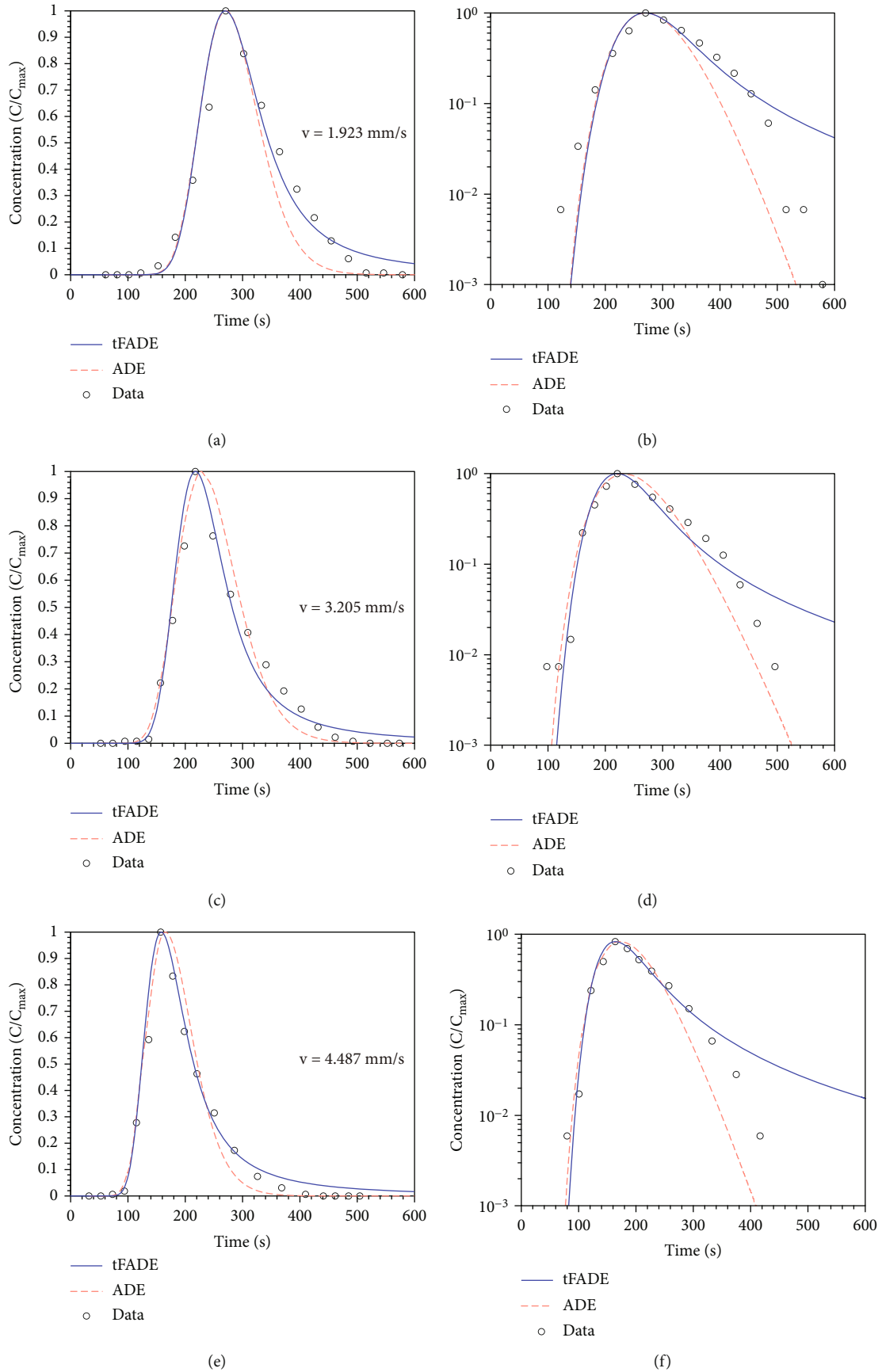
Figure 5: Fitting BTCs for the BBF transport using tFADE and ADE in the granite fracture with flow velocities.

TABLE 3: Model errors for the BBF transport in the granite fracture with 2.60 mm aperture.

| Model | ADE | | tFADE | |
Velocity (mm/s)	r^2	RMSE	r^2	RMSE
1.923	0.915	0.094	0.964	0.058
3.205	0.961	0.067	0.969	0.055
4.487	0.967	0.064	0.976	0.050

"U"-shaped curves indicating that the RTDs follow Gaussian distribution and the power-law tailing behavior does not happen. With the increase of Re and Pe, the r^2 of the power-law function increases. It indicates that the transport pattern is changing into non-Fickian transport. Fitting results with power function in Figure 4(b) show the obvious power-law decay of RTDs. The larger Re and Pe, controlled by adjusting the flow velocity, lead to the larger fitted exponent increase which indicates the heavier tail. This phenomenon is consistent with the study of Dou et al. [50]. The increasing exponents may be due to the growth of the recirculation zones and eddy which lead to multirate exchange processes with the increasing Re [13]. The increase of Re and Pe will lead to the heterogeneity of the flow field, thus affecting the migration of solute and making the tailing behavior more obvious.

The convection plays a dominant role in the transport process in this study, which is controlled by the velocity field. It has been revealed that the RTDs tend to be more symmetric and follow a Gaussian distribution with the increase of travel distance which leads to the scaling effect [37, 48]. The traveling distance and the structure of the velocity field may be the main cause which leads to the difference of BTCs in the two groups of experiments. It should be mentioned that time is taken as the x-coordinate instead of the analyzed pore volume because the sampling method is used to measure the concentration of BBF in this study and the early arrival behavior was hard to be observed accurately. The tailing behavior as the typical characteristic of the subdiffusion was mainly discussed in this paper.

4.2. Model Comparison in the Weak Non-Fickian Transport Case. In order to evaluate the precision of the tFADE, the ADE and the tFADE are employed to fit the measured BTCs of BBF transport. Figure 5 shows the measured and fitted BTCs in group 1. To better observe the capacity of capturing the tailing behavior of the tFADE, logarithmic coordinates are set. A more gradual drop can be noticed in the BTC fitted by the tFADE than those fitted by the ADE. The relatively slow drop is controlled by the fractional-order α. The declining α delays the arrival of the peak at the same time. In the case of Fickian transport, the advantages of the tFADE are not obvious.

The associated values of RMSE and r^2 for the ADE and the tFADE are summarized in Table 3. The coefficient r^2 value is greater than 0.9, and RMSE is less than 0.1, illustrating the satisfactory precision of both the tFADE and the

ADE in fitting BBF transport. The fitting errors of the tFADE are close to those of the ADE.

4.3. Model Comparison in the Anomalous Transport Case. To compare the performance of the tFADE in capturing the BBF transport in a single smooth or rough fracture, the BTCs for transport are fitted by the two models. The fitted BTCs for the fracture with an average aperture of 4 mm are shown in Figure 6, and the log charts are shown in the inserts. Tailing behaviors can be observed in the BTCs, and a more obvious phenomenon can be found in the rough fracture. The roughness elements enhance the retardation of BBF transport, which leads to subdiffusion. The difference between the fitting results of the tFADE and ADE is obvious. Though the ADE can capture the peak of the measured BTCs approximately, it cannot be used to capture the latter half of BTCs. In contrast, the tFADE can capture the trends of the measured BTCs overall and the tailing behaviors can be accurately described.

Besides the global error, the errors of the measured BTC are also calculated after the peak value using the two models. As shown in Table 4, the tFADE is more effective than the ADE in the rough fractures by comparing the r^2 and RMSE values. The tFADE is a precise model to capture solute transport in the fracture when non-Fickian transport happens especially in the fracture with complex morphology. Comparing the error in the phase of concentration decline, the precision of the tFADE is obviously improved for the rough fracture, which indicates the advantage of the tFADE in capturing the tailing behaviors.

The errors of the tFADE and ADE in the experiments of group 2 are presented in Figure 7. The circular and square markers represented the errors for the rough and smooth case, respectively. The dotted line is drawn as a reference for the accuracy comparison between the two models. Most of the points are distributed in the upper left part in the dotted line, indicating that the fitting accuracy of the tFADE is better than that of the ADE. As shown in Figure 7, the circular markers distribute on the left of the square markers indicating that the superiority of the tFADE is more obvious in capturing the transport process in the rough fracture. The subplot of Figure 7 presents RMSE comparison between the two models, and a similar phenomenon can be summarized as the major. The roughness elements affect the BBF transport by causing recirculation zones which enhance the heterogeneity of the flow field dictating the mass transfer [12, 51, 52]. The fractional operator has obvious advantages in capturing BBF transport in heterogeneous flow fields in the single fracture.

4.4. Fitting Parameters of the tFADE. The responses of fitting parameters of the tFADE to experimental conditions are summarized in Table 5. V_1 is the measured average flow velocity. V_2 is the best-fit flow velocity, and D is the diffusion coefficient. In Table 5, V_2 is much less than V_1 in both two groups of experiments. It should be noted that V_1 there represents the average flow velocity and the transport velocity of the BBF can be affected by the local velocity variability which
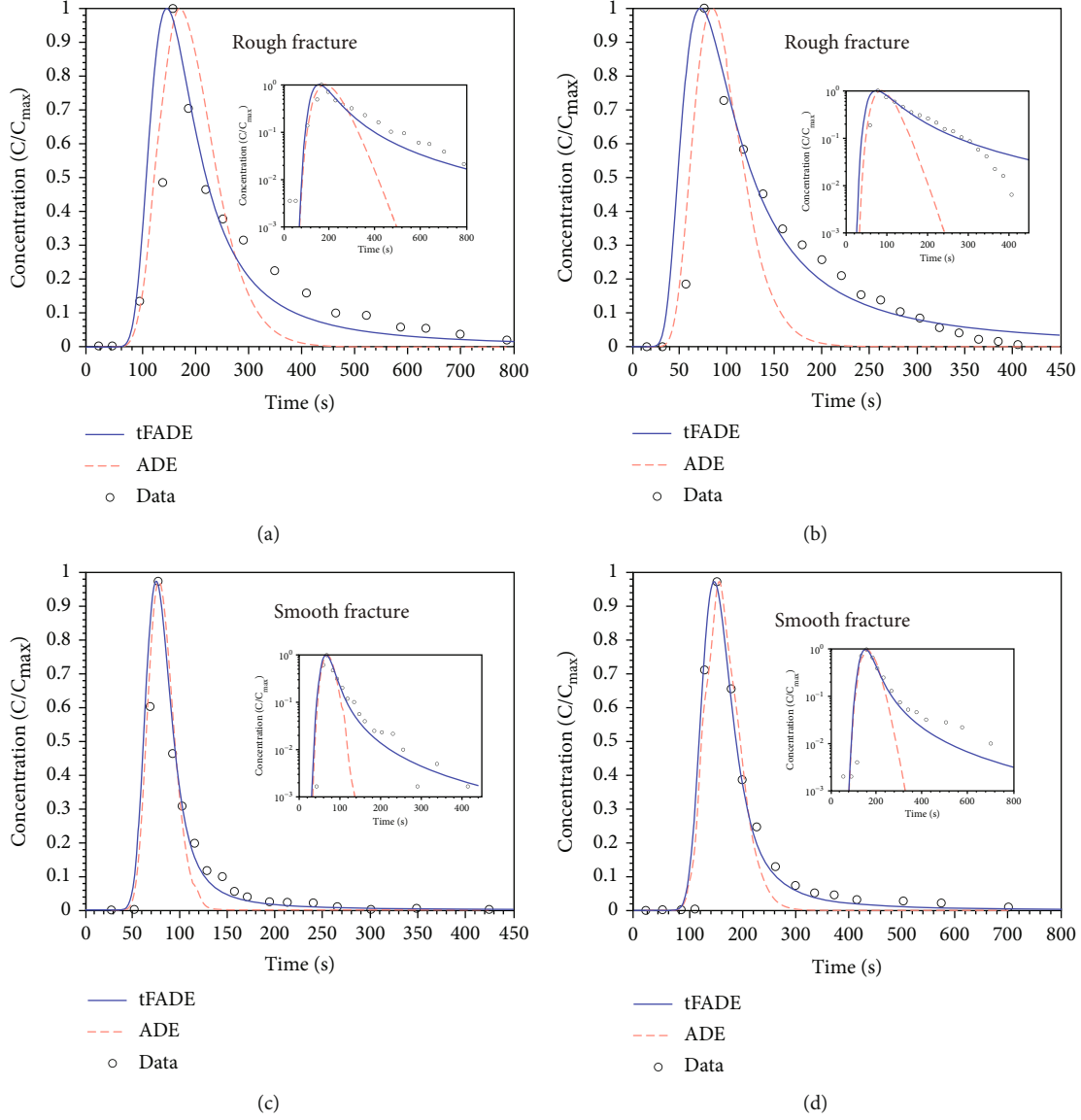
Figure 6: Fitting BTCs for the BBF transport using tFADE and ADE in the rough fracture (a, b) and the smooth fracture (c, d) with the average aperture of 4 mm.

Table 4: Model errors for the BBF transport in the plexiglass fracture with average aperture of 2 mm.

Model		ADE				tFADE			
Velocity (mm/s)	$\triangle/e$	r^2	RMSE	r^2_{tail}	$RMSE_{tail}$	r^2	RMSE	r^2_{tail}	$RMSE_{tail}$
1.375	1	0.855	0.137	0.866	0.142	0.967	0.051	0.972	0.054
2.5	1	0.758	0.154	0.786	0.161	0.984	0.035	0.984	0.037
2.75	0	0.949	0.768	0.952	0.077	0.956	0.066	0.993	0.026
5	0	0.925	0.080	0.934	0.080	0.917	0.078	0.995	0.019

may be caused by fracture heterogeneity [53]. It may be the reason for the deviation of V_2 and V_1. With the increase of measured flow velocity, V_2 also presents an increasing trend. As the pattern two of group 2 shown in Table 6, V_2 decreases with the increase of average aperture which results in the decreasing flow velocity with the increasing mean aperture. It indicates that V_2 decreases with the increasing

aperture in the smooth single fracture. The same trend can be found in the rough fracture. It is because the flow rate is constant in each experiment of group 2. The increasing aperture causes a wider flow section which leads to the decrease of flow velocity.

Dispersion coefficient (D), as a physical parameter to consider the heterogeneity of the fracture, is affected by the
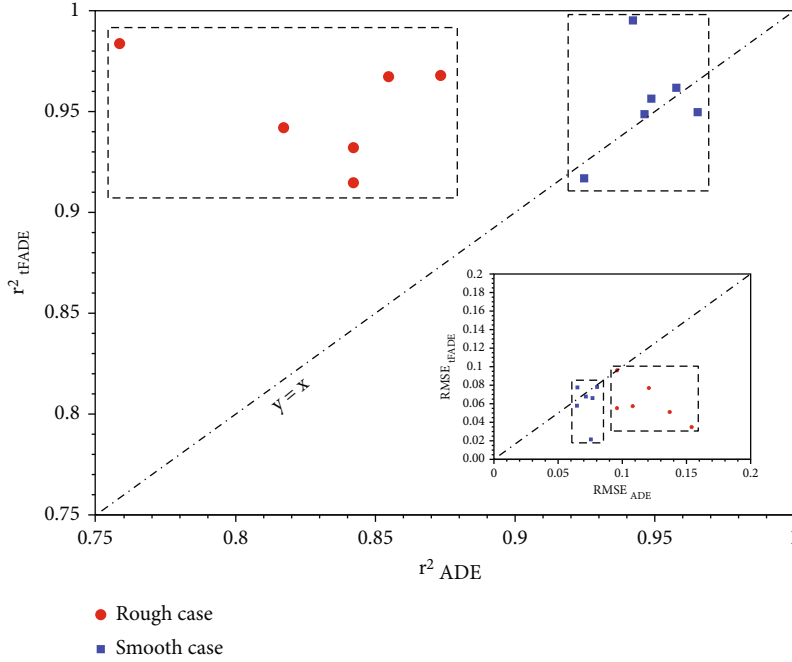
FIGURE 7: Scatter diagram of r^2 and RMSE for the tFADE and ADE in the group 2.

TABLE 5: Fitting parameters by the tFADE in the experiments of group 1.

Pattern	e (mm)	$\triangle/e$	V_1 (mm/s)	V_2 (mm/s$^\alpha$)	D (10^{-4} m^2/s$^\alpha$)	α	r^2	RMSE
	1.71	0.09	2.924	0.128	1	0.924	0.9853	0.0385
	1.71	0.09	4.873	0.151	1	0.920	0.9794	0.0473
	1.71	0.09	6.823	0.220	1	0.916	0.9231	0.0961
Pattern 1	2.60	0.1	1.923	0.137	1	0.930	0.9636	0.0582
	2.60	0.1	3.205	0.170	1	0.925	0.9692	0.0547
	2.60	0.1	4.487	0.247	1	0.898	0.9756	0.0503
	2	0.34	2.308	0.092	1	0.949	0.9650	0.0600
	2	0.34	3.846	0.149	1	0.947	0.9695	0.0548
Pattern 2	2	0.34	5.385	0.274	1	0.930	0.9789	0.0480
	3	0.23	1.538	0.110	1	0.968	0.9590	0.0586
	3	0.23	2.564	0.167	1	0.947	0.9804	0.0416
	3	0.23	3.590	0.311	1	0.889	0.9815	0.0410

hydraulic aperture in the previous studies. However, the variation in this study was negligible (Tables 5 and 6). This is because D is much lower than the flow velocity, and Pe in our experiments is over 4×10^3 in which case the transverse dispersion is negligible [8, 23]. Thus, it can be considered as a constant value for every single group of experiments.

The value of the fractional derivative order (α) is an important parameter to describe the anomalous diffusion. In Table 5, α is insensitive to the variation of the measured flow velocity in both the granite and the plexiglass fractures in the range of 0.898 to 0.930. The inconspicuous range of the order indicated the unremarkable variation of the solute retention time. This is because the increasing Re is the cause of the growth of recirculation zones while the Re was small in these experiments [54]. In addition, the geometry structure of the fracture also affects the streamline and leads to

the anomalous transport. As seen in pattern two of group 1, the value of α decreased with the increase of the flow velocity which indicated the longer retention time of solute transport with the enhancing of the heterogeneity of the flow field.

The aperture is another factor affecting the value of α. As seen in Table 6, the value of α increased with the average aperture in pattern 2 of group 2, while the trend is not obvious in the pattern 1. It should be noted that the roughness of the fracture in pattern 2 is constant with the increase of the average aperture, while it decreases in pattern 1. When the aperture of the fractures increased, heterogeneity of the flow field attenuates and anomalous transport tends to approximate normal transport. The roughness of fractures contributes to secondary flows in the flow field such as eddies which partly interferes with the solute transport process

TABLE 6: Fitting parameters by the tFADE in the experiments of group 2.

Pattern	e (mm)	$\triangle/e$	V_1 (mm/s)	V_2 (mm/s$^\alpha$)	D (10^{-4} m^2/s$^\alpha$)	α	r^2	RMSE
	4	1	1.375	0.3	4	0.850	0.9673	0.0511
	4	1	2.5	0.7	4	0.765	0.9837	0.0348
Pattern 1	5	0.8	1.1	0.396	4	0.840	0.9420	0.0770
	5	0.8	2	0.672	4	0.845	0.9147	0.0960
	6	0.67	0.917	0.275	4	0.855	0.9321	0.0552
	6	0.67	1.67	0.504	4	0.842	0.9679	0.0574
	2	0	2.75	0.528	4	0.894	0.9564	0.0661
	2	0	5	0.969	4	0.890	0.9169	0.0781
Pattern 2	3	0	1.83	0.324	4	0.927	0.9497	0.0776
	3	0	3.33	0.608	4	0.938	0.9618	0.0579
	4	0	1.375	0.236	4	0.931	0.9952	0.0215
	4	0	5	0.498	4	0.942	0.9487	0.0678

[13, 55]. Hence, comparing to α in the smooth case, the value of α in the rough fracture in the same average aperture is relatively smaller overall indicating the complex transport process. The roughness elements were set with sharp corners in this work which caused resistance to flow and generated eddies to affect the transport process heavily [56].

5. Summary and Conclusions

In this work, two groups of experiments on BBF transport with different fracture media, relative roughness, flow rates, and fracture apertures were conducted. The potential cause of anomalous transport case was discussed briefly. The classical ADE and the tFADE were applied to capture the measured breakthrough curves (BTCs), and both Fickian and non-Fickian transports were conducted to evaluate the performance of the tFADE. The response of the fitting parameters and fitting errors of the tFADE was qualitatively analyzed. The main findings drawn from the experimental and fitting results are summarized as follows:

(1) The experimental results showed that the more obvious tailing behavior occurred under the relatively short solute transport distance. Relatively larger Pe enhanced the non-Fickian effect, and the measured RTDs demonstrated a notable power-law drop

(2) The fitting results show that when non-Fickian transport is inconspicuous, both the ADE and tFADE can capture the transport process with satisfactory precision. However, when tailing behaviors which represent the non-Fickian transport occur, the classical ADE fails to capture the transport process while the tFADE can describe it well, especially in the reduction stage after the peak

(3) An analysis of the physical meaning and response of the parameters of the tFADE indicates that the best-fit velocity presented a similar trend as the flow velocity increased. The best-fit velocity is notably smaller than the measured value. With the aperture increasing, the value of the fractional derivative

order increased indicating the relatively low heterogeneity. The rough elements caused the eddy in the flow field and enhanced the heterogeneity, which lead to a smaller α

The tFADE conducted in this study provides a precise approach for capturing the solute transport process in single fractures. The contribution of this study is to provide understanding of the applicability and parameter responses of the tFADE which help better understand the physical meaning of the model. Since artificial roughness was considered in this study, the performance of the tFADE in rougher fractures and the sensibility of the fractional order to the roughness should be further investigated. The limitation of this study is that the flow velocity was considered as stable, while in reality, it might be variable temporally.

Nomenclature

α: The order of fractional differentiation (−)
C: The concentration of the solute (NL^{-3})
C_0:   The dimensionless injected concentration (−)
C_p: The dimensionless concentration under pulse injection condition (−)
C_s: The dimensionless concentration under step injection condition (−)
d: The apparent fracture aperture (L)
D: The dispersion coefficient (L^2T^{-1})
D_m: The molecular diffusion coefficient (L^2T^{-1})
μ: The dynamic fluid viscosity ($ML^{-1}T^{-1}$)
Pe: Peclet number (−)
Q: The flow rate (L^3T^{-1})
r^2:   The coefficient of determination (−)
Re: Reynolds number (−)
RMSE: The root mean square error (−)
ρ: The fluid density (ML^{-3})
t: The time (T)
t_0:   The duration of solution injection (T)
t':   The dimensionless time (−)
v: The average flow velocity (LT^{-1})

V: The advective velocity (LT^{-1})
V_f: The volume of the fracture (L^3)
x: The spatial coordinate of the solute along the direction of flow (L).

Data Availability

The data that support the findings of this study are available from the corresponding author, Yong Liu, upon reasonable request.

Conflicts of Interest

The authors declare that they have no known competing financial interests or personal relationships that could have appeared to influence the work reported in this paper.

Acknowledgments

References

[1] C. Cherubini, C. I. Giasi, and N. Pastore, "Evidence of non-Darcy flow and non-Fickian transport in fractured media at laboratory scale," *Hydrology and Earth System Sciences*, vol. 17, no. 7, pp. 2599–2611, 2013.

[2] L. Zou, L. Jing, and V. Cvetkovic, "Modeling of solute transport in a 3D rough-walled fracture–matrix system," *Transport in Porous Media*, vol. 116, no. 3, pp. 1005–1029, 2017.

[3] G. Moradi and B. Mehdinejadiani, "Modelling solute transport in homogeneous and heterogeneous porous media using spatial fractional advection-dispersion equation," *Soil and Water Research*, vol. 13, no. 1, pp. 18–28, 2018.

[4] G. Moradi and B. Mehdinejadiani, "An experimental study on scale dependency of fractional dispersion coefficient," *Arabian Journal of Geosciences*, vol. 13, no. 11, 2020.

[5] Y. W. Tsang, C. F. Tsang, F. V. Hale, and H. Rock, "Tracer transport in a stochastic continuum model of fractured media," *Water Resources Research*, vol. 32, no. 10, pp. 3077–3092, 1996.

[6] M. Dentz, A. Cortis, H. Scher, and B. Berkowitz, "Time behavior of solute transport in heterogeneous media: transition from anomalous to normal transport," *Advances in Water Resources*, vol. 27, no. 2, pp. 155–173, 2004.

[7] Z. Chen, J. Qian, and H. Qin, "Experimental study of the non-darcy flow and solute transport in a channeled single fracture," *Journal of Hydrodynamics*, vol. 23, no. 6, pp. 745–751, 2011.

[8] F. Bauget and M. Fourar, "Non-Fickian dispersion in a single fracture," *Journal of Contaminant Hydrology*, vol. 100, no. 3–4, pp. 137–148, 2008.

[9] B. Mohammadi and B. Mehdinejadiani, "Numerical simulation of solute transport in saturated porous media with bounded domains," *Groundwater*, vol. 59, pp. 892–904, 2021.

[10] J. Zhou, C. Li, L. Wang, H. Tang, and M. Zhang, "Effect of slippery boundary on solute transport in rough-walled rock fractures under different flow regimes," *Journal of Hydrology*, vol. 598, article 126456, 2021.

[11] Z. Wang, C. Zhou, F. Wang, C. Li, and H. Xie, "Channeling flow and anomalous transport due to the complex void structure of rock fractures," *Journal of Hydrology*, vol. 601, article 126624, 2021.

[12] J. Zhou, L. Wang, Y. Chen, and M. B. Cardenas, "Mass transfer between recirculation and main flow zones: is physically based parameterization possible?," *Water Resources Research*, vol. 55, no. 1, pp. 345–362, 2019.

[13] S. H. Lee, I. W. Yeo, K. K. Lee, and R. L. Detwiler, "Tail shortening with developing eddies in a rough-walled rock fracture," *Geophysical Research Letters*, vol. 42, no. 15, pp. 6340–6347, 2015.

[14] B. Berkowitz, A. Cortis, M. Dentz, and H. Scher, "Modeling non-fickian transport in geological formations as a continuous time random walk," *Reviews of Geophysics*, vol. 44, no. 2, pp. 1–49, 2006.

[15] S. Geiger, A. Cortis, and J. T. Birkholzer, "Upscaling solute transport in naturally fractured porous media with the continuous time random walk method," *Water Resources Research*, vol. 46, no. 12, pp. 1–13, 2010.

[16] M. Fourar and G. Radilla, "Non-Fickian description of tracer transport through heterogeneous porous media," *Transport in Porous Media*, vol. 80, no. 3, pp. 561–579, 2009.

[17] W. E. Bardsley, "Temporal moments of a tracer pulse in a perfectly parallel flow system," *Advances in Water Resources*, vol. 26, no. 6, pp. 599–607, 2003.

[18] Z. Chen, H. Zhan, G. Zhao, Y. Huang, and Y. Tan, "Effect of roughness on conservative solute transport through synthetic rough single fractures," *Water (Switzerland)*, vol. 9, no. 9, 2017.

[19] A. Cortis and J. Birkholzer, "Continuous time random walk analysis of solute transport in fractured porous media," *Water Resources Research*, vol. 44, no. 6, pp. 1–11, 2008.

[20] A. Nowamooz, G. Radilla, M. Fourar, and B. Berkowitz, "Non-Fickian transport in transparent replicas of rough-walled rock fractures," *Transport in Porous Media*, vol. 98, no. 3, pp. 651–682, 2013.

[21] M. T. Genuchten and P. J. Wierenga, "Mass transfer studies in sorbing porous media I. Analytical solutions," *Soil Science Society of America Journal*, vol. 40, no. 4, pp. 473–480, 1976.

[22] L. Sun, H. Qiu, C. Wu, J. Niu, and B. X. Hu, "A review of applications of fractional advection–dispersion equations for anomalous solute transport in surface and subsurface water," *Wiley Interdisciplinary Reviews: Water*, vol. 7, no. 4, pp. 1–21, 2020.

[23] J. Qian, H. Zhan, Z. Chen, and H. Ye, "Experimental study of solute transport under non-Darcian flow in a single fracture," *Journal of Hydrology*, vol. 399, no. 3–4, pp. 246–254, 2011.

[24] R. Schumer, M. M. Meerschaert, and B. Baeumer, "Fractional advection-dispersion equations for modeling transport at the Earth surface," *Journal of Geophysical Research: Earth Surface*, vol. 114, no. 4, pp. 1–15, 2009.

[25] H. Sun, Y. Wang, J. Qian, Y. Zhang, and D. Zhou, "An investigation on the fractional derivative model in characterizing sodium chloride transport in a single fracture*," *European Physical Journal Plus*, vol. 134, no. 9, 2019.

[26] D. A. Benson, S. W. Wheatcraft, and M. M. Meerschaert, "Application of a fractional advection-dispersion equation," *Water Resources Research*, vol. 36, no. 6, pp. 1403–1412, 2000.

[27] Q. Huang, G. Huang, and H. Zhan, "A finite element solution for the fractional advection-dispersion equation," *Advances in Water Resources*, vol. 31, no. 12, pp. 1578–1589, 2008.

[28] D. A. Benson, M. M. Meerschaert, and J. Revielle, "Fractional calculus in hydrologic modeling: a numerical perspective," *Advances in Water Resources*, vol. 51, pp. 479–497, 2013.

[29] B. Ross, "The development of fractional calculus 1695-1900," *Historia Mathematica*, vol. 4, no. 1, pp. 75–89, 1977.

[30] B. Mehdinejadiani and P. Fathi, "Analytical solutions of space fractional Boussinesq equation to simulate water table profiles between two parallel drainpipes under different initial conditions," *Agricultural Water Management*, vol. 240, article 106324, 2020.

[31] H. Jafari, B. Mehdinejadiani, and D. Baleanu, "Fractional calculus for modeling unconfined groundwater," *Applications in Engineering, Life and Social Sciences*, vol. 7, pp. 119–138, 2019.

[32] R. Metzler and J. Klafter, "The random walk's guide to anomalous diffusion: a fractional dynamics approach," *Physics Reports*, vol. 339, no. 1, pp. 1–77, 2000.

[33] X. Li, Y. Zhang, D. M. Reeves, and C. Zheng, "Fractional-derivative models for non-Fickian transport in a single fracture and its extension," *Journal of Hydrology*, vol. 590, article 125396, 2020.

[34] R. M. Garrard, Y. Zhang, S. Wei, H. G. Sun, and J. Qian, "Can a time fractional-derivative model capture scale-dependent dispersion in saturated soils?," *Groundwater*, vol. 55, no. 6, pp. 857–870, 2017.

[35] F. Liu, V. V. Anh, I. Turner, and P. Zhuang, "Time fractional advection-dispersion equation," *Journal of Applied Mathematics and Computing*, vol. 13, no. 1–2, pp. 233–245, 2003.

[36] R. Schumer, D. A. Benson, M. M. Meerschaert, and B. Baeumer, "Fractal mobile/immobile solute transport," *Water Resources Research*, vol. 39, no. 10, pp. 1–12, 2003.

[37] L. Zou, L. Jing, and V. Cvetkovic, "Assumptions of the analytical solution for solute transport in a fracture- matrix system," *International Journal of Rock Mechanics and Mining Sciences*, vol. 83, pp. 211–217, 2016.

[38] M. Dejam, H. Hassanzadeh, and Z. Chen, "Shear dispersion in a fracture with porous walls," *Advances in Water Resources*, vol. 74, pp. 14–25, 2014.

[39] D. L. Koch and J. F. Brady, "Nonlocal dispersion in porous media: nonmechanical effects," *Chemical Engineering Science*, vol. 42, no. 6, pp. 1377–1392, 1987.

[40] Z. Dou, B. Sleep, H. Zhan, Z. Zhou, and J. Wang, "Multiscale roughness influence on conservative solute transport in self-affine fractures," *International Journal of Heat and Mass Transfer*, vol. 133, pp. 606–618, 2019.

[41] L. Wang and M. B. Cardenas, "Transition from non-Fickian to Fickian longitudinal transport through 3-D rough fractures: scale-(in)sensitivity and roughness dependence," *Journal of Contaminant Hydrology*, vol. 198, pp. 1–10, 2017.

[42] C. Yu, A. W. Warrick, and M. H. Conkin, "A moment method for analyzing breakthrough curves of step inputs," *Water Resources Research*, vol. 35, no. 11, pp. 3567–3572, 1999.

[43] M. Flury and H. Flühler, "Brilliant blue FCF as a dye tracer for solute transport studies-a toxicological overview," *Journal of Environmental Quality*, vol. 23, no. 5, pp. 1108–1112, 1994.

[44] M. Flury and H. Flühler, "Tracer characteristics of brilliant blue FCF," *Soil Science Society of America Journal*, vol. 59, no. 1, pp. 22–27, 1995.

[45] J. Cai, Z. Zhou, and Y. Huang, "Laboratory experiments on solute transport in a partial transfixion single fracture," *Journal of Hydrodynamics*, vol. 23, no. 5, pp. 570–579, 2011.

[46] T. Kone, F. Golfier, L. Orgogozo et al., "Impact of biofilm-induced heterogeneities on solute transport in porous media," *Water Resources Research*, vol. 50, no. 11, pp. 9103–9119, 2014.

[47] V. Tzelepis, K. N. Moutsopoulos, J. N. E. Papaspyros, and V. A. Tsihrintzis, "Experimental investigation of flow behavior in smooth and rough artificial fractures," *Journal of Hydrology*, vol. 521, pp. 108–118, 2015.

[48] Y. Liu, Y. Liu, Q. Luo, H. Li, and J. Qian, "Experimental and numerical study of bimolecular reactive transport in a single rough-wall fracture," *Journal of Hydrology*, vol. 594, article 125944, 2021.

[49] D. Bolster, M. Dentz, and T. Le Borgne, "Solute dispersion in channels with periodically varying apertures," *Physics of Fluids*, vol. 21, no. 5, 2009.

[50] Z. Dou, Z. Chen, Z. Zhou, J. Wang, and Y. Huang, "Influence of eddies on conservative solute transport through a 2D single self- affine fracture," *International Journal of Heat and Mass Transfer*, vol. 121, pp. 597–606, 2018.

[51] Q. Zhang, S. Luo, H. Ma, X. Wang, and J. Qian, "Simulation on the water flow affected by the shape and density of roughness elements in a single rough fracture," *Journal of Hydrology*, vol. 573, p. 456, 2019.

[52] M. Dejam, H. Hassanzadeh, and Z. Chen, "Shear dispersion in a rough-walled fracture," *SPE Journal*, vol. 23, no. 5, pp. 1669–1688, 2018.

[53] L. Wang and M. B. Cardenas, "Non-Fickian transport through two-dimensional rough fractures: assessment and prediction," *Water Resources Research*, vol. 50, pp. 871–884, 2014.

[54] D. Bolster, Y. Méheust, T. Le Borgne, J. Bouquain, and P. Davy, "Modeling preasymptotic transport in flows with significant inertial and trapping effects - the importance of velocity correlations and a spatial Markov model," *Advances in Water Resources*, vol. 70, pp. 89–103, 2014.

[55] S. Briggs, B. W. Karney, and B. E. Sleep, "Numerical modeling of the effects of roughness on flow and eddy formation in fractures," *Journal of Rock Mechanics and Geotechnical Engineering*, vol. 9, no. 1, pp. 105–115, 2017.

[56] J. Qian, Z. Chen, H. Zhan, and H. Guan, "Experimental study of the effect of roughness and Reynolds number on fluid flow in rough-walled single fractures: a check of local cubic law," *Hydrological Processes*, vol. 25, no. 4, pp. 614–622, 2011.

WILEY | Hindawi

Research Article
Study on Reasonable Chain Pillar Size in a Thick Coal Seam

Kun Zhang,[1,2] **Fengfeng Wu** [iD]**,**[1,2] **and Xin Yue** [iD][1,2]

[1]*Key Laboratory of Deep Coal Resource Mining, Ministry of Education, China University of Mining and Technology,*
 Xuzhou 221116, China
[2]*School of Mines, China University of Mining and Technology, Xuzhou 221116, China*

Correspondence should be addressed to Fengfeng Wu; wufengfeng@cumt.edu.cn

In order to solve the problem of low coal recovery rate caused by leaving large coal pillars in deep mines, the study determined the reasonable width of the section pillar, which based on the theory of coal pillar stress distribution, taking the 4102 headgate of Wenjiapo coal mine as the engineering background. Field monitoring and numerical simulation results show that the influence range of the lateral abutment pressure in the goaf is 50~56 m, and the abutment stress distribution in the coal pillar resembles a hump with two peaks of 38.9 MPa and 33.6 MPa, respectively. The positions of the double peaks are located at 12 m and 36 m in the coal pillar, respectively. In the range of "hump," the section pillar vertical stress is in the original rock stress and is relatively stable. It can be regarded as an elastic zone in the coal pillar with strong bearing capacity, the coal in other areas have already undergone plastic yielding, and the bearing capacity has been reduced; the width of coal pillars in the determined section has been reduced from 46 m to 33 m, which is a reduction of 13 m. The research results have been applied in the 4106 headgate in the same mining area, and good test results have been obtained. The maximum subsidence of the roof-to-floor and rib-to-rib convergence is 286 mm and 150 mm, this indicates that its deformation was within the allowable limits, and the cross-section area was sufficient to satisfy the requirements.

1. Introduction

More than 90% of underground mines use longwall mining methods, and coal pillar has always been the main way to isolate the goaf and maintain the roadway in Chinese coal mine mining [1]. According to the current research status at home and abroad, there are mainly two ways to retain coal pillar. The first is the wide coal pillar method, which arranges the roadway outside the pressure peak to reduce the damage to the roadway; the other is the yield pillar or nonpillar method, which is used to reduces the width of coal pillar and reduces resource waste [2–4].

The research and development level of the two roadway protection methods also have their own characteristics, and they have been widely used under different conditions. Coal mines in central and western China (Shanxi, Shaanxi, Inner Mongolia, etc.) have gradually entered the stage of deep thick seam mining [5]. However, the actual production process of most existing coal mines has been troubled by the width of coal

pillars, which are mostly 50 m in width. Above, large coal pillars not only cannot be recovered but also easily cause the roadway to be arranged in the stress-increasing area, which is an important reason of major accidents [6–8]. Especially now scientific and green mining is advocated, higher requirements are put forward for the determination of the width of coal pillars.

In terms of theoretical research, domestic and foreign scholars have done a lot of research on coal pillar retention and put forward various theories such as effective area theory, large slab fissure theory, two-zone constraint theory, and limit equilibrium theory [9–12]. Each theory has certain applicable conditions: the effective area theory can only be used when the excavation area is large, the width and interval of the coal pillars are the same, the width of the plastic zone calculated by the large slab crack theory is proportional to the width of the coal pillar, obviously inconsistent with the actual situation, and the two-zone constraint theory believes that the coal pillar is composed of a yield zone and an elastic core zone, which better explains the form of the stress distribution of the coal

pillar, but the selection of the relevant parameters of the formula requires a large amount of on-site measured data or coal and rock strength test.

Domestic research on the distribution of abutment pressure in the coal pillar is mostly based on the theory of limit equilibrium zones. The most important thing for the establishment of related models and theoretical derivation is to establish a reasonable basis for determining the limit equilibrium state [13–16]. Hou et al. deduced the corresponding abutment pressure distribution formula and gave the calculation method of the width of the limit equilibrium zone and applied it in the coal pillar setting of the mining area [17]. Kang et al. explained the setting of coal pillars under different circumstances, such as nonpillar and yield pillar [18–20]. Based on the analysis of the overlying rock movement characteristics of the stope, Zhang et al. clarified the transfer load-bearing mechanism of the roof in the wedge-shaped area on the goaf side and proposed the technical idea of optimizing the residual stress of the coal pillar [21]. Li et al. analyzed the deformation of the roadway surrounding rock under different coal mine geological conditions and found that the factors affecting the stability of yield coal pillar include: coal seam strength, coal seam thickness, coal seam depth, immediate roof strength, influence of driving and mining, support strength, and narrow coal pillar width [22].

Combined with field tests and numerical simulation, the width of section pillar is proved to be reasonable is also studied. The influence law of the reasonable width of the coal pillar is studied, and on this basis, a method that can not only meet the stability requirements of the coal pillar but also improve the resource recovery rate is proposed. The research results will provide a theoretical basis for the economy and safety of section pillar.

2. Background

2.1. Engineering Background. Wenjiapo Mine located in the Binchang coal mining area was a typical Chinese deep coal mine, with an excavation depth of almost 600 m ~700 m below the ground. The shaft station was buried at an average burial depth of 650 m. The entry was a rectangular section with a width of 5.7 m and a height of 3.65 m. The fully mechanized full seam top coal caving mining method was employed. The width of the section pillar is 46 m (see Figure 1), the coal pillar is relatively broken during the mining, and stability of the surrounding rocks of the roadway is bad. The width of the coal pillar needs to be optimized.

The 4102 headgate is in the 4# coal seam, with an average thickness of 4.8 m. The roof rock strata are, in ascending order, mudstone (2.31 m), fine sandstone (1.4 m), mudstone (2.1 m), powder sandstone (8.8 m), and coarse sandstone (10.2 m), while those below are, in descending order, mudstone (2.6 m), medium sandstone (6.7 m), and siltstone (9.1 m). The roadway has a height of 3.65 m and a width of 5.7 m (Figure 2).

2.2. Determination of Rock Mechanic Parameters. In order to have a detailed understanding of the surrounding rock properties of 4102 headgate, the surrounding rock of 4102 headgate was selected to collect coal and rock samples without structural belts and faults, avoiding the construction of the

project, and after the sampling was completed, the PVC was sealed in the underground, after being transported to the laboratory for standardized processing (see Figure 3).

The rock mechanics parameters are measured on the SANS (TAW-2000) microcomputer controlled electrohydraulic servo rock triaxial testing machine (see Figure 4). The maximum axial load of the test system is 2000 kN, the maximum lateral pressure is 500 kN, and the maximum shear load is 500 kN.

After sampling in the 4102 headgate, standard specimens were made, and the rock mechanics performance parameters were measured as shown in Table 1.

3. Theoretical Analysis Stress Distribution in the Coal Pillar

After the roadway excavation is finished, the overburden pressure is redistributed, and a certain range of mining-induced stress zone will be formed in the coal pillar. Due to the influence of the mining-induced stress, it is believed that the coal and rock mass within a certain width of the coal pillar has been damaged. It is generally believed that the abutment pressure at the edge of the coal pillar is zero. As the depth increases, the abutment pressure gradually increases until it reaches the peak value of the vertical stress in the coal pillar [23–25]. The specific area from the coal pillar boundary to the peak vertical stress is called the yield zone and is also called the plastic zone width in the coal pillar [26–28].

3.1. The Vertical Stress Distribution in the Coal Pillar after Working Face Mining. In this section, the coal pillar is divided into inner plastic zone and elastic zone, and the study is carried out according to the quadratic curve. The integrated coal vertical stress in the plastic zone is calculated by the theory of limit equilibrium zone, and the integrated coal stress in the elastic zone is fitted by the Weibull distribution function. Substituting the relevant parameters to obtain the vertical stress in the coal pillar and finally determine the reasonable width of the coal pillar. In theoretical calculations, some necessary assumptions should be made to make the answer to the problem simple. The basic assumptions are [29–31] as follows:

(1) The coal pillar is regarded as an ideal elastic body, which conforms to the reasonable assumptions of continuity, complete elasticity, uniformity, and isotropy in elastic mechanics

(2) The internal shear damage in the coal pillar obeys the Mohr Coulomb criterion

(3) The stress limit equilibrium zone is at the elastic-plastic junction

(4) Before the coal pillar yields, the internal displacement and deformation in the coal pillar are small

After the roadway excavation is finished, the vertical stress distribution in the integrated coal is plotted as curves (see Figure 5).
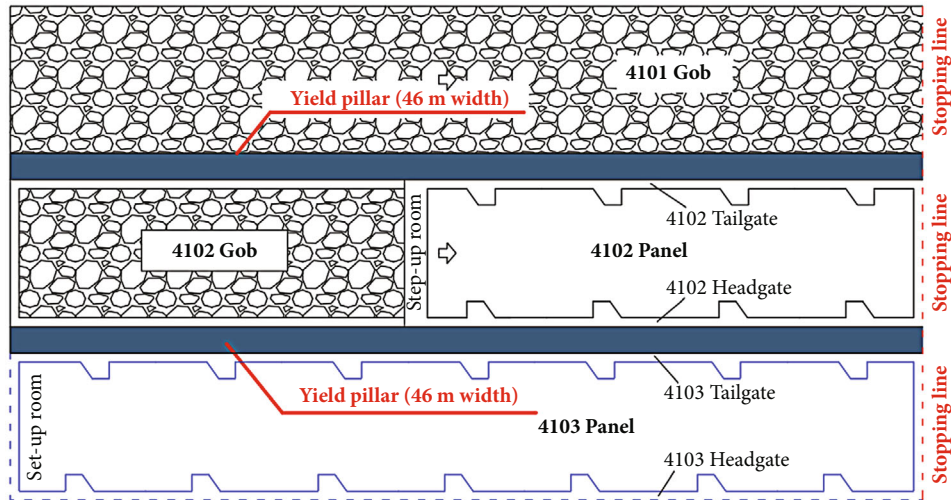
FIGURE 1: Schematic diagram of the project.
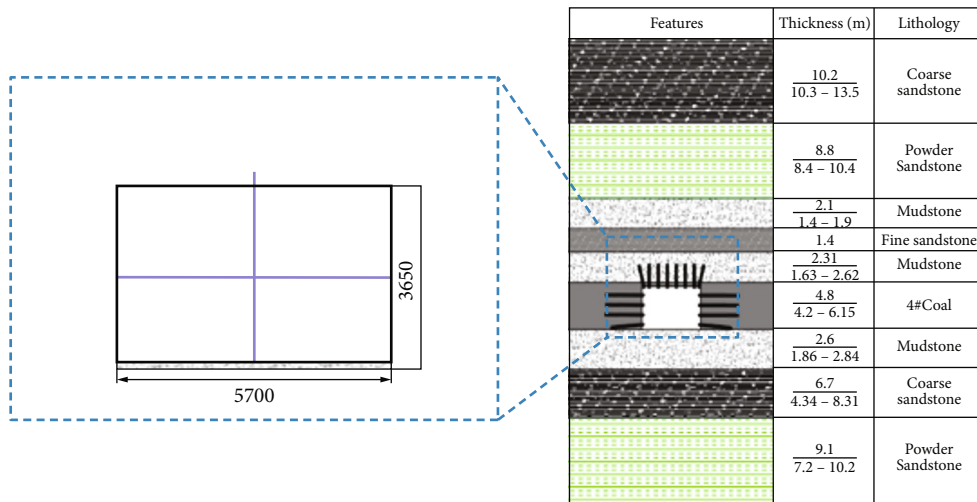
FIGURE 2: The lithological characteristics of the section and surrounding rock of 4102 headgate.
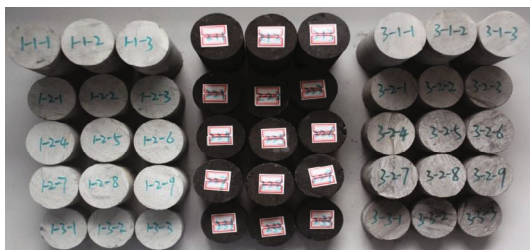
FIGURE 3: No. 4 coal seam rock formation specimens.

FIGURE 4: Experimental system for determining rock mechanical properties.

In Figure 5, $F(\varepsilon)$ is the influence of working face mining on the vertical stress of on the right side of integrated coal, and $f_1(\varepsilon)$ is the influence on the integrated coal stress in the plastic zone. The vertical stress in the plastic zone of coal pillar (lateral abutment pressure) is the limit equilibrium state; $f_2(\varepsilon)$ is the influence on the stress elastic zone of coal pillar [32–34].

TABLE 1: Measurement results of rock mechanical parameters.

Lithology	Compressive strength/ MPa	Shear strength/ MPa	Tensile strength/ MPa	Poisson ratio	Cohesion/ MPa	Friction/°
Silty mudstone	11.3	29	1.8	0.29	6.8	35
Fine sandstone	50.9	86.7	2.8	0.24	13.2	49
Pelitic siltstone	30.4	50.4	2.2	0.28	11.1	36
Coal	5.8	9.1	1.4	0.32	3.4	29
Mudstone	9.7	21.1	1.59	0.3	5.3	32
Medium fine sandstone	46.4	39.5	2.7	0.26	11.7	46
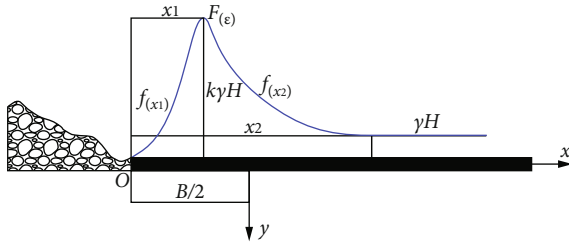
FIGURE 5: Vertical stress distribution in the integrated coal after working face mining.

It can be calculated by formula (1).

$$f_1(\varepsilon) = \left(\frac{C_0}{\tan\varphi} + \frac{p_i}{\lambda_1}\right) e^{\frac{2\tan}{m\lambda_1}(\varepsilon+B/2)} - \frac{C_0}{\tan\varphi}\varepsilon \in [-B/2,\ x_1 - B/2), \quad (1)$$

where C_0 is the coal seam interface cohesion, 6.62 MPa, φ is the internal friction angle of the coal seam interface, 28.81°, p_i is the bolt supporting strength, 0.2 MPa, λ_1 side pressure coefficient in the coal pillar, 1, m the height of the roadway, 3.8 m, B the width of coal pillar, 46 m, x_1 the plastic zone range in the coal pillar after working face mining, m.

The range of the plastic zone is calculated by formula (2):

$$x_1 = \frac{m\lambda_1}{2\tan\varphi}\ln\left[\left(k_1\gamma H + \frac{C_0}{\tan\varphi}\right)/\left(\frac{C_0}{\tan\varphi} + \frac{p_i}{\lambda_1}\right)\right], \quad (2)$$

where k_1 is the increasing coefficient vertical stress in coal pillar during working face mining.

The vertical stress in the coal pillar outside the plastic zone satisfies the Weibull distribution, and the Weibull distribution function expression is

$$w(x) = e\frac{x}{x_w}e^{-\frac{x}{x_w}}, \quad (3)$$

where x is the random variable, the distance from any point of the original rock stress zone to the coal rib, and x_w is the scale parameter.

Combined with the distribution law of the internal stress of the coal pillar outside the plastic zone, substituting the relevant parameters, $f_2(\varepsilon)$ is

$$f_2(\varepsilon) = (k_1 - 1)\gamma H, \varepsilon \in [x_1 - B/2, +\infty), \quad (4)$$

where

$$s = (\varepsilon + x_f + B/2 - x_1)/x_{f_\circ}, \quad (5)$$

where γ is the bulk density, 2.5kN/m³, H is the buried depth of the roadway, 650 m, and x_f is the parameter that adjusts the degree of urgency of the function.

In formula (4), $f_2(\varepsilon)$ is a single-peak function, and when $\varepsilon = x_1 - B/2$, the peak value $f_2(\varepsilon)$ is $k_1\gamma H$. The peak value $f_2(\varepsilon)$ increases with k_1; so, the value of the stress peak can be adjusted by changing it to reflect the degree of influence of the mining face on the peak abutment pressure of the coal pillar center. Increase or decrease x_f to adjust the degree of gradualness and urgency in the $f_2(\varepsilon)$ descending process during the $\varepsilon \longrightarrow +\infty$ process and gradually decrease to the original rock stress as it develops into the deep part of the coal seam. According to the above analysis, it can be seen that the influence of working face mining on the central abutment pressure in the coal pillar is

$$F(\varepsilon) = \begin{cases} \left(\frac{C_0}{\tan\varphi} + \frac{p_i}{\lambda_1}\right)e^{\frac{2\tan\varphi}{m\lambda_1}(\varepsilon+\frac{B}{2})} - \frac{C_0}{\tan\varphi}, \varepsilon \in \left[-\frac{B}{2}, x_1 - \frac{B}{2}\right), \\ (k_1-1)\gamma Hse^{1-s} + \gamma H, \varepsilon \in \left[x_1 - \frac{B}{2}, +\infty\right). \end{cases}$$

$$(6)$$

3.2. Determination of the Reasonable Width of the Coal Pillar. According to the production geological conditions of Wenjiapo Mine and related test results, combined with numerical simulation results, the calculation parameters are as follows: average buried depth of roadway H is 650 m, rock layer density ρ is 2.5×10^3 kg/m³, coal seam thickness h is 4.8 m, bolt supporting strength p_i is 0.2 MPa, coal seam cohesive force C_0 is 6.62 MPa, coal seam internal friction angle φ is 28.81°, integrated coal abutment pressure increases coefficient 1.5 after working face mining, the abutment pressure increase coefficient on one side of the body is 1.3, and the side pressure coefficient in the plastic zone is 1.0.

The basic condition for maintaining the stability of the coal pillar in the roadway protection is as follows: after plastic deformation occurs on both sides of the coal pillar, there is an elastic core with a certain width in the center of the coal

pillar, and the width of the elastic core is not less than twice the height of the coal pillar. Therefore, the reasonable width of coal pillar in the 4102 headgate face is

$$B > x_0 + 2h + x_1,$$
$$x_0 = \frac{h\lambda_1}{2\tan\varphi} \ln\left[\left(k_1\gamma H + \frac{C_0}{\tan\varphi}\right) \Big/ \left(\frac{C_0}{\tan\varphi} + \frac{P_i}{\lambda_1}\right)\right],$$

$$(7)$$

where x_0 is the width of plastic zone on the left side of the coal pillar, x_1 is the width of the plastic zone on the right side of the coal pillar, λ_1 is the increase coefficient of the abutment pressure in the integrated coal after the mining, 1.5, k_1 is the inner stress coefficient in the plastic zone is 1.0, and $\lambda2$ is the increase coefficient of abutment pressure on the side of coal body after excavation of roadway 1.3.

$$x_1 = \frac{h\lambda_2}{2\tan\varphi} \ln\left[\left(k_1\gamma H + \frac{C_0}{\tan\varphi}\right) \Big/ \left(\frac{C_0}{\tan\varphi} + \frac{P_i}{\lambda_1}\right)\right]. \quad (8)$$

Because the width of the coal pillar is different, the width of the corresponding coal pillar's plastic zone is also different. Substituting the parameter to solve formula (8), x_0 is 11.2 m, x_1 is 8.9 m, and B is bigger than 29.7 m.

4. Measurement of Lateral Stress in Working Face

The borehole stress gauge was used to measure the stress distribution in the coal pillar during the 4102 working face mining in order to analyze the stress distribution of the coal pillar. Due to the large coal pillar width, it is difficult to construct horizontal small-diameter deep holes, and the drilling cannot penetrate the 46 m coal pillar. Therefore, the two roadways are arranged equally, and the measuring stations are arranged in front of the workface, that is, the 4102 headgate and the 4103 tailgate. The strain gauges are located 3 m, 6 m, 9 m, 12 m, 15 m, 18 m, and 21 m, within the pillar with a distance of about 1 m (see Figure 6).

After collecting and processing the measured data, the distribution of the abutment pressure in the coal pillar is obtain to draw a curve (see Figure 7).

The lateral abutment pressure in the coal pillar continues to increase with the mining (see Figure 7); the lateral abutment pressure distribution in the coal pillar resembles a hump with two peaks of 38.9 MPa and 33.6 MPa, respectively, and the positions of the double peaks are located 12 m and 36 m in the coal pillar, respectively. The range of the "hump" is roughly 17 m ~34 m. In the range of 17 m width range, the vertical stress in the coal pillar is 15 MPa~20 MPa, which is basically in the original rock stress with small difference. It can be regarded as an elastic zone with a certain width in the coal pillar and has a strong bearing capacity. The analysis shows that the width of the coal pillar can be appropriately reduced, and the width of the "hump" is can be reduced, but it still has enough elastic zone to play the bearing role.

It was suggested that the optimization of coal pillars can reduce the width of the "hump", and its width can be reduced from 46 m to 26~35 m.

5. Numerical Simulation Analysis of Coal Pillar Stress Distribution

Using the FLAC^{3D} software to simulate and analyze the stress distribution in the coal pillar and the deformation and failure process of the two mining roadways to provide guidance for the reasonable determination of the coal pillar width [35–37], the numerical model must meet the following conditions. In order to meet these conditions, the numerical model must have the following steps:

(1) Geometry and geology of the model, based in project information of mining and drilling

(2) Boundary conditions and restrictions on the edges of the model to simulate the continuity of the medium

(3) Material properties (solid rock) are found in the place, being these criteria-based properties of classification

(4) Initial stress field of the model, based on stress measurements or empirical methods

(5) Sequence of excavation of galleries to simulate the redistribution of stresses and displacements of the massif caused by the excavation

(6) Analysis of results to determine whether the rock mass or the type of treatment used for control of deformations is satisfactory (or not).

5.1. Numerical Model. Using FLAC^{3D} software to establish a numerical calculation model according to the geological conditions of Wenjiapo Mine, the model includes No. 4 coal and a total of 28 layers of upper and lower rock formations, and the size of the model is $206 \times 150 \times 91$ m. Horizontal displacement constraints are imposed on the boundaries on both sides and front and rear boundaries, vertical displacement constraints are imposed on the bottom boundary, and uniformly distributed loads are imposed on the upper boundary. The uniformly distributed loads are calculated based on the weight of the overlying rock. The density of the overburden is 2500 kg/m^3, the buried depth of the No. 4 coal seam is determined to be 650 m, the uniform load of 16.95 MPa is applied to the upper part of the model to simulate the weight of the overburden, and the lateral pressure coefficient is 1.

The mechanical parameters of model coal and rock mass are shown in Table 2.

The numerical calculation model is balanced with the initial stress (see Figure 8).

5.2. Simulation of the Original Coal Pillar Width. The vertical stress distribution in the section coal pillars when the 4102 working face is advanced at 0 m, 40 m, 80 m, and 120 m is simulated and calculated the vertical stress distribution in the coal pillar (see Figure 9).
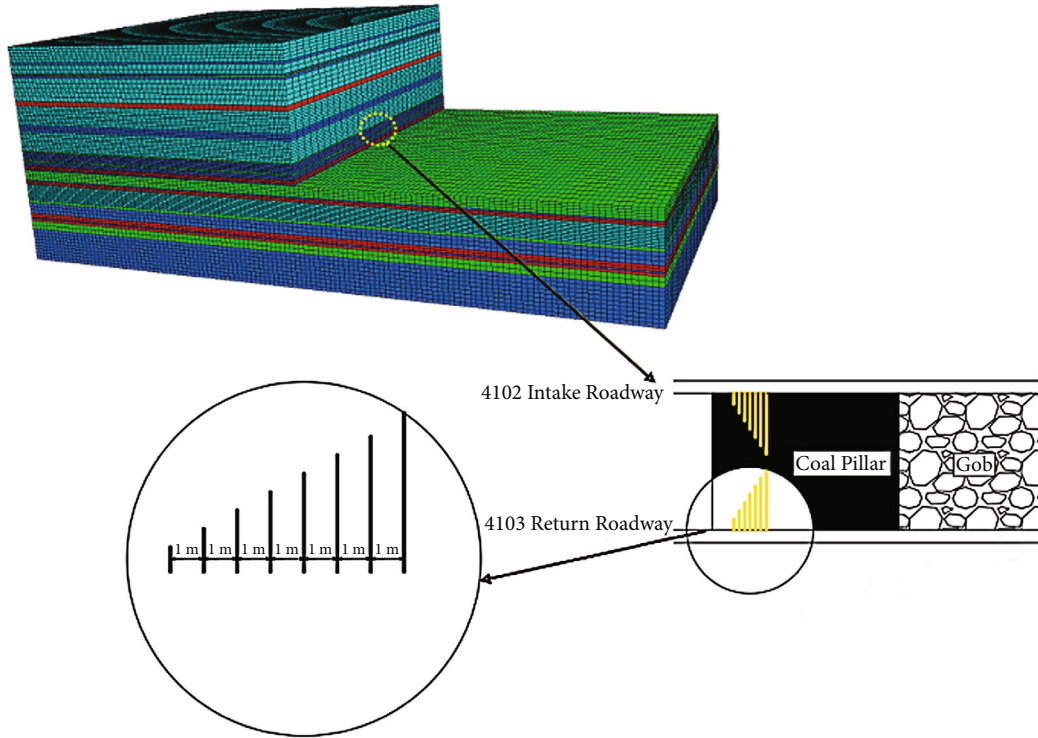
FIGURE 6: Borehole stress gauge monitoring station.
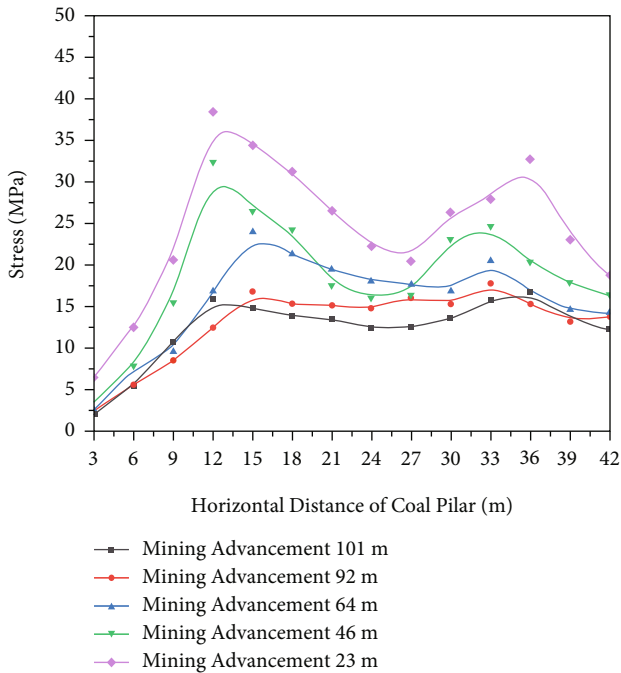
FIGURE 7: Distribution diagram of lateral abutment pressure in the coal pillar.

The vertical stress distribution data obtained by numerical simulation is plotted as curves (Figure 10).

It can be seen from Figure 10 that as the working face advancing, the vertical stress in the coal pillar continues to increase under the influence of mining-induced stress; the

vertical stress distribution curve in the coal pillar resembles "a hump with two peaks" of 33.5 MPa and 34.3 MPa, respectively, the positions of the double peaks of each curve are approximately at 11 m and 37 m in the coal pillar, and the width of "hump" is roughly in the range of 17 m ~36 m. In the range of "hump," the abutment pressure in the coal pillar is 19 MPa~25 MPa, which is close to the stress of primary rock. It can be regarded as a certain width of elastic zone in the coal pillar, which has strong bearing capacity, and the coal in the other ranges has already undergone plastic yielding and only has a certain bearing capacity. The width of the "hump" (see Figure 10) can be appropriately reduced.

5.3. The Abutment Pressure Distribution Law in the Coal Pillar with Different Widths. According to the geological conditions of Wenjiapo Coal Mine, the coal pillar width x is 15 m, 25 m, 33 m, and 46 m, respectively and the abutment pressure distribution law in the coal pillar and the displacement of roadway surrounding rock during roadway driving and mining. The simulation process is divided into 4 steps: the first step is the calculation of the original rock stress balance; the second step is the calculation of the mining influence of the 4103 working face in the upper section; the third step is the roadway driving and bolt support of the 4102 working face in this section protection calculation; the fourth step is calculation of mining influence of 4102 working face in this section. The simulation diagram is shown (see Figure 11), where x is the width of the coal pillars, which are 15 m, 25 m, 33 m, and 46 m, respectively.

In the case of leaving coal pillars with different widths, the vertical stress in the coal pillars distribution was curve can be obtained directly by software (see Figure 12).

TABLE 2: Model parameters.

Lithology	Tensile strength/MPa	Cohesion/MPa	Friction/°	Bulk modulus/GPa	Shear modulus/GPa
Mudstone	1.25	1.70	26.44	0.82	0.49
Sandstone	1.51	1.47	23.16	0.70	0.46
Siltstone	1.43	3.14	35.85	1.07	0.77
Coal	0.72	1.99	26.81	0.35	0.14

(a)

(b)
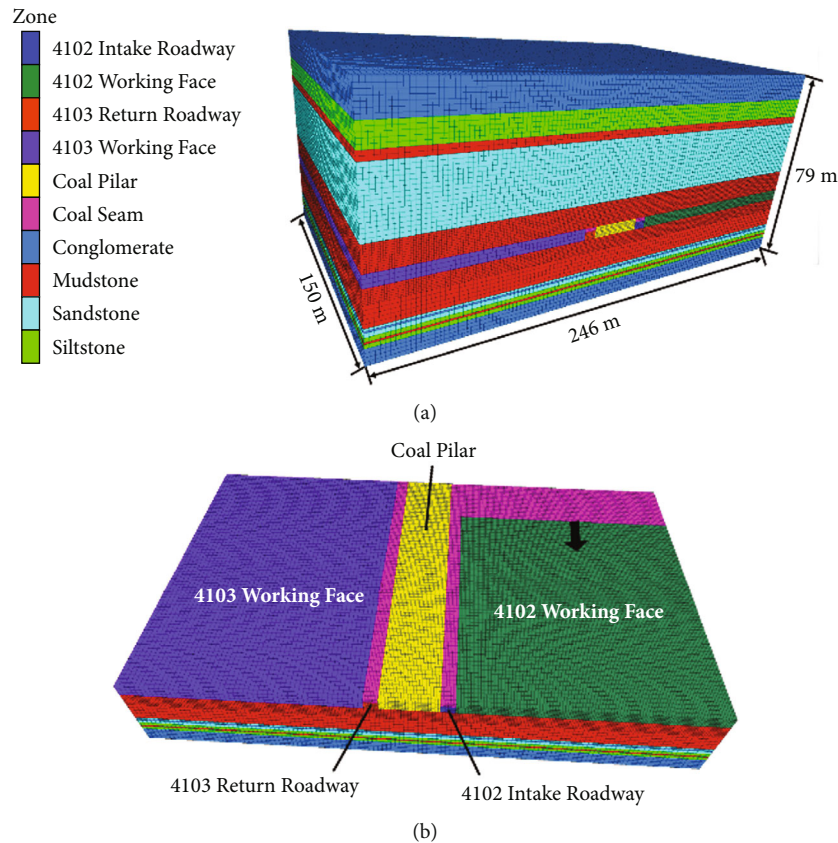
FIGURE 8: Geometric model of simulations.

The vertical stress in the summary simulation results is shown in Figures 13 and 14.

In Figure 13, during the driving of the 4102 headgate, the vertical stress in the coal pillar caused by the different coal pillar width is different:

(a) When the width of the coal pillar is 15 m and 25 m, the stress in the coal pillar presents a single peak parabolic distribution, and the peak position is not in the center of the coal pillar. In the case of 15 m coal pillar, the peak center is biased to the side of the coal pillar near the roadway, and the deviation distance is about 1.5 m; when the coal pillar widens to 25 m, the vertical stress in the coal pillar gradually presents a trapezoidal distribution, and the peak position shifts from the side of the roadway to the side of the goaf. The deviation distance increases with the increase of the width of the coal pillar, and the deviation distance is about 1.5 m

(b) When the coal pillar width is 33 m and 46 m, the stress distribution in the coal pillar is the same as that before the coal pillar width is not reduced. In these two cases, the peak value is in the form of "a hump with two peaks." When the coal pillar is 33 m, the peak value of the coal pillar is at 16 m and 27 m into the coal pillar, and the peak vertical stress in the range of "hump" is close to the original rock stress which can be considered as an elastic core zone with good bearing capacity; when the coal pillar is 44 m, the peak of the coal pillar is 12 m and 27 m deep into the coal pillar

(c) When the coal pillars are 15 m and 25 m, the peak stress of the coal pillar is greater than that of the coal pillars of 33 m and 46 m, because the coal pillar is in the high stress area and the stress concentration of the coal pillar is higher; the first two of the coal pillars plastic zone are larger, because the first two of the coal pillar plastic zone are larger, the abutment pressure

(a) Vertical stress of 0 m advancing the working face

(b) Vertical stress of 40 m advancing the working face

(c) Vertical stress of 80 m advancing the working face

(d) Vertical stress of 120 m advancing the working face
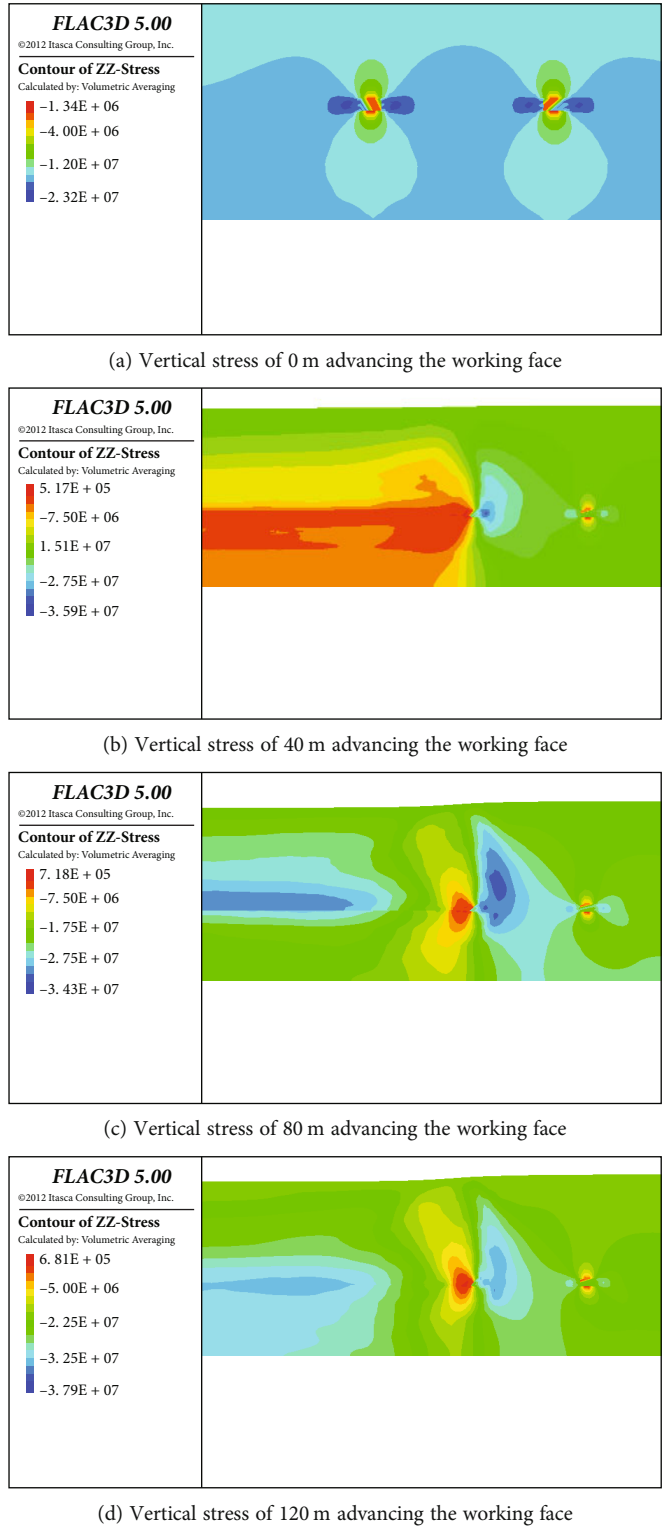
FIGURE 9: Vertical stress diagram of coal pillar during No. 4102 working face mining.

shifts to the deep part of the coal seam, and the coal at the side edge of the goaf is more fragmented

In Figure 14, during the mining of the 4102 working face, the vertical stress in the coal pillar caused by the different coal pillar width is different:

(a) Compared with roadway driving, the vertical stress in the coal pillar is more concentrated during the mining. The most concentrated stress is when the coal pillar width is 25 m. At this time, the peak stress reaches 38.8 MPa, which is 2.4 times the original rock stress; during the mining period, the vertical
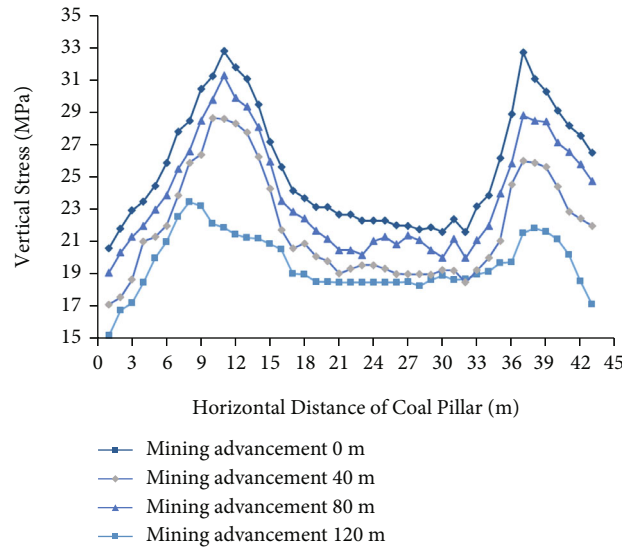
Figure 10: Vertical stress distribution curve of coal pillar during 4102 working face advancing.
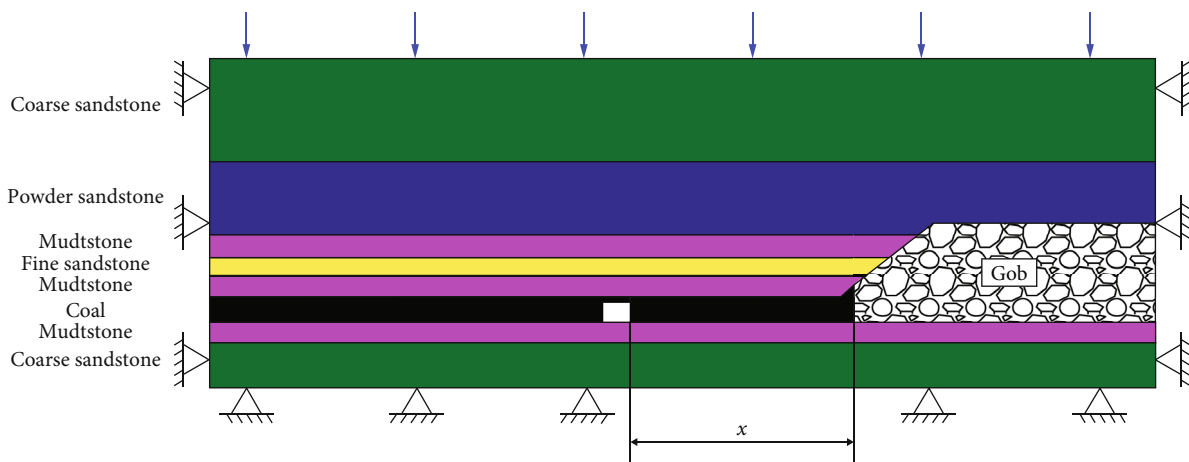
Figure 11: Diagrams of simulation schemes for different coal pillars.

stress curves of the four coal pillars did not change much, and the shape of the stress curves was still similar to that during driving

(b) During the mining period, the low-stress area at the edge of the coal pillar expands, and the peak vertical stress in the coal pillar moves to the inside of the coal pillar. As the coal pillars are subjected to relatively large loads during the mining process, the edges of the coal pillars undergo plastic failure

It can be seen from the above analysis that under the same mining conditions, the smaller the width of the coal pillar, the more concentrated the load on the coal pillar, the peak stress will shift inward, the elastic core range in the middle part will decrease, and the width of the plastic zone will increase. Therefore, discussing the reasonable width of the coal pillar, it should be consider the impact of the stress environment in which the coal pillars are located.

5.4. Comparison of Plastic Zone in the Different Coal Pillars. The range of the plastic zone of coal pillars with different widths is shown in Figure 15.

It can be seen from Figure 16 that when the width of the coal pillar is 46 m and 33 m, a large range of elastic areas can be seen in the coal pillar, there is basically no plastic failure in the elastic area, it has a higher bearing capacity, and the elastic areas of the coal pillar are, respectively, 60% and 55%; when the coal pillar width is 15 m and 25 m, the elastic area in the coal pillar basically disappears, the entire coal pillar has basically undergone plastic failure, the elastic area is basically completely lost, and the proportion of the plastic area is close to 100%. In particular, the 15 m coal pillar has basically lost its bearing capacity due to excessive deformation, and the reason is that the roof has broken at the edge of the goaf. Coupled with the influence of secondary mining, the roof of roadway continues to bend and sink, and the abutment pressure transfers to the coal pillar. Due to the integrated coal has a greater bearing capacity, the crushing

(a) Coal pillar width 46 m

(b) Coal pillar width 33 m

(c) Coal pillar width 25 m

(d) Coal pillar width 15 m
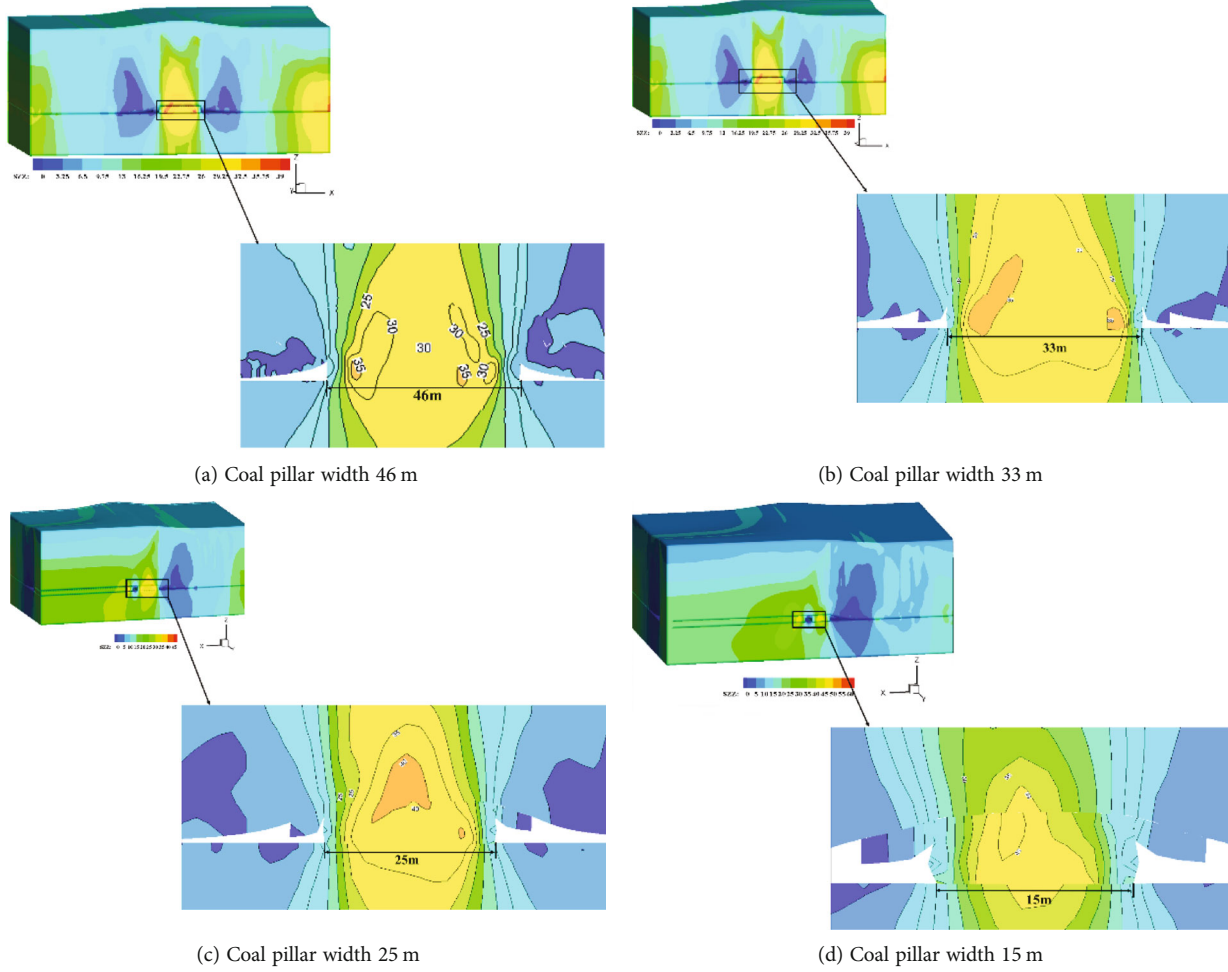
FIGURE 12: Vertical stress in the different coal pillars width.
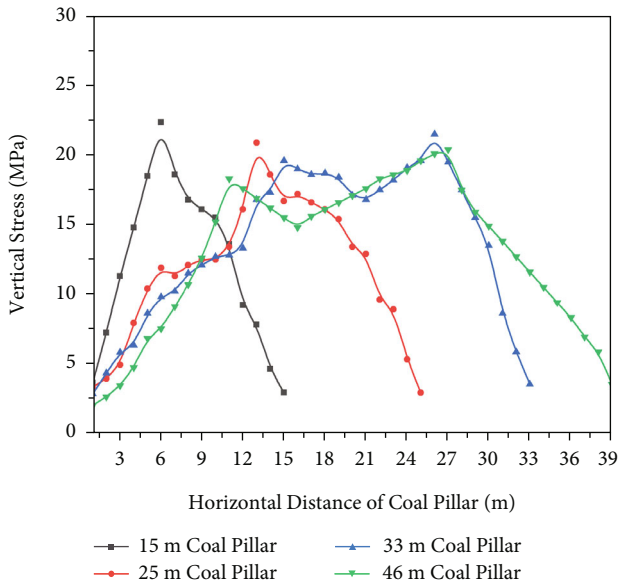
FIGURE 13: Vertical stress during different pillar driving.
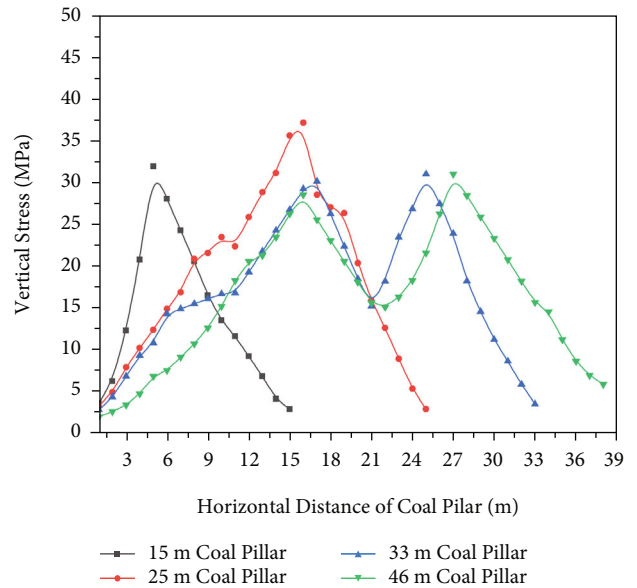
FIGURE 14: Vertical stress during different pillar mining.

(a) Coal pillar width 46 m

(b) Coal pillar width 33 m

(c) Coal pillar width 25 m

(d) Coal pillar width 15 m
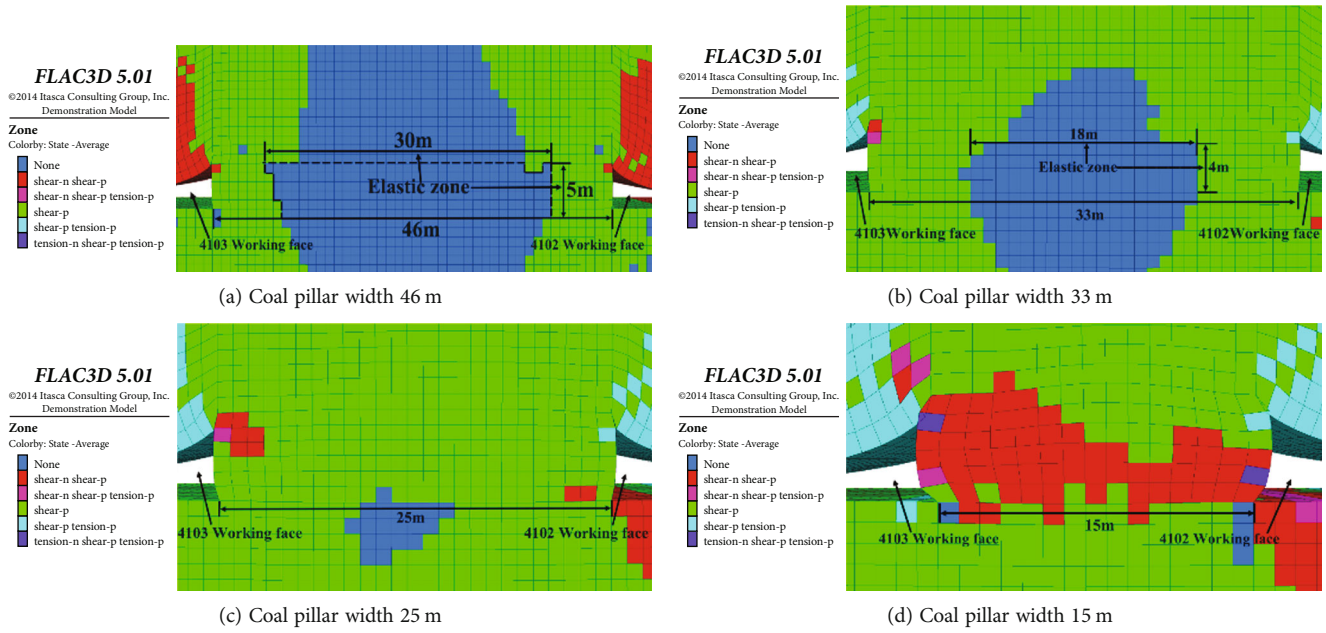
FIGURE 15: The plastic zones in coal pillars with different widths.
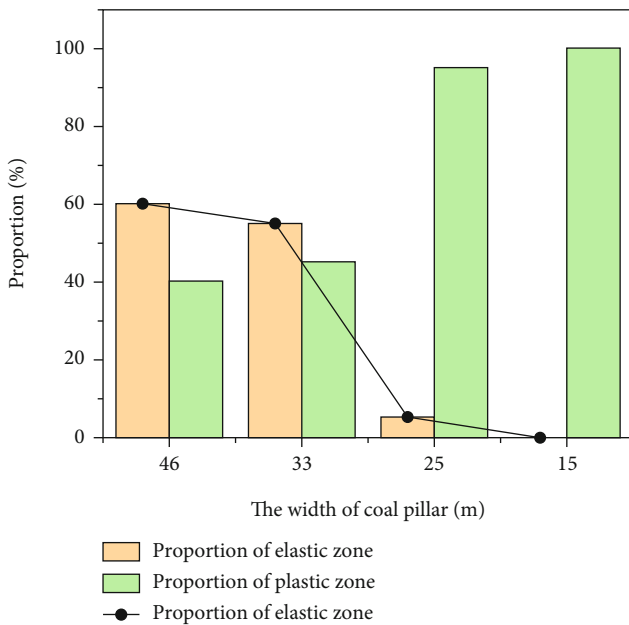
FIGURE 16: Variation curve of plastic zone in coal pillars with different widths.

scope and impact in surrounding rock of the roadway are smaller than the goaf side. The coal pillar sill will produce a certain range of plastic zone, the bolts located in the broken zone will fail, the bolt supporting capacity will decrease, the degree of broken roadway surrounding rock will increase, and the stability of coal pillar will decrease.

5.5. Determination of the Width of the Coal Pillar. In summary, when the coal pillar is 33 m, the vertical stress distribution still presents a form of "a hump with two peaks" during working face mining. The positions of the double peaks are about 18 m and 27 m in the coal pillar, respectively. The range of the "hump" in the coal pillar is roughly 10 m ~12 m. Within this width, the supporting pressure of the coal pillar is at a relatively high level with the superimposed disturbances of the two stopings. Compared with the 46 m coal pillar, the stress level is not significantly increased, and the stress peak change is small. It can be regarded as a certain amount of the coal pillar. The width of the elastic zone has a strong bearing capacity; the coal in other areas of the coal pillar has completely plastically yielded and only has a certain bearing capacity.

Compared with the 33 m coal pillar, the 15 m and 25 m coal pillars have larger plastic zones and higher stress concentration. Although the stress level and the development degree of the plastic zone for the 46 m coal pillars are almost the same as those of the 33 m coal pillars, it is due to the resource utilization, and the width of coal pillar was determined to be 33 m.

6. Field Test

Based on the previous research results, field test of coal pillar retention was carried out on the 4106 headgate in the same panel. The width of section pillar is 33 m, and there are a monitoring section every 100 m to monitor the deformation of the surrounding rock of the roadway during the workface mining (see Figure 17).

During the mining process of the roadway surrounding rock (see Figure 17), the monitoring section is outside the range of 70 m from the working face, and the roadway roof-floor displacement and deformation rate are small, closed to 0 mm/d; in the range of 50 m, the roof subsidence and the deformation of the coal rib convergence have increased to varying degrees. Especially, in the 24 m mining area, the surface displacement in the roadway began to increase rapidly. During the entire mining
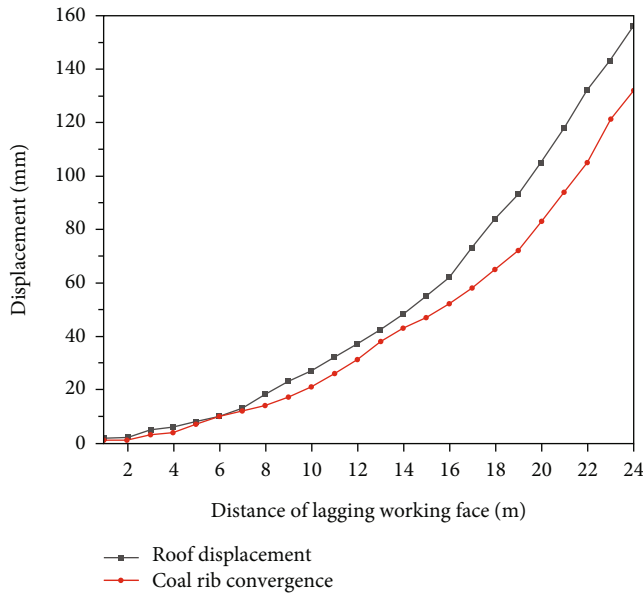
FIGURE 17: Deformation of surrounding rock of roadway.

FIGURE 18: Roadway surrounding rock control effect.

process, the maximum roof subsidence was 153 mm, and the maximum displacement of the coal rib convergence was 132 mm. The deformation rate was smaller in the early stage and increased in the later stage. There was no obvious displacement, which proved that the roadway control was reasonable and effective.

The on-site monitoring results show that it is reasonable to leave the coal pillar width of 33 m, and the control effect of the surrounding rock of the roadway is good (see Figure 18).

7. Conclusions

(1) It can be seen from the measured data that the abutment pressure in the coal pillar increasing with the working face mining and presents a form of "a hump with two peaks." The positions of the double peaks are 12 m and 36 m in the coal pillar, and the distances of "two peaks" are 24 m. The peaks are 38.9 MPa and 33.6 MPa, respectively. The range of the curve "hump" is roughly 17 m ~34 m. In the range of 17 m width, the abutment pressure in the coal pillar is

between 15 MPa and 20 MPa, which is the original rock stress with little change. It can be regarded as an elastic zone with a certain width in the coal pillar and has a strong bearing capacity; numerical simulation analysis results in a law similar to the measured data ("a hump with two peaks"). Therefore, the coal pillar can be appropriately reduced

(2) The stress concentration in the coal pillar (15 m and 25 m) is 15% ~30% higher than wider coal pillar (33 m and 46 m); the damage area of the plastic zone also accounts for a larger proportion. The ratio is 45% and 46%, and there is still a large area of elastic zone; the coal pillars are basically completely damaged when the coal pillars width is 25 m and 15 m, and the plastic zone accounts for 100%. Based on comprehensive considerations, the width of the remaining coal pillars is determined to be 33 m

(3) After field measurement, it is found that the maximum displacement of the roof and floor is 153 mm, the maximum displacement of the two sides is 132 mm, and the deformation is small; the deformation rate is small in the early stage and increased in the later stage. There is no obvious displacement changed, which proves that the roadway control is reasonable. The overall displacement during the mining period is not large, which proves that the coal pillar has a good field application effect and can be used under the same geological conditions

Data Availability

The data used to support the findings of this study are included within the article. The excel data used to support the findings of this study are included within the supplementary information file.

Conflicts of Interest

The authors declare that they have no conflicts of interest.

Acknowledgments

References

[1] X. H. Li, M. H. Ju, S. K. Jia, and Z. Chong, "Study of influential factors on the stability of narrow coal pillar in gob-side entry driving and its engineering application," *Journal of Mining & Safety Engineering*, vol. 33, no. 5, pp. 761–769, 2014.

[2] W. R. He, F. L. He, D. D. Chen, and Q. Chen, "Pillar width and surrounding rock control of gob-side roadway with mechanical caved mining in extra-thick coal seams under hard-thick main roof," *Journal of Mining & Safety Engineering*, vol. 37, no. 2, pp. 349–358, 2020.

[3] L. G. Wang and X. X. Miao, "Study on catastrophe characteristics of the destabilization of coal pillars," *Journal of China Coal Society*, vol. 36, no. 1, pp. 7–11, 2007.

[4] Z. Yuan, Z. Wan, F. Li, and C. Hou, "Stability of coal pillar in gob-side entry driving under unstable overlying strata and its coupling support control technique," *International Journal of Mining Science and Technology*, vol. 23, no. 2, pp. 204–210, 2013.

[5] D. Ma, J. J. Wang, X. Cai et al., "Effects of height/diameter ratio on failure and damage properties of granite under coupled bending and splitting deformation," *Engineering Fracture Mechanics*, vol. 220, article 106640, 2019.

[6] R. Guy, M. Kent, and F. Russell, "An assessment of coal pillar system stability criteria based on a mechanistic evaluation of the interaction between coal pillars and the overburden," *International Journal of Mining Science and Technology*, vol. 27, no. 1, pp. 9–15, 2017.

[7] G. F. Songa and S. L. Yang, "Probability and reliability analysis of pillar stability in South Africa," *International Journal of Mining Science and Technology*, vol. 28, no. 4, pp. 715–719, 2018.

[8] R. Mohammad, F. H. Mohammad, and M. Abbas, "Development of a time-dependent energy model to calculate the mining-induced stress over gates and pillars," *Journal of Rock Mechanics and Geotechnical Engineering*, vol. 7, no. 3, pp. 306–317, 2015.

[9] Q. Sun, J. Zhang, F. Ju, L. Li, and X. Zhao, "Research and application of schemes for constructing concrete pillars in large section finishing cut in backfill coal mining," *International Journal of Mining Science and Technology*, vol. 25, no. 6, pp. 915–920, 2015.

[10] L. J. Ding and Y. H. Liu, "Stress distribution and failure depth analysis of mining floor in close distance thick coal seam group," *Fresenius Environment bulletin*, vol. 27, no. 3, pp. 1896–1903, 2018.

[11] L. X. Wu and J. Z. Wang, "Calculation of width of yielding zone of coal pillar and analysis of influencing factors," *Journal of China Coal Society*, vol. 20, no. 6, pp. 625–631, 1995.

[12] X. G. Zheng, Z. G. Yao, and N. Zhang, "Stress distribution of coal pillar with gob-side entry driving in the process of excavation & mining," *Journal of Min-ing & Safety Engineering*, vol. 29, no. 4, pp. 459–465, 2012.

[13] C. Q. Han, K. Z. Zhang, and X. B. Xu, "Study on failure regularity and reasonable dimension of district sublevel small coal pillar," *Journal of Mining & Safety Engineering*, vol. 24, no. 3, pp. 370–373, 2017.

[14] J. B. Bai, C. J. Hou, and H. F. Huang, "Numerical simulation study on stability of narrow coal pillar of roadway driving along goaf roadway," *Chinese Journal of Rock Mechanics and Engineering*, vol. 23, no. 20, pp. 3475–3479, 2004.

[15] H. P. Kang, D. L. Niu, and Z. Zhang, "Deformation characteristics of surrounding rock and supporting technology of gob-side entry retaining in deep coal mine," *Chinese Journal of Rock Me-chanics and Engineering*, vol. 29, no. 10, pp. 1977–1987, 2010.

[16] K. X. Zhang, Y. D. Jiang Yaodong, and Z. B. Zhang, "Determining the reasonable width of narrow pillar of roadway in gob entry driving in the large pillar," *Journal of Mining & Safety Engineering*, vol. 31, no. 2, pp. 255–262, 2014.

[17] C. J. Hou and X. J. Li, "Stability principle of large and small structure of surrounding rock in fully mechanized caving roadway along goaf," *Journal of China Coal Society*, vol. 26, no. 1, pp. 1–6, 2001.

[18] H. P. Kang, L. X. Yan, and X. P. Guo, "Multi-lane retaining wall rock is arranged in the mining face. Deformation characteristics and support technology," *Chinese Journal of Rock Mechanics and Engineering*, vol. 31, no. 10, pp. 2022–2036, 2013.

[19] H. P. Kang, X. Zhang, L. P. Si, Y. Wu, and F. Gao, "In-situ stress measurements and stress distribution characteristics in underground coal mines in China," *Engineering Geology*, vol. 116, no. 3, pp. 333–345, 2010.

[20] H. P. Kang, "The development of roadway surrounding rock control technology in China for 70 years and its prospect," *Chinese Journal of Rock Mechanics and Engineering*, vol. 46, no. 1, pp. 1–30, 2021.

[21] N. Zhang, F. Xue, and C. L. Han, "Technical challenges and countermeasures of the co-excavation of coal and gas with no-pillar retains in deep coalmine," *Journal of China Coal Society*, vol. 40, no. 10, pp. 2251–2259, 2015.

[22] Y. P. Wu, H. W. Wang, and P. S. Xie, "Analysis of surrounding rock macro stress arch-shell of longwall face in steeply dipping seam mining," *Journal of China Coal Society*, vol. 37, no. 4, pp. 559–564, 2011.

[23] D. Ma, J. X. Zhang, H. Y. Duan et al., "Reutilization of gangue wastes in underground backfilling mining: overburden aquifer protection," *Chemosphere*, vol. 264, article 128400, 2021.

[24] M. C. He, F. Zhao, and M. Ca, "A novel experimental technique to simulate pillar burst in laboratory," *Rock Mechanics and Rock Engineering*, vol. 48, no. 5, pp. 1833–1848, 2015.

[25] D. S. Li, D. H. Li, and C. S. Song, "Modified application of limit equilibrium theory in strip coal pillar design," *Journal of Liaoning Technical University*, vol. 1, no. 1, pp. 125–128, 2003.

[26] G. S. Jia and L. J. Kang, "Study on the stability of coal pillars in mining roadways for fully mechanized caving mining," *Journal of China Coal Society*, vol. 27, no. 1, pp. 7–10, 2002.

[27] Y. F. Zou and H. B. Chai, "Research status and existing problems of stability of strip coal pillars in China," *Journal of Mining and Safety Engineering*, vol. 2, no. 1, pp. 78–83, 2006.

[28] H. X. Zhou, Q. L. Yang, and Y. P. Cheng, "Methanedrainage and utilization in coal mines with strong coal and gas outburst dangers: a case study in Luling mine, China," *Journal of Natural Gas Science and Engineering*, vol. 20, no. 6, pp. 357–365, 2014.

[29] S. L. Kong, Y. P. Cheng, and T. X. Ren, "A sequential approach to control gas for the extraction of multi-gassy coal seams from traditional gas well drainage to mining-induced stress relief," *Applied Energy*, vol. 131, no. 23, pp. 67–78, 2014.

[30] W. Shi, H. T. Liu, C. Liang, and H. S. Jia, "Research on mine pressure behave law in mining of face under the coal pillar," *Advanced Materials Research*, vol. 217, no. 43, pp. 1721–1724, 2011.

[31] J. X. Yang and C. Y. Liu, "Calculation and analysis of stress in strata under gob pillars," *Journal of Central South University*, vol. 22, no. 3, pp. 1026–1036, 2015.

[32] J. X. Yang and C. Y. Liu, "Effects of load distribution exerting on coal pillars on the stress and energy distribution of the floor strata," *Acta Montanistica Slovaca*, vol. 21, no. 2, pp. 102–112, 2016.

[33] D. Ma, S. B. Kong, Z. H. Li, Q. Zhang, Z. H. Wang, and Z. L. Zhou, "Effect of wetting-drying cycle on hydraulic and

mechanical properties of cemented paste backfill of the recycled solid wastes," *Chemosphere*, vol. 282, article 131163, 2021.

[34] D. Broek, *Elementary Engineering Fracture Mechanics*, Springer Science & Business Media, 2012.

[35] D. C. Wang, S. C. Li, and Q. Wang, "Reasonable width of roadway pillar in deep thick coal seam with fully mechanized caving along goaf," *Chinese Journal of Rock Mechanics and Engineering*, vol. 33, no. 3, pp. 539–548, 2014.

[36] X. S. Zhang, "Determination of reasonable width of coal pillar supporting roadway in deep coal seam group along goaf," *Coal Carbon Journal*, vol. 4, no. 1, pp. 28–35, 2011.

[37] H. S. Wang, D. S. Zhang, S. G. Li, W. A. N. G. Lin, and W. U. Lin-zi, "Rational width of narrow coal pillar based on the fracture line location of key rock B in main roof," *Journal of Mining & Safety Engineering*, vol. 31, no. 11, pp. 10–16, 2014.

WILEY | Hindawi

Research Article

Model of Overlying Strata Structure in Large Mining Height Excavating Condition and Calculation of Support Working Resistance

Fengfeng Wu [iD],[1,2] **Xin Yue** [iD],[1,2] **Jingxuan Yang** [iD],[1,2] **Beiju Du** [iD],[1,2] **Jian Zhang** [iD],[1,2] **and Bo Lv** [iD][1,2]

[1]*Key Laboratory of Deep Coal Resource Mining, Ministry of Education, China University of Mining and Technology, Xuzhou, Jiangsu 221116, China*
[2]*School of Mines, China University of Mining and Technology, Xuzhou, Jiangsu 221116, China*

Correspondence should be addressed to Xin Yue; yuexin@cumt.edu.cn

Aiming at the wide range of rock strata movement and collapse, poor stability and high damage rate of the working face support and being prone to crushing of the support in large mining height face, analog simulation, theoretical analysis, and field measurements have been carried out to analyze roof breaking structure form and calculation method of support reasonable support resistance of large mining height face. The researches show that, affected by the space of the mined-out area, the roof of the large mining height working face will take on the structural form of "combined suspended beam-nonhinged roof-hinged roof"; the interaction system between the support and the surrounding rock consists of "hinged roof structure," "nonhingeable roof structure," "combined suspension beam structure," and the support. The support resistance should adapt to the change of the overlying rock structure's instability movement, bearing the weight of the structure itself and the additional load generated by the movement. Combining with the mining conditions of Jinhuagong Coal Mine's large mining height face in Datong mining area, the reasonable support resistance of the working face support is analyzed. The mine pressure monitoring shows that the ZZ13000/28/60 type support and shield hydraulic support can meet the requirements of roof control; the research results ensure the safe mining of the large mining height face.

1. Introduction

The thickness of coal strata occurrence in numerous mine areas exceeds 3.5 m in China, i.e., Yanzhou mine areas in Shandong Province, Xishan, Datong, Lu′an, and Jincheng mine areas in Shanxi Province [1–3]. The excavating techniques of thick coal strata, to a large extent, determine the development of technological level of the entire coal mining industry as well as the utilization of economic benefit in China [4–8]. Due to the advantages of high resource recovery and small amount of gas discharge of the excavation of coal strata with large mining height, it has become the main development direction and primary technical approach of the safe and efficient excavation of thick coal strata in Chinese mine areas [9, 10]. In recent years, significant

breakthrough had been achieved in the development of associated equipment for the excavation of mine area with large mining height which significantly accelerated the development of excavating techniques for thick coal seam with large mining height [4, 5]. However, years of on-site measurement and abundant theoretical studies showed that, with the increase of excavating depth of the coal strata and the height of support, the stability of the surrounding rock support system weakened and the accident rate exceeded 19% [11, 12]. Common incidents of runover and damage of support occurred due to insufficient working resistance of support at the working face [11]. For example, Jinhuagong Coal Mine is one of the large scale mine areas owned by Datong Coal Mine Group in China which locates at 12.5 km to the west of Datong City. The area of mine is 41 km², the

designed production capacity is 4.5 Mt/a, and the average excavating depth of coal strata is 5.7 m. The lithological character of the roofing is mainly sandy strata with high hardness. During the mining period of No. 8218 working face, a total of 3 support crushing incidents occurred and a total period of 21 days of normal production was affected [13].

The existing production practice has confirmed that the overlying strata structure directly relates to the basic problems of stope strata control, such as the causes of stope accidents, the source of roof pressure, the principle of stope support, and the determination of various parameters [14]. Scholars have conducted many studies on the overlying rock structure of working face, which has promoted the solution of the problem of stope roof control. Yan et al. [15] put forward the structure theory of 'short cantilever beam-hinged rock beam' in large mining height stope. Xu et al. [16] put forward the structure theory of 'cantilever beam + masonry beam' in large mining height fully mechanized mining stope. Wang et al. [17] established the structure model of 'cantilever beam + masonry beam' based on the mining conditions of super large mining height working face and analyzed the coupling relationship and control method of strength, stiffness, and stability of hydraulic support and surrounding rock in super large mining height working face. Ju et al. [18] discussed the influence of key strata on the breaking characteristics and working resistance of support in large mining height fully mechanized mining face. Yin [19] put forward the structure model of 'cutting body' for shallow buried large mining height working face. Regarding the calculation of the support load and working resistance of the large mining height face, the traditional empirical formula and engineering analogy methods are still used. Zhang et al. [20] used the position equation method to theoretically analyze the support working resistance of the medium-buried large mining height fully mechanized mining face. Qiu et al. [21] checked the support strength of the shallow buried and large mining height working face through the load empirical formula and the actual measurement statistical method.

However, due to the complexity of the conditions of occurrence as well as the specialty of the excavating techniques for large mining height coal strata, when guided by conventional mining pressure and strata control theory, it is likely that the activity of working face roofing is unclear and the mechanism of mining pressure appearance is unknown, thus hindering the efficient and safe production of the coal mine. Therefore, on the basis of existing research, further analyze the relationship of support and surrounding rocks in large mining height excavating condition through the pattern of fracturing and destabilization overlying strata of working face with large mining height and the structure of the roof structure and thus provide effective and rational roof control techniques, which have great theoretical significance and practical value for the efficient and safe production of coal strata with large mining height.

Based on the engineering background of Jinhuagong Coal Mine, this paper adopts the research methods of physical simulation test, numerical simulation, theoretical analysis, and field measurement to explore the morphology and characteristics of overburden structure in large mining height working face. Based on the results of physical test and numerical analysis, a mechanical model is established to analyze the interaction between support and surrounding rock under this mining condition, and the calculation method of reasonable support resistance under large mining height is deduced to guide the reasonable selection of support and roof control under large mining height. The correctness of the calculation method is verified by engineering practice.

2. Overlying Strata Structure Form of Large Mining Height Mining Face

2.1. Physical Simulation of Overlying Strata Structure

2.1.1. Similarity Model Establishment.
In order to evaluate the characteristics of movement and structural mode of overlying rock roofing in large mining height condition, No. 8218 large mining height working face of Jinhuagong Coal Mine was selected as background to conduct physical similar simulation experiment.

2D plane stress experimental station was used to conduct similarity analysis. The size of the experiment model is length × width × height = 2500 × 200 × 2000 mm. The selection of similar analog constants [22] is shown in Table 1. According to similar constants and actual mechanical parameters of coal and rock mass, the physical and mechanical parameters and proportions of the physical model rock formation are calculated, as shown in Table 2. The model is laid in layers along the horizontal direction, and talcum powder and mica powder are sprinkled between the layers. After the model is dry, paint the surface of the model with white ash, and lay vertical and horizontal observation lines on the surface of the model. The intersection of the two lines is used as the observation point. According to the buried depth of the coal seam, the weight of the overlying rock layer is compensated by external force, and the experimental paving model is shown in Figure 1.

2.1.2. Physical Simulation Experiment Results.
The results of the experiment are shown in Figure 2. The following can be seen:

(1) During the advancement of 20 m of the working face, the immediate roof fractured in a periodic order and acted directly on the support of the mine area in the mode of combined cantilever beam structure. The overlying rock strata above the immediate roof remained intact. With the increase of distance of advancement, different amount of settlement of the sublayers of the overlying rock strata led to the delamination of the sublayers.

(2) When the working face advanced to 70 m, the collapsed height at the gob increased. The caving gangue gradually filled the space of the gob to support the fractured blocks of the overlying rock strata. However, as the caving gangue was in the initial extrusion

TABLE 1: Primary similarity constants of similar simulation experiment.

Primary similarity constants	Ratio (model: original)
Geometric similarity ratio	1 : 80
Similarity constant of volumetric weight	1.5
Similarity constant of stress	120
Similarity constant of time	8.9

TABLE 2: Physical and mechanical parameters of coal strata with large mining height.

Serial number	Lithological characteristics	Paved thickness of the model (cm)	Compressive strength (kPa)	No. of mixture	Sublayer
14	Medium gritstone	4.8	392	455	3
13	Gritstone	6.8	383	455	4
12	Fine sandstone	14.2	450	337	4
11	Coal	1.5	167	764	
10	Sandy shale	6.5	208	546	3
9	Coal	1.2	167	764	
8	Sandy shale	6.5	208	546	3
7	Fine sandstone	2.0	358	455	
6	Sandy shale	3.8	208	546	2
5	Medium sandstone	11.5	392	455	3
4	Gritstone	11.2	358	455	3
3	Fine sandstone	2.9	450	337	
2	Sandy shale	1.1	217	546	
1	Coal	7.1	167	764	

Note. The meaning of No. of mixture: the first digit represents the ratio of sand to cement, and the second and third digits represent the ratio of calcium carbonate to gypsum in the cement. For example, No. 455 of mixture in the table indicates that the sand-to-rubber ratio is 4 : 1, and the calcium carbonate: gypsum in a cement is 5 : 5.
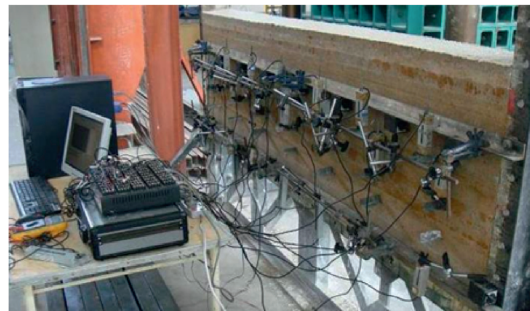
FIGURE 1: Two-dimensional plane stress test bench.

(a)	(b)	(c)
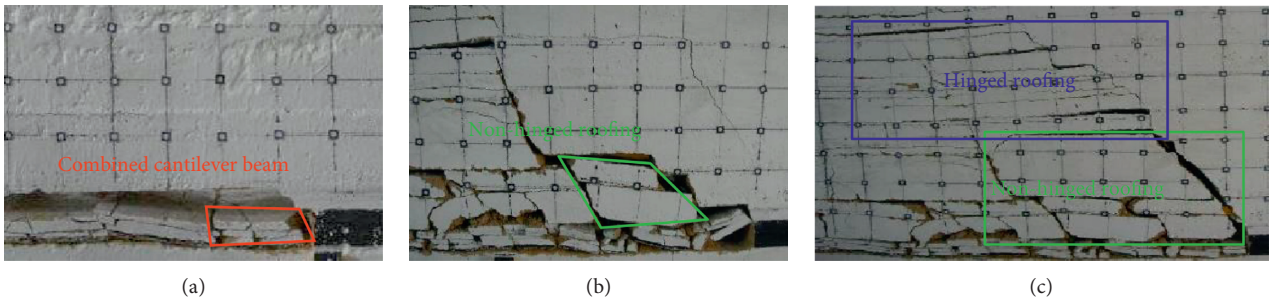
FIGURE 2: Damage mode of overlying rock during the advancement of working face. (a) Working face advanced to 20 m; (b) working face advanced to 70 m; (c) working face advanced to 120 m.

stage, the compactness was low and the amount of extrusion was large, the settlement of roofing exceeded the ultimate allowable settlement between the fractured blocks, and thus hinged rock-beam structure could not be formed between the blocks. Instead, nonhinged rock-beam structure existed.

(3) When the working face advanced to 120 m, the space of overlying rock strata reduced and the amount of extrusion of the caving gangue at the gob became limited. The allowable settlement of the fractured roofing was smaller than the ultimate amount of rotation of the overlying rock strata. In addition, large extrusion existed between the fractured blocks. As a result, masonry beam structure was formed between the fractured blocks of the high roofing.

2.2. Numerical Simulation of Breaking Motion Characteristics of Overburden Strata

2.2.1. Numerical Model Establishment. The UDEC2D numerical calculation model is established based on the engineering geological conditions and mining technical conditions of No. 8218 fully mechanized mining face in Jinhuagong Coal Mine.

Model size is height × width = 100 m × 200 m. The constitutive relationship of surrounding rock used in the numerical calculation model is Mohr-Coulomb criterion, stress-displacement mixed boundary, uniform vertical compressive stress is applied to the upper boundary of the model, and horizontal compressive stress varying with depth is applied on both sides. According to the mechanical test data of the coal seams and roof and floor rocks of No. 8218 working face provided by Jinhuagong Coal Mine, the deformation parameters of the coal seams and roof and floor rocks under the Mohr-Coulomb strength criterion are estimated through the GSI geological strength index and the Hoek-Brown strength criterion as shown in Table 3 below.

2.2.2. Numerical Simulation Results. Figure 3 shows the simulation results of the fracture movement characteristics of the overlying strata in the mining process of the working face. It can be seen from the figure that when the working face is at the position of the open cut, the overhang length of the first layer of sandy shale is small and does not reach its limit span. It is a cantilever structure with fixed ends at both ends, as shown in Figure 3(a). As the working face continues to advance, the first and second layered rock formations bend and sink, causing separation from the upper layer. The first and second layered roofs collapsed for the first time, with a collapsed height of 3.2 m, and thickness and hardness of the overlying third layer named coarse sandstone are large, the limit span is large, and the bending deformation of the coarse sandstone is small. As the working face continues to advance, due to the large goaf space at this time, the collapsed first and second layered roof fill the goaf. The height of the zone is limited, and the coarse sandstone roof has a large bending and sinking

space. The working face is advanced to 52 m, as shown in Figure 3(b). The coarse sandstone roof collapses and the height of the collapse is 12.2 m. Similarly, due to the large space in the goaf at this time, the collapsed roof rock layer is insufficient to fill the mined-out area, and the allowable sinking space is greater than the limit subsidence of the overlying rock. The overlying rock breaks and collapses and enters the mined-out area. This part of the roof is in the form of a combined cantilever beam above the support. When the working face advances to 66 m, the overlying sandy shale breaks and collapses, filling the mined-out area to a greater degree, and the allowable sinking space is already very small, as shown in Figure 3(c); the roof is in a state of nonarticulated structure. At this time, the collapse height reaches 38.7 m; when the working face advances to 92 m, the overburden fine sandstone collapses for the first time. Because the free space below is filled with falling gangue, the allowable subsidence is less than the thickness of the fine sandstone roof, forming a hinged structure, as shown in Figure 3(d); when the working face advances to 110 m, the fine sandstone roof collapses for the first time, as shown in Figure 3(e); when the working face advances to 130 m, the fine sandstone roof collapses for the second time, as shown in Figure 3(f).

2.3. Structural Features of Overlying Rock Roof in Stope.

Based on the foregoing simulation results, it can be seen that the large mining height working face is affected by the goaf space, and the roof breaking structure of the goaf has the following characteristics:

(1) During the initial mining period of the working face, the immediate roofing existed in the form of combined cantilever beam structure. Affected by the lithological characteristics of the roofing, there is a certain amount of difference in the suspended length of the combined cantilever beam structure. For normal soft roofing, such as mud stone, shale, and sandy shale, the fracturing line lies on the tail beam of the support and the support of the working face mainly carries the weight of the overlying rock. For harder roofing, such as sandstone, limestone, and glutenite, the fracturing line normally lies behind the tail beam of the support by a certain distance and cantilever structure is formed. In this case, apart from sustaining the weight of the collapsed roofing, the support is also subjected to the moment of the cantilever roofing.

(2) The blocks of the nonhinged roofing structure are regularly arranged and there is no compressive action between the blocks. For normal soft roofing, such as mud stone, shale, and sandy shale, the nonhinged roofing structure transforms to combined cantilever beam structure. For harder roofing, such as sandstone, limestone, and glutenite, the fractured dimension of the nonhinged roofing structure is large and the supporting action from the gangue in the gob increases. As a result, the effect on

TABLE 3: The physical and mechanical property parameters of the numerical simulation experimental model coal.

Serial number	Lithologic characters	Thickness/m	Bulk density (kg/m³)	Volume modulus (GPa)	Shear modulus (GPa)	Internal friction angle/°	Cohesion (MPa)	Tensile strength (MPa)
15	Grit stone	20.0	2580	8.4	3.72	37	8.27	6.22
14	Fine sandstone	13.4	2580	7.1	2.91	37	5.45	4.06
13	Moderate coarse sandstone	3.8	2580	9.4	6.76	40	6.63	5.27
12	Grit stone	5.4	2580	8.4	3.72	37	8.27	6.22
11	Fine sandstone	11.4	2580	7.1	2.91	37	5.45	4.06
10	Coal seam	1.22	1400	7.22	1.8	28	2.82	3.13
9	Sandy shale	5.22	2420	4.2	2.91	35	4.52	2.47
8	Coal seam	0.96	1400	7.2	1.8	28	2.82	3.13
7	Sandy shale	5.21	2420	4.2	2.91	35	4.52	2.47
6	Fine sandstone	1.60	2580	7.1	2.91	37	5.45	4.06
5	Sandy shale	3.10	2420	4.2	2.91	35	4.52	2.47
4	Medium sandstone	9.20	2580	9.6	4.7	32	7.20	5.21
3	Grit stone	9.00	2580	8.4	3.72	37	8.27	6.22
2	Fine sandstone	2.30	2580	7.1	2.91	37	5.45	4.06
1	Sandy shale	0.90	2420	4.2	2.91	35	4.52	2.47
	Coal seam	5.70	1400	7.2	1.8	28	2.82	3.13

(a)   (b)   (c)

(d)   (e)   (f)
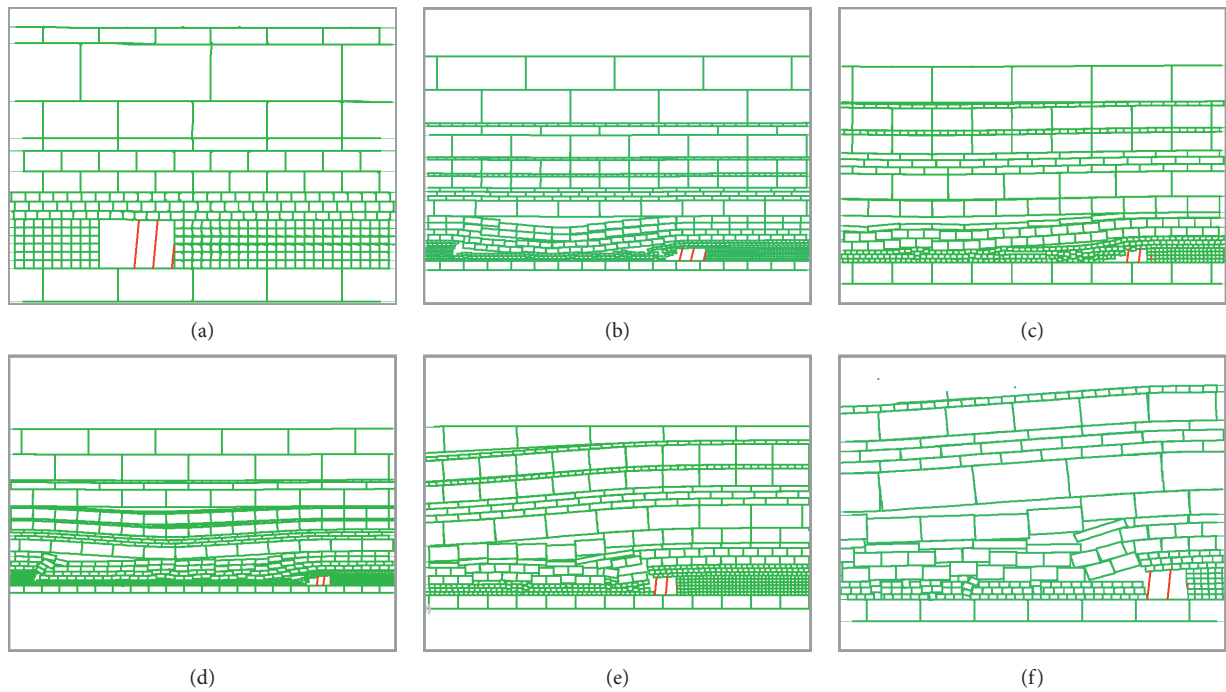
FIGURE 3: Numerical simulation of overburden failure mode. (a) Open-off cut position; (b) working face advanced to 52 (m); (c) working face advanced to 66 (m); (d) working face advanced to 92 (m); (e) first periodic collapse of basic roof; (f) second periodic collapse of basic roof.

the underneath combined cantilever beam structure is reduced.

(3) When the hard rock strata above the nonhinged roofing fracture, the allowable settlement is limited and the fractured blocks form hinged roofing structure due to mutual extrusion. Unconnected fracturing appears on the overlying roofing and the roofing is primarily subjected to bending settlement.

The "combined cantilever structure-nonhinged roof structure-hinged roof structure" model of the overlying rock roof of the large mining height working face is shown in Figure 4.
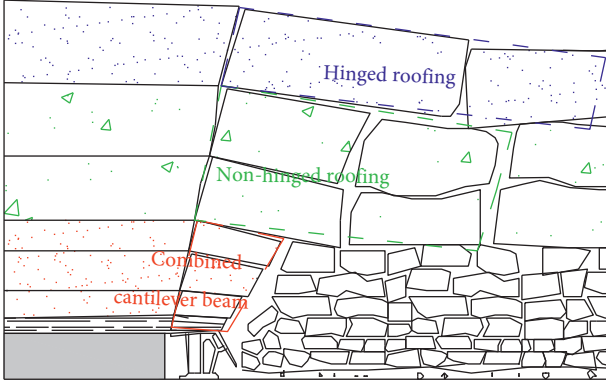
Figure 4: Roof structure model of large mining height working face.

3. Relationship between Support and Surrounding Rock and Calculation of Support Resistance

With the increase of mining height, the failure range of overlying strata and the degree of motion instability increase, which will cause the increase of mining pressure. Therefore, under the condition of fully mechanized mining with large mining height, the interaction between support and surrounding rock is the key problem related to the influence of roof breaking and instability on support and the determination of reasonable working resistance of support.

According to the above analysis, after ignoring the influence of the floor, the interaction system of the surrounding rock of the support in the fully mechanized mining face with large mining height is composed of the support-combined cantilever beam structure-nonhinged roof structure-hinged roof structure, as shown in Figure 5.

The working state and supporting quality of the support affect the stability of the combined cantilever beam structure and the nonhinged roof structure, and the stability of the latter two in turn affects the support. As the external condition of the support, the combined cantilever beam structure and the nonhinged roof structure system, the hinged roof structure has a significant impact on its stability. Due to the existence of the influence angle of the coal wall support in the stope and the fact of the continuous advancement of the working face, the rotation of the hinged roof structure is uncontrollable. Therefore, the motion and action of the hinged roof are dominant in the interaction system of the surrounding rock of the support.

This structural model is derived under the condition of the hard roof of Jinhuagong Coal Mine. The overburden structure is also the form of expression under the most difficult conditions of rock formation control in the large mining height face, and it describes the temporal and spatial characteristics of the overburden movement instability in the large mining height and large mining space. However, as analyzed above, with the change of the lithological conditions of the overlying rock roof, the structure of the overlying rock will also change. For example, when the direct roof lithology is weak rock formations such as mudstone and shale, the lower composite cantilever structure will not exist, and when the thickness of the weak direct roof rock layer is very thick, the nonhinged roof will also not exist. Therefore, the structural characteristics of the thick coal seam and large mining height overlying rock should be analyzed in detail according to the specific conditions of the overlying rock. To sum up, this structural model is also a general model of overlying strata structure in large mining height stopes in thick coal seams.

3.1. Interaction between Roof Combined Cantilever Beam Structure and Support. Before the breaking and instability of the key strata above, the support of the working face mainly bears the structural action of the combined cantilever beam of the direct roof strata. The stress model of the support of the working face and the combined cantilever beam of the direct roof strata in the coal seam with large mining height is shown in Figure 6.

In Figure 6, P_Z is the support resistance of working face, and c is the distance between the support resistance action point and the roof fracture line position (generally located in the coal wall position). $H_{11} \sim h_{1k}$ are the layered thickness of combined cantilever beam structure, respectively. $\alpha_{11} \sim \alpha_{1k}$ are the layered fracture angles of the combined cantilever beam roof, respectively. k is the total number of combined cantilever rock strata. $P_{11} \sim P_{1k}$ are the layered weight of combined cantilever beam structure, respectively. $l_{11} \sim l_{1k}$ are the layered fracture sizes of combined cantilever beam structure, respectively. R_x is the force of overlying rock above combined cantilever beam on combined cantilever beam structure. l_x is the distance between overburden force above combined cantilever beam and roof fracture line.

Taking the moment of O point in the graph, the equilibrium conditions of the immediate roof combined cantilever beam structure are calculated as follows:

$$
\begin{aligned}
P_z c \geq \frac{1}{2} P_{11} \left(h_{11} \cot \alpha_{11} + l_{11} \right) + P_{12} \left(\frac{1}{2} h_{12} \cot \alpha_{12} + \frac{1}{2} l_{12} + h_{11} \cot \alpha_{11} \right) \\
+ \cdots + P_{1k} \left(\frac{1}{2} h_{1k} \cot \alpha_{1k} + \frac{1}{2} l_{1k} + \sum_{i=1}^{k-1} h_{1i} \cot \alpha_{1i} \right) + R_x \left(l_x + \sum_{i=1}^{k} h_{1i} \cot \alpha_{1i} \right).
\end{aligned}
\tag{1}
$$
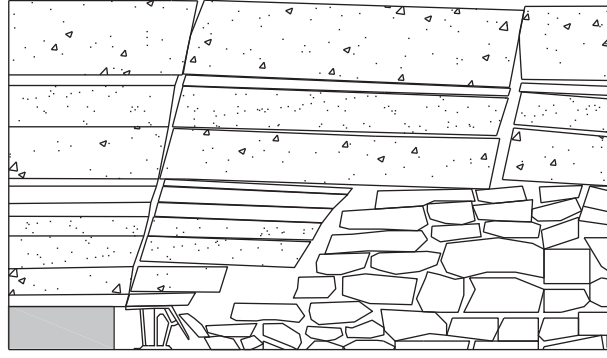
FIGURE 5: The relationship between support surrounding rock of fully mechanized working face with large mining height.
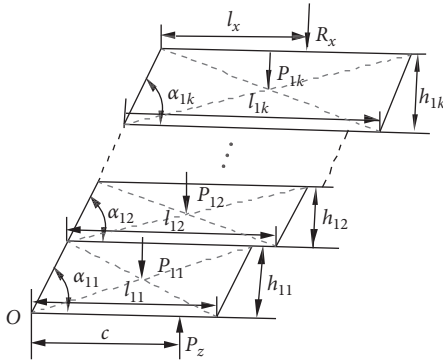
FIGURE 6: Roof combined cantilever beam structural model.

Among them: h_{1i} is the i layer thickness of combined cantilever beam roof, while i is the sequence number of layered roof.

After the consolidation of formula (1), the stability condition of the combined cantilever beam roof structure in coal seam with large mining height is obtained as follows:

$$P_z c \geq \frac{1}{2} \sum_{i=1}^{k} P_{1i} \left(h_{1i} \cot \alpha_{1i} + l_{1i} \right) + \sum_{j=2}^{k} \sum_{i=1}^{j-1} P_{1j} h_{1i} \cot \alpha_{1i}$$
$$+ R_x \left(l_x + \sum_{i=1}^{k} h_{1i} \cot \alpha_{1i} \right). \tag{2}$$

It can be seen from formula (2) that the stability conditions of the roof combined cantilever beam structure are not only related to the weight, thickness, fracture angle, roof fracture size, and the bearing capacity of the working face support itself and the position of the action point of the multilayer roof of the cantilever beam structure, but also affected by the indirect force of the overlying strata of the combined cantilever beam structure and the position of the action point.

Before the overlying strata of the roof combined cantilever beam structure are unstable and broken, the force of the complete roof structure of the overlying strata on the broken roof combined cantilever beam structure can be ignored, namely, $R_x = 0$.

According to formula (2), the support resistance under the critical instability condition of the roof combined cantilever beam structure in the working face of large mining height coal seam can be determined as

$$P_z = \frac{1}{2c} \left[\sum_{i=1}^{k} P_{1i} \left(h_{1i} \cot \alpha_{1i} + l_{1i} \right) + 2 \sum_{j=2}^{k} \sum_{i=1}^{j-1} P_{1j} h_{1i} \cot \alpha_{1i} \right]. \tag{3}$$

By formula (3), the support resistance of the combined cantilever beam roof structure of the working face in the large mining height coal seam mainly depends on the weight, thickness, fracture angle, roof fracture size, and the position of the working face support resistance.

When the roof fracture angle takes a certain value, the relationship between the support resistance and the position of the support action point is shown in Figure 7.

It can be seen from Figure 6 that, under certain roof fracture angle, the support resistance of the working face decreases with the increase of the distance between the position of the support action point and the roof fracture line, which is easy to understand from the perspective of the torque balance of the roof combined cantilever beam structure. It can also be seen that the support resistance of the working face tends to decrease with the increase of the roof fracture angle, but with the increase of the position distance of the support action point, the variation gradient of the support resistance of the working face increases with the increase of the roof fracture angle.

3.2. Interaction between Roof Nonhinged Structure and Combined Cantilever Beam Structure.
The stress characteristics of nonhinged roof structure are shown in Figure 8.

From Figure 8, it can be seen that the nonhinged roof structure is not only affected by the weight of its own rock strata and overburden load, but also supported by the cantilever beam structure from the lower roof and the caving gangue in the goaf. At this time, the roof structure maintains balance and stability under the synergy of various forces. The O point moment of the nonhinged roof composite structure is taken, and the mechanical equilibrium conditions of the roof structure are obtained as follows:
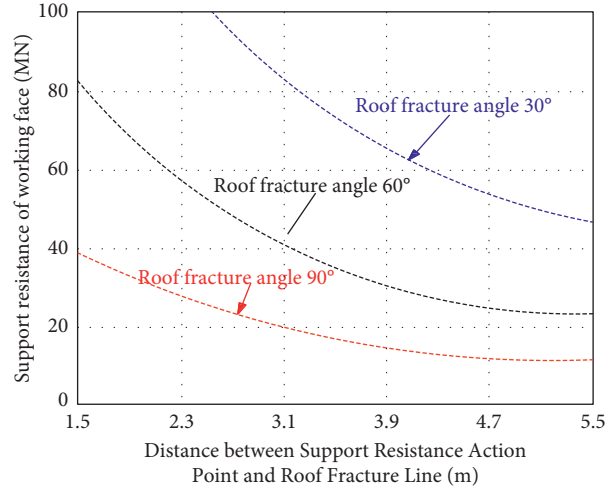
Figure 7: The relationship between support resistance and point action.
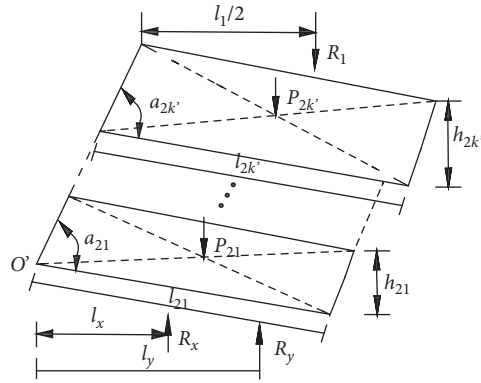
Figure 8: The model of nonhinged roof structure.

$$R_x l_x + R_y l_y \geq \frac{1}{2} P_{21} \left(h_{21} \cot \alpha_{21} + l_{21} \right) + P_{22} \left(\frac{1}{2} h_{22} \cot \alpha_{22} + \frac{1}{2} l_{22} + h_{21} \cot \alpha_{21} \right)$$

$$+ \cdots + P_{2k'} \left(\frac{1}{2} h_{2k'} \cot \alpha_{2k'} + \frac{1}{2} l_{2k'} + \sum_{i=1}^{k'-1} h_{2i} \cot \alpha_{2i} \right) + R_1 \left(\frac{1}{2} l_1 + \sum_{i=1}^{k'} h_{2i} \cot \alpha_{2i} \right). \tag{4}$$

Among them: R_x and R_y are the force of the lower combined cantilever beam and the goaf caving gangue on the overlying nonhinged roof structure. l_x and l_y are the distance between the forces R_x, R_y and O$'$ point. R_1 and l_1 are the force and position of action point of overlying strata on nonhinged roof structure. k' is the total number of nonhinged roof layers. P_{2i}, l_{2i}, h_{2i}, and α_{2i} are the weight, length, thickness, and fracture angle of the i-stratification of nonhinged roof structure; i value is $1 \sim k'$.

After combining formula (4), the stability condition of nonhinged roof structure is obtained as follows:

$$R_x l_x + R_y l_y \geq \frac{1}{2} \sum_{i=1}^{k'} P_{2i} \left(h_{2i} \cot \alpha_{2i} + l_{2i} \right) + \sum_{j=2}^{k'} \sum_{i=1}^{j-1} P_{2j} h_{2i} \cot \alpha_{2i} + R_1 \left(\frac{l_1}{2} + \sum_{i=1}^{k'} h_{2i} \cot \alpha_{2i} \right). \tag{5}$$

It can be seen from formula (5) that the load from the overlying rock of the roof structure and the weight of the structure itself maintain a certain balance under the combined action of the lower combined cantilever beam structure and the falling gangue in the goaf. Under certain roof overburden load conditions, there is an inverse

correlation between the force of the combined cantilever beam structure on the working face and the support force of the gangue in the goaf. Improving the support effect of the gangue in the goaf will play a positive role in reducing the force of the combined cantilever beam structure.

From formula (5), the bearing relationship of roof combined cantilever beam structure and goaf caving gangue on overlying nonhinged roof structure is satisfied:

$$R_x l_x + R_y l_y = \frac{1}{2} \sum_{i=1}^{k'} P_{2i} (h_{2i} \cot \alpha_{2i} + l_{2i}) + \sum_{j=2}^{k'} \sum_{i=1}^{j-1} P_{2j} h_{2i} \cot \alpha_{2i}. \tag{6}$$

Combined with goaf gangue support force calculation formula (7):

$$R_y = \lambda \sum_{i=1}^{k'} P_{2i}. \tag{7}$$

According to the stability condition of roof combined cantilever beam shown in formula (2), the support resistance of working face under the critical instability condition of nonhinged roof structure is

$$P_z = \frac{\left[(1/2) \sum_{i=1}^{k} P_{1i} (h_{1i} \cot \alpha_{1i} + l_{1i}) + \sum_{j=2}^{k} \sum_{i=1}^{j-1} P_{1j} h_{1i} \cot \alpha_{1i} + R_x \left(l_x + \sum_{i=1}^{k} h_{1i} \cot \alpha_{1i} \right) \right]}{c}. \tag{8}$$

The stress characteristics of 'working face support-goaf gangue-roof combined cantilever beam structure-roof nonhinged structure' are shown in Figure 9.

The working face support is stable under the combined action of overburden roof weight and goaf gangue. Combining formula (2) and formula (5), the support resistance under the action of nonhinged roof structure is calculated as

$$P_z = \frac{(G_1 + G_2 + G_3)}{c}. \tag{9}$$

Among them:

$$G_1 = \frac{1}{2} \left[\sum_{i=1}^{k} P_{1i} (h_{1i} \cot \alpha_{1i} + l_{1i}) + \sum_{i=1}^{k'} P_{2i} (h_{2i} \cot \alpha_{2i} + l_{2i}) \right],$$

$$G_2 = \sum_{j=2}^{k} \sum_{i=1}^{j-1} P_{1j} h_{1i} \cot \alpha_{1i} + \sum_{j=2}^{k'} \sum_{i=1}^{j-1} P_{2j} h_{2i} \cot \alpha_{2i}, \tag{10}$$

$$G_3 = \frac{1}{l_x} \left[\frac{1}{2} \sum_{i=1}^{k'} P_{2i} (h_{2i} \cot \alpha_{2i} + l_{2i}) + \sum_{j=2}^{k'} \sum_{i=1}^{j-1} P_{2j} h_{2i} \cot \alpha_{2i} - R_y l_y \right] \left(\sum_{i=1}^{k} h_{1i} \cot \alpha_{1i} \right) - R_y l_y.$$

Among them: G1, G2, and G3 are the working resistance components related to the weight of overburden roof, the relevant geometric dimensions, the gangue force in goaf, and the position of action point, respectively.

3.3. Interaction between Roof Articulated Structure and Nonarticulated Structure.
Considering that the allowable deflection space of overlying rock at the layer position of hinged roof structure is limited, and the force distribution between the roof layers is relatively uniform, the force between the hinged roof layers is simplified as the concentrated load acting on the middle of the layered fracture block, and the mechanical model is established with two key rock blocks as the research objects, as shown in Figure 10.

In the figure, P_1 and P_2 are the loads (including self-weight) borne by the block. θ_1 and θ_2 are the rotation angles of two adjacent blocks, respectively. w_1 and w_2 are the subsidence of the two blocks, respectively. Q_A and Q_C are the friction forces on the block contact surface. R_1 and R_2 are the support forces of the two blocks under the lower rock stratum, respectively. l_1 and l_2 are the fracture lengths of the two blocks, respectively. T is the horizontal thrust between block structures.

The geometric relations of the block structure in the process of motion are satisfied:

$$w_1 = l_1 \sin \theta_1,$$

$$w_2 = l_1 \sin \theta_1 + l_2 \sin \theta_2,$$

$$a_1 = \frac{1}{2} (h - l_1 \sin \theta_1), \tag{11}$$

$$a_2 = \frac{1}{2} (h - l_2 \sin \theta_2).$$

Among them: h is the thickness of broken roof strata. a_1 and a_2 are the length of the extrusion contact surface
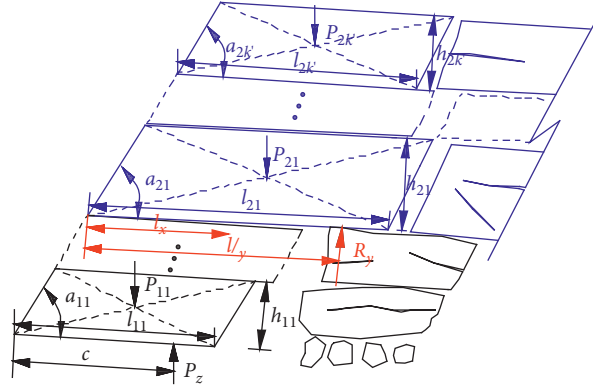
Figure 9: Nonhinged roof structure of bearing system under stress.
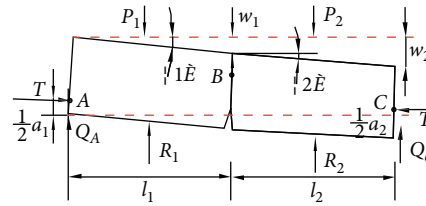
Figure 10: The movement structure and force of two key blocks.

between the two blocks, respectively. Since the contact between the broken blocks under strong extrusion force is a plastic hinge relationship, it is assumed that the position of the action point of the horizontal thrust is half of the length of the extrusion contact surface.

The hinged roof structure is in equilibrium under the combined action of surrounding rock load. According to the equilibrium conditions in the vertical direction of the structure:

$$P_1 + P_2 = Q_A + R_1 + R_2 + Q_c. \tag{12}$$

According to the moment equilibrium conditions $\sum M_A = 0$ and $\sum M_B = 0$ at A and B points in the graph, the following results are obtained:

$$\frac{1}{2}Ta_1 + \frac{1}{2}P_1l_1 + P_2\left(l_1 + \frac{1}{2}l_2\right) - T\left(\frac{1}{2}a_2 - w_2\right)$$
$$- Q_c\left(l_1 + l_2\right) - R_2\left(l_1 + \frac{1}{2}l_2\right) - R_1l_1 = 0, \tag{13}$$

$$\frac{1}{2}P_2l_2 + T\left(w_2 - w_1 + h - a_2\right) - Q_cl_2 - \frac{1}{2}R_2l_2 = 0. \tag{14}$$

For ease of description, $i_1 = h/l_1$ and $i_2 = h/l_2$ are set here to reflect the block size of the broken block. The smaller the value is, the larger the length of the broken block is. Combining formulas (13) and (14), the extrusion force between the broken blocks and the friction force on the extrusion surface are calculated as follows:

$$
\begin{cases}
T = \dfrac{2\left(P_1 - 2R_1 + P_2 - R_2\right)}{2\left(i_1 + i_2\right) + \left(6 + i_1/i_2\right)\sin\theta_2 - 3\,\sin\theta_1}, \\[3mm]
Q_c = \dfrac{\left(P_1 - 2R_1 + P_2 - R_2\right)\left(3\,\sin\theta_2 + i_2\right)}{2\left(i_1 + i_2\right) + \left(6 + i_1/i_2\right)\sin\theta_2 - 3\,\sin\theta_1} + \dfrac{1}{2}\left(P_2 - R_2\right), \\[3mm]
Q_A = P_1 - R_1 + \dfrac{1}{2}\left(P_2 - R_2\right) - \dfrac{\left(P_1 - 2R_1 + P_2 - R_2\right)\left(3\,\sin\theta_2 + i_2\right)}{2\left(i_1 + i_2\right) + \left(6 + i_1/i_2\right)\sin\theta_2 - 3\,\sin\theta_1}.
\end{cases}
\tag{15}
$$

It can be seen from the calculation of the whole structure of the masonry beam that $R_2 = 1.03P_2$, and because the right block is clamped by the overlying rock roof and the falling gangue in the goaf, the stress characteristics in the vertical direction of the block can be approximately expressed as

$R_2 = P_2$. In the process of coal seam mining, the roof periodic breaking, due to the change of roof occurrence conditions, is small; the roof periodic breaking step distance is basically the same, so here take $l_1 = l_2$; the stress characteristics of hinged block of overburden roof are
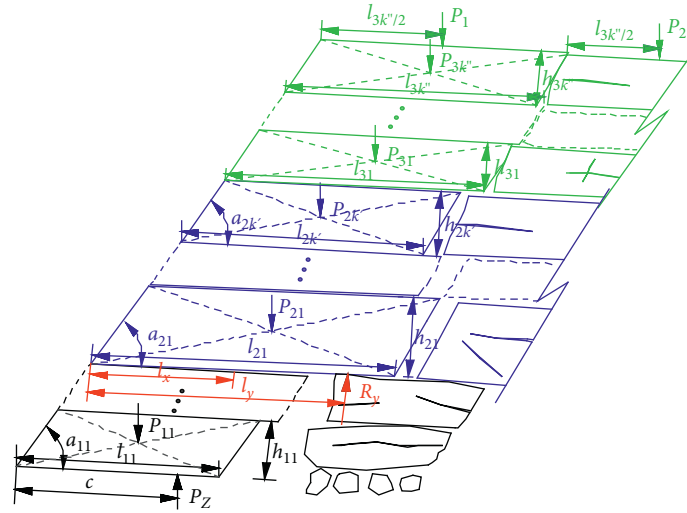
Figure 11: Rock movement characteristics under the hinged roof structure.

$$T = \frac{2(P_1 - 2R_1)}{4i + 7 \sin \theta_2 - 3 \sin \theta_1}, \tag{16}$$

$$Q_c = \frac{(P_1 - 2R_1)(3 \sin \theta_2 + i)}{4i + 7 \sin \theta_2 - 3 \sin \theta_1}, \tag{17}$$

$$Q_A = P_1 - R_1 - \frac{(P_1 - 2R_1)(3 \sin \theta_2 + i)}{4i + 7 \sin \theta_2 - 3 \sin \theta_1}. \tag{18}$$

Among them, $i = i_1 = i_2$.

The mechanical characteristics of the bearing system of 'working face support-goaf caving gangue-roof composite suspension beam-nonarticulated roof-articulated roof' are shown in Figure 11.

The discussion of roof nonhinged structure and combined cantilever beam structure has been discussed in the previous paper, so this paper focuses on the analysis of overburden hinged roof structure. The roof hinged structure maintains balance and stability under the weight of overlying strata, surrounding rock support, and extrusion force. The structural stress characteristics are shown in Figure 12.

In the figure, R_1 is the force of the lower nonhinged roof structure on the hinged roof. k'' is the total number of layers of hinged roof. P_{3i}, l_{3i}, h_{3i}, and α_{3i} are the weight, length, thickness, and fracture angle of the i-stratification roof of hinged roof structure; i value is $1 \sim k''$. $Q_A k''$ and $Q_B k''$ are the friction forces on the extrusion surface of the hinged roof breaking block, respectively. $T_3 k''$ is the extrusion force on the extrusion surface of the broken block.

Similarly, according to the moment equilibrium condition of the hinged roof structure, the calculation results are as follows:

$$\frac{1}{2}\sum_{i=1}^{k'} T_{3i}a_{3i} + \sum_{j=2}^{k'}\sum_{i=1}^{j-1} T_{3j}h_{3i} - \sum_{j=2}^{k'}\sum_{i=1}^{j-1} Q_{Aj}h_{3i} \cot \alpha_{3i} + P_1\left(\frac{l_{3k'}}{2} + \sum_{i=1}^{k'} h_{3i} \cot \alpha_{3i}\right) + \frac{1}{2}\sum_{i=1}^{k'} P_{3i}h_{3i} \cot \alpha_{3i}$$

$$+ \frac{1}{2}\sum_{i=1}^{k'} P_{3i}l_{3i} + \sum_{j=2}^{k'}\sum_{i=1}^{j-1} P_{3j}h_{3i} \cot \alpha_{3i} - \sum_{j=2}^{k'}\sum_{i=1}^{j-1} Q_{Bj}h_{3i} \cot \alpha_{3i} - \sum_{i=1}^{k'} Q_{Bi}l_{3i} - \sum_{j=1}^{k'}\sum_{i=1}^{j} T_{3j}h_{3i} + \sum_{i=1}^{k'} T_{3i}w_{3i} + \frac{1}{2}\sum_{i=1}^{k'} T_{3i}a_{3i} - \frac{1}{2}R_1 l_{31} = 0. \tag{19}$$

The force of the roof hinge structure on the lower strata is

$$R_1 = \frac{\left\{\sum_{i=1}^{k'}\left[2T_{3i}(a_{3i} - h_{3i} + w_{3i}) + (P_{3i} + 2P_1)h_{3i} \cot \alpha_{3i} + (P_{3i} - 2Q_{Bi})l_{3i}\right] + 2\sum_{j=2}^{j-1}\sum_{i=1}^{j-1}(P_{3j} - Q_{Aj} - Q_{Bj})h_{3i} \cot \alpha_{3i} + P_1 l_{3k'}\right\}}{l_{31}}. \tag{20}$$
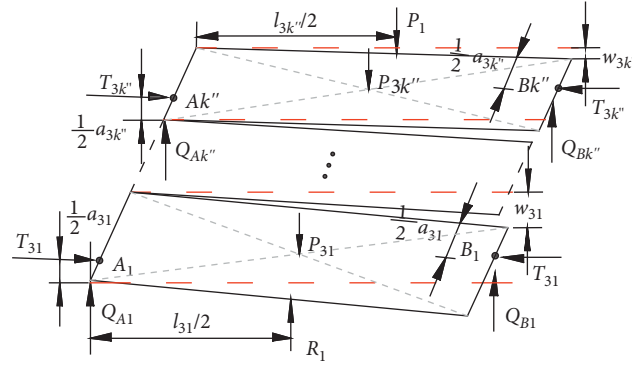
FIGURE 12: The force characteristic of hinged roof structure.

3.4. Determination of Working Resistance of Support in Working Face. The stress of stope support comes from the effect of direct roof weight and basic roof movement on support. The overlying strata structure of support in fully mechanized mining face with large mining height is composed of hinged roof structure, nonhinged roof structure, and combined cantilever beam structure. The instability movement of a certain structure will have an impact on the support of working face, which is reflected in the strata behavior of working face, mainly the change of support working resistance. Therefore, the support resistance should be able to adapt to the change of instability movement of overburden structure, bearing the weight of structure itself and the additional load generated by movement. Based on the analysis of the previous sections and formulas (2), (5), and (18), the calculation formula of working resistance of working face support is

$$P_z = p_1 + p_2 + p_3 + p_4. \tag{21}$$

Among them:

$$
\begin{aligned}
p_1 &= \frac{(1/2)\sum_{i=1}^{k} P_{1i}\left(h_{1i}\cot\alpha_{1i}+l_{1i}\right)+\sum_{j=2}^{k}\sum_{i=1}^{j-1}P_{1j}h_{1i}\cot\alpha_{1i}+\sum_{j=2}^{k'}\sum_{i=1}^{j-1}P_{2j}h_{2i}\cot\alpha_{2i}+(1/2)\sum_{i=1}^{k'}P_{2i}\left(h_{2i}\cot\alpha_{2i}+l_{2i}\right)-R_y l_y}{c}, \\[2mm]
p_2 &= \frac{1}{cl_{31}}\left(\frac{l_{31}}{2}+\sum_{i=1}^{k'}h_{2i}\cot\alpha_{2i}\right)\left\{2\sum_{j=2}^{k''}\sum_{i=1}^{j-1}\left(P_{3j}-Q_{Aj}-Q_{Bj}\right)h_{3i}\cot\alpha_{3i}+P_1 l_{3k''}+\sum_{i=1}^{k''}\left[2T_{3i}\left(a_{3i}-h_{3i}+w_{3i}\right)+\left(P_{3i}+2P_1\right)h_{3i}\cot\alpha_{3i}\right.\right. \\[2mm]
&\quad \left.\left.+\left(P_{3i}-2Q_{Bi}\right)l_{3i}\right]\right\}, \\[2mm]
p_3 &= \frac{1}{cl_x}\left[\frac{1}{2}\sum_{i=1}^{k'}P_{2i}\left(h_{2i}\cot\alpha_{2i}+l_{2i}\right)+\sum_{j=2}^{k'}\sum_{i=1}^{j-1}P_{2j}h_{2i}\cot\alpha_{2i}-R_y l_y\right]\sum_{i=1}^{k}h_{1i}\cot\alpha_{1i}, \\[2mm]
p_4 &= \frac{1}{cl_{31}l_x}\left[\left(\frac{l_{31}}{2}+\sum_{i=1}^{k'}h_{2i}\cot\alpha_{2i}\right)\sum_{i=1}^{k}h_{1i}\cot\alpha_{1i}\right]\left\{2\sum_{j=2}^{k''}\sum_{i=1}^{j-1}\left(P_{3j}-Q_{Aj}-Q_{Bj}\right)h_{3i}\cot\alpha_{3i}+P_1 l_{3k''}\right. \\[2mm]
&\quad \left.+\sum_{i=1}^{k''}\left[2T_{3i}\left(a_{3i}-h_{3i}+w_{3i}\right)+\left(P_{3i}+2P_1\right)h_{3i}\cot\alpha_{3i}+\left(P_{3i}-2Q_{Bi}\right)l_{3i}\right]\right\}.
\end{aligned}
\tag{22}
$$

Among them: $p_1 \sim p_4$ are the support resistance components of working face under articulated roof structure.

It can be seen that p_1 is mainly the component of support resistance caused by the combined cantilever beam of overlying strata, the weight of rock strata of nonhinged roof structure, and the support effect of gangue in goaf, p_2 is mainly the resistance component caused by the weight of hinged roof strata and the interaction between hinged broken blocks, p_3 is mainly caused by the nonhinged roof structure and the additional effect of goaf caving gangue, and p_4 mainly comes from the additional effect during the movement of hinged roof breaking block.

4. Case Analysis

4.1. Determination of the Working Resistance of the Support. Based on the mining conditions of No. 8218 large mining height coal seam face of Jinhuagong Coal Mine, combined with the research on the interaction relationship between the

abovementioned overlying rock structure and the support, the characteristics of the overlying rock structure of the coal roof are analyzed, and the support resistance of the working face is calculated. To provide reference for analyzing the appearance and mechanism of rock pressure on working face:

(1) Firstly, analyze the force of the combined cantilever structure on the support of the working face under the action of the combined cantilever beam structure. The height of the roof composite cantilever beam structure is about 26.1 m. It can be determined that the roof composite cantilever beam structure under the coal seam mining conditions of Jinhuagong Coal Mine is composed of the first to sixth layered roofs above the coal seam. The physical and mechanical characteristics of the roof composite cantilever structure rock are shown in Table 4.

Substituting the relevant data in Table 4 into formula (3), the change characteristics of the support resistance of the working face with the roof fracture angle are obtained, as shown in Figure 13.

Results that have been achieved have shown that the fracture angle of sandstone roofs is generally 85~90°, and the fracture angle in the physical simulation is 85°. Therefore, according to the conditions of Jinhuagong Coal Mine and the physical simulation test, the fracture angle of 85° is selected for the calculation of the working resistance. The other parameters are shown in Table 4. Only the role of the combined cantilever structure is considered, and the support resistance of the working face is about 12 MN.

(2) The nonhinged roof structure of No. 8218 high mining height coal seam is composed of the 7th~10th roof stratification of the overlying rock, and its physical and mechanical characteristics are shown in Table 5.

The relevant data in Table 5 are substituted into formula (5). If the hinged structure of the overlying rock roof is stable, and the fracture angle of the nonhinged roof is 85 ~ 90°, the support resistance of No. 8218 working face with large mining height should be between 12 and 13 MN when the combined cantilever beam and the nonhinged roof structure are considered.

(3) Finally, the stress of working face support under the action of articulated roof structure is analyzed. The hinged roof structure of working face is the masonry beam structure after the broken roof of No. 11 fine medium coarse sandstone, and its physical and mechanical characteristics are shown in Table 6.

The relevant data is substituted into formula (18) to calculate the force on the lower strata when the hinged roof structure is stable:

$$R_1 = T_{31} \left(\sin \theta_1 - i_{31} \right) + \left(P_{31} + 2P_1 \right) i_{31} \cot \alpha_{31} \\ + \left(P_{31} - 2Q_{B1} + P_1 \right). \tag{23}$$

According to formulas (16)~(18) and the equilibrium condition in the vertical direction of the rock stratum, the extrusion force between the broken blocks of the hinged roof and the friction force on the extrusion contact surface are calculated as follows:

$$T_{31} = \frac{2 \left(P_1 + P_{31} - 2R_1 \right)}{4i_{31} + 7 \sin \theta_2 - 3 \sin \theta_1}, \tag{24}$$

$$Q_{B1} = P_{31} + \frac{\left(P_1 - 2R_1 \right) \left(3 \sin \theta_2 + i_{31} \right)}{4i_{31} + 7 \sin \theta_2 - 3 \sin \theta_1}. \tag{25}$$

Among them, $i_{31} = h_{31}/l_{31}$.

Combined with the above calculation results, the support resistance of No. 8218 fully mechanized working face with large mining height should be between 13 and 15 MN. Therefore, the reasonable support working resistance of No. 8218 large mining height working face in Jinhuagong Coal Mine should not be less than 15 MN.

4.2. Working Face Support Selection. No. 8210 fully mechanized mining face with large mining height is the second large mining height working face in mine mining. Its position is the same as No. 8218 large mining height working face in No. 402 panel of 12 # coal seam, and the same coal seam is mined. In order to prevent similar crushing accidents in No. 8210 large mining height working face, and taking into account the existing equipment in the mining area, the ZZ13000/28/60 hydraulic support produced by Shanxi Pingyang Heavy Industry Machinery Co., Ltd., is selected in No. 8210 working face. The main technical parameters, as shown in Table 7, are supplemented by advanced blasting presplitting roof control technology measures to control the roof.

4.3. The Measured Analysis of Strata Behaviors. The ground pressure behavior of No. 8210 working face with large mining height was measured on-site. The automatic pressure recorder of Youluoka fully mechanized coal mining was used to continuously record the pressure behavior of the support in the working face. According to the difference of strata behaviors in the inclined direction of the working face, the working face is divided into three measuring areas. Five measuring lines are arranged at the positions of 25 #, 40 #, 55 #, 70 #, and 80 # supports in the central measuring area, and one measuring line is arranged at the positions of 10 # and 89 # supports at both ends, as shown in Figure 14.

The measured results show that the average end resistance of the support in the working face is 8731 kN, accounting for 67.2% of the rated working resistance of the support (13000 kN). During roof weighting, the maximum working resistance of working face support is 12611 kN, accounting for 97.0% of the rated working resistance of support. The average time-weighted working resistance of the support is 8540 kN, accounting for 65.7% of the rated working resistance of the support, and the maximum value is 11186 kN. The maximum time-weighted resistance is about 86.1% of the rated resistance of the support in the working

TABLE 4: The physical and mechanical characteristics of the roof combination of cantilever structure of No. 8218 large mining height working face.

Serial number	Lithology	Density kg/m³	Thickness (m)	Tensile strength (MPa)	Top plate force (MPa)	Breaking step (m)	Weight of broken block (MN)
6	Fine sandstone	2438	1.60	4.06	0.09	4.90	1.21
5	Sandy shale	1426	3.10	2.47	0.11	1.56	0.32
4	Medium sandstone	2453	9.20	5.21	0.22	3.80	1.66
3	Coarse sandstone	2683	9.00	6.22	0.44	15.47	3.40
2	Fine sandstone	2645	2.30	4.06	0.59	8.88	1.34
1	Sandy shale	2468	0.90	2.47	0.05	3.43	0.16
	Coal seam	1476	4.14				
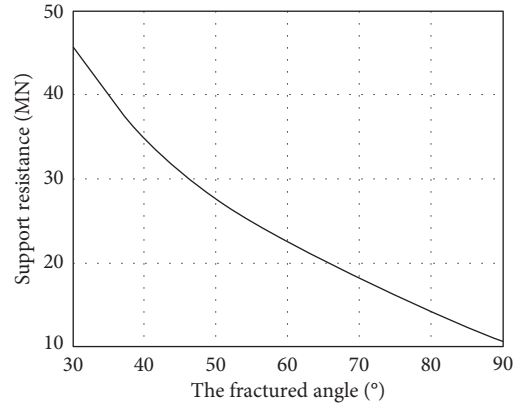
FIGURE 13: The relationship of stent resistance and the roof fracture angle of combination cantilever ($c = 5.5$ m).

TABLE 5: The physical and mechanical characteristics of the nonhinged roof structure of No. 8218 large mining height working face.

Serial number	Lithologic characters	Density kg/m³	Thickness (m)	Tensile strength (MPa)	Roof stress (MPa)	Break step (m)	Broken block weight (MN)
0	Coal seam	1423	1.22	3.13	0.01	3.45	0.30
9	Sandy shale	2514	5.22	2.47	0.19	17.11	5.79
8	Coal seam	1423	0.96	3.13	0.24	30.89	7.42
7	Sandy shale	2514	5.21	2.47	0.19	17.11	5.79

TABLE 6: The physical and mechanical characteristics of the hinged roof structure of No. 8218 large mining height working face.

Serial number	Lithologic characters	Density kg/m³	Thickness (m)	Antitension degree (MPa)	Roof by force (MPa)	Breaking step distance (m)	Broken blocks weight (MN)
13	Moderate coarse sandstone	2685	3.8	5.27	0.26	20.86	
12	Grit stone	2647	5.4	6.22	0.40	23.64	
11	Fine sandstone	2732	11.4	4.06	0.68	36.93	10.24

TABLE 7: The main support technical parameters of the ZZ13000/28/60.

Pattern	Four-column support shield
Height (lowest/highest)	2800/6000 mm
Width (minimum/maximum)	1660/1860 mm
Center distance	1750 mm
Setting load	10128 kN
Working resistance	13000 kN
Specific pressure in front of bottom plate	1.0~3.5 MPa
Support strength	1.24~1.28 MPa
Pumping station pressure	31.5 MPa
Maneuverability pattern	The control of this frame
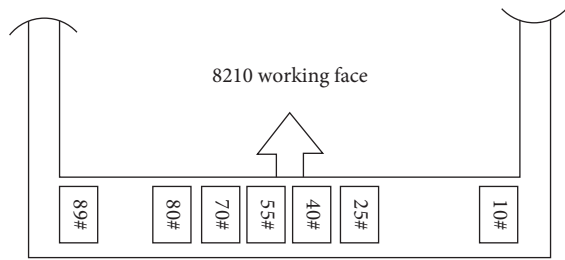
FIGURE 14: The face pressure observation station layout of No. 8210 working face in large fully mechanized mining face.

face. It shows that, during the normal mining period of the working face, the support ability of the working face is high, which can meet the control requirements of the roof of the coal seam with large mining height, and there is no frame crushing accident in the working face, and the support efficiency is fully exerted.

In summary, the selected ZZ13000/28/60 four-column support shield hydraulic support can meet the roof control requirements of No. 8210 large mining height working face.

5. Conclusions

(1) In the mining process of large mining height working face, the immediate roof of overlying strata exists in the form of combined cantilever beam. With the increase of caving height, the caving gangue gradually fills the goaf space. The bending subsidence of the broken block of the overlying strata of the combined cantilever beam is supported by the caving gangue. At this time, the allowable subsidence space of the goaf exceeds the allowable subsidence of the limit extrusion between the broken blocks of the roof, and the hinged rock-beam structure cannot be formed between the blocks. This part of the rock exists in the form of nonhinged structure. Because the broken block of the nonhinged structure rock is large and the arrangement is regular after collapse, when the rock above the nonhinged structure is broken, the extrusion pressure between the broken blocks is relatively large, and finally the articulated roof structure is formed. The overlying strata roof of fully mechanized mining face with large mining height presents the morphological characteristics of 'combined cantilever beam structure-nonhinged roof structure-hinged roof structure'.

(2) When the working face with large mining height is mined, the overlying strata have a large range of movement and collapse, and the different lithology characteristics of the roof strata lead to the new characteristics of the overlying strata structure. The roof strata between the support and the hinged roof structure cannot be simply regarded as the immediate roof. The interaction system between the support and the surrounding rock is composed of the hinged roof structure-the nonhinged roof structure-the combined cantilever beam structure-the support. The stability of the overburden structure and its

influencing factors are studied. According to the principle of the interaction between the support and the surrounding rock, the support resistance should be able to adapt to the change of the instability movement of the overburden structure, bearing the weight of the structure and the additional load generated by the movement, and the calculation formula of the support resistance of the working face is obtained.

(3) The reasonable support resistance of hydraulic support in No. 8210 large mining height working face is determined. The field observation results show that the selected ZZ13000/28/60 four-column support shield hydraulic support can meet the requirements of roof control. During the mining of the working face, there was no support crushing accident in the working face, and the rib spalling of the coal wall was effectively controlled, which ensured the safe mining of the working face with large mining height and achieved significant economic and social benefits.

Data Availability

This is an open access article distributed under the creative commons attribution license, which permits unrestricted use, distribution, and reproduction in any medium, provided the original work is properly cited.

Conflicts of Interest

The authors declare that there are no conflicts of interest regarding the publication of this paper.

Acknowledgments

References

[1] G. F. Wang and Y. H. Pang, "Full-mechanized coal mining and caving mining method evaluation and key technology for thick coal seam," *Journal of China Coal Society*, vol. 43, no. 1, pp. 33–42, 2018.

[2] M. G. Qian, P. W. Shi, and J. L. Xu, *Ground Pressure and Strata Control*, China University of Mining and Technology Press, China, 2013.

[3] M. G. Qian, *Key Strata Theory of Strata Control*, China University of Mining and Technology Press, Xuzhou, China, 2013.

[4] J. H. Wang, "Present status and development tendency of fully mechanized coal mining technology and equipment with high cutting height in China," *Coal Science and Technology*, vol. 34, no. 1, pp. 4–7, 2006.

[5] Y. Ning, *Comprehensive Mechanized Mining Technology and Equipment with Large Mining Height in china*, China Coal Industry Publishing House, Beijing, China, 2012.

[6] Y. Q. Xu, *Coal Mining*, China University of Mining and Technology Press, Xuzhou, China, 1999.

[7] F. L. He, M. G. Qian, and C. Y. Liu, *Support Surrounding Rock Support System of High Yield and High Efficiency Working Face*, China University of Mining and Technology Press, Xuzhou, China, 1997.

[8] N. E. Yasitli and B. Unver, "3D numerical modeling of longwall mining with top-coal caving," *International Journal of Rock Mechanics and Mining Sciences*, vol. 42, no. 2, pp. 219–235, 2005.

[9] D. B. Mao and L. J. Kang, "Longwall top coal caving mining with higher mining height and its feasibility," *Coal Mining Technology*, vol. 9, no. 1, pp. 11–14, 2003.

[10] Q. M. Liu and D. B. Mao, "Research on adaptability of full-mechanized caving mining with large," *Mining-height Original Research Article Procedia Engineering*, vol. 26, pp. 652–658, 2011.

[11] P. L. Gong, *Theory of Surrounding Rock and Application Study of the Coal Face with Greater Mining Height*, China Coal Industry Publishing House, Beijing, China, 2006.

[12] P. L. Gong, Z. M. Jin, and H. J. Hao, "Research on stability test for fully mechanized mining support with large mining height," in *Proceedings of the Second International Symposium on Mining Technology*, pp. 246–251, Greenland, 2001.

[13] Q. X. Huang, W. G. Liu, and Y. S. Tian, "Observation on the law of strata behavior in shallow seam and high mining height face," *Ground Pressure and Strata Control*, vol. 20, no. 3, pp. 58-59, 2003.

[14] Z. H. Li, K. Yang, and X. Z. Hua, "Disaster-causing mechanism of instability and 'macroscopic-big-small' structures of overlying strata in longwall mining," *Journal of China Coal Society*, vol. 45, no. S2, pp. 541–550, 2020.

[15] S. H. Yan, X. W. Yin, and H. J. Xu, "Roof structure of short cantilever-articulated rock beam and calculation of support resistance in full-mechanized face with large mining height," *Journal of China Coal Society*, vol. 36, no. 11, pp. 1816–1820, 2011.

[16] J. L. Xu and J. F. Ju, "Structural morphology of key stratum and its influence on strata behaviors in fully mechanized face with super-large mining height," *Chinese Journal of Rock Mechanics and Engineering*, vol. 30, no. 8, pp. 1547–1556, 2011.

[17] G. F. Wang, Y. H. Pang, M. Z. Li, and Y. Ma, "Hydraulic support and coal wall coupling relationship in ultra large height mining face," *Journal of China Coal Society*, vol. 42, no. 2, pp. 518–526, 2017.

[18] J. Ju and J. Xu, "Structural characteristics of key strata and strata behaviour of a fully mechanized longwall face with 7.0m height chocks," *International Journal of Rock Mechanics and Mining Sciences*, vol. 58, pp. 46–54, 2013.

[19] X. W. Yin, "Cutting block structure model of overburden with shallow buried coal seam and ultra-large mining height working face," *Journal of China Coal Society*, vol. 44, no. 7, pp. 1961–1970, 2019.

[20] C. L. Zhang, L. Guo, and M. P. Zhang, "Measurements of working resistance and adaptability analysis of shield in fully mechanized coal face with large mining height and medium buried depth," *Coal Mine Machinery*, vol. 41, no. 6, pp. 68–71, 2020.

[21] F. Q. Qiu, L. Zhu, and W. Z. Gu, "Mining pressure law and working resistance of support in face with large mining height in shallow seam," *Safety in Coal Mines*, vol. 51, no. 11, pp. 243–247, 2020.

[22] H. C. Li, *Similar Simulation Test of Mine Pressure*, China University of Mining and Technology Press, Xuzhou, China, 1988.

WILEY | Hindawi

Research Article

Enhancement of Coal Permeability Using Aqueous NaCl with Microwave Irradiation

Weiming Guan [ID],[1,2] **Qi Qi** [ID],[1,2] **Senlin Nan** [ID],[1,2] **Haichao Wang,**[1] **Xin Li,**[1] **Yingyuan Wen,**[1,2] **Junhui Yao,**[1,2] **and Yanyan Ge**[1]

[1]*College of Geology and Mining Engineering, Xinjiang University, Urumqi 830047, China*
[2]*Autonomous Region Experimental Teaching Demonstration Center for Geology and Mining Engineering, Xinjiang University, Urumqi 830047, China*

Correspondence should be addressed to Qi Qi; xjuqiqi@163.com

Water in coal pores can generate strong steam explosions when treated with microwave irradiation. In order to improve the sensitivity of coal reservoirs to microwaves, we used varying concentrations of NaCl on the pore solution, which further increased the effect of microwaves on permeability enhancement. In our experiments, we selected 3 ratios of water content and 5 different concentrations of NaCl. The changes of coal water content and permeability before and after irradiation were compared. In addition, changes in coal surface temperature and internal thermal power were analyzed through thermal imaging and random sphere numerical modeling. Results showed that the increase of the proportion of solution mass and the ion concentration in the solution improved the overall dielectric properties of coal rock samples. After microwave irradiation, the average reduction rate of water content in coal rock samples increased with the increase of ion concentration in the solution. Both the average surface temperature of the coal rock samples and the average electromagnetic heating power gradually increased; this increases the temperature rise rate and maximum temperature of coal rock samples under the same irradiation time, which is conducive to better rapid accumulation of steam pressure, thereby improving the pore structure more effectively. Finally, the maximum growth rate of permeability reached 466.18%. This work provides a novel train of thought to enhance coal permeability by using microwave irradiation.

1. Introduction

Recent development of clean energy technologies, the impact of Covid-19, and the significant reduction in coal demand by OECD countries have resulted in reduction in global coal consumption. In 2019, consumption decrease was of 0.6%. In addition, its share of primary energy reached the lowest level in 16 years (27%) [1]. The International Energy Agency (IEA) also predicted that the use of coal will continue to decline in the future [2]. Nevertheless, 3.90 billion tons of standard coal were produced in China in 2020. Thus, coal still plays a dominant role in China's primary energy structure [3], accounting for about 60% [4]. In coal underground mineral deposits, the working faces gradually shift to the deeper part of the formation as mining opera-

tions progress to deeper levels. Also, coal and gas explosions may cause serious injuries to the personnel [5], events that are especially catastrophic [6]. In coal mines, gas has become an important factor restricting the efficiency of mining activities [7, 8]. At the same time, coalbed methane is an efficient and clean energy [9]. The estimated amount of China's shallow coalbed methane resources at 2000 meters and above is 36.81 trillion cubic meters. Therefore, it is likely that the exploitation of coalbed methane will be safe and of great energy benefit [10, 11].

Enhancement of coal seam permeability is generally carried out by hydraulic fracturing [12, 13]. In the case of Xinjiang, China, there is a reduced water supply [14] as well as arid and semiarid [15, 16] environments. Therefore, there is an urgent need for new options that enhance the
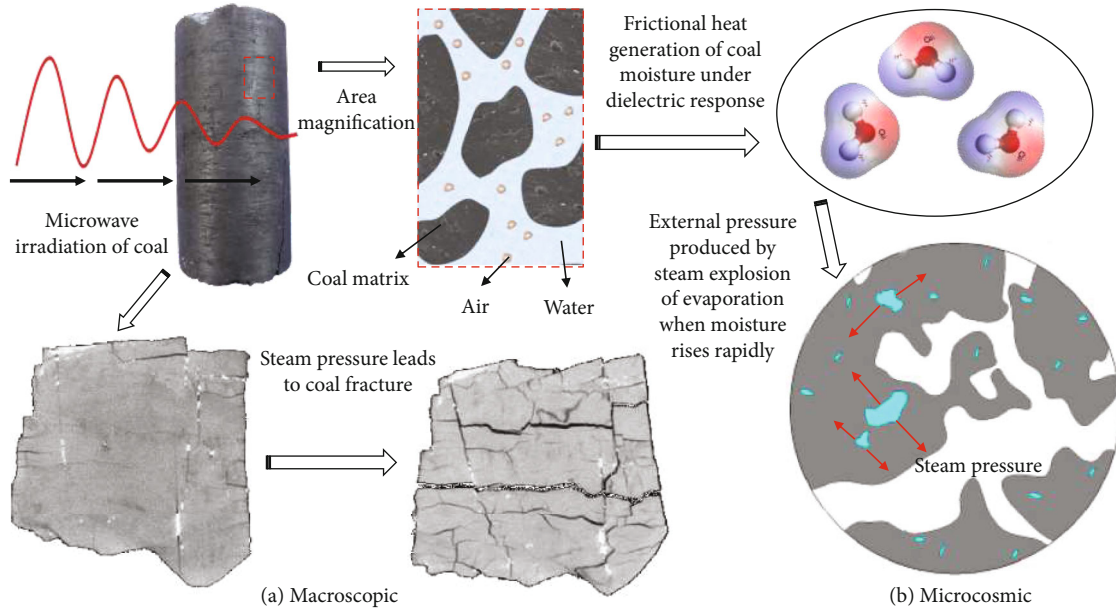
FIGURE 1: Explosion of water vapor contained in coal rocks after microwave heating.
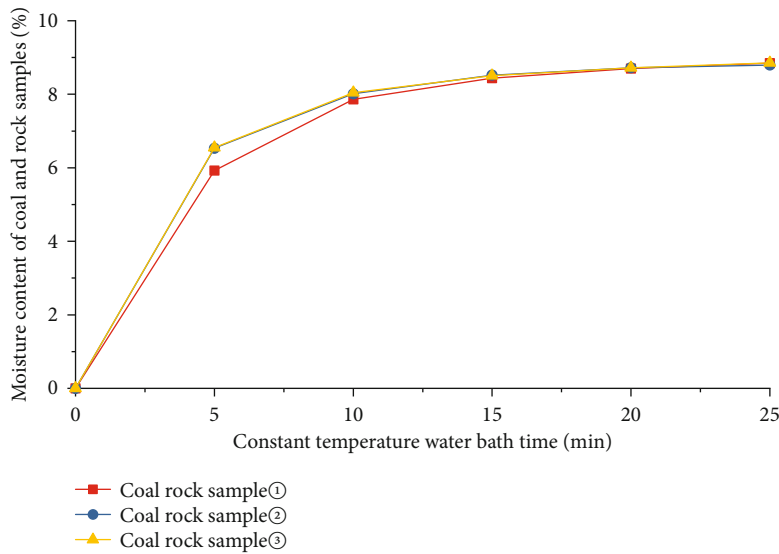
FIGURE 2: Determination of saturated moisture content of coal rock (Jiangsu Kexi Instrument Co., Ltd. HH-XMTD203 water bath, temperature 20°C).

permeability of coal reservoirs. Multiple studies have shown that microwave can effectively increase the porosity and permeability of coal reservoirs [17–19]. It has also been determined that high-pressure water vapor (microwave frequency 2.45 GHz, microwave power 1 kW, irradiation time 240 s, coal sample temperature 222°C, relative atmospheric pressure 1.54 kPa) in the pore structure may cause pore deformation, destruction, and interconnection [20, 21]. The moisture present in the coal reservoir displays a dielectric loss greater than that in the coal matrix; therefore, it may be selectively heated using microwaves [22–24]. We have also previously shown that the water contained in coal rocks can be quickly heated under microwave irradiation. The water vapor that is formed in this process exerts a high

pressure on the inner wall of the pores, eventually destroying the pore structure and increasing the connectivity [25]. Figure 1 displays the macro- and microprocesses of explosion caused by water vapor contained in the coal; of course, in the process of microwave heating, the cracks in the coal are not only caused by steam pressure but also caused by the imbalance of the thermal stress, the thermal decomposition of natural filler, and so on.

Coal, a porous medium, displays a limited water storage capacity, as shown in Figure 2; with the extension of constant temperature water bath time, the water content of the three groups of coal rock samples increased more and more slowly and finally reached the upper limit of their own water storage. Therefore, there is always an upper limit to increase

TABLE 1: Experimental design.

NaCl concentration, P_k (g/L) Moisture content, Q_j (%)	$Q_1 = 2$	$Q_2 = 4$	$Q_3 = 6$
$P_1 = 0$	1	1	1
$P_2 = 16$	1	1	1
$P_3 = 32$	1	1	1
$P_4 = 48$	1	1	1
$P_5 = 64$	1	1	1

the permeability under microwave irradiation by increasing the water content of coal. Previous studies have demonstrated that microwaves are more efficiently absorbed in solutions containing ions [26]. Microwave frequency dipole polarization is considered the most important conversion mechanism for microwave heating [27]. Once the solution containing ions is placed in the microwave field, the ions follow the alternating electric field and move rapidly and repeatedly in changing directions [28]. The migration of ions forms a current that is lost as thermal energy. Therefore, the introduction of ions in the water can significantly improve its microwave absorption performance.

Pickles et al. [29] studied the influence of magnetite on the kinetics of microwave drying of low-order bituminous coal. Results indicated that the addition of magnetite as absorbent improved the process of microwave drying. Wang et al. [30] used microwave heating for the pyrolysis of lignite. These researchers demonstrated that, in the absence of additives, the temperature of lignite only reached about 200°C after irradiation with a microwave power of 700 W for 10 minutes. In contrast, the temperature of lignite significantly increased when ferroferric oxide was used as absorbent. In this case, the temperature of the sample reached 800°C after 3 minutes of irradiation at the same microwave power. Zhou [31] found out that, when a 2.34% NaCl solution was added to coal, the dielectric constant of this material rapidly increased. As a consequence, the conversion efficiency of microwave irradiation into heat was enhanced in 64%. Based on these data, we consider increasing the ion concentration of the aqueous solution present in coal in order to improve its ability to absorb microwaves. The purpose of the present research was to investigate the influence of the increase of ion mass ratio and ion concentration on coal permeability when this material was exposed to microwave irradiation. We used physical and numerical experiments in order to clarify the mechanism of permeability improvement when microwave steam explosion is used.

2. Experimental Procedure

The experimental design (Table 1) consisted of 15 different experimental conditions. Moisture content values were 2%, 4%, and 6%, and NaCl concentrations of 0 g/L, 16 g/L, 32 g/L, 48 g/L, and 64 g/L were selected with only one replicate per condition. The changes of physical parameters (including coal permeability, water content, surface temperature,

and internal temperature) of the samples before and after microwave irradiation were analyzed and compared.

Experiments consisted of two parts where coal permeability was measured before (Part I) and after (Part II) microwave irradiation under different conditions. The first step was to weigh the mass of the coal rock sample M_g after it was completely dried. The second step was to determine the initial permeability of the coal sample before microwave irradiation k_q. The third step was to obtain the maximum moisture content of the coal sample ω_i. In the fourth step, NaCl aqueous solutions with different concentrations were prepared and coal samples were soaked until saturation and air-dried until proper moisture content was achieved. The fifth step was to carry out the microwave irradiation treatment and record the temperature afterwards. The sixth step was to test and obtain the permeability of the coal sample after microwave irradiation k_h. The flow chart is shown in Figure 3.

2.1. Coal Sample Preparation. Cylindrical coal samples with a diameter of 25 mm and a height of 25 mm were obtained from the Fukang mining area located in Xinjiang, China. Then, unified cylindrical coal rock samples with a height of 25 mm and a diameter of 25 mm were made. The coal rock samples were labeled with numbers 1 to 15. Materials were dried for 6 h at a temperature of 110°C using the ZK-2020 vacuum drying oven produced by Chongqing Wuhuan Test Instrument Co., Ltd. Later, inspection drying was carried out and continued for 1 hour each time. Coal samples were considered to be completely dried when the mass of the coal sample was reduced by no more than 2% after two consecutive dryings. The weighing record of mass M_g is shown in Table 2.

2.2. Pore Parameter Measurements. In order to determine the permeability of the dried coal rock samples, we used the AP-608 overburden porosity-permeability tester developed by Coretest, an American rock core experiment system company. The confining pressure during the test was set to 500 PSI (3.4475 MPa), the osmotic pressure was set to 200 PSI (1.379 MPa), the test gas was high-purity nitrogen, and the transient method was used for measurement. Table 3 displays the basic permeability parameters k_q of coal rock samples before microwave irradiation.

2.3. Determination of the Content of Saturated Water. Completely dried coal rock samples were placed into the HH-XMTD203 water bath (Jiangsu Kexi Instrument Co., Ltd.) for saturation with distilled water. Water temperature was set up to 20°C and the saturation time to 60 minutes. The mass of the saturated sample was recorded as M_s. After weighing, the maximum moisture content $\omega_{k,j}$ was calculated using the mass of completely dried coal rock samples M_g, as shown in the following equation.

$$\omega_{k,j} = \frac{M_s - M_g}{M_g} \times 100\%. \tag{1}$$

Because there is an upper limit on the water retention of different coal rock samples, the experiment requires that the

Test process 1 : Permeability test of original coal rock sample

Test process 2 : Permeability test of coal and rock samples under different conditions

(a) Coal sample; (b) ZK-2020 vacuum drying oven; (c) Electronic balance; (d) Newsail commercial microwave oven; (e) Water saturation of samples under different conditions; (f) AP-608 overburden porosity-permeability tester; (g) Infrared imaging thermometer.

FIGURE 3: Permeability test flow chart.

TABLE 2: Mass (g) of completely dried coal samples.

NaCl concentration, P_k (g/L) Moisture content, Q_j (%)	$Q_1 = 2$	$Q_2 = 4$	$Q_3 = 6$
$P_1 = 0$	12.453	13.576	13.605
$P_2 = 16$	11.389	14.323	13.059
$P_3 = 32$	8.348	12.699	14.050
$P_4 = 48$	11.759	11.625	13.012
$P_5 = 64$	12.325	12.235	12.211

TABLE 4: Maximum moisture content (%) of coal rock samples $\omega_{k,j}$.

NaCl concentration, P_k (g/L) Moisture content, Q_j (%)	$Q_1 = 2$	$Q_2 = 4$	$Q_3 = 6$
$P_1 = 0$	9.12	9.87	9.94
$P_2 = 16$	8.86	9.26	10.43
$P_3 = 32$	10.05	9.20	10.13
$P_4 = 48$	9.18	9.98	10.86
$P_5 = 64$	9.19	9.56	10.61

TABLE 3: Initial permeability (mD) of coal rock samples.

NaCl concentration, P_k (g/L) Moisture content, Q_j (%)	$Q_1 = 2$	$Q_2 = 4$	$Q_3 = 6$
$P_1 = 0$	0.9977	0.5614	0.2401
$P_2 = 16$	0.5083	0.2245	0.1625
$P_3 = 32$	0.3460	0.2225	0.1525
$P_4 = 48$	0.2344	0.1803	0.1490
$P_5 = 64$	0.2288	0.1567	0.0835

TABLE 5: Time of microwave irradiation to coal rock samples (s).

NaCl concentration, P_k (g/L) Moisture content Q_j (%)	$Q_1 = 2$	$Q_2 = 4$	$Q_3 = 6$
$P_1 = 0$	29	32	32
$P_2 = 16$	27	34	31
$P_3 = 32$	20	30	33
$P_4 = 48$	28	27	31
$P_5 = 64$	29	29	29

coal rock samples can store 6% of water, so we tested the upper limit of water retention of each coal rock sample, as shown in Table 4. It is found that the upper limit of water saturation of all the coal rock samples is greater than 6%, so all coal rock samples meet the experimental requirements.

2.4. Preparation of Coal Samples Containing NaCl Solution. Dried coal samples were soaked in 50 mL of different NaCl concentrations until saturation. Later, corresponding mois-

ture content was achieved after air-drying. In general, after air-drying occurs, part of the water evaporates and the NaCl remains in the sample. As a result, NaCl concentration in the coal pores gradually increases, resulting in a final concentration higher than the preset value. Therefore, in order to determine the NaCl mass (g) that should be added to 50 mL of water, we considered the saturated moisture content $\omega_{k,j}$ of each coal sample, the preset moisture content Q_j of the experimental scheme, and the preset NaCl

TABLE 6: Change in moisture content in coal rock samples after microwave irradiation (%).

NaCl concentration, P_k (g/L) Moisture content, Q_j (%)	$Q_1 = 2$		$Q_2 = 4$		$Q_3 = 6$		Average reduction rate
	Moisture content after microwave irradiation	Reduction rate of moisture content	Moisture content after microwave irradiation	Reduction rate of moisture content	Moisture content after microwave irradiation	Reduction rate of moisture content	
$P_1 = 0$	1.96	1.79	3.85	3.74	5.49	8.56	4.69
$P_2 = 16$	1.95	2.38	3.79	5.13	5.37	10.46	5.99
$P_3 = 32$	1.95	2.64	3.79	5.26	4.98	16.97	8.29
$P_4 = 48$	1.94	3.05	3.76	5.95	3.93	34.43	14.48
$P_5 = 64$	1.93	3.37	3.67	8.37	3.59	40.18	17.31
Average value		2.64		5.69		22.12	

concentration P_k. The formula is deduced as follows: (1) soak the coal pillar in pure water until the water is saturated and record the water saturation mass of the coal pillar as M_s; (2) the salt added to the water is calculated as $(M_g \times Q_j)/50 \times P_k$; (3) the mass of water that can be stored in coal rock samples is calculated as $M_s - M_g$; and (4) the formula for the mass of NaCl to be added for soaking 50 mL water of coal pillar is shown in the following equation.

$$\mathrm{NaCl}_{50\mathrm{ml}} = \frac{M_g \times Q_i \times P_k}{M_s - M_g}. \quad (2)$$

The calculated NaCl mass was used to prepare the corresponding NaCl aqueous solution, and the coal rock samples were soaked to reach a water-saturated state. Then, the samples were air-dried. During the drying process, when the coal sample mass reached 1.06, 1.04, and 1.02 times the value of the quality control, that is, the completely dried mass M_g, coal samples with different NaCl concentrations at moisture content of 6%, 4%, and 2% were obtained.

2.5. Determination of Microwave Irradiation Duration. Throughout its formation, coal is affected by long-term high temperature and high pressure environments, the diversity of coal-forming plants, and complex physical and chemical changes. This leads to high coal heterogeneity, and thus, the mass of each sample is slightly different. Differences in individual weight of the samples may cause variations in the absorption of microwave energy by the coal rocks. In order to eliminate these potential variations, the irradiation time was calculated using the following equation.

$$T_{i,j} = \frac{M_g}{M_A} \times 30. \quad (3)$$

For the microwave experiment, we used the Newsail commercial microwave oven. The microwave power was set to 2 kW and the microwave frequency to 2.45 GHz, and the specific duration of microwave irradiation is shown in Table 5.

After irradiation, an UTi-165A thermal imaging camera was used to take pictures and measure temperature. The

mass of the samples after irradiation was also obtained and recorded.

3. Results

3.1. Changes in Moisture Content. As shown in Table 6, the moisture content of the coal samples after microwave irradiation was lower than the initial one. Data indicated that as the initial coal moisture content increased, the reduction rate of the coal moisture after the microwave treatment also increased. The average reduction rates at initial moisture content conditions of 2%, 4%, and 6% were 2.64%, 5.69%, and 22.12%, respectively. In addition, with increasing initial NaCl concentrations in the internal coal solution, the average decrease rate of the moisture content after microwave irradiation also increased. The average reduction rate of moisture content under NaCl concentrations of 0 g/L, 16 g/L, 32 g/L, 48 g/L, and 64 g/L were 4.69%, 5.99%, 8.29%, 14.48%, and 17.31%, respectively.

3.2. Changes in Permeability. As shown in Table 7, the permeability of the coal samples after microwave irradiation increased as compared with the initial permeability. Distribution of the increase rate of permeability in each coal sample and under the same coal rock moisture content indicated that the greater the NaCl concentration, the higher the increased permeability rate after microwaving. NaCl concentrations of 0 g/L, 16 g/L, 32 g/L, 48 g/L, and 64 g/L resulted in an increase rate in average permeability of 196.37%, 216.39%, 343.51%, 465.80%, and 466.18%, correspondingly.

4. Promotion Mechanism of Ionic Solution in Microwave Irradiation of Coal Rock

The experimental test shows that the NaCl aqueous solution in coal rock samples will have a positive impact on the permeability of coal rock samples. In order to find out how NaCl aqueous solution affects the dielectric properties of coal and rock and then affects the temperature change of coal rock samples under the action of microwave, it will be discussed below.

TABLE 7: Changes in coal moisture content after microwave irradiation (%).

NaCl concentration, P_k (g/L) Moisture content, Q_j (%)	$Q_1 = 2$		$Q_2 = 4$		$Q_3 = 6$		Average growth rate
	Permeability before microwave irradiation	Permeability after microwave irradiation	Permeability before microwave irradiation	Permeability after microwave irradiation	Permeability before microwave irradiation	Permeability after microwave irradiation	
$P_1 = 0$	0.9977	2.2285	0.5614	0.8799	0.2401	1.2214	196.37%
$P_2 = 16$	0.5083	0.8216	0.2245	0.8602	0.1625	0.6571	216.39%
$P_3 = 32$	0.3460	0.5776	0.2225	1.6077	0.1525	0.6726	343.51%
$P_4 = 48$	0.2344	0.7624	0.1803	0.8572	0.1490	1.3361	465.80%
$P_5 = 64$	0.2288	0.5888	0.1567	0.7912	0.0835	0.7818	466.18%

4.1. Mechanism of the Effect of Ionic Solutions on Dielectric Properties of Coal Rocks.

Coal rock is a porous medium where dielectric properties are mainly determined by the volume of air and moisture and coal matrix characteristics. Among them, the dielectric response of moisture in the microwave field far exceeds that of air and coal. This section studies the mechanism through which the proportion of solution mass and solution ion concentration affects the dielectric properties of coal.

4.1.1. Effect of Solvent to Solute Mass Ratio on Dielectric Properties of Coal Rocks.

Dielectric loss and Joule heat loss occur when microwaves are irradiated on different materials. Under the action of an electric field, the polar molecules present in these materials undergo relaxation polarization and resonance polarization processes, which lead to dielectric loss. At the same time, under a given electric potential, an electric current is generated inside the dielectric material. This process causes the loss of Joule heat. These two phenomena are the key to heat generation. According to previous studies, the total electromagnetic power loss that occurs when microwaves irradiate the medium can be calculated according to the following equation:

$$P_w = 2\pi f \varepsilon_w'' \varepsilon_0 |E|^2, \tag{4}$$

where P_w (W/m^3) is the electromagnetic loss thermal power density; f is the frequency of the electric field (Hz); ε_w'' is the imaginary part of the relative complex permittivity of the heated object, which characterizes the ability of the substance to absorb and lose electromagnetic field energy; $\varepsilon_0 = 8.85\mathrm{e} - 12$ F/m is the dielectric constant in vacuum; and $|E|$ (V/m) is the modulus of the electric field intensity.

According to Equation (4), in addition to the microwave power and microwave frequency, the factors affecting the microwave heating of a substance mainly depend on the inherent dielectric properties of the heated material. The dielectric constant is an important factor that determines the increment in temperature of coal. A significant amount of tests have been conducted to determine the dielectric constant of coal rocks. It is generally believed that the real part of the dielectric constant of the coal rock matrix is between 1.6 and 2.5, and the imaginary part of the dielectric constant is between 0.05 and 0.2 [32]. The real and imaginary values of the dielectric water constant are much higher than those of the coal matrix, which are 80 and 9, respectively [33, 34].

Since the coal rock is a mixed substance, the imaginary part of the mixed relative complex permittivity can be estimated considering the imaginary part of the mixed relative complex permittivity and volume ratio of each substance. In general, as the moisture content increases, the overall dielectric properties of the coal rocks also increase. Under the same microwave power and irradiation time, the internal temperature of the coal rocks continuously increases. High temperatures and pressures cause the violent evaporation of water. In this processes, the greater the initial moisture content of the coal, the greater the reduction rate of the coal's moisture content after microwave irradiation (Figure 4). The higher the moisture content in the coal rocks, the greater the rate of temperature increase, the higher the temperature of the coal rock, and the higher the sources of steam. When the volume is limited, especially when the pore volume inside the coal rock is small, the pressure of the expanding gas on the inner wall of the pore increases. Since the force area does not change, the absolute vapor pressure inside the coal rock rapidly increases.

At the same time, because of its particular properties, the total porosity of coal rocks displays a maximum value. Thus, there is an upper limit on the amount of water they can hold, and in consequence, there is a certain upper limit for the overall improvement of the dielectric properties of coal samples. In order to further improve the dielectric response of water to the microwave field, it is necessary to explore the influence of ion concentration on the dielectric properties of coal rocks.

4.1.2. Effect of Ion Concentration on Dielectric Properties of Coal Rocks.

As Figure 5 displays, permeability of the coal rocks increased with increasing NaCl concentrations. Outlier data occurred because of the high heterogeneity in the coal samples. Anomalies occurred because pores and fissures connected to the outside expanded and connected by means of the high water vapor pressure, causing a substantial increase in permeability. Thus, the increment in moisture content and NaCl concentration can effectively increase the permeability of coal after microwave irradiation. Compared to a completely dry coal sample, under high moisture content and high NaCl concentration, coal permeability increased 4.66 times after microwave irradiation. Under
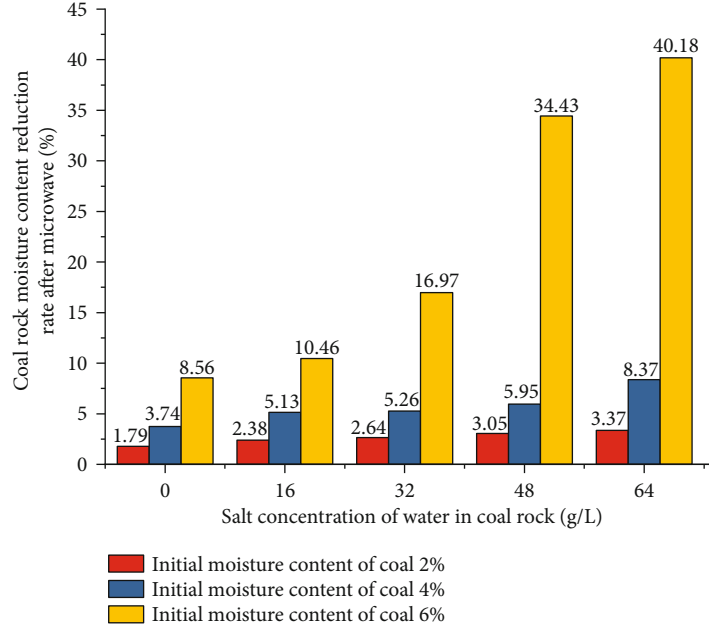
FIGURE 4: Reduction in moisture content rate after microwave irradiation (%).
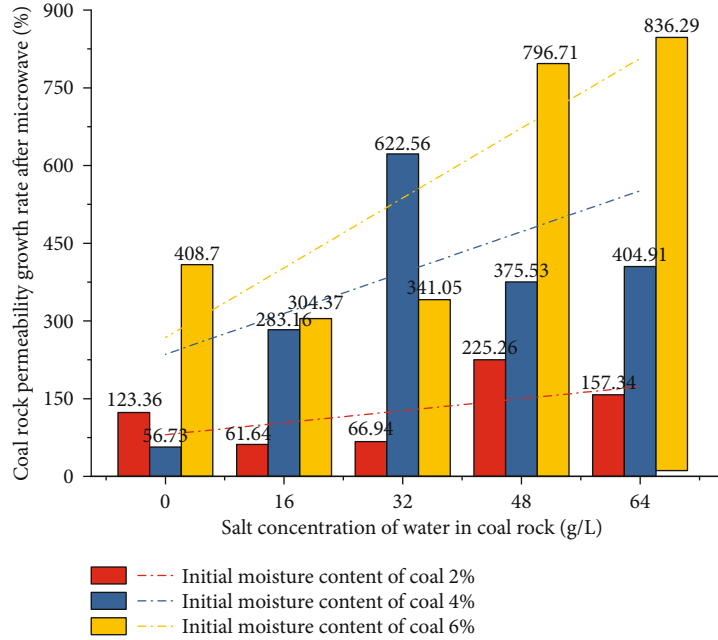
FIGURE 5: Increasing rate of coal rock permeability.

the same moisture content conditions, results indicated that by increasing the ion concentration of the solution, the average permeability increased 1.91 times in the three cases.

Adding NaCl to the solution can greatly increase the imaginary part of the complex permittivity of water, which can be calculated according to the following equation:

$$\varepsilon''_w = \frac{\omega\tau_w(\varepsilon_{w0} - \varepsilon_{w\infty})}{1 + (\omega\tau_w)^2} + \frac{\sigma}{\omega\varepsilon_0}, \tag{5}$$

where ω (Hz) corresponds to the angular frequency, f (Hz) is the frequency of the electric field, τ_w (s) is the relaxation time of water polarization, ε_{w0} (F/m) is the dielectric constant of water in an electrostatic field, $\varepsilon_{w\infty} = 4.9$ F/m represents the dielectric constant at high frequency, $\varepsilon_0 = 8.854 * 10^{-12}$ F/m is the dielectric constant of vacuum, and σ (S/m) is the conductivity of water.

Equation (5) indicates that the relaxation time τ_w of the polarization of water media in the microwave field and the dielectric constant ε_{w0} of water in the electrostatic field are

(a)

(b)
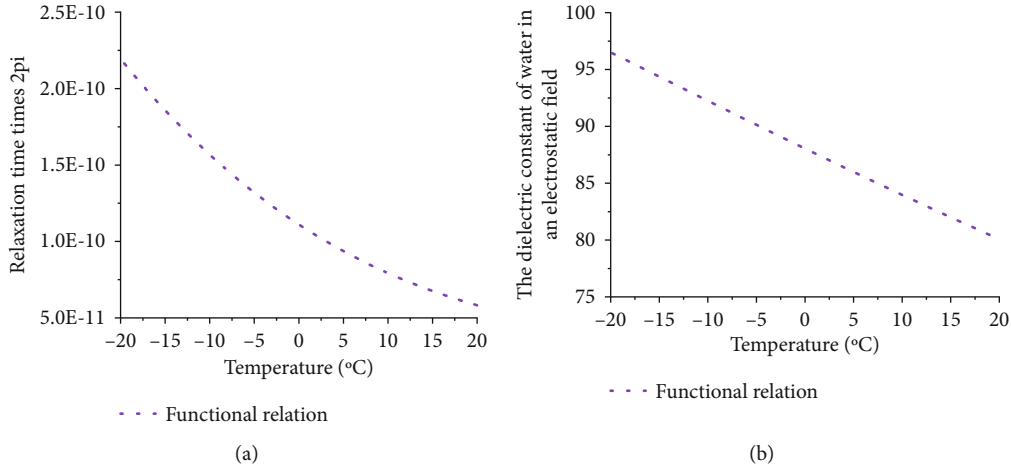
FIGURE 6: τ_w and ε_{w0} as a function of temperature: (a) τ_w as a function of temperature; (b) ε_{w0} as a function of temperature.
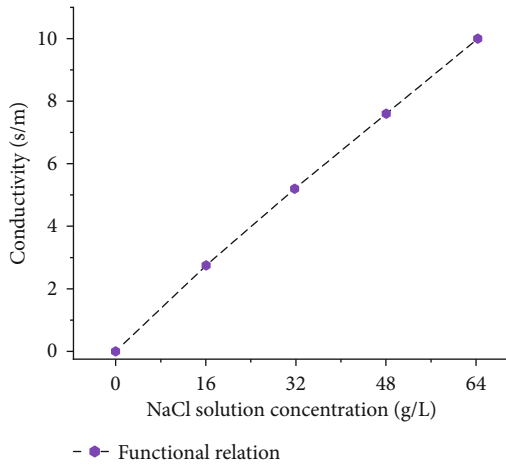
FIGURE 7: Relationship between NaCl concentration and conductivity of the solution.

important parameters that affect the dielectric loss of water. They are functions of temperature, as seen in equations (6) and (7), as shown in Figures 6(a) and 6(b).

$$2\pi\tau_w = 1.1109 \times 10^{-10} - 3.824 \times 10^{-12} T + 6.938 \\ \times 10^{-14} T^2 - 5.096 \times 10^{-16} T^3, \tag{6}$$

$$\varepsilon_{w0} = 88.045 - 0.4147 T + 6.295 \times 10^{-4} T^2 \\ + 1.075 \times 10^{-5} T^3. \tag{7}$$

Conductivity 6, which is closely related to the ion concentration of the solution, is the most important parameter that affects Joule heat loss. The higher the electrical conductivity, the stronger the ability of the coal rock samples to absorb an electromagnetic field, and the more intense the dielectric response under the same moisture content. In the present research, NaCl was used to increase the ion concentration of water present in the coal rock samples, thereby increasing the conductivity of the aqueous solution. The concentration of NaCl and the conductivity of the solution are shown in Figure 7.

According to data shown in Figure 7, with increasing NaCl concentrations, conductivity also increased. NaCl concentrations of 0 g/L, 16 g/L, 32 g/L, 48 g/L, and 64 g/L resulted in conductivity values of 0 s/cm, 2.75 s/m, 5.2 s/m, 7.6 s/m, and 10s/m, respectively. This increment was extremely high for NaCl-containing solutions, greatly increasing the imaginary part of the dielectric constant of water. As a result, the moisture in the coal rock samples can be heated more quickly in the microwave field, also quickly evaporating and generating the steam explosion. The release of a large amount of high temperature and high pressure steam significantly improved the pore opening, dredging, and reaming. This also shows that the addition of NaCl significantly improved coal permeability (Figure 5).

4.2. Mechanism of the Effect of Ion Concentration on Temperature Distribution in the Coal Rocks.
Through the above analysis, it is found that after injecting NaCl solution, the imaginary part of the dielectric constant of water increases greatly and then increases the overall temperature of coal rock samples. Therefore, the surface temperature test and internal temperature numerical simulation of coal rock samples with different NaCl concentrations after microwave irradiation were carried out, and the specific promotion effect of NaCl solution on coal rock sample temperature and the mechanism of increasing permeability were explored.

4.2.1. Influence of Ion Concentration on Surface Temperature Distribution in Coal Rocks.
The pictures taken by the UTi-165A thermal imager for temperature measurement are shown in Table 8. The average temperature of the original coal before microwave irradiation is 22.6°C. Figure 8 summarizes the temperature characterization of coal rock samples under 15 different conditions.

Figure 8 shows that the relationship between NaCl concentrations and temperature of the coal rocks after microwave irradiation properly fitted a linear equation. The trend basically showed a linear increase. Under the same microwave power, the average temperatures of coal rock

TABLE 8: Mapping of coal surface temperature distribution after microwave irradiation.

NaCl concentration, P_k (g/L) Moisture content Q_j (%)	$Q_1 = 2$	$Q_2 = 4$	$Q_3 = 6$
$P_1 = 0$			
$P_2 = 16$			
$P_3 = 32$			
$P_4 = 48$			
$P_5 = 64$			

FIGURE 8: Surface temperature of water-bearing coal rocks after microwave treatment.

samples with of NaCl solution concentrations of 16 g/L, 32 g/L, 48 g/L, and 64 g/L were 62.5°C, 68.6°C, 73.9°C, and 82.9°C, respectively. Compared with the average temperature of 53.4°C of coal rock samples without NaCl aqueous solution, the temperature increased by 17.04%, 28.46%, 38.4%, and 55.2%, respectively.

Temperature was the most important factor that directly determined the internal pressure in coal rocks. The rapid increase in temperature presents the following benefits: (1) Extremely high temperature is conducive to large temperature gradients, especially in mixtures with complex internal components such as coal rock samples. Components of coal rocks include the coal matrix, different minerals, water, and various volatile compounds, among others. The dielectric properties of different materials also vary, which easily cause the thermal stress distribution and unevenness of the coal rock samples in the microwave field. The higher the extreme temperature, the stronger the unevenness, and the more likely to produce the tearing effect on the primary fissures inside the coal body, as well as the cracking effect of the pores. (2) Temperature increase indicates that the rate of heating of the coal body is accelerated. The rapid increase in temperature favors the rapid formation of water vapor. This means that in the same period of time, coal samples containing NaCl solutions accumulate more water vapor as compared to those where no aqueous solution are present. According to the ideal state gas equation, when other conditions are the same, the higher the amount of gas, the higher the pressure generated inside the pores. This process favors the expansion of pores and cracks. Under pressure, pores more likely transform into larger pores, and some of them maybe also broken and connected with small cracks. Independent cracks may connect with each other or with the external environment. This process greatly improves the permeability of coal rocks.

Overall temperature of coal rocks can be determined through physical analysis. However, the specific temperature inside the coal rock cannot be measured. Therefore, in the present investigation, numerical simulation was used to study the internal changes of coal after microwave irradiation and to explore the influence of ion concentration on the internal temperature distribution.

4.2.2. The Influence of Ion Concentration on Internal Temperature Distribution in Coal Rocks. The COMSOL Multiphysics numerical analysis software was adopted for microwave heating simulation. A three-dimensional model was established according to the actual situation. The coal rock was 25 mm in diameter and 25 mm in height. In order to simulate the pores of coal, since the average porosity of 15 coal samples used in this experiment was 30%, 100 spheres were randomly arranged in the coal model material, and the volume of spheres accounted for 30% of the model volume. After calculation, the diameter of each sphere was 2.064 mm. Seven, 14, and 20 microspheres were randomly selected as water-bearing pores to simulate the coal rock with water content of 2%, 4%, and 6%, respectively. The model is shown in Figure 9. The following ideal conditions were set up during the entire simulation process: (1) The composition of coal rock did not change during the entire microwave irradiation process. (2) The thermodynamic and electrical parameters of each substance remained unchanged. (3) Both the inner wall of the microwave oven and the waveguide were considered perfect magnetic conductors. (4) Only the influence of the proportion of aqueous solution and ion concentration on coal temperature was considered; on the other hand, we did not consider the influence of radiative and convective heat transfers on coal temperature.

The maximum body temperature of coal rock samples was extracted in the microwave heating simulation, and the results are shown in Figure 10. As observed, the maximum body temperature of coal rock samples after microwave irradiation also increases with the increase of ion concentration of the NaCl solution, and the internal temperature is greater than the surface temperature. However, different from the above, the maximum surface temperature of coal rock samples measured in the physical experiment basically increases linearly with the increase of ion concentration of the NaCl solution, while the increase rate of the maximum body temperature of coal samples in the simulation becomes slower and slower with the increase of ion concentration of the NaCl solution. This is closely related to the penetration depth of the microwave to the coal rock samples.

When the microwave enters the medium, the medium absorbs the microwave energy and converts it into heat energy. The field strength of microwave decreases continuously with the increase of the depth of the incident medium. The depth reflects the penetration ability of the microwave in the medium. When the microwave enters the coal sample, the surface energy density of the coal rock sample becomes the largest, and its energy decreases exponentially with the penetration of the microwave into the coal rock sample. In order to characterize the attenuation ability of the material to the microwave power, the microwave penetration depth (d_p) is employed, which is defined as the distance when the

(a)

(b)

(c)
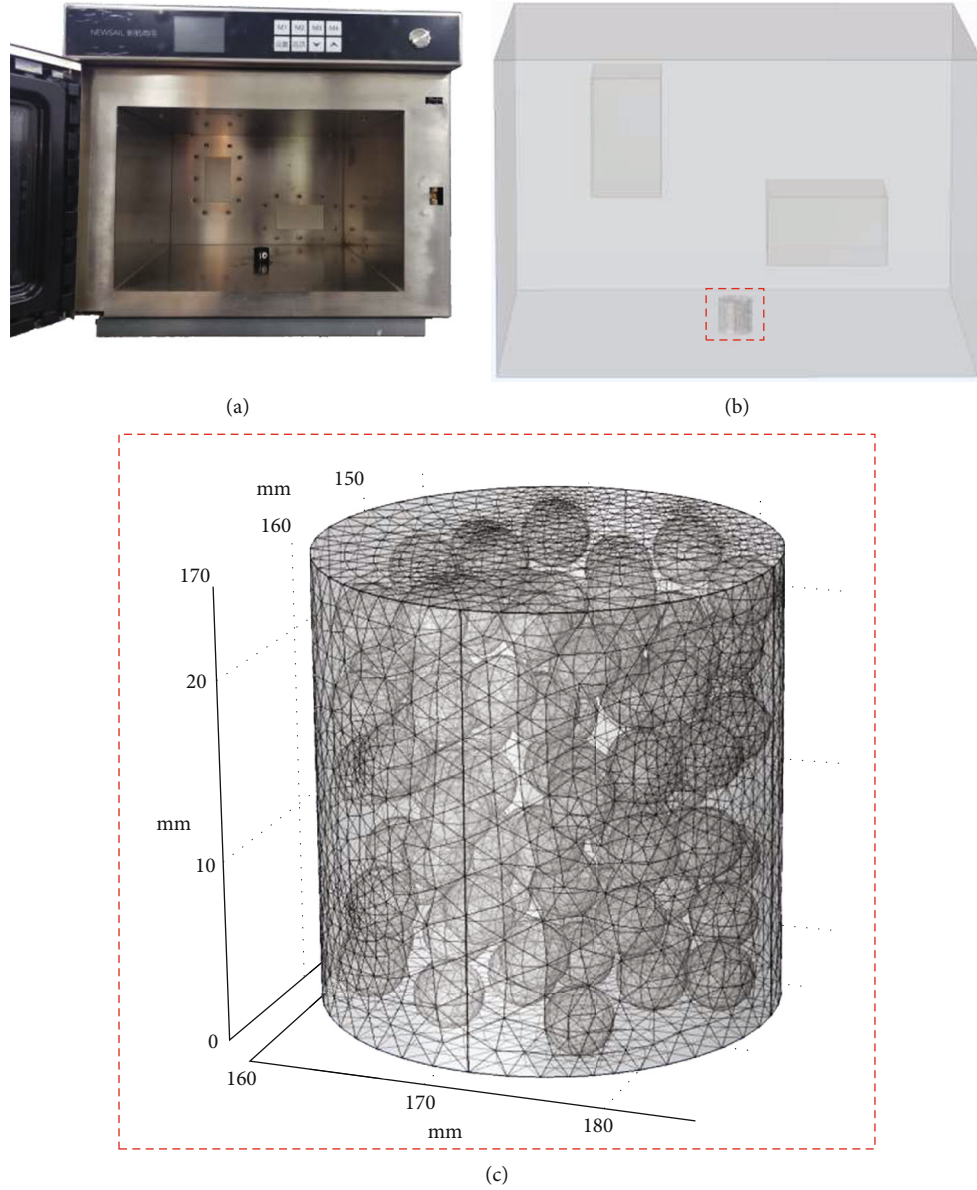
FIGURE 9: Surface temperature of water-bearing coal rock after microwave treatment: (a) microwave oven; (b) three-dimensional numerical model; (c) random sphere numerical model.

microwave power is reduced from the surface value of the medium to the surface value e^{-1} (about 36.79%) [35]:

$$d_p = \frac{c_0}{2\sqrt{2}\pi f \sqrt{\varepsilon'\left[\sqrt{1+\left(\varepsilon''/\varepsilon'\right)^2}-1\right]}}, \quad (8)$$

where C_0 is the speed of light, in m/s; f is the microwave frequency; ε' represents the real part of the dielectric constant; and ε'' is the imaginary part of the dielectric constant. In this study, for the coal rock with the same moisture content, the real part of the dielectric constant of coal samples is basically unchanged. According to equation (5), the addition of the NaCl solution only greatly improves the imaginary part of the dielectric constant. According to equation (8), with the increase of the imaginary part of the dielectric constant, the overall microwave penetration depth of coal samples will be smaller and smaller. Therefore, under microwave irradiation, the attenuation loss of medium on the surface of coal samples is the smallest, and the energy density of microwave is the largest. The basic temperature curve of coal rock sample surface presents a linear growth trend. With the increase of ion concentration of the NaCl solution, the overall microwave penetration depth of coal samples decreases, resulting in a gradual decline of the rise rate of the maximum body temperature of coal rock samples.

In order to clarify the absorption of microwave energy in different positions of coal rock samples, the dielectric loss power density P_d (in W/m^3) of different spatial positions was extracted in the microwave heating simulation. This parameter is used to express the microwave energy absorbed
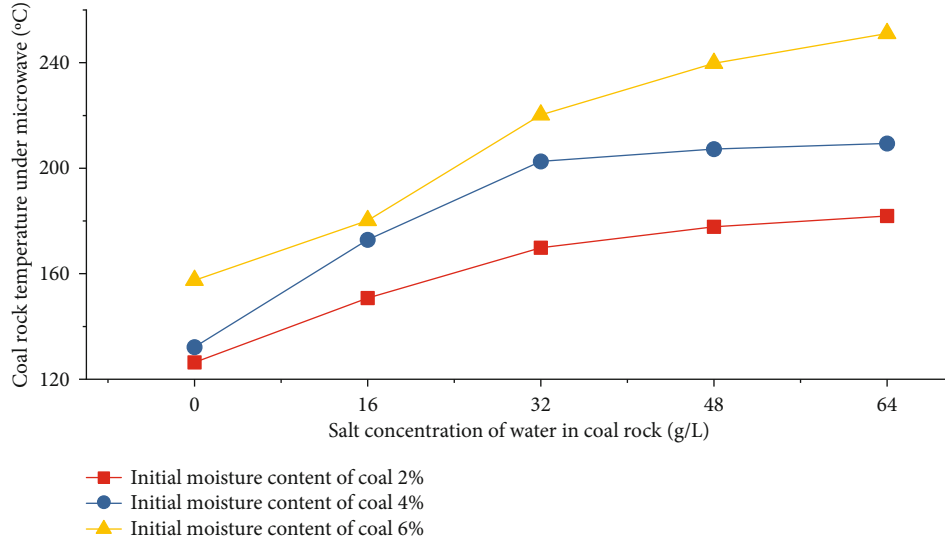
Figure 10: Simulation of maximum body temperature of coal rock samples.
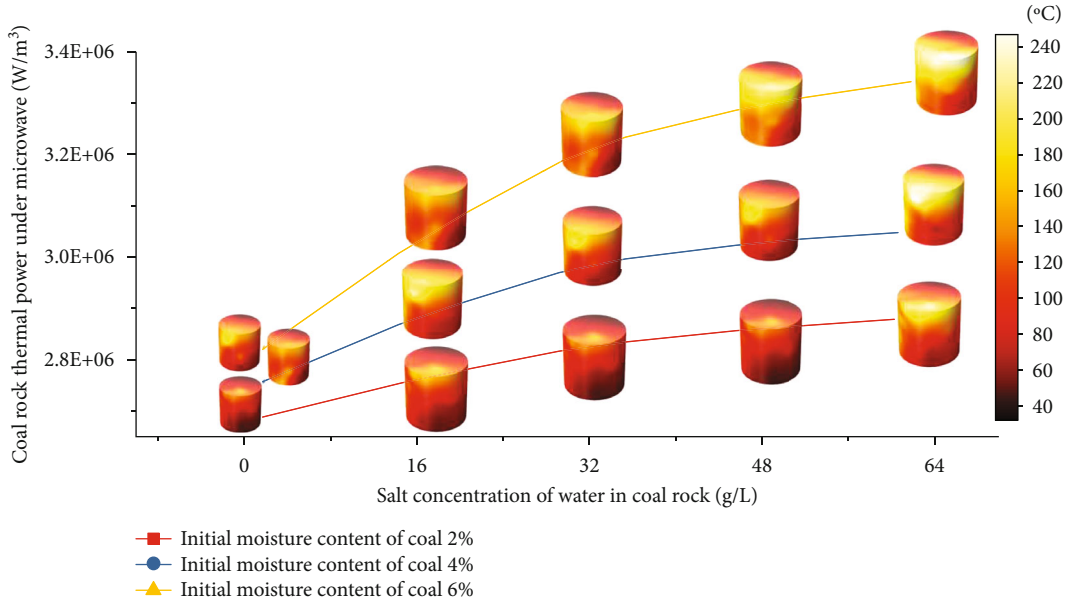
Figure 11: Numerical simulation results.

per unit volume in unit time at any spatial position (position z) inside the dielectric material.

As shown in Figure 11, it can be seen that in the longitudinal direction the water content increases continuously at the same NaCl concentration; in the transverse direction, the NaCl concentration increases at the same horizontal water content. Whether horizontal or vertical, the temperature of coal samples is getting higher and higher, and the area of high temperature is getting larger and larger (see the light white part of the simulated coal pillar). The average power density of dielectric loss in coal samples under different conditions is arranged as shown in Figure 11. As observed, the average power density of dielectric loss in coal samples increases with the increase of NaCl concentration,

which is consistent with the maximum temperature inside the coal samples.

The dielectric loss power density P_d can be expressed as [36]

$$P_d(z) = \frac{\omega}{c} \frac{4\varepsilon''S_0 e^{-2\alpha z}}{\sqrt{\varepsilon'^2 + \varepsilon''^2} + \sqrt{2\left(\sqrt{\varepsilon'^2 + \varepsilon''^2} + \varepsilon'\right) + 1}}, \quad (9)$$

where S_0 corresponds to the average energy flow density of the microwave generator and is determined by the microwave power. According to the equation, the average power density P_d of dielectric loss of coal rock samples under the

same irradiation condition is mainly determined by the imaginary part of the relative dielectric constant of the medium. In this study, under the condition of constant water content and with the increase of NaCl concentration, the real part of the dielectric constant is basically unchanged, while the imaginary part increases greatly, which leads to the increase of the overall dielectric loss power density of the coal sample; that is, the coal samples absorb more and more microwave energy in unit time, which effectively improves the overall temperature of the coal samples.

As suggested by combination of the penetration depth d_p and the average power density P_d of the dielectric loss, firstly, the addition of the NaCl solution can improve the dielectric response of coal rock samples in the microwave field, so that the coal rock can absorb more energy and produce higher temperature in unit time, which helps to generate greater steam pressure and promote the expansion of original pores and fissures, and may generate new fissures. Meanwhile, with the increase of the NaCl concentration, the penetration depth decreases, this may lead to the thermal stress distribution inside and outside the coal rock becoming more uneven, the original mechanical equilibrium field inside the coal rock may be broken, new fissures are produced, and the original pores/fissures will also develop and connect under the effect of internal steam pressure, which may improve the conditions of pores and fissures and enhance the overall permeability of coal rock samples.

5. Conclusions

(1) As the mass proportion of the ionic solution increased, the overall dielectric properties of the coal rock samples increased. In addition, the average decrease rate of the moisture content after microwave irradiation also increased. These results showed that more water was involved in the steam explosion

(2) The increase of NaCl aqueous solution concentration reduces the penetration ability of the microwave in the coal rock sample, so more energy will be concentrated on the surface of sample, which is well proven by the thermal imaging temperature test. The test result indicates that the average surface temperature of coal samples at four different concentrations of NaCl increased by 17.04%, 28.46%, 38.4%, and 55.2% as compared with those samples without NaCl. At the same time, the NaCl aqueous solution enhances the overall microwave absorption capacity of coal samples, which is well proven by the maximum temperature and dielectric loss thermal power density of samples in numerical analysis. As observed, the average power density of dielectric loss in coal samples increases with the increase of NaCl concentration; this change trend is consistent with the maximum temperature inside the coal samples

(3) Both physical and numerical experiments show that the NaCl solution can effectively enhance the temperature of coal rock samples with microwave irradi-

ation. Higher temperature will make it more possible to increase the steam pressure in the pores, which may be more conducive to the connection and expansion of the pores. It should be pointed out that the increase of steam pressure is not the only reason for the microcracking process, but it is a favorable factor

(4) As the concentration of the ionic solution increased, the average growth rate of the overall permeability was 196.37%, 216.39%, 343.51%, 465.80%, and 466.18%. At a same moisture content, increasing NaCl concentration enhanced permeability 1.91 times

Data Availability

The data that support the findings of this study are available on request from the corresponding author.

Conflicts of Interest

The authors declare that there are no conflicts of interest regarding the publication of this paper.

Acknowledgments

References

[1] BP, *Statistical Review of World Energy*, Group BP. International Energy Agency, 2020.

[2] International Energy Agency, *World energy outlook*, 2021.

[3] National Bureau of Statistics of the People's Republic of China, "Statistical bulletin of national economic and social development in 2020 of the People's Republic of China," 2021.

[4] State Energy Administration of the People's Republic of China, "13th five year plan for energy development of the People's Republic of China," 2016.

[5] B. Nie, J. Gong, L. Yang, C. Peng, Y. Fan, and L. Zhang, "Experimental analysis on gas and solid residues of pre-and post-explosion coal dust," *Energy & Fuels*, vol. 35, no. 2, 2020.

[6] V. N. Odintsev and I. E. Shipovskii, "Simulating explosive effect on gas-dynamic state of outburst-hazardous coal band," *Journal of Mining Science*, vol. 55, no. 4, pp. 556–566, 2019.

[7] H. Li, B. Lin, Y. Hong et al., "Effects of in-situ stress on the stability of a roadway excavated through a coal seam," *International Journal of Mining Science and Technology*, vol. 27, no. 6, pp. 917–927, 2017.

[8] H. Li, B. Lin, W. Yang, Y. Gao, and T. Liu, "Effects of an underlying drainage gallery on coal bed methane capture effectiveness and the mechanical behavior of a gate road," *Journal of Natural Gas Science and Engineering*, vol. 27, pp. 616–631, 2015.

[9] J. Zhang, L. Si, J. Chen, M. Kizil, C. Wang, and Z. Chen, "Stimulation techniques of coalbed methane reservoirs," *Geofluids*, vol. 2020, Article ID 5152646, 23 pages, 2020.

[10] Y. Qin, T. A. Moore, J. Shen, Z. Yang, Y. Shen, and G. Wang, "Resources and geology of coalbed methane in China: a

review," *International Geology Review*, vol. 60, no. 5-6, pp. 777–812, 2018.

[11] C. Guo, H. Shao, S. Jiang, Y. Wang, K. Wang, and Z. Wu, "Effect of low-concentration coal dust on gas explosion propagation law," *Powder Technology*, vol. 367, pp. 243–252, 2020.

[12] X. Li, X. Fu, J. Tian et al., "Heterogeneities of seepage pore and fracture of high volatile bituminous coal core: implications on water invasion degree," *Journal of Petroleum Science and Engineering*, vol. 183, 2019.

[13] X. Li, X. Fu, P. G. Ranjith, and Y. Fang, "Retained water content after nitrogen driving water on flooding saturated high volatile bituminous coal using low-field nuclear magnetic resonance," *Journal of Natural Gas Science and Engineering*, vol. 57, pp. 189–202, 2018.

[14] S. Li, Q. Tang, J. Lei, X. Xu, J. Jiang, and Y. Wang, "An overview of non-conventional water resource utilization technologies for biological sand control in Xinjiang, Northwest China," *Environmental Earth Sciences*, vol. 73, no. 2, pp. 873–885, 2015.

[15] J. Feng, L. Zhao, Y. Zhang, L. Sun, X. Yu, and Y. Yu, "Can climate change influence agricultural GTFP in arid and semi-arid regions of Northwest China?," *Journal of Arid Land*, vol. 12, no. 5, pp. 837–853, 2020.

[16] Q. Wang, P. M. Zhai, and D. Qi, "New perspectives on 'warming-wetting' trend in Xinjiang, China," *Advances in Climate Change Research*, vol. 11, no. 3, pp. 252–260, 2020.

[17] G. Hu, N. Yang, G. Xu, and J. Xu, "Experimental investigation on variation of physical properties of coal particles subjected to microwave irradiation," *Journal of Applied Geophysics*, vol. 150, pp. 118–125, 2018.

[18] Y. Hong, B. Lin, C. Zhu, and H. Li, "Effect of microwave irradiation on petrophysical characterization of coals," *Applied Thermal Engineering*, vol. 102, pp. 1109–1125, 2016.

[19] Y. Hong, B. Lin, W. Nie, C. J. Zhu, Z. Wang, and H. Li, "Microwave irradiation on pore morphology of coal powder," *Fuel*, vol. 227, pp. 434–447, 2018.

[20] H. Li, C. Zheng, J. Lu et al., "Drying kinetics of coal under microwave irradiation based on a coupled electromagnetic, heat transfer and multiphase porous media model," *Fuel*, vol. 256, p. 115966, 2019.

[21] H. Li, B. Lin, W. Yang et al., "Experimental study on the petrophysical variation of different rank coals with microwave treatment," *International Journal of Coal Geology*, vol. 154-155, pp. 82–91, 2016.

[22] J. Yao, M. Tao, R. Zhao, S. S. Hashemi, and Y. Wang, "Effect of microwave treatment on thermal properties and structural degradation of red sandstone in rock excavation," *Minerals Engineering*, vol. 162, p. 106730, 2021.

[23] S. Marland, A. Merchant, and N. Rowson, "Dielectric properties of coal," *Fuel*, vol. 80, no. 13, pp. 1839–1849, 2001.

[24] J. M. Forniés-Marquina, J. C. Martín, J. P. Martínez, J. L. Miranda, and C. Romero, "Dielectric characterization of coals," *Canadian Journal of Physics*, vol. 81, no. 3, pp. 599–610, 2003.

[25] Q. Qi, W. Guan, X. Li, Y. Ge, S. Nan, and H. Liu, "Mechanism of increasing the permeability of water-bearing coal rock by microwave steam explosion," *Geofluids*, vol. 2021, Article ID 6661867, 13 pages, 2021.

[26] R. J. Meredith, *Engineers' Handbook of Industrial Microwave Heating*, Iet, 1998.

[27] C. Chan and Y. Chen, "Demulsification of W/O emulsions by microwave radiation," *Separation Science and Technology*, vol. 37, no. 15, pp. 3407–3420, 2002.

[28] Z. Ji, J. Wang, Z. Yin, D. Hou, and Z. Luan, "Effect of microwave irradiation on typical inorganic salts crystallization in membrane distillation process," *Journal of Membrane Science*, vol. 455, pp. 24–30, 2014.

[29] C. A. Pickles, F. Gao, and S. Kelebek, "Microwave drying of a low-rank sub-bituminous coal," *Minerals Engineering*, vol. 62, pp. 31–42, 2014.

[30] N. Wang, J. Yu, A. Tahmasebi et al., "Experimental study on microwave pyrolysis of an Indonesian low-rank coal," *Energy & Fuels*, vol. 28, no. 1, pp. 254–263, 2014.

[31] F. Zhou, *Upgrading lignite through drying and pyrolysis with microwave irradiation*, Zhejiang University, 2016.

[32] H. Zhu, T. Gulati, A. K. Datta, and K. Huang, "Microwave drying of spheres: coupled electromagnetics-multiphase transport modeling with experimentation. Part I: model development and experimental methodology," *Food and Bioproducts Processing*, vol. 96, pp. 314–325, 2015.

[33] R. Cherbański and L. Rudniak, "Modelling of microwave heating of water in a monomode applicator - Influence of operating conditions," *International Journal of Thermal Sciences*, vol. 74, pp. 214–229, 2013.

[34] A. Abdelgwad and T. Said, "Measured dielectric permittivity of contaminated sandy soil at microwave frequency," *Journal of Microwaves, Optoelectronics and Electromagnetic Applications*, vol. 15, no. 2, pp. 115–122, 2016.

[35] Z. Peng, X. Lin, Z. Li et al., "Dielectric characterization of Indonesian low-rank coal for microwave processing," *Fuel Processing Technology*, vol. 156, pp. 171–177, 2017.

[36] Y. Zhang, K. Tuo, Y. Yan, W. P. MA, M. Y. FANG, and S. Q. LIU, "Study on dielectric response characteristics of low-rank coal," *Coal Engineering*, vol. 50, no. 4, pp. 135–140, 2018.

WILEY | Hindawi

Research Article

The Pressure Buildup Well Test Analysis considering Stress Sensitivity Effect for Deepwater Composite Gas Reservoir with High Temperature and Pressure

Yihua Gao [iD],[1] Ruizhong Jiang,[2] Xiangdong Xu,[3] Zhaobo Sun,[3] Zhiwang Yuan [iD],[1] Kang Ma,[1] Bin Jiang,[1] Botao Kang,[1] Guoning Chen,[1] and Chenxi Li[1]

[1]*CNOOC Research Institute Co., Ltd., Beijing 100028, China*
[2]*School of Petroleum Engineering, China University of Petroleum (East China), Qingdao 266580, China*
[3]*CNOOC International Co., Ltd., Beijing 100027, China*

Correspondence should be addressed to Yihua Gao; gyhupc@163.com

Some deepwater gas reservoirs with high temperature and pressure have obvious stress sensitivity effect resulting in difficulty in well test interpretations. The influence of stress sensitivity effect on the pressure drawdown well test is discussed in many papers. However, the influence on the pressure buildup well test is barely discussed. For practices in oilfields, the quality of pressure data from the drawdown stage of well test is poor due to the influence of production fluctuation. Thus, the pressure data from the buildup stage is used for well test interpretations in most cases. In order to analyze the influence of stress sensitivity effect on the pressure buildup well test, this paper establishes a composite gas reservoir pressure buildup well test model considering the stress sensitivity effect and the hysteresis effect. Numerical solutions to both pressure drawdown and buildup well test models are obtained by the numerical differentiation method. The numerical solutions are verified by comparing with analytical solutions and the homogeneous gas reservoir well test solution. Then, the differences between pressure drawdown and buildup well test curves considering the stress sensitivity effect are compared. The parameter sensitivity analysis is conducted. Compared with the conventional well test curve, the pressure derivative curve of pressure drawdown well test considering the stress sensitivity effect deviates upward from the 0.5 horizontal line at the inner zone radial flow stage, while it deviates upward from the $M/2$ (mobility ratio/2) horizontal line at the outer zone radial flow stage. However, for the pressure buildup well test curve considering the stress sensitivity effect, the pressure derivative curve gradually descends to the 0.5 horizontal line at the inner zone radial flow stage, while it descends to the $M/2$ (mobility ratio/2) horizontal line at the outer zone radial flow stage. The pressure derivative curve of pressure buildup well test considering the hysteresis effect is higher than the curve without considering the hysteresis effect, because the permeability cannot be recovered to its original value in the buildup stage after considering the hysteresis effect. Meanwhile, skin factor and mobility ratio have different effects on pressure drawdown and buildup well test curves. Based on the model, a well test interpretation case from a deepwater gas reservoir with high temperature and pressure is studied. The result indicates that the accuracy of the interpretation is improved after considering the stress sensitivity effect, and the skin factor will be exaggerated without considering the stress sensitivity effect.

1. Introduction

Well test is an important way to obtain physical parameters and evaluate the development performance of gas reservoirs [1–9]. It can help to understand the seepage mechanism and the development law of gas reservoirs with high temper-

ature and pressure. Compared with the conventional gas reservoir, there is more obvious rock deformation during the development process of the gas reservoir with high temperature and pressure resulting in stronger stress sensitivity effect [10–15]. Thus, it is necessary to consider the influence of stress sensitivity effect on well test curves. Many experiments

and production practices show that there is irreversible deformation in some reservoirs during the development process [16–18]. Reservoir permeability decreases with the decrease of formation pressure. However, the permeability cannot be completely recovered to its original value after the formation pressure increases to the initial value if there is irreversible deformation in reservoirs. This phenomenon is called the hysteresis effect [18].

At present, many researchers have studied the influence of stress sensitivity effect on well test curves. However, the influence on the pressure drawdown well test is mainly discussed in these studies [19–30]. For practices in oilfields, the quality of pressure data from the drawdown stage of well test is poor due to the influence of production fluctuation. Thus, the pressure data from the buildup stage is used in most cases of well test interpretations for its good data quality [31–34]. For conventional well test interpretations, the superposition principle is used to obtain solutions to pressure buildup well test models from that of pressure drawdown well tests. However, for well test models considering the stress sensitivity effect, the seepage differential equations are nonlinear equations, and the superposition principle cannot be directly used for nonlinear equations to obtain the solutions to pressure buildup well test models [31]. Therefore, it is necessary to analyze the influence of stress sensitivity effect on the pressure buildup well test to guide well test interpretations. However, the studies about pressure buildup well test models considering the stress sensitivity effect are not sufficient. Zhang et al. established pressure buildup well test models considering the stress sensitivity effect for vertical fractured well and vertical well in a homogeneous reservoir [18, 31]. One of the researches mainly discussed the influence of stress sensitivity effect and hysteresis effect on the variation of fracture conductivity for vertical fractured well in a homogeneous reservoir at the buildup stage [18]. Another research only discussed the influence of stress sensitivity effect on vertical well in a homogeneous reservoir at the buildup stage [31]. There are few researches about the pressure buildup well test of composite gas reservoir considering both the stress sensitivity effect and the hysteresis effect.

Thus, the paper establishes theoretical pressure drawdown and buildup well test models for the composite gas reservoir with high temperature and pressure considering both the stress sensitivity effect and the hysteresis effect. The solutions to these models are obtained by the numerical differentiation method. The numerical solutions to pressure drawdown and buildup well test models are verified by comparing with analytical solutions [23] and the homogeneous gas reservoir well test solution [31]. The differences between pressure buildup and drawdown well test curves considering the stress sensitivity effect are analyzed. The parameter sensitivity analysis is conducted. Then, a field case from a gas reservoir with high temperature and pressure is presented indicating that the accuracy of interpretation is improved after considering the stress sensitivity effect.

2. Model Description and Solution

2.1. Physical Model and Basic Assumptions.
A physical model of a vertical well with fixed gas production rate in a composite gas reservoir is established shown in Figure 1. The basic assumptions of the model are as follows:

(1) An isotropic gas reservoir is bounded by impermeable layers at the bottom and top. The gas reservoir has two zones with different permeability and porosity. The radius of inner zone boundary is r_1, and the outer zone boundary is infinite

(2) The vertical gas well is on production at fixed rate with the initial pressure p_i followed by a shut-in stage

(3) The gas in the reservoir is highly compressible fluid with the compressibility C_g, compressibility factor Z, and viscosity μ_g

(4) Considering the stress sensitivity effect and the hysteresis effect, the gas reservoir permeability changes with the formation pressure resulting in irreversible deformation to the reservoir

(5) The gravity effect is negligible. The temperature in the reservoir is constant at production and shut-in stages

(6) The effect of wellbore storage is considered by a constant wellbore storage coefficient. The effective wellbore radius is used to describe the skin damage

2.2. Mathematical Model

2.2.1. Characterization of Stress Sensitivity Effect and Hysteresis Effect.
The stress sensitivity coefficient γ is used to describe the change of reservoir permeability with the pressure. Some experimental studies indicate that the relationship between the reservoir permeability and the pressure change conforms to the exponential form [23, 35, 36]. The changes of reservoir permeability with the pressure at pressure drawdown and buildup stages are shown in Figure 2.

At the pressure drawdown stage, the stress sensitivity effect can be described by Equation (1):

$$\gamma_d = \frac{1}{k_{id}}\frac{dk}{dp} \Rightarrow k_d = k_{id}\exp\left[-\gamma_d(p_i - p_d)\right]. \tag{1}$$

At the pressure buildup stage, the stress sensitivity effect and the hysteresis effect can be described by Equation (2):

$$\begin{aligned}\gamma_b = \frac{1}{k_{ib}}\frac{dk}{dp} &\Rightarrow k_b = k_{ib}\exp\left[-\gamma_b(p_i - p_b)\right]\\ &= k_{id}\exp\left[-(\gamma_d - \gamma_b)(p_i - p_d)\right]\exp\left[-\gamma_b(p_i - p_b)\right],\end{aligned} \tag{2}$$

where γ_d and γ_b are the stress sensitivity coefficients at pressure drawdown and buildup stage, 1/Pa; there will be the hysteresis effect when γ_b is less than γ_d; k_{id} is the initial permeability of gas reservoir, m²; k is the permeability of gas reservoir, m²; p is the pressure of gas reservoir, Pa; p_i is the initial pressure of gas reservoir, Pa; p_d and p_b are the gas reservoir pressure at pressure drawdown and buildup stages,
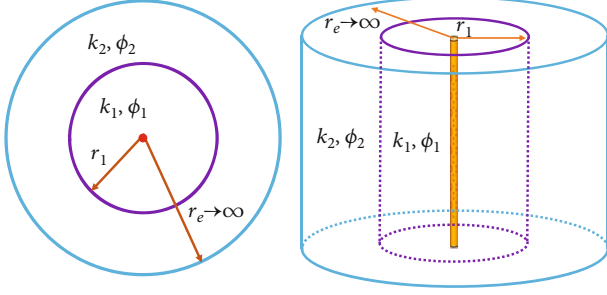
Figure 1: Physical model of vertical well producing in composite gas reservoir.
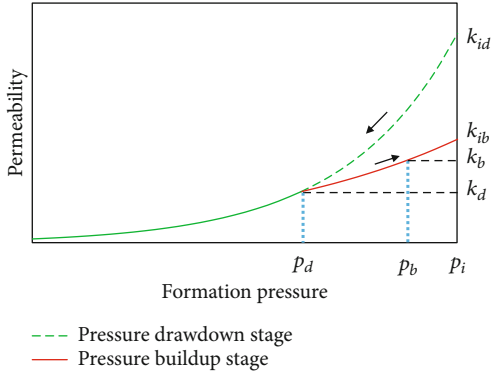
Figure 2: The change of reservoir permeability with pressure.

Pa; k_d and k_b are the gas reservoir permeability at pressure drawdown and buildup stages, m^2; k_{ib} is the maximum permeability value that can be restored after the gas reservoir pressure increases to the initial pressure, m^2.

The gas pseudo-pressure is generally used in gas reservoir well tests, and the definition of the gas pseudo-pressure is as Equation (3):

$$\psi = 2 \int_{p_{sc}}^{p} \frac{p}{\mu Z} dp, \tag{3}$$

where ψ is the gas pseudo-pressure, Pa/s; μ is the gas viscosity, Pa.s; Z is the gas compressibility factor, decimal; p_{sc} is the pressure at the standard condition, Pa.

Substituting Equation (3) into Equations (1) and (2), stress sensitivity equations in the pseudo-pressure form can be expressed as Equations (4) and (5):

$$\gamma_d = \frac{1}{k_{id}} \frac{dk}{dp} = \frac{1}{k_{id}} \frac{dk}{d\psi_d} \frac{d\psi_d}{dp} = \frac{1}{k_{id}} \frac{dk}{d\psi_d} \frac{p}{\mu Z}, \tag{4}$$

$$\gamma_b = \frac{1}{k_{ib}} \frac{dk}{dp} = \frac{1}{k_{ib}} \frac{dk}{d\psi_b} \frac{d\psi_b}{dp} = \frac{1}{k_{ib}} \frac{dk}{d\psi_b} \frac{p}{\mu Z}. \tag{5}$$

Then, stress sensitivity coefficients in the pseudo-pressure form can be obtained as Equations (6) and (7):

$$\gamma_d^* = \frac{\gamma_d}{(p/(\mu Z))} = \frac{1}{k_{id}} \frac{dk}{d\psi_d} \Rightarrow k_d = k_{id} \exp\left[-\gamma_d^*(\psi_i - \psi_d)\right], \tag{6}$$

$$\gamma_b^* = \frac{\gamma_b}{(p/(\mu Z))} = \frac{1}{k_{ib}} \frac{dk}{d\psi_b} \Rightarrow k_b = k_{ib} \exp\left[-\gamma_b^*(\psi_i - \psi_b)\right], \tag{7}$$

where γ_d^* and γ_b^* are stress sensitivity coefficients in the pseudo-pressure form at pressure drawdown and buildup stages, Pa/s; ψ_i is the initial pseudo-pressure, Pa/s; ψ_d and ψ_b are the pseudo-pressure at pressure drawdown and buildup stages, Pa/s.

2.2.2. Pressure Drawdown Well Test Model. The differential equation of natural gas seepage considering the stress sensitivity effect and the hysteresis effect is as Equation (8):

$$\frac{1}{r} \frac{\partial}{\partial r} \left[k(p) r \frac{p}{Z\mu} \frac{\partial p}{\partial r} \right] = \phi \frac{\partial}{\partial t} \left(\frac{p}{Z} \right), \tag{8}$$

where r is the radius, m; $k(p)$ is the permeability considering the stress sensitivity effect and the hysteresis effect, m^2; t is time, s; ϕ is porosity, decimal.

For the pressure drawdown well test, the comprehensive seepage differential equation considering the stress sensitivity effect in the inner zone of composite gas reservoir is as Equation (9):

$$\frac{1}{r} \frac{\partial}{\partial r} \left[k_{i1} e^{-\gamma_d(p_i - p_1)} r \frac{p_1}{Z\mu_1} \left(\frac{\partial p_1}{\partial r} \right) \right] = \phi_1 \frac{\partial}{\partial t} \left(\frac{p_1}{Z} \right), \tag{9}$$

where k_{i1} is the initial inner zone permeability of composite gas reservoir, m^2; p_1 is the inner zone pressure of composite gas reservoir, Pa; μ_1 is the inner zone gas viscosity of composite gas reservoir, Pa.s; ϕ_1 is the inner zone porosity of composite gas reservoir, decimal.

The comprehensive seepage differential equation considering the stress sensitivity effect in the outer zone of composite gas reservoir is as Equation (10):

$$\frac{1}{r} \frac{\partial}{\partial r} \left[k_{i2} e^{-\gamma_d(p_i - p_2)} r \frac{p_2}{Z\mu_2} \left(\frac{\partial p_2}{\partial r} \right) \right] = \phi_2 \frac{\partial}{\partial t} \left(\frac{p_2}{Z} \right), \tag{10}$$

where k_{i2} is the initial outer zone permeability of composite gas reservoir, m^2; p_2 is the outer zone pressure of composite gas reservoir, Pa; μ_2 is the outer zone gas viscosity of composite gas reservoir, Pa.s; ϕ_2 is the outer zone porosity of composite gas reservoir, decimal.

After substituting Equation (3) into Equations (9) and (10), gas comprehensive seepage differential equations in the pseudo-pressure form can be expressed as Equations (11) and (12):

$$\frac{1}{r} \frac{\partial \psi_1}{\partial r} + \frac{\partial^2 \psi_1}{\partial r^2} + \gamma_d^* \left(\frac{\partial \psi_1}{\partial r} \right)^2 = \frac{\phi_1 \mu_1 C_g}{k_{i1}} e^{\gamma_d^*(\psi_i - \psi_1)} \frac{\partial \psi_1}{\partial t}, \tag{11}$$

$$\frac{1}{r} \frac{\partial \psi_2}{\partial r} + \frac{\partial^2 \psi_2}{\partial r^2} + \gamma_d^* \left(\frac{\partial \psi_2}{\partial r} \right)^2 = \frac{\phi_2 \mu_2 C_g}{k_{i2}} e^{\gamma_d^*(\psi_i - \psi_2)} \frac{\partial \psi_2}{\partial t}, \tag{12}$$

where ψ_1 is the inner zone pseudo-pressure, Pa/s; ψ_2 is the outer zone pseudo-pressure of composite gas reservoir, Pa/s; C_g is the gas compressibility coefficient, Pa^{-1}.

The initial condition can be expressed as Equation (13):

$$\psi_1(r, t = 0) = \psi_2(r, t = 0) = \psi_i. \tag{13}$$

The inner boundary considering the skin damage and the well storage effect for the pressure drawdown well test can be expressed as Equation (14):

$$\left[re^{-\gamma_d^*(\psi_i - \psi_1)} \frac{\partial \psi_1}{\partial r} \right]\Bigg|_{r=r_{we}} = \frac{q_{sc} p_{sc} T}{\pi k_{i1} h T_{sc} Z_{sc}} + \frac{C \mu_1}{2\pi k_{i1} h} \frac{\partial \psi_1}{\partial t}, \tag{14}$$

where $r_{we} = r_w \exp(-S)$ is the effective well radius, m; S is the skin factor, dimensionless; q_{sc} is the production of gas well at the standard condition, m^3/s; T_{sc} is the temperature at the standard condition, K; T is the formation temperature, K; C is the wellbore storage coefficient, m^3/Pa; h is the effective thickness of reservoir, m.

The pressure and flow rate are equal in the interface between the inner zone and the outer zone as described in Equations (15) and (16):

$$\frac{k_{i1} e^{-\gamma_d^*(\psi_i - \psi_1)}}{\mu_1} \frac{\partial \psi_1}{\partial r}\Bigg|_{r=r_1} = \frac{k_{i2} e^{-\gamma_d^*(\psi_i - \psi_2)}}{\mu_2} \frac{\partial \psi_2}{\partial r}\Bigg|_{r=r_1}, \tag{15}$$

$$\psi_1(r = r_1, t) = \psi_2(r = r_1, t), \tag{16}$$

where r_1 is the inner zone radius, m.

Considering the infinite outer boundary, Equation (17) is obtained:

$$\lim_{r \longrightarrow \infty} \psi_2(r, t) = \psi_i. \tag{17}$$

Thus, the mathematical model of composite gas reservoir pressure drawdown well test considering the stress sensitivity effect can be expressed as Equation (18):

$$\begin{cases} \dfrac{1}{r}\dfrac{\partial \psi_1}{\partial r} + \dfrac{\partial^2 \psi_1}{\partial r^2} + \gamma_d^* \left(\dfrac{\partial \psi_1}{\partial r} \right)^2 = \dfrac{\phi_1 \mu_1 C_g}{k_{i1}} e^{\gamma_d^*(\psi_i - \psi_1)} \dfrac{\partial \psi_1}{\partial t}, \\[3mm] \dfrac{1}{r}\dfrac{\partial \psi_2}{\partial r} + \dfrac{\partial^2 \psi_2}{\partial r^2} + \gamma_d^* \left(\dfrac{\partial \psi_2}{\partial r} \right)^2 = \dfrac{\phi_2 \mu_2 C_g}{k_{i2}} e^{\gamma_d^*(\psi_i - \psi_2)} \dfrac{\partial \psi_2}{\partial t}, \\[3mm] \left[re^{-\gamma_d^*(\psi_i - \psi_1)} \dfrac{\partial \psi_1}{\partial r} \right]\Big|_{r=r_{we}} = \dfrac{q_{sc} p_{sc} T}{\pi k_{i1} h T_{sc} Z_{sc}} + \dfrac{C \mu_1}{2\pi k_{i1} h} \dfrac{\partial \psi_1}{\partial t}, \\[3mm] \dfrac{k_{i1} e^{-\gamma_d^*(\psi_i - \psi_1)}}{\mu_1} \dfrac{\partial \psi_1}{\partial r}\Big|_{r=r_1} = \dfrac{k_{i2} e^{-\gamma_d^*(\psi_i - \psi_2)}}{\mu_2} \dfrac{\partial \psi_2}{\partial r}\Big|_{r=r_1}, \\[3mm] \psi_1(r, t = 0) = \psi_2(r, t = 0) = \psi_i, \\[2mm] \psi_1(r = r_1, t) = \psi_2(r = r_1, t), \\[2mm] \lim\limits_{r \longrightarrow \infty} \psi_2(r, t) = \psi_i. \end{cases} \tag{18}$$

In order to obtain the dimensionless mathematical model, some dimensionless variables are introduced as follows:

$$\begin{aligned} \psi_{1D} &= \frac{\pi k_{i1} h T_{sc}(\psi_i - \psi_1)}{q_{sc} p_{sc} T}, \\[2mm] \psi_{2D} &= \frac{\pi k_{i1} h T_{sc}(\psi_i - \psi_2)}{q_{sc} p_{sc} T}, \\[2mm] t_D &= \frac{k_{i1} t}{\phi_1 \mu_1 C_g r_w^2}, \\[2mm] \omega &= \frac{\phi_1 C_{g1}}{\phi_2 C_{g2}}, \\[2mm] r_D &= \frac{r}{r_{we}} = \frac{r}{r_w \exp(-S)}, \\[2mm] r_{1D} &= \frac{r_1}{r_{we}} = \frac{r_1}{r_w \exp(-S)}, \\[2mm] \gamma_{dD}^* &= \gamma_d \frac{\mu_i Z_i}{2 p_i} \frac{q_{sc} p_{sc} T}{\pi k_{i1} h T_{sc}}, \\[2mm] \gamma_{bD}^* &= \gamma_b \frac{\mu_i Z_i}{2 p_i} \frac{q_{sc} p_{sc} T}{\pi k_{i1} h T_{sc}}, \\[2mm] M &= \frac{k_{i1}/\mu_1}{k_{i2}/\mu_2}, \\[2mm] C_D &= \frac{C}{2\pi h \phi_1 C_g r_w^2}, \end{aligned} \tag{19}$$

where ψ_{1D} is the dimensionless pseudo-pressure in the inner zone; ψ_{2D} is the dimensionless pseudo-pressure in the outer zone; t_D is the dimensionless time; ω is the storage ratio between the inner zone and the outer zone; r_D is the dimensionless radius; r_{1D} is the dimensionless inner zone radius; γ^*_{dD} and γ^*_{bD} are dimensionless stress sensitivity coefficients at pressure drawdown and buildup stages, respectively; M is the mobility ratio between the inner zone and the outer zone; C_D is the dimensionless wellbore storage coefficient.

Substituting dimensionless variables into Equation (18), the dimensionless mathematical model of the pressure drawdown well test considering the stress sensitivity effect can be expressed as Equation (20):

$$\begin{cases} \dfrac{1}{r_D}\dfrac{\partial \psi_{1D}}{\partial r_D} + \dfrac{\partial^2 \psi_{1D}}{\partial r_D^2} - \gamma_{dD}^* \left(\dfrac{\partial \psi_{1D}}{\partial r_D} \right)^2 = \dfrac{e^{\gamma_{dD}^* \psi_{1D}}}{e^{2S}} \dfrac{\partial \psi_{1D}}{\partial t_D}, \\[3mm] \dfrac{1}{r_D}\dfrac{\partial \psi_{2D}}{\partial r_D} + \dfrac{\partial^2 \psi_{2D}}{\partial r_D^2} - \gamma_{dD}^* \left(\dfrac{\partial \psi_{2D}}{\partial r_D} \right)^2 = \dfrac{\omega}{M} \dfrac{e^{\gamma_{dD}^* \psi_{2D}}}{e^{2S}} \dfrac{\partial \psi_{2D}}{\partial t_D}, \\[3mm] \left(C_D \dfrac{\partial \psi_{1D}}{\partial t_D} - e^{-\gamma_{dD}^* \psi_{1D}} \dfrac{\partial \psi_{1D}}{\partial r_D} \right)\Big|_{r_D = 1} = 1, \\[3mm] \psi_{1D}(r_D, t_D = 0) = \psi_{2D}(r_D, t_D = 0) = 0, \\[3mm] e^{-\gamma_{dD}^* \psi_{1D}} \dfrac{\partial \psi_{1D}}{\partial r_D}\Big|_{r_D = r_{1D}} = e^{-\gamma_{dD}^* \psi_{2D}} \dfrac{1}{M} \dfrac{\partial \psi_{2D}}{\partial r_D}\Big|_{r_D = r_{1D}}, \\[3mm] \psi_{1D}(r_D = r_{1D}, t_D) = \psi_{2D}(r_D = r_{1D}, t_D), \\[2mm] \lim\limits_{r_D \longrightarrow \infty} \psi_{2D}(r_D, t_D) = 0. \end{cases} \tag{20}$$

2.2.3. Pressure Buildup Well Test Model. For the pressure buildup well test, the gas production q_{sc} in the inner boundary condition Equation (14) is zero. The stress sensitivity coefficient of the pressure buildup stage is introduced into

the mathematical model. Similarly, the dimensionless mathematical model of the pressure buildup well test considering the stress sensitivity effect and the hysteresis effect can be expressed as Equation (21):

$$
\begin{cases}
\dfrac{1}{r_D}\dfrac{\partial \psi_{1D}}{\partial r_D} + \dfrac{\partial^2 \psi_{1D}}{\partial r_D^2} - \gamma_{bD}^*\left(\dfrac{\partial \psi_{1D}}{\partial r_D}\right)^2 = R_1 \dfrac{e^{\gamma_{bD}^*\psi_{1D}}}{e^{2S}}\dfrac{\partial \psi_{1D}}{\partial t_D}, \\[2ex]
\dfrac{1}{r_D}\dfrac{\partial \psi_{2D}}{\partial r_D} + \dfrac{\partial^2 \psi_{2D}}{\partial r_D^2} - \gamma_{bD}^*\left(\dfrac{\partial \psi_{2D}}{\partial r_D}\right)^2 = R_2 \dfrac{\omega}{M}\dfrac{e^{\gamma_{bD}^*\psi_{2D}}}{e^{2S}}\dfrac{\partial \psi_{2D}}{\partial t_D}, \\[2ex]
\left(R_1 C_D \dfrac{\partial \psi_{1D}}{\partial t_D} - e^{-\gamma_{bD}^*\psi_{1D}}\dfrac{\partial \psi_{1D}}{\partial r_D}\right)\bigg|_{r_D=1} = 0, \\[2ex]
\psi_{1D}(r_D, t_D = 0) = \psi_{2D}(r_D, t_D = 0) = 0, \\[2ex]
e^{-\gamma_{bD}^*\psi_{1D}}\dfrac{\partial \psi_{1D}}{\partial r_D}\bigg|_{r_D=r_{1D}} = e^{-\gamma_{bD}^*\psi_{2D}}\dfrac{1}{M}\dfrac{\partial \psi_{2D}}{\partial r_D}\bigg|_{r_D=r_{1D}}, \\[2ex]
\psi_{1D}(r_D = r_{1D}, t_D) = \psi_{2D}(r_D = r_{1D}, t_D), \\[2ex]
\lim_{r_D \longrightarrow \infty} \psi_{2D}(r_D, t_D) = 0,
\end{cases}
\tag{21}
$$

where R_1 is the ratio of the initial permeability and the maximum permeability that can be restored after the gas reservoir pressure increases to the initial value in the inner zone, dimensionless; R_2 is the ratio of the initial permeability and the maximum permeability that can be restored after the gas reservoir pressure increases to the initial value in the outer zone, dimensionless.

2.3. Solutions to Mathematical Models

2.3.1. Solution to Pressure Drawdown Well Test Model by Perturbation Method. Kikani and Pedrosa proposed the perturbation method to solve the mathematical model for the pressure drawdown well test considering the stress sensitivity effect [23]. First, the dimensionless pseudo-pressure is transformed as Equation (22):

$$
\psi_{1D} = \frac{-\ln\left(1 - \gamma_{dD}^*\xi_{1D}\right)}{\gamma_{dD}^*}, \psi_{2D} = \frac{-\ln\left(1 - \gamma_{dD}^*\xi_{2D}\right)}{\gamma_{dD}^*}. \tag{22}
$$

Substituting Equation (22) into Equation (20), the dimensionless pressure drawdown well test mathematical model can be transformed as Equation (23):

$$
\begin{cases}
\dfrac{1}{r_D}\dfrac{\partial \xi_{1D}}{\partial r_D} + \dfrac{\partial^2 \xi_{1D}}{\partial r_D^2} = \dfrac{e^{-2S}}{(1-\gamma_{dD}^*\xi_{1D})}\dfrac{\partial \xi_{1D}}{\partial t_D}, \\[2ex]
\dfrac{1}{r_D}\dfrac{\partial \xi_{2D}}{\partial r_D} + \dfrac{\partial^2 \xi_{2D}}{\partial r_D^2} = \dfrac{\omega}{M}\dfrac{e^{-2S}}{(1-\gamma_{dD}^*\xi_{2D})}\dfrac{\partial \xi_{2D}}{\partial t_D}, \\[2ex]
\left(C_D \dfrac{\partial \xi_{1D}}{\partial t_D} - r_D \dfrac{\partial \xi_{1D}}{\partial r_D}\right)\bigg|_{r_D=1} = \dfrac{1}{(1-\gamma_{dD}^*\xi_{1D})}, \\[2ex]
\xi_{1D}(r_D = r_{1D}, t_D) = \xi_{2D}(r_D = r_{1D}, t_D), \\[2ex]
\dfrac{\partial \xi_{1D}}{\partial r_D}\bigg|_{r_D=r_{1D}} = \dfrac{1}{M}\dfrac{\partial \xi_{2D}}{\partial r_D}\bigg|_{r_D=r_{1D}}, \\[2ex]
\xi_{1D}(r_D, t_D = 0) = \xi_{2D}(r_D, t_D = 0) = 0, \\[2ex]
\lim_{r_D \longrightarrow \infty} \xi_{2D}(r_D, t_D) = 0.
\end{cases}
\tag{23}
$$

After applying zero-order approximation to ξ_{1D} and ξ_{2D} in Equation (23) [23], the new mathematical model can be expressed as Equation (24):

$$
\begin{cases}
\dfrac{1}{r_D}\dfrac{\partial \xi_{1D}}{\partial r_D} + \dfrac{\partial^2 \xi_{1D}}{\partial r_D^2} = e^{-2S}\dfrac{\partial \xi_{1D}}{\partial t_D}, \\[2ex]
\dfrac{1}{r_D}\dfrac{\partial \xi_{2D}}{\partial r_D} + \dfrac{\partial^2 \xi_{2D}}{\partial r_D^2} = \dfrac{\omega}{M}e^{-2S}\dfrac{\partial \xi_{2D}}{\partial t_D}, \\[2ex]
\left(C_D \dfrac{\partial \xi_{1D}}{\partial t_D} - r_D \dfrac{\partial \xi_{1D}}{\partial r_D}\right)\bigg|_{r_D=1} = 1, \\[2ex]
\xi_{1D}(r_D = r_{1D}, t_D) = \xi_{2D}(r_D = r_{1D}, t_D), \\[2ex]
\dfrac{\partial \xi_{1D}}{\partial r_D}\bigg|_{r_D=r_{1D}} = \dfrac{1}{M}\dfrac{\partial \xi_{2D}}{\partial r_D}\bigg|_{r_D=r_{1D}}, \\[2ex]
\xi_{1D}(r_D, t_D = 0) = \xi_{2D}(r_D, t_D = 0) = 0, \\[2ex]
\lim_{r_D \longrightarrow \infty} \xi_{2D}(r_D, t_D) = 0.
\end{cases}
\tag{24}
$$

Equation (24) is the same as the well test model of composite gas reservoir without considering the stress sensitivity effect [37]. Based on the Laplace transform and the property of Bessel function, the solution to Equation (24) in the Laplace space can be expressed as Equation (25):

$$
\bar{\xi}_{wD} = \frac{1}{u}\frac{R_{TP}}{uC_D R_{TP} + \beta M_{TP}}, \tag{25}
$$

where u is the variable in the Laplace space,

$$
R_{TP} = 1 + \frac{I_0(\beta)}{K_0(\beta)}\frac{\left[\beta K_0\left(r_{1D}\sqrt{N}\beta\right)K_1(r_{1D}\beta) - \left(\sqrt{N}/M\right)\beta K_0(r_{1D}\beta)K_1\left(r_{1D}\sqrt{N}\beta\right)\right]}{\left[\left(\sqrt{N}/M\right)\beta K_1\left(r_{1D}\sqrt{N}\beta\right)I_0(r_{1D}\beta) + \beta K_0\left(r_{1D}\sqrt{N}\beta\right)I_1(r_{1D}\beta)\right]},
$$

$$
M_{TP} = \frac{K_1(\beta)}{K_0(\beta)} - \frac{I_1(\beta)}{K_0(\beta)}\frac{\left[\beta K_0\left(r_{1D}\sqrt{N}\beta\right)K_1(r_{1D}\beta) - \left(\sqrt{N}/M\right)\beta K_0(r_{1D}\beta)K_1\left(r_{1D}\sqrt{N}\beta\right)\right]}{\left[\left(\sqrt{N}/M\right)\beta K_1\left(r_{1D}\sqrt{N}\beta\right)I_0(r_{1D}\beta) + \beta K_0\left(r_{1D}\sqrt{N}\beta\right)I_1(r_{1D}\beta)\right]},
$$

$$
\beta = \sqrt{u}\exp(-S), N = \frac{\omega}{M}. \tag{26}
$$

Based on the numerical inversion method and the perturbation method [23], the solution to the pressure drawdown well test model considering the stress sensitivity effect for the composite gas reservoir can be expressed as Equation (27):

$$
\psi_{wD} = \frac{-\ln\left(1 - \gamma_{dD}^*\xi_{wD}\right)}{\gamma_{dD}^*}. \tag{27}
$$

For the conventional well test without considering the stress sensitivity effect, the solution to the pressure buildup well test mathematical model, which is a linear equation, can be obtained by the superposition principle based on the solution to the pressure drawdown well test model. However, the superposition principle cannot be applied to the well test model considering the stress sensitivity effect, which is a nonlinear equation. Thus, it is difficult to get the

solution to the pressure buildup well test model considering the stress sensitivity effect by the superposition principle.

2.3.2. Solutions to Pressure Drawdown and Buildup Well Test Models by Numerical Method.
The well test models considering the stress sensitivity effect and the hysteresis effect as Equations (20) and (21) are second-order nonlinear equations. The analytical solution to the pressure drawdown well test model obtained by the perturbation method is an approximate result. Thus, the numerical differentiation method is used to solve these equations.

Considering dramatic pressure changes near the wellbore, the unequal-space grid division is used. Taking $x_D = \ln r_D$, Equation (28) is obtained:

$$\frac{\partial \psi_D}{\partial r_D} = e^{-x_D} \frac{\partial \psi_D}{\partial x_D}, \quad \frac{\partial^2 \psi_D}{\partial r_D^2} = e^{-2x_D} \frac{\partial^2 \psi_D}{\partial x_D^2} - e^{-2x_D} \frac{\partial \psi_D}{\partial x_D}. \quad (28)$$

Substituting Equation (28) into the dimensionless pressure drawdown well test model Equation (20), the model can be written as Equation (29):

$$\begin{cases} \dfrac{\partial^2 \psi_{1D}}{\partial x_D^2} - \gamma_{dD}^* \left(\dfrac{\partial \psi_{1D}}{\partial x_D} \right)^2 = \dfrac{e^{2x_D + \gamma_{dD}^* \psi_{1D}}}{e^{2S}} \dfrac{\partial \psi_{1D}}{\partial t_D}, \\[2mm] \dfrac{\partial^2 \psi_{2D}}{\partial x_D^2} - \gamma_{dD}^* \left(\dfrac{\partial \psi_{2D}}{\partial x_D} \right)^2 = \dfrac{\omega}{M} \dfrac{e^{2x_D + \gamma_{dD}^* \psi_{2D}}}{e^{2S}} \dfrac{\partial \psi_{2D}}{\partial t_D}, \\[2mm] \left(C_D \dfrac{\partial \psi_{1D}}{\partial t_D} - e^{-\gamma_{dD}^* \psi_{1D}} \dfrac{\partial \psi_{1D}}{\partial x_D} \right) \Big|_{x_D = 0} = 1, \\[2mm] \psi_{1D}(x_D = \ln r_{1D}, t_D) = \psi_{2D}(x_D = \ln r_{1D}, t_D), \\[2mm] e^{-\gamma_{dD}^* \psi_{1D}} \dfrac{\partial \psi_{1D}}{\partial x_D} \Big|_{x_D = \ln r_{1D}} = e^{-\gamma_{dD}^* \psi_{2D}} \dfrac{1}{M} \dfrac{\partial \psi_{2D}}{\partial x_D} \Big|_{x_D = \ln r_{1D}}, \\[2mm] \psi_{1D}(x_D, t_D = 0) = \psi_{2D}(x_D, t_D = 0) = 0, \\[2mm] \lim\limits_{x_D \to \infty} \psi_{2D}(x_D, t_D) = 0. \end{cases} \quad (29)$$

The difference in space is as Equation (30):

$$x_D(i) = \begin{cases} (i-1)\Delta x_{1D} & i = 1, 2, 3, \cdots, N, \\ \ln r_{1D} + (i-N)\Delta x_{2D} & i = N+1, N+2, N+3, \cdots, NN, \end{cases} \quad (30)$$

where $\Delta x_{1D} = \ln r_{1D}/(N-1)$; $\Delta x_{2D} = \ln (R_D/r_{1D})/(NN - N)$; N is the discrete number in space of the inner zone, NN is the total discrete number in space of inner and outer zones, and R_D is the dimensionless outer zone boundary radius.

The logarithmic interval is taken for time as Equation (31):

$$t_D(j) = 10^{-6+(j-1)\Delta t}, \quad \Delta t = \frac{\log (T_D) + 6}{O - 1}, \quad (31)$$

where $j = 1, 2, 3, \cdots O$, O is the discrete number of time and T_D is the dimensionless time at the end of the simulation.

For the dimensionless well test mathematical model Equation (29), the finite difference discretization is carried out in space and time as Equations (30) and (31). Then,

the seepage equation discretization result for the composite gas reservoir can be expressed as Equation (32):

$$a(i)\psi_{Di-1}^j + b(i)\psi_{Di}^j + c(i)\psi_{Di+1}^j + d(i)\left(\psi_{Di}^j \right)^2 + e(i)\psi_{Di}^j \psi_{Di+1}^j$$
$$+ f(i)\left(\psi_{Di+1}^j \right)^2 + g(i)e^{r_{dD}^* \psi_{Di}^j} + h(i)\psi_{Di}^j e^{r_{dD}^* \psi_{Di}^j} = 0. \quad (32)$$

When $i = 1, 2, \cdots, N$, then

$$\begin{aligned} a(i) &= \frac{1}{\Delta x_{1D}^2}, \\[2mm] b(i) &= -\frac{2}{\Delta x_{1D}^2}, \\[2mm] c(i) &= \frac{1}{\Delta x_{1D}^2}, \\[2mm] d(i) &= -\frac{\gamma_{dD}^*}{\Delta x_{1D}^2}, \\[2mm] e(i) &= \frac{2\gamma_{dD}^*}{\Delta x_{1D}^2}, \\[2mm] f(i) &= -\frac{\gamma_{dD}^*}{\Delta x_{1D}^2}, \\[2mm] g(i) &= \frac{e^{2(i-1)\Delta x_{1D}}}{e^{2S}\left(t_D^j - t_D^{j-1} \right)} \psi_{Di}^{j-1}, \\[2mm] h(i) &= -\frac{e^{2(i-1)\Delta x_{1D}}}{e^{2S}\left(t_D^j - t_D^{j-1} \right)}. \end{aligned} \quad (33)$$

When $i = N+1, N+2, \cdots, NN$, then

$$\begin{aligned} a(i) &= \frac{1}{\Delta x_{2D}^2}, \\[2mm] b(i) &= -\frac{2}{\Delta x_{2D}^2}, \\[2mm] c(i) &= \frac{1}{\Delta x_{2D}^2}, \\[2mm] d(i) &= -\frac{\gamma_{dD}^*}{\Delta x_{2D}^2}, \\[2mm] e(i) &= \frac{2\gamma_{dD}^*}{\Delta x_{2D}^2}, \\[2mm] f(i) &= -\frac{\gamma_{dD}^*}{\Delta x_{2D}^2}, \\[2mm] g(i) &= \frac{\omega}{M} \frac{e^{2(i-1)\Delta x_{2D}}}{e^{2S}\left(t_D^j - t_D^{j-1} \right)} \psi_{Di}^{j-1}, \\[2mm] h(i) &= -\frac{\omega}{M} \frac{e^{2(i-1)\Delta x_{2D}}}{e^{2S}\left(t_D^j - t_D^{j-1} \right)}. \end{aligned} \quad (34)$$

The discretization result of the initial condition can be expressed as Equation (35):

$$\psi_{Di}^1 = 0, i = 1, 2, \cdots, NN. \quad (35)$$

The discretization result of the inner boundary condition can be expressed as Equation (36):

$$b(1)\psi_{D1}^j + c(1)\psi_{D2}^j + g(1)e^{\gamma_{aD}^* \psi_{Di}^j} + h(1)\psi_{D1}^j e^{\gamma_{aD}^* \psi_{Di}^j} = 0, \quad (36)$$

where

$$\begin{aligned}
b(1) &= -\frac{1}{\Delta x_{1D}}, \\
c(1) &= \frac{1}{\Delta x_{1D}}, \\
g(1) &= 1 + \frac{C_D \psi_{D1}^{j-1}}{t_D^j - t_D^{j-1}}, \\
h(1) &= -\frac{C_D}{t_D^j - t_D^{j-1}}.
\end{aligned} \quad (37)$$

The discretization result of the interface condition can be expressed as Equation (38):

$$\frac{\psi_{DN} - \psi_{DN-1}}{\Delta x_1} = \frac{1}{M}\frac{\psi_{DN+1} - \psi_{DN}}{\Delta x_2}. \quad (38)$$

The discretization result of the outer boundary condition can be expressed as Equation (39):

$$\psi_{DNN}^j = 0. \quad (39)$$

As for the pressure buildup test, the model is obtained after modifying the internal boundary condition and introducing the stress sensitivity coefficient of the buildup stage. Then, the seepage equation discretization result for the composite gas reservoir at the buildup stage can be expressed as Equation (40):

$$\begin{aligned}
&a(i)\psi_{Di-1}^j + b(i)\psi_{Di}^j + c(i)\psi_{Di+1}^j + d(i)\left(\psi_{Di}^j\right)^2 \\
&+ e(i)\psi_{Di}^j \psi_{Di+1}^j + f(i)\left(\psi_{Di+1}^j\right)^2 + g(i)e^{\gamma_{bD}^* \psi_{Di}^j} \\
&+ h(i)\psi_{Di}^j e^{\gamma_{bD}^* \psi_{Di}^j} = 0.
\end{aligned} \quad (40)$$

When $i = 1, 2, \cdots, N$, then

$$\begin{aligned}
a(i) &= \frac{1}{\Delta x_{1D}^2}, \\
b(i) &= -\frac{2}{\Delta x_{1D}^2}, \\
c(i) &= \frac{1}{\Delta x_{1D}^2}, \\
d(i) &= -\frac{\gamma_{bD}^*}{\Delta x_{1D}^2}, \\
e(i) &= \frac{2\gamma_{bD}^*}{\Delta x_{1D}^2}, \\
f(i) &= -\frac{\gamma_{bD}^*}{\Delta x_{1D}^2}, \\
g(i) &= R_1 \frac{e^{2(i-1)\Delta x_{1D}}}{e^{2S}\left(t_D^j - t_D^{j-1}\right)}\psi_{Di}^{j-1}, \\
h(i) &= -R_1 \frac{e^{2(i-1)\Delta x_{1D}}}{e^{2S}\left(t_D^j - t_D^{j-1}\right)}.
\end{aligned} \quad (41)$$

When $i = N + 1, N + 2, \cdots, NN$, then

$$\begin{aligned}
a(i) &= \frac{1}{\Delta x_{2D}^2}, \\
b(i) &= -\frac{2}{\Delta x_{2D}^2}, \\
c(i) &= \frac{1}{\Delta x_{2D}^2}, \\
d(i) &= -\frac{\gamma_{bD}^*}{\Delta x_{2D}^2}, \\
e(i) &= \frac{2\gamma_{bD}^*}{\Delta x_{2D}^2}, \\
f(i) &= -\frac{\gamma_{bD}^*}{\Delta x_{2D}^2}, \\
g(i) &= R_2 \frac{\omega}{M} \frac{e^{2(i-1)\Delta x_{2D}}}{e^{2S}\left(t_D^j - t_D^{j-1}\right)}\psi_{Di}^{j-1}, \\
h(i) &= -R_2 \frac{\omega}{M} \frac{e^{2(i-1)\Delta x_{2D}}}{e^{2S}\left(t_D^j - t_D^{j-1}\right)}.
\end{aligned} \quad (42)$$

The discretization result of the inner boundary condition at the buildup stage can be expressed as Equation (43):

$$b(1)\psi_{D1}^j + c(1)\psi_{D2}^j + g(1)e^{\gamma_{bD}^* \psi_{Di}^j} + h(1)\psi_{D1}^j e^{\gamma_{bD}^* \psi_{Di}^j} = 0, \quad (43)$$
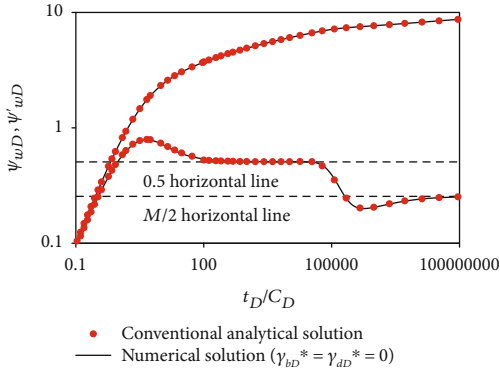
Figure 3: Comparison between the numerical solution and the analytical solution to the pressure drawdown well test model without considering the stress sensitivity effect.

Figure 4: Comparison between the numerical solution and the perturbation solution to the pressure drawdown well test considering the stress sensitivity effect.

Figure 5: Comparison of the homogeneous gas reservoir pressure buildup well test curve obtained from the paper and the research of Zhang and He.
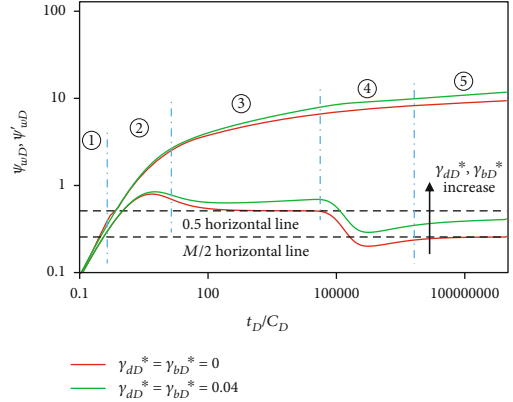
Figure 6: Well test curves for the pressure drawdown well test in composite gas reservoir.
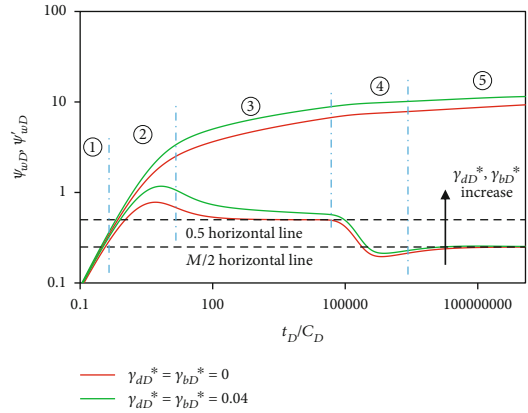
Figure 7: Well test curves for the pressure buildup well test in composite gas reservoir.

Figure 8: Well test curves of the pressure drawdown well test under different stress sensitivity coefficients.

FIGURE 9: Well test curves of the pressure buildup well test under different stress sensitivity coefficients.

FIGURE 10: Well test curves of the pressure drawdown well test considering the hysteresis effect.

FIGURE 11: Well test curves of the pressure buildup well test considering the hysteresis effect.

FIGURE 12: Well test curves of the pressure drawdown well test under different skin factors.

FIGURE 13: Well test curves of the pressure buildup well test under different skin factors.

where

$$
\begin{aligned}
b(1) &= -\frac{1}{\Delta x_{1D}}, \\
c(1) &= \frac{1}{\Delta x_{1D}}, \\
g(1) &= R_1 \frac{C_D \psi_{D1}^{j-1}}{t_D^j - t_D^{j-1}}, \\
h(1) &= -R_1 \frac{C_D}{t_D^j - t_D^{j-1}}.
\end{aligned}
\tag{44}
$$

The discretization results of the interface condition and the outer zone boundary condition for the pressure buildup well test are the same as Equations (38) and (39).

Numerical well test models of drawdown and buildup stages for the composite gas reservoir considering the stress sensitivity effect and the hysteresis effect are established by Equations (32)–(39) and Equations (40)–(43). The Newton-Simpson method is used to solve the nonlinear equation to obtain pressure drawdown and buildup well test solutions.

3. Type Curve of Composite Gas Reservoir Well Test

3.1. Model Verification

3.1.1. Verification of Pressure Drawdown Well Test Model. When dimensionless stress sensitivity coefficients γ_{dD}^{*} and γ_{bD}^{*} are taken as zero, the model is the same as the conventional pressure drawdown well test model of composite gas reservoir [37]. In order to verify the model in the paper, the type curve obtained by the numerical method without considering the stress sensitivity effect is compared with the conventional composite gas reservoir well test curve obtained by the analytical solution shown in Figure 3.

As shown in Figure 3, the type curves of pressure drawdown well test obtained by the numerical solution and the analytical solution are the same when dimensionless stress sensitivity coefficients are set to zero. The curves show common characteristics. The pressure derivative curve is a 0.5 horizontal line at the inner zone radial flow stage, while it is a $M/2$ (mobility ratio/2) horizontal line at the outer zone radial flow stage. Thus, the numerical solution in the paper is reliable.

In order to further verify the model, the type curves of pressure drawdown well test considering the stress sensitivity effect obtained by the numerical method and the perturbation method [23] are compared shown in Figure 4.

It can be seen from Figure 4 that the numerical solution is consistent with the solution obtained by the perturbation method, which verifies the reliability of the numerical solution.

3.1.2. Verification of Pressure Buildup Well Test Model. In order to verify the pressure buildup well test model of composite gas reservoir in the paper, the model is simplified into a homogeneous gas reservoir model considering the stress sensitivity effect by setting $M = 1$, $\omega = 1$, and $\gamma_{bD}^{*} = \gamma_{dD}^{*}$. With those parameter settings, the model does not reflect the influence of the hysteresis effect and the differences of permeability and porosity between the inner zone and the outer zone. Then, the result of the model is compared with the research of Zhang and He [31] shown in Figure 5.

It can be seen from Figure 5 that the well test curve obtained from the simplified model in the paper is consistent with the curve from the research of Zhang and He [31]. Thus, the numerical solution to the pressure buildup well test model in the paper is reliable.

3.2. Type Curve Analysis. Figures 6 and 7 are type curves for pressure drawdown and buildup well tests in a composite gas reservoir. The corresponding parameter values are $C_D = 1$, $S = 1$, $M = 0.5$, $\omega = 1$, $r_{1D} = 500$, $\gamma_{dD}^{*} = 0$ or 0.04, and $\gamma_{bD}^{*} = 0$ or 0.04. And when $\gamma_{dD}^{*} = \gamma_{bD}^{*} = 0$, the well test model is suitable for the conventional composite gas reservoir; when $\gamma_{dD}^{*} = \gamma_{bD}^{*} = 0.04$, the model is suitable for the composite gas reservoir considering the stress sensitivity effect.

It can be seen from Figures 6 and 7 that type curves of the composite gas reservoir well test considering the stress sensitivity effect can be divided into five basic flow regimes including ① the wellbore storage stage, ② the transition stage dominated by the skin factor, ③ the inner zone radial flow stage, ④ the transition stage between the inner zone and outer zone radial flow stages, and ⑤ the outer zone radial flow stage. The characteristics of the wellbore storage stage are not affected by the stress sensitivity effect. The transition stage and the radial flow stage are significantly affected by the stress sensitivity effect. For the pressure drawdown well test shown in Figure 6, the pseudo-pressure curve has a significant uplift compared with the conventional well test curve indicating a larger pressure drawdown at the same dimensionless time t_D after considering the stress sensitivity effect; the pseudo-pressure derivative curve at the inner zone radial flow stage gradually deviates upward from the 0.5 horizontal line indicating the permeability decreases with the increase of the pressure drawdown at the inner zone radial flow stage; the pseudo-pressure derivative curve at the outer zone radial flow stage gradually deviates upward from the $M/2$ (mobility ratio/2) horizontal line indicating the permeability decreases with the increase of the pressure drawdown at the outer zone radial flow stage.

For the pressure buildup well test shown in Figure 7, the pseudo-pressure curve has a significant uplift compared with the conventional well test curve after considering the stress sensitivity effect; the pseudo-pressure derivative curve at the inner zone radial flow stage gradually descends towards the 0.5 horizontal line indicating the permeability increases with the increase of the formation pressure during the buildup stage, while the pseudo-pressure derivative curve at the outer zone radial flow stage gradually descends towards the $M/2$ horizontal line. The pseudo-pressure derivative curve is slightly higher than the $M/2$ horizontal line at the outer zone radial flow stage indicating that the formation pressure is close to the initial pressure.

3.3. Parameter Sensitivity Analysis

3.3.1. The Effect of Stress Sensitivity Coefficient. The type curves of pressure drawdown and buildup well tests considering the stress sensitivity effect under different stress sensitivity coefficients are shown in Figures 8 and 9. The corresponding parameter values are $C_D = 1$, $S = 1$, $r_{1D} = 500$, $M = 0.5$, $\omega = 1$, and $\gamma_{dD}^{*} = \gamma_{bD}^{*} = 0$, 0.02, 0.04, and 0.06.

As shown in Figure 8, for the pressure drawdown well test, as stress sensitivity coefficients γ_{dD}^{*} and γ_{bD}^{*} increase, the pseudo-pressure curve gradually rises, and the pseudo-pressure derivative curve deviates upward from the 0.5 horizontal line at the inner zone radial flow stage, while it deviates upward from the $M/2$ (mobility ratio/2) horizontal line at the outer zone radial flow stage. The changes indicate that the pressure drawdown becomes larger, and the permeability becomes lower at the same dimensionless time t_D as stress sensitivity coefficients increase.

For the pressure buildup well test shown in Figure 9, as stress sensitivity coefficients γ_{dD}^{*} and γ_{bD}^{*} increase, the pseudo-pressure and pseudo-pressure derivative curves gradually rise, which means that the speed of formation pressure buildup is quicker as stress sensitivity coefficients γ_{dD}^{*} and γ_{bD}^{*} increase. The pseudo-pressure derivative
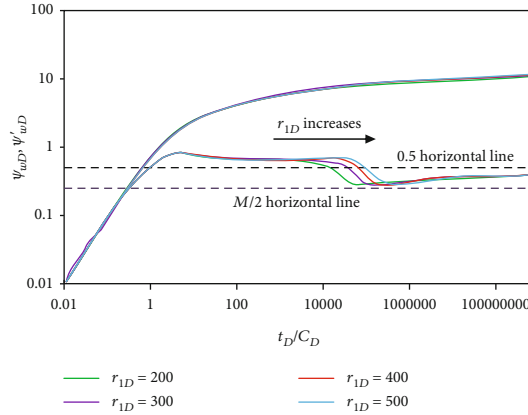
FIGURE 14: Well test curves of the pressure drawdown well test under different inner zone radii.
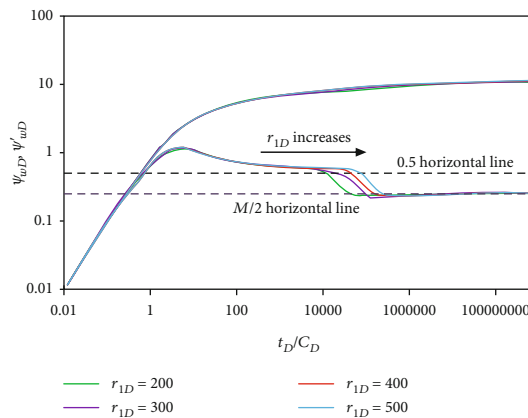
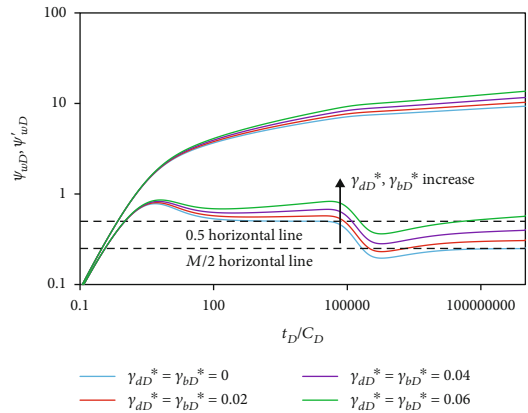FIGURE 15: Well test curves of the pressure buildup well test under different inner zone radii.

curve at the inner zone radial flow stage gradually descends towards the 0.5 horizontal line, while the pseudo-pressure derivative curve at the outer zone radial flow stage gradually descends towards the $M/2$ (mobility ratio/2) horizontal line in all cases.

3.3.2. The Effect of Hysteresis Effect. The type curves of pressure drawdown and buildup well tests considering the hysteresis effect are shown in Figures 10 and 11. The corresponding parameter values are $C_D = 1$, $S = 1$, $r_{1D} = 500$, $M = 0.5$, $\omega = 1$, $\gamma_{dD}^* = 0.1$, and $\gamma_{bD}^* = 0.1$, 0.05, and 0.01.

As shown in Figure 10, for the pressure drawdown well test with one production stage followed by one shut-in stage, the stress hysteresis effect has no effect on the curve of pressure drawdown well test due to the same stress sensitivity coefficient γ_{dD}^* at the pressure drawdown stage.

For the pressure buildup well test curve shown in Figure 11, as the stress sensitivity coefficient γ_{bD}^* of buildup stage decreases, and the pseudo-pressure derivative curve gradually rises at both inner zone and outer zone radial flow stages. Moreover, the transition stage between inner zone and outer zone radial flow stages appears later. Because the lower stress sensitivity coefficient of buildup stage γ_{bD}^* is, the slower of permeability recovery speed is. The final permeability recovery value is also smaller at the pressure buildup stage.

3.3.3. The Effect of Skin Factor. The type curves of pressure drawdown and buildup well tests considering the stress sensitivity effect under different skin factors are shown in Figures 12 and 13. The corresponding parameter values are $C_D = 1$, $\gamma_{dD}^* = \gamma_{bD}^* = 0.04$, $M = 0.5$, $\omega = 1$, $r_{1D} = 500$, and $S = -1$, 1, 3, and 5.

As shown in Figures 12 and 13, the pseudo-pressure curves of pressure drawdown and buildup well tests both have an uplift as the skin factor S increases indicating a larger pressure drawdown or buildup at the same dimensionless time t_D. At the inner zone or outer zone radial flow stages, the pseudo-pressure derivative curves of pressure drawdown well test obviously deviate upward as the skin factor increases, but the pseudo-pressure derivative curves at the radial flow stage of pressure buildup well test are not affected by the skin factor. This feature is different from that of the conventional composite gas reservoir well test curve. For conventional composite gas reservoir well test type curves under different skin factors, the pseudo-pressure derivative curves for both pressure drawdown and buildup well tests are 0.5 horizontal lines at inner zone radial flow stages. Those are $M/2$ horizontal lines at the outer zone radial flow stages.

3.3.4. The Effect of Inner Radius. The type curves of pressure drawdown and buildup well tests considering the stress
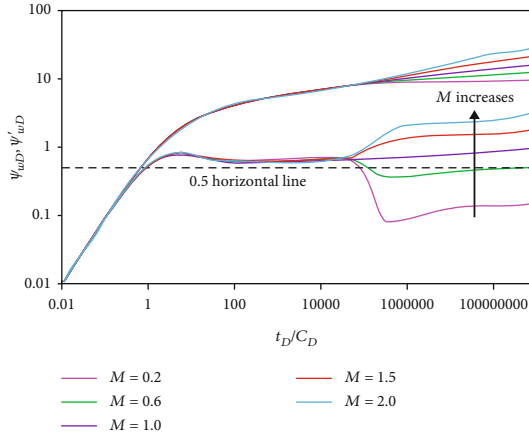
FIGURE 16: Well test curves of the pressure drawdown well test under different mobility ratios.

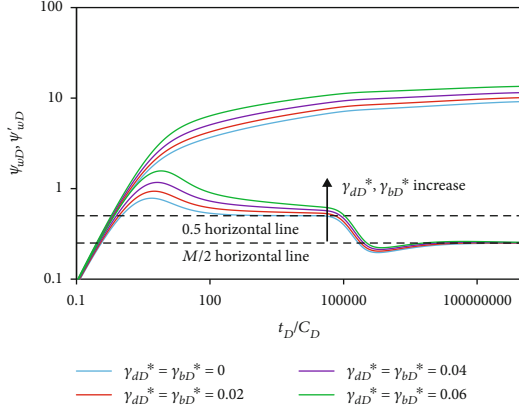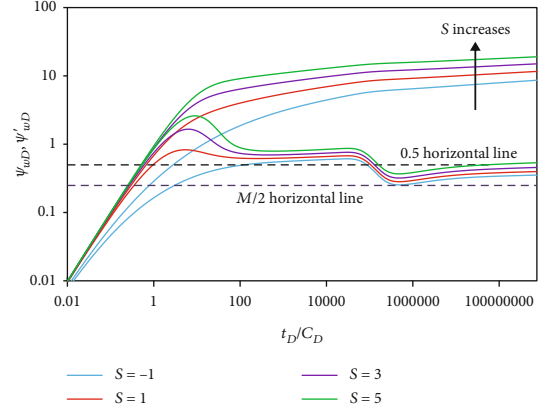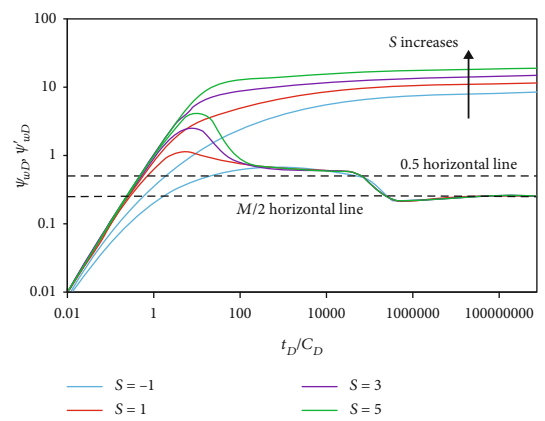FIGURE 17: Well test curves of the pressure buildup well test under different mobility ratios.
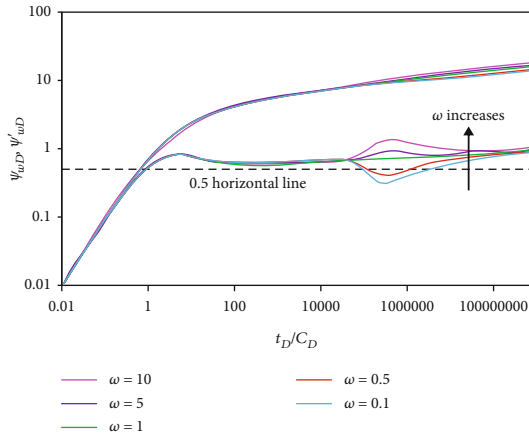
FIGURE 18: Well test curves of the pressure drawdown well test under different storage ratios.

FIGURE 19: Well test curves of the pressure buildup test under different storage ratios.

TABLE 1: The basic parameters of gas well test in the deepwater gas reservoir.

Parameters	Values
Well type	Vertical well
Initial pressure (MPa)	72.91
Reservoir temperature (°C)	167.68
Effective thickness (m)	9.1
Wellbore radius (m)	0.127
Porosity (decimal)	0.2197
Rock compressibility (MPa^{-1})	0.000501
Relative density of natural gas (decimal)	0.764
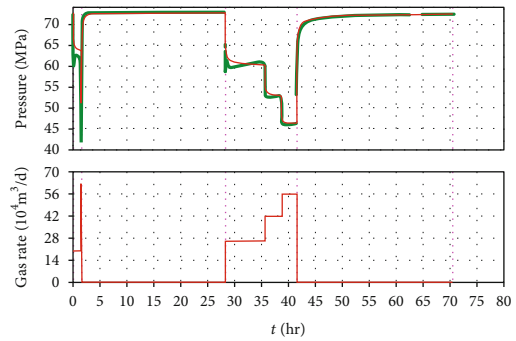
FIGURE 20: The pressure history of the well in the deepwater gas reservoir.

sensitivity effect under different inner radii are shown in Figures 14 and 15. The corresponding parameter values are $C_D = 1$, $S = 1$, $\gamma_{dD}{}^* = \gamma_{bD}{}^* = 0.04$, $M = 0.5$, $\omega = 1$, and $r_{1D} = 200, 300, 400,$ and 500.

As shown in Figures 14 and 15, the radius of inner zone mainly affects the duration of inner zone radial flow. The larger inner zone radius leads to a longer duration of inner zone radial flow and a later appearance of the transition stage between inner zone and outer zone radial flow stages.

(a)

(b)

(c)

(d)
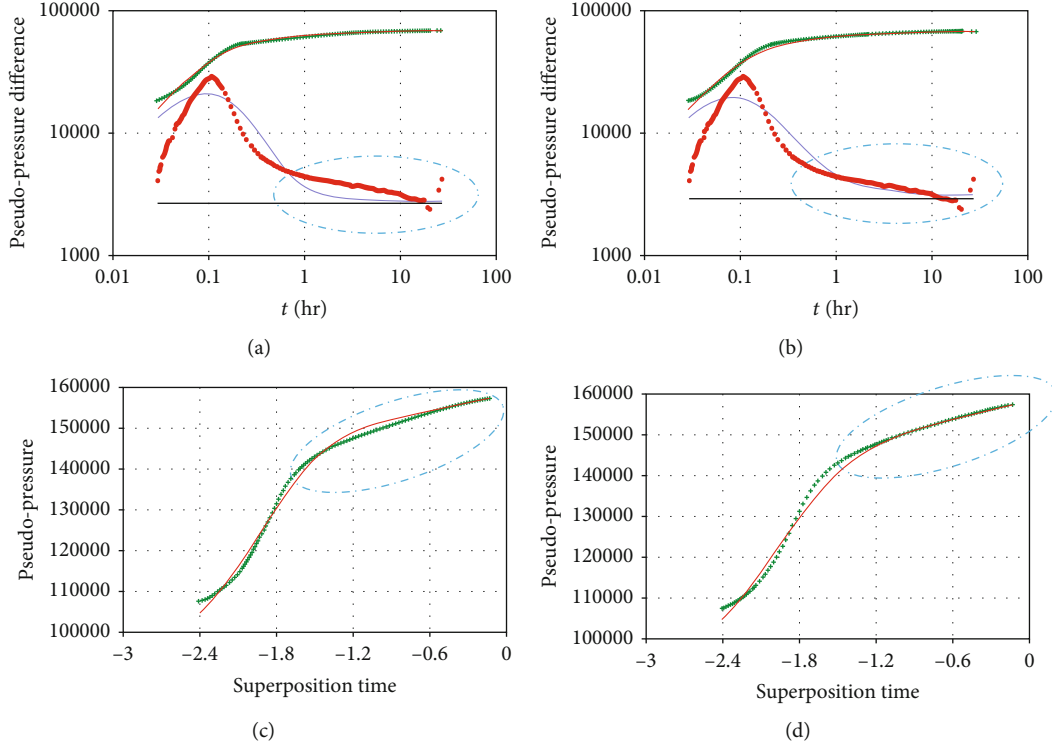
FIGURE 21: Comparison of interpretation results with and without considering the stress sensitivity effect. (a, b) Well test interpretation results in the double logarithmic curve. (a) The interpretation result without considering the stress sensitivity effect. (b) The interpretation result considering the stress sensitivity effect. (c, d) Well test interpretation results in the semilogarithm curve. (c) The interpretation result without considering the stress sensitivity effect. (d) The interpretation result considering the stress sensitivity effect.

3.3.5. The Effect of Mobility Ratio. The type curves of pressure drawdown and buildup well tests considering the stress sensitivity effect under different mobility ratios are shown in Figures 16 and 17. The corresponding parameter values are $C_D = 1$, $S = 1$, ${\gamma_{dD}}^* = {\gamma_{bD}}^* = 0.04$, $\omega = 1$, $r_{1D} = 500$, and $M = 0.2, 0.6, 1.0, 1.5$, and 2.

As shown in Figures 16 and 17, for the pressure drawdown well test, the mobility ratio mainly affects characteristics of the transition stage and the outer zone radial flow stage. A larger mobility ratio leads to a higher pseudo-pressure and pseudo-pressure derivative curve at the outer zone radial flow stage indicating a larger pressure drawdown and a lower permeability in the outer zone at the same dimensionless time. For the pressure buildup well test, the mobility ratio has an effect on both inner zone and outer zone radial flow stages. A larger mobility ratio leads to a higher pseudo-pressure and pseudo-pressure derivative curve in both two flow regimes. The feature is different from the pressure buildup well test curve of conventional composite gas reservoir. The mobility ratio has no effect on the pseudo-pressure derivative of both pressure drawdown and buildup well tests at the inner zone radial flow stage for the conventional well test curve.

3.3.6. The Effect of Storage Ratio. The type curves of pressure drawdown and buildup well tests considering the stress sensitivity effect under different storage ratios are shown in Figures 18 and 19. The corresponding parameter values are

$C_D = 1$, $S = 1$, ${\gamma_{dD}}^* = {\gamma_{bD}}^* = 0.04$, $r_{1D} = 500$, $M = 1$, and $\omega = 0.1, 0.5, 1, 5$, and 10.

As shown in Figures 18 and 19, when the storage ratio ω is greater than 1, the curve shows a small hump at the transition stage between inner zone and outer zone radial flow stages indicating that the inner zone storage capacity is greater than that of the outer zone. When the storage ratio ω is less than 1, the curve shows a small concave.

4. Case Study

Taking a case from a deepwater gas reservoir with high temperature and pressure as an example, the basic parameter of the well is shown in Table 1. The pressure history of the well is shown in Figure 20.

Taking the second buildup stage to conduct the well test interpretation, interpretation results are shown in Figure 21 and Table 2. It can be seen that there is no obvious boundary response in the well test curve; thus, the well test model is chosen as the infinite model with a constant well storage coefficient and skin factor. The pressure derivative curve of the pressure buildup well test has obvious downward trend indicating the influence of the stress sensitivity effect. Therefore, a well test model considering the stress sensitivity effect is used in the well test interpretation of this case. Besides, the results of well test interpretation with and without considering the stress sensitivity effect are compared shown in Figure 21 and Table 2.

TABLE 2: Comparison of interpretation results with and without considering the stress sensitivity effect.

Parameters	Considering the stress sensitivity effect	Without considering the stress sensitivity effect	Variation amplitude of the interpretation parameters (%)
Well storage coefficient (m^3/MPa)	0.280	0.283	1.06
Skin factor	3.50	5.46	56.0
Permeability (mD)	5.54	6.50	17.3
Stress sensitivity coefficient (MPa^{-1})	0.012	–	–
Mobility ratio	1.0	1.0	–
Storage ratio	1.0	1.0	–

It can be seen from Table 2 and Figure 21 that better fitting results of pressure curves can be obtained after considering the stress sensitivity effect. The skin factor will be exaggerated without considering the stress sensitivity effect. Therefore, the accuracy of the well test interpretation for the deepwater gas reservoir with high temperature and pressure is improved after considering the stress sensitivity effect.

5. Conclusion

The paper establishes a composite gas reservoir pressure buildup well test model considering the stress sensitivity and the hysteresis effect to guide well test interpretations for high temperature and pressure composite gas reservoirs in deepwater. Based on the research, the following conclusions are obtained:

(1) The solutions to composite gas reservoir pressure drawdown and buildup well test models considering the stress sensitivity and the hysteresis effect are obtained by the numerical differentiation method. Then, the solution to pressure drawdown well test model is verified by comparing with the analytical solution obtained by the perturbation method and the analytical solution to the conventional well test model. The solution to the pressure buildup well test model is verified by comparing with the homogeneous gas reservoir well test solution from the research of Zhang and He after setting $M = 1$, $\omega = 1$, and $\gamma^*_{bD} = \gamma^*_{dD}$

(2) The differences between pressure drawdown and buildup well test curves considering the stress sensitivity effect and the hysteresis effect are compared. The main flow regimes affected by the stress sensitivity effect are the inner zone and outer zone radial flow stages. The pressure derivative curve of pressure drawdown well test considering the stress sensitivity effect deviates upward from the 0.5 horizontal line at the inner zone radial flow stage, while it deviates upward from the M/2 (mobility ratio/2) horizontal line at the outer zone radial flow stage. However, for the pressure buildup well test curve considering the stress sensitivity effect, the pressure derivative

curve gradually descends to the 0.5 horizontal line at the inner zone radial flow stage, while it descends to the M/2 (mobility ratio/2) horizontal line at the outer zone radial flow stage. The pressure derivative curve considering the hysteresis effect is higher than the curve without considering the hysteresis effect for the pressure buildup well test, because the permeability cannot be recovered to its original value in the buildup stage after considering the hysteresis effect

(3) The effects of different parameters such as stress sensitivity coefficient, hysteresis effect coefficient, skin factor, inner radius, mobility ratio, and storage ratio on type curves are analyzed. The stress sensitivity coefficient, skin factor, and mobility ratio have different effects on pressure drawdown and buildup well test curves after considering the stress sensitivity effect, which are different from conventional well test curves without considering the stress sensitivity effect

(4) A well test interpretation case from the deepwater gas reservoir with high temperature and pressure is studied. The result indicates that the accuracy of interpretation is improved after considering the stress sensitivity effect. The skin factor will be exaggerated without considering the stress sensitivity effect

Data Availability

The data used to support the findings of this study are available from the corresponding author upon request.

Conflicts of Interest

The authors declare no conflict of interest.

Authors' Contributions

Conceptualization was done by Yihua Gao; methodology was done by Yihua Gao, Ruizhong Jiang, and Zhaobo Sun; validation was done by Yihua Gao, Xiangdong Xu, Zhaobo Sun, and Zhiwang Yuan; the original draft preparation was done by Yihua Gao; the review and editing were done by

Xiangdong Xu, Kang Ma, Zhiwang Yuan, Bin Jiang, Botao Kang, Guoning Chen, and Chenxi Li.

Acknowledgments

References

[1] D. Meunier, C. Kabir, and M. Wittmann, "Gas well test analysis: use of normalized pseudovariables," *SPE Formation Evaluation*, vol. 2, no. 4, pp. 629–636, 1987.

[2] A. Azamifard, M. Hekmatzadeh, and B. Dabir, "Evaluation of gas condensate reservoir behavior using velocity dependent relative permeability during the numerical well test analysis," *Petroleum*, vol. 2, no. 2, pp. 156–165, 2016.

[3] Y. Zhao, L. Zhang, J. Zhao, J. X. Luo, and B. N. Zhang, ""Triple porosity" modeling of transient well test and rate decline analysis for multi-fractured horizontal well in shale gas reservoirs," *Journal of Petroleum Science and Engineering*, vol. 110, pp. 253–262, 2013.

[4] W. Xu, Z. Liu, J. Liu et al., "New understanding of transient pressure response in the transition zone of oil-water and gas-water systems," *Geofluids*, vol. 2018, 15 pages, 2018.

[5] Y. Xu, X. Li, and Q. Liu, "Pressure performance of multi-stage fractured horizontal well with stimulated reservoir volume and irregular fractures distribution in shale gas reservoirs," *Journal of Natural Gas Science and Engineering*, vol. 77, p. 103209, 2020.

[6] W. Xu, R. Liu, H. Yang, L. Zhang, and Y. Yang, "Investigation of well testing reservoirs with multiphase flow in a mature field," *SIMULATION*, vol. 97, no. 2, pp. 83–96, 2021.

[7] Y. Xu, X. Li, Q. Liu, S. Yang, and X. Tan, "A semi-analytical solution of finite-conductivity multi-wing fractured well in naturally fractured reservoirs by boundary element method," *Journal of Petroleum Science and Engineering*, vol. 203, p. 108584, 2021.

[8] D. Xia, Z. Yang, D. Li, Y. Zhang, X. Zhao, and L. Yao, "Research on numerical method for evaluation of vertical well volume fracturing effect based on production data and well test data," *Journal of Petroleum Exploration and Production*, vol. 11, no. 4, pp. 1855–1863, 2021.

[9] M. Gong, J. Zhang, Z. Yan, and J. Wang, "Prediction of inter-well connectivity and interference degree between production wells in a tight gas reservoir," *Journal of Petroleum Exploration and Production Technology*, vol. 11, no. 8, pp. 3301–3310, 2021.

[10] I. Fatt and D. Davis, "Reduction in permeability with overburden pressure," *Journal of Petroleum Technology*, vol. 4, no. 12, p. 16, 1952.

[11] Y. Li, X. Li, F. Wu et al., "Experimental study on stress sensitivity of high-temperature and high-pressure sandstone gas reservoirs in Yingqiong Basin," *Energy Science & Engineering*, vol. 8, no. 11, pp. 4116–4125, 2020.

[12] R. Nie, Z. Wang, Z. Chen et al., "Stress-sensitive permeability of matrix cores and artificially fractured cores with nonproppant-filled fractures under high-pressure conditions," *Geophysics*, vol. 86, no. 3, pp. M59–M75, 2021.

[13] Y. Yang, L. Tao, H. Yang et al., "Stress sensitivity of fractured and vuggy carbonate: an X-Ray computed tomography analysis," *Journal of Geophysical Research: Solid Earth*, vol. 125, no. 3, article e2019JB018759, 2020.

[14] Y. Liu, J. Y. Leung, R. J. Chalaturnyk, and C. J. Virues, "New insights on mechanisms controlling fracturing-fluid distribution and their effects on well performance in shale-gas reservoirs," *SPE Production & Operations*, vol. 34, no. 3, pp. 564–585, 2019.

[15] Y. Liu, L. Liu, J. Y. Leung, and G. J. Moridis, "Sequentially coupled flow and geomechanical simulation with a discrete fracture model for analyzing fracturing fluid recovery and distribution in fractured ultra-low permeability gas reservoirs," *Journal of Petroleum Science and Engineering*, vol. 189, p. 107042, 2020.

[16] N. Cao and G. Lei, "Stress sensitivity of tight reservoirs during pressure loading and unloading process," *Petroleum Exploration and Development*, vol. 46, no. 1, pp. 138–144, 2019.

[17] D. Zhang, P. Ranjith, M. Perera, and C. P. Zhang, "Influences of test method and loading history on permeability of tight reservoir rocks," *Energy*, vol. 195, article 116902, 2020.

[18] Z. Zhang, S. He, G. Liu, X. Guo, and S. Mo, "Pressure buildup behavior of vertically fractured wells with stress-sensitive conductivity," *Journal of Petroleum Science and Engineering*, vol. 122, pp. 48–55, 2014.

[19] R. Raghavan, J. Scorer, and F. Miller, "An investigation by numerical methods of the effect of pressure-dependent rock and fluid properties on well flow tests," *Society of Petroleum Engineers Journal*, vol. 12, no. 3, pp. 267–275, 1972.

[20] V. F. Samaniego, W. E. Brigham, and F. G. Miller, "On the determination of reservoir fluids considering pressure-dependent rock and fluid properties," *Society of Petroleum Engineers Journal*, vol. 17, no. 2, pp. 141–150, 1977.

[21] F. Samaniego and H. Cinco-Ley, "On the determination of the pressure-dependent characteristics of a reservoir through transient pressure testing," in *SPE Annual Technical Conference and Exhibition*, San Antonio, Texas, 1989.

[22] O. A. Pedrosa, "Pressure transient response in stress-sensitive formations," in *SPE California Regional Meeting*, Oakland, California, 1986.

[23] J. Kikani and O. A. Pedrosa, "Perturbation analysis of stress-sensitive reservoirs (includes associated papers 25281 and 25292)," *SPE Formation Evaluation*, vol. 6, no. 3, pp. 379–386, 1991.

[24] M. Franquet, M. Ibrahim, R. A. Wattenbarger, and J. B. Maggard, "Effect of pressure-dependent permeability in tight gas reservoirs, transient radial flow," in *Canadian International Petroleum Conference*, Calgary, Alberta, 2004.

[25] J. M. Thompson, M. Nobakht, and D. M. Anderson, "Modeling well performance data from overpressured shale gas reservoirs," in *Canadian Unconventional Resources and International Petroleum Conference*, Calgary, Alberta, Canada, 2010.

[26] M. Arif, A. A. Bhatti, A. S. Khan, and S. AfrazHaider, "An alternative approach for well test analysis and production performance in tight gas reservoirs considering stress dependent permeability," in *SPE/PAPG Annual Technical Conference*, Islamabad, Pakistan, 2012.

[27] H. Wang, "Performance of multiple fractured horizontal wells in shale gas reservoirs with consideration of multiple mechanisms," *Journal of Hydrology*, vol. 510, pp. 299–312, 2014.

[28] W. Xu, X. Wang, X. Hou, K. Clive, and Y. Zhou, "Transient analysis for fractured gas wells by modified pseudo-functions in stress-sensitive reservoirs," *Journal of Natural Gas Science and Engineering*, vol. 35, pp. 1129–1138, 2016.

[29] Y. Xu, X. Li, Q. Liu, and X. Tan, "Pressure performance of multi-stage fractured horizontal well considering stress sensitivity and dual permeability in fractured gas reservoirs," *Journal of Petroleum Science and Engineering*, vol. 201, p. 108154, 2021.

[30] A. S. Bhullar, G. E. Stewart, and R. W. Zimmerman, "Perturbation solution for one-dimensional flow to a constant-pressure boundary in a stress-sensitive reservoir," *Transport in Porous Media*, vol. 137, no. 3, pp. 471–487, 2021.

[31] Z. Zhang and S. He, "Pressure buildup behavior in deformable medium formation," *Journal of Chongqing University*, vol. 36, no. 11, pp. 108–114, 2013.

[32] S. Rui, T. Yahui, B. Xiaoming, Q. Hongfeng, Y. Shiquan, and L. Xingwei, "Initial evaluation for well testing of volcanic gas reservoir in Xushen Gas Field," *Acta Petrolei Sinica*, vol. 27, Supplement, pp. 142–146, 2006.

[33] L. Chen, "Establishment and solution of the mathematical model of multiphase water hammer in gas wells," *Acta Petrolei Sinica*, vol. 38, no. 7, pp. 813–820, 2017.

[34] J. Lin, H. He, and Y. Wang, "A well test analysis model of generalized tube flow and seepage coupling," *Petroleum Exploration and Development*, vol. 48, no. 4, pp. 923–934, 2021.

[35] W. Xiao, T. Li, M. Li, J. Zhao, L. Zheng, and L. Li, "Evaluation of the stress sensitivity in tight reservoirs," *Petroleum Exploration and Development*, vol. 43, no. 1, pp. 115–123, 2016.

[36] Y. Wei, J. Wang, W. Yu et al., "A smart productivity evaluation method for shale gas wells based on 3D fractal fracture network model," *Petroleum Exploration and Development*, vol. 48, no. 4, pp. 911–922, 2021.

[37] Y. Liu, B. Yan, Y. Zhai, and H. Yin, "Transient pressure behavior in a homogeneous composite reservoir," *Acta Petrolei Sinica*, vol. 15, no. 1, pp. 92–100, 1994.

Research Article

Multiscale Research on Pore Structure Characteristics and Permeability Prediction of Sandstone

M. A. Shi-Jia,[1,2] **L. I. N. Yuan-Jian** ⬤**,**[1,3] **L. I. U. Jiang-Feng** ⬤**,**[1,2] **Kundwa Marie Judith,**[1] **Ishimwe Hubert,**[4] **and W. A. N. G. Pei-lin**[1]

[1]*The State Key Laboratory for GeoMechanics and Deep Underground Engineering, and School of Mechanics and Civil Engineering, China University of Mining and Technology, Xuzhou 221000, China*
[2]*Key Laboratory of Deep Earth Science and Engineering (Sichuan University), Ministry of Education, Chengdu, China*
[3]*School of Education, Nanchang Institute of Science and Technology, Nanchang 330108, China*
[4]*School of Resources and Geosciences, China University of Mining and Technology, Xuzhou 221116, China*

Correspondence should be addressed to L. I. N. Yuan-Jian; yuanjianlin@cumt.edu.cn and L. I. U. Jiang-Feng; jeafliu@hotmail.com

The random existence of many irregular pore structures in geotechnical materials has a decisive influence on its permeability and other macroscopic properties. The analysis and characterization of the micropore structure of the material and its permeability are of great significance for geotechnical engineering. In this study, digital images with different magnifications were used to examine the pore structure and permeability of sandstone samples. The image processing method is used to obtain binary images, and then, the pore size distribution method is used to calculate the pore size distribution. Therefore, based on the Hagen-Poiseuille formula, we get the prediction value of material's permeability and compare it with the value obtained from mercury intrusion porosimetry (MIP). It is found that different microscopic images with different magnification and various statistical methods of pore size have a specific influence on the characterization of pore structure and permeability prediction. The porosity of different magnifications is not the same, and the results obtained at higher magnifications are more consistent with the results obtained with MIP. With the increase of magnification, we can observe more pores in large sizes. The effect of CPSD (continuous pore size distribution) in pore size statistics is better than that of DPSD (discrete pore size distribution). In permeability prediction, the prediction result of higher magnification images are closer to the instrument test value, and the value of DPSD is more significant than that of CPSD. In future research, an appropriate method should be selected to obtain a reasonable prediction of the permeability of the target material.

1. Introduction

For the characterization of sandstone reservoirs, porosity, pore size distribution, and permeability are essential parameters for reservoir evaluation. A sandstone sample usually contains many irregular, variable-sized, randomly distributed, interconnected pores, which become the main accumulation places and percolation channels for hydrocarbon fluids. The porosity determines the storage capacity of hydrocarbons, while the pore size distribution and permeability directly affect the transport capacity of hydrocarbons [1–4]. Therefore, the macroscopic gas permeability experiment can usually obtain the gas transport mode but cannot

reveal its transport mechanism [5–8]. On the other hand, microscopic analysis can observe the development of pores and fractures in the sample, which provides a direct basis for studying the seepage evolution mechanism of a rock mass. Therefore, microscopic analysis of the pore structure and permeability can help to reveal the distribution of oil and gas in sandstone reservoirs and the microscopic transport mechanism [9, 10].

The main methods of studying microscopic pore structure in the existing work are divided into two categories. The first category methods use the physical measure to evaluate the pore throat radius distribution, connectivity, and pore structure parameters, and it includes MIP, nitrogen

adsorption, and nuclear magnetic resonance (NMR) [8, 11, 12]. The second category methods use precision instruments to obtain digital images containing the microscopic morphology of a sample, such as computed tomography (CT), scanning electron microscope (SEM), and transmission electron microscopy (TEM) [13, 14]. The first category methods are widely used in existing research. Still, it has some disadvantages: the pore size distribution of the specimen can be well characterized by MIP, but the higher pressure can affect the pore structure of the sample itself, thus affecting the characterization of the pore structure. Nitrogen adsorption can only characterize pores with a radius of less than 100 nm. NMR is a nondestructive technique that simulates the specimen and indicates a wide pore size, but its accuracy depends on calibration experiments. These pore structure characterization methods all have a common disadvantage. They do not allow visual observation of the pore structure of the rock samples [1, 15].

For the second category, such as CT, SEM, and TEM, the pore structure of the sample can be directly observed. The three-dimensional pore structure of the sample can be seen using computed tomography, but it is difficult to characterize the pores on the nanoscale. TEM is suitable for measuring sample's morphology, but the test requires a relatively thin piece to allow the passage of electrons. SEM can characterize the pores at different scales, from the nanoscale to the millimeter scale. Furthermore, the previous study found specific differences in the pore structure properties (porosity, pore size distribution, etc.) characterized by SEM images of different scales [2, 3, 13]. Therefore, different magnifications of SEM images were performed in this study to examine and quantify the pore structure of the same sample.

The next section of this paper is organized as a followup: the SEM images are first acquired at different magnifications and studied from different scales. Then, a reasonable threshold value is selected based on the correlation threshold determination algorithm to binarise the image segmentation. The pore size distribution is then calculated based on the discrete and continuous pore size distribution algorithms. Finally, permeability prediction is based on the Hagen-Poiseuille equation and the previous pore size distribution information. Simultaneously, the results of the digital image-based calculations are compared to those of laboratory experiments (e.g., mercury pressure experiments and gas permeability experiments) to verify the adaptability and accuracy of the relevant algorithms.

2. Materials and Methodology

2.1. SEM Image Scanning and Image Information.
Using a Quantatm 250 scanning electron microscope introduced by China University of Mining and Technology from the FEI Company in the United States, sandstone is scanned by SEM. The equipment has an excellent stable operation of ultralow vacuum/low vacuum and sample signal collection effect. The density of the intact sandstone sample is 2.565 ± 0.1 g/cm^2. The porosity measured by the mercury injection method is 4.52%. The main mineral components of sandstone include quartz, potassium feldspar, plagioclase, calcite, siderite, and clay minerals (Illite, Kaolinite, Chlorite, and Smectite). The collected sandstone samples are 10 mm ∗ 10 mm ∗ 10 mm fragments (as shown in Figure 1). SEM images of sandstone with different magnifications are obtained by a scanning electron microscope, with 600-fold, 1200-fold, and 2000-fold, respectively. The resolution of the SEM image is relatively high, and it is easier to obtain digital images of different scales. While CT can get pore sizes on the nanoscale, SEM can acquire pores as tiny as a micron. The pixel accuracy of different images is shown in Table 1. As can be observed that the increase of magnification, the smaller the pixel accuracy of the image is, that is, the smaller the pore structure is observed.

2.2. Methodology

2.2.1. Method for Calculating Porosity.
Following binary segmentation of the digital image, pores' pixels are assigned a value of 0, while the remaining matrix is assigned a value of 1. The porosity φ is calculated as follows:

$$\varphi = \frac{S_\varphi}{S} \times 100\%, \tag{1}$$

where φ stands for porosity, %; S_φ represents the area of the pore; S represents the total area of the image.

2.2.2. Characterization of Pore Size Distribution.
There are two main algorithms for determining the pore size distribution (PSD) of a sample using digital images: DPSD and CPSD. The main difference between DPSD and CPSD is that CPSD takes into account pore geometry when extracting pore size distribution. The principal idea of the "continuous PSD" at a specific pore radius r_s is to determine the amount of pore volume (3D) or a rather pore area (2D), which potentially can be covered with spheres and circles of the radius r_s in 3D and 2D, respectively. Even a single unconnected pore object becomes not a single value only but instead possesses its PSD, as it is inspected individually. In contrast, the principle of the CPSD algorithm is similar to the mercury injection method. For DPSD, the sizes of their volume and their area are determined subsequently for the 3D case and the 2D case, respectively. A respective pore radius may be determined for each pore object from such volume or area by calculating the radius of its size-equivalent sphere or circle. The primary approach is to convert irregular pores to circles or spheres using the equal area principle [16]. To further understand the binary principle, two images are presented in Figure 2.

2.2.3. Permeability Calculation.
Hagen-Poiseuille law is a physical law in nonideal fluid dynamics. It proposes that when an incompressible Newtonian fluid passes through a long cylindrical tube with a particular section in laminar flow [8, 17], the velocity distribution of the section is

$$v = \frac{\Delta P}{4\mu L}\left(R^2 - r^2\right), \tag{2}$$

where r is the distance from the center of the circle; ΔP is the
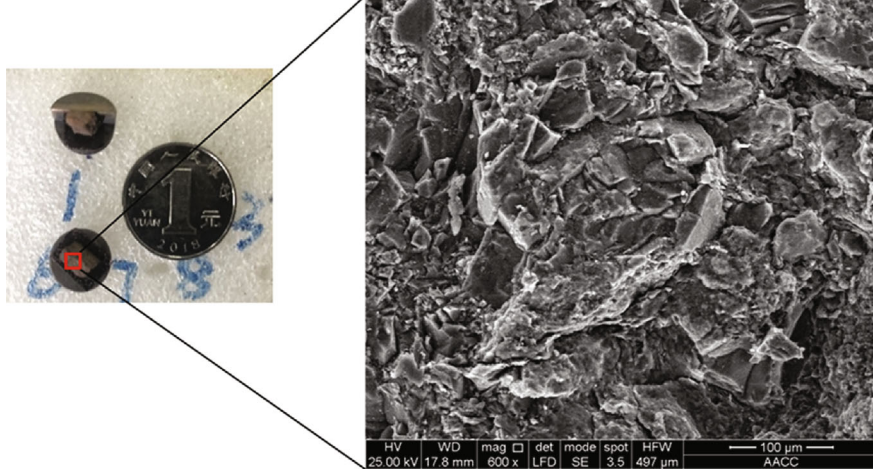
FIGURE 1: A sandstone sample and scanning sample.

TABLE 1: Resolution of images with different magnifications.

Magnification	600x	1200x	2000x
Pixel accuracy (μm/pixel)	0.481	0.240	0.145

pressure difference between the two ends of the pipe, which is expressed in MPa; μ is hydrodynamic viscosity, which is expressed in Pa•s; L is the length of the cylindrical pipe, which is expressed in μm; R is the radius of the cylindrical tube, which is expressed in μm. By integrating Equation (2) over the entire cross-section, the total volume flow of the fluid through the cross-section of the pipeline can be obtained as follows:

$$Q = \frac{\pi R^4 \Delta P}{8 \mu L}. \tag{3}$$

As seen in Figure 3, it is considered that the total flow through the pore structure of the sample and the total flow through each small pore are equal to each other, then it can be obtained:

$$Q = \sum Q_i, \tag{4}$$

where Q is the total instantaneous flow of the sample microstructure, expressed in mm^3/s; Q_i is the flow rate of each tiny pore expressed in mm^3/s. As seen from Darcy's law, the flow of fluids also follows Darcy's law:

$$Q = \frac{kA}{\mu L} \Delta P, \tag{5}$$

where k is permeability, which is expressed in m^2; A is the cross-sectional area of the fluid, which is expressed in mm^2.

In combination with (3), (4), and (5), the following can be obtained:

$$\frac{kA}{\mu L} \Delta P = Q = \sum Q_i = \sum \frac{\pi R_i^4}{8 \mu L} \Delta P. \tag{6}$$

The expression of permeability can be further simplified as follows:

$$k = \frac{\pi}{8A} \sum R_i^4 = \frac{1}{8A} \sum A_i R_i^2, \tag{7}$$

where R_i is pore radius, which is expressed in mm; A_i is the radius R_i of pore area, which is expressed in mm^2.

According to Equation (7) and the simplified internal pore, the permeability of sandstone can be predicted by a digital image.

3. Results and Analysis

3.1. Gray Threshold Selection. As shown in Figure 4, digital images with different magnification are adopted in this study, showing that SEM images can more intuitively observe the pore structure of sandstone. The darker pixels mean the pore of sandstone, while the lighter pixels are seen as the matrix. Before the quantitative characterization of the pore structure, image preprocessing is needed to lay a foundation for subsequent analysis. Brightness and contrast adjustments, image denoising, and image enhancement are all examples of image preprocessing. Generally speaking, for SEM images, the image quality is usually better. Image denoising does not have a significant impact on the subsequent characterization of the image. The change in brightness will not significantly affect the shape of the gray distribution curve (within a specific range). However, the difference in contrast has a significant effect on the shape of the gray distribution curve. Through the above method, the digital image obtained by processing is shown in Figure 5. It can be seen that the pore and matrix structure

(a) Principle of discrete pore size distribution algorithm

(b) Principle of continuous pore size distribution algorithm
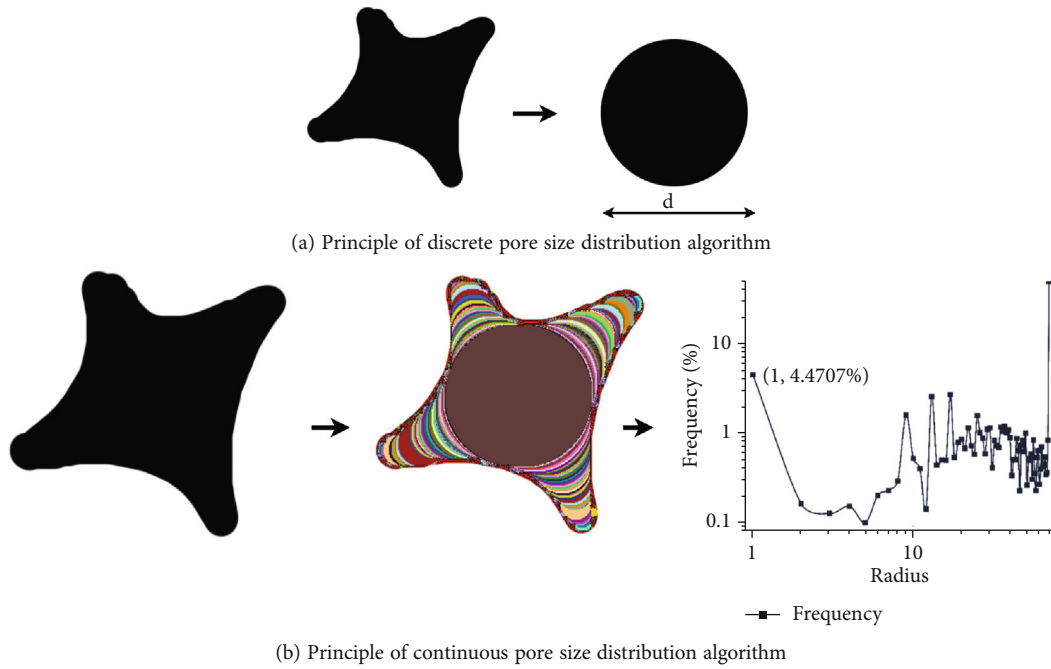
Figure 2: Comparison of calculation principles between DPSD and CPSD with the same pore structure.
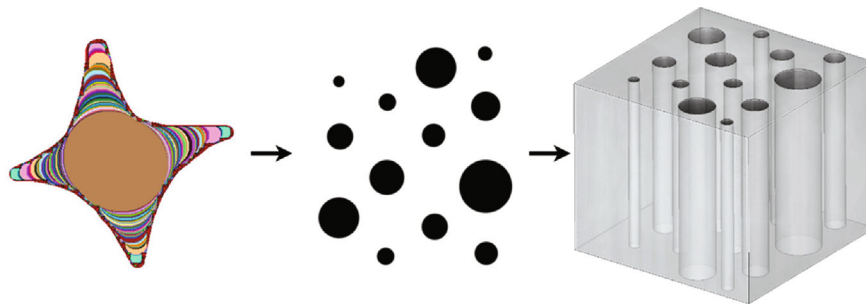
Figure 3: Capillary bundle model of porous media.
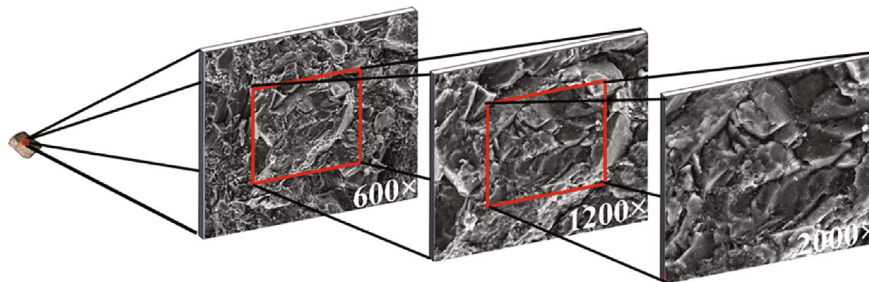
Figure 4: SEM images of different scales of a sandstone sample.
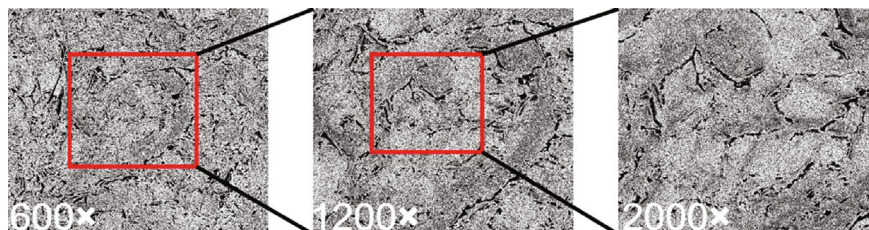
Figure 5: SEM images after preprocessing.
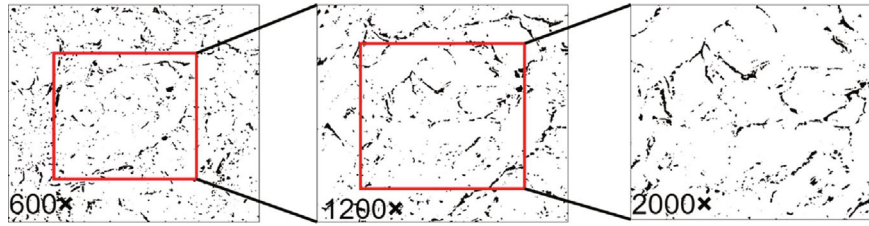
FIGURE 6: SEM images after segmentation.
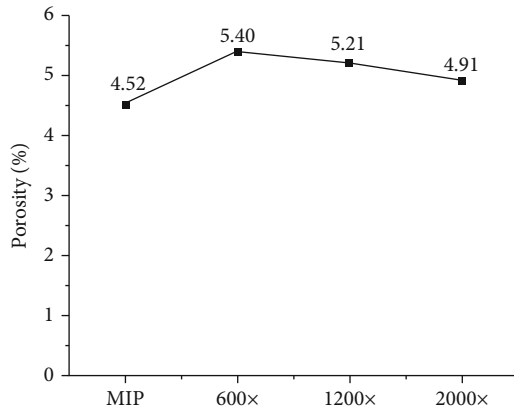
FIGURE 7: Porosity calculation results based on digital images and MIP.

can be better identified and distinguished in the preprocessed image.

The segmentation threshold is the most important way to segment a pore structure from the digital image. The threshold determination methods suitable for geomaterials are mainly divided into threshold algorithm determination and artificial selection. Different algorithms have a significant impact on threshold determination and subsequent segmentation results. Therefore, a detailed comparative analysis is required to reach a more appropriate threshold value before determining the threshold value. In particular, the thresholds of digital images with different magnifications are 21, 23, and 28, respectively. After binary segmentation [2, 3], the binary image is shown in Figure 6, where we can see that the pore structure can be easily virtually identified.

3.2. Pore Structure Characteristics of Images with Different Scales

3.2.1. Porosity Calculation.
According to the threshold segmentation results in the previous section, combined with Equation (1), the porosity of images with different magnifications is shown in Figure 7. Compared with the MIP result, it can be seen that the extraction results of apparent porosity are relatively close to the MIP result, especially when the magnification is 2000 times. According to Figure 7, it can be seen that the porosity extracted from the SEM digital image of sandstone is relatively reliable, although there are some differences.

3.2.2. Pore Size Distribution Calculation.
This work determines the distribution of pore sizes in a microscopic image at different magnifications based on CPSD and DPSD techniques mentioned in Munch's research. The pore sizes measured by MIP can be found to be smaller than those based on digital images. The pixel accuracy of the 2000x image is $0.145\,\mu$m (continuous) and $0.08\,\mu$m (discrete), while the pore size range of the CPSD experiment is 0.004-$0.25\,\mu$m. The CPSD results are closer to the MIP than the CPSD results. The peak pore size for the three magnification images is $1.44\,\mu$m (30.64%), $0.72\,\mu$m (27.68%), and $0.43\,\mu$m (21.33%), respectively. Thus, most pores that can be characterized based on digital image techniques are on the micron scale. It is interesting to note that digital image-based methods can effectively characterize large pores, whereas MIP completely ignores pores of this scale. Therefore, the pore size distribution can be better represented at full scale if the two tools are combined.

Figures 8(a) and 8(b) show the calculation results based on CPSD and DPSD. Although the two calculation methods are fundamentally different, at 600 magnification, large pores account for a greater proportion of the results. On the contrary, most of the calculation results at a magnification of 2000 are small-sized pores. Apparently, as the magnification increases, the field of view of the image is reduced to a certain extent, and obtained pores are less, so the proportion of pores of different sizes change to a particular time. Comparing the pore size distribution in the same image obtained by various methods, it is found that the large-sized pores account for a more significant proportion of the DPSD calculation results based on the same image. Still, the CPSD calculation results are primarily small- and medium-sized pores. Therefore, the pore size measured by DPSD is too large.

3.3. Permeability Prediction Based on Images with Different Scales.
Based on the pore size distribution obtained in the previous work, we used the Hagen-Poiseuille method to calculate sample's permeability. The calculation results are shown in Figure 9.

The predicted permeability values were found to be decreasing as the magnification increased: the permeability calculated for the three magnification images were $2.49 \times 10^{-14}\,m^2$ (discrete $9.21 \times 10^{-14}\,m^2$), $8.14 \times 10^{-14}\,m^2$ ($4.08 \times 10^{-14}\,m^2$), and $3.94 \times 10^{-14}\,m^2$ ($2.16 \times 10^{-14}\,m^2$), respectively. According to the principle of permeability calculation, it is clear that the permeability size is closely related to the pore size distribution and porosity. In addition, it can

(a) CPSD

(b) DPSD
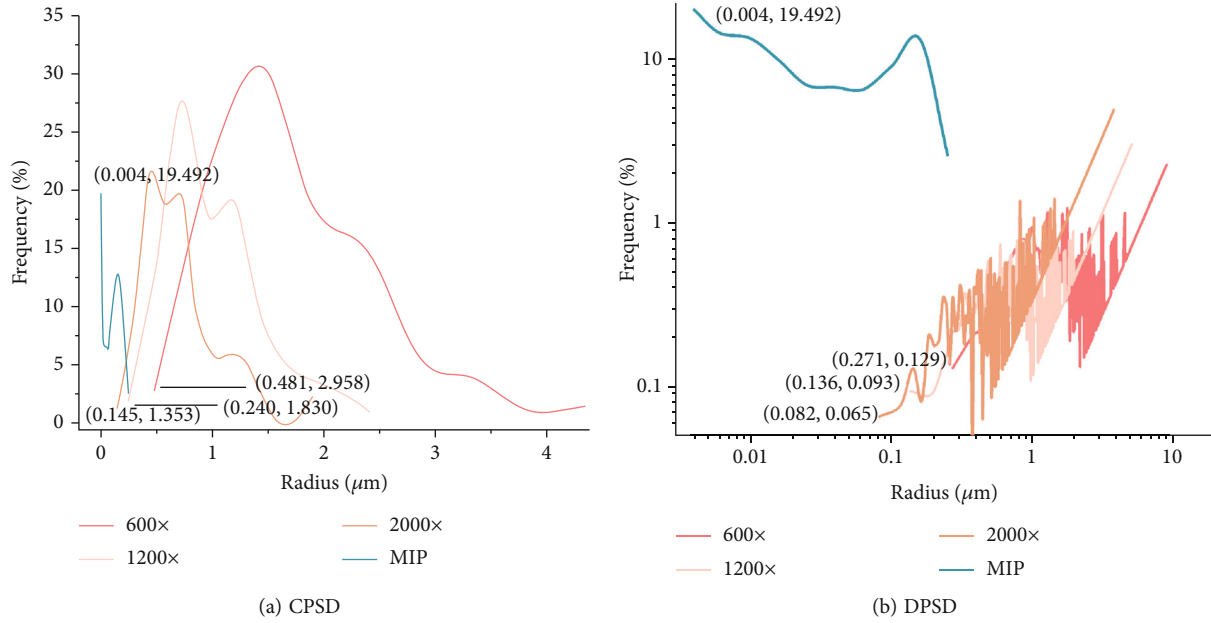
Figure 8: Calculation results of pore size distribution based on digital images and MIP.
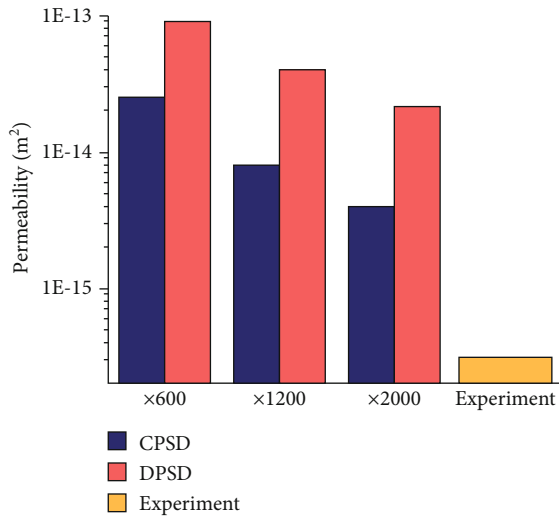
Figure 9: Permeability calculation results based on digital images and laboratory experiments.

be found that the proportion of pore area in the field of view is more significant, and most of them are large pores, with tiny pores below $0.6\,\mu$m accounting for only 3%. Hence, its permeability prediction is higher when image's magnification is 600. While the proportion is of 2000 rises to 50%. Meanwhile, according to Figure 7, the figure of porosity shows a marked decrease, and there is a similar trend in the volume of pore space per unit area of view, leading to the drop of permeability.

Compared to DPSD, the value of permeability prediction by CPSD is smaller. Although DPSD measures a slight increase in the proportion of macropores, DPSD classifies

and sizes pores based on the connectivity components of the binary image. In contrast, CPSD treats pixels that can be covered in a moving sweep of same-sized circles as same-sized pores. In order to convert the pore size and area obtained by CPSD into the permeability value of the Hagen-Poiseuille formula, we use Equation (7), assuming that the pores are circular. After that, they used the radius of the circle instead of the radius of the corresponding area circle to calculate the pore size. Specifically, as in the first step of Figure 3, the large pore sizes are primarily concentrated in the middle of the port area, where the radius of the equivalent area circle is larger than the radius of the maximum inner tangent circle. However, the CPSD pore size considers the maximum inner tangent circle radius, as detailed by Muench and Holzer [16]. It means that the same pore, compared to the DPSD, is treated by the CPSD as several smaller pore sizes. Therefore, the CPSD measurement leads to a small permeability prediction based on the Hagen-Poiseuille hypothesis about the pore geometry.

The predicted value is higher when compared to the measured value. The difference between the two is 1 to 2 orders of magnitude. Pore spaces of tiny size are difficult to perceive and measure due to image acquisition magnification limitations. In addition, the tortuosity of the pore network is not considered in the permeability calculations, nor is the complexity of the 3D pore network. These result in a large gap between the predicted permeability values based on microscopic images and equipment testing. In the future, the superposition and fusion of some images of different scales can be carried out to obtain an accurate three-dimensional model based on multiscale digital images. Furthermore, some quantitative characterization experiments based on the cross-scale 3D digital model may be closer to the experimental test results.

4. Conclusion

In this paper, a scanning electron microscope is used to obtain images of a sandstone sample for different magnifications of its microstructure. A threshold segmentation method is selected to segment the image. Then, the pore distribution of different sizes is measured based on the continuous pore size distribution and discrete pore size distribution methods. Finally, the Hagen-Poiseuille permeability calculation method is selected based on digital images to calculate sample's permeability.

The magnification of the image acquisition affects the perceived porosity and subsequent calculations. It is found that the magnification of the image has a noticeable effect on the characterization of the pore structure. As the magnification increases, the field of view of the image becomes smaller, and the perceived pores are less. The greater the magnification, the more pores, and medium pores are observed. As the proportion of macropores decreases, the predicted value of permeability decreases slightly. Pore distribution measurement methods have a noticeable impact on the pore size statistics and permeability calculations. Due to the difference in the pore size calculation principle of the two algorithms, the permeability calculated based on CPSD is lower than that of DPSD, which is larger than the experimental result. The difference is about one to two orders of magnitude. In the future, to obtain a more accurate prediction, a three-dimensional digital model should be established. There are usually two ways to get a three-dimensional digital model. One is to perform three-dimensional reconstruction through X-CT scanning. Another method is to use the simulated annealing method to reconstruct the SEM image in three dimensions. Additionally, the tortuosity of the pore network and the complexity of the 3D pore network should be considered.

Data Availability

Some or all data, models, or code generated or used during the study are available from the corresponding author by request.

Conflicts of Interest

The authors declare that they have no conflicts of interest.

Acknowledgments

References

[1] Y. Chen, S. Hu, K. Wei, R. Hu, C. Zhou, and L. Jing, "Experimental characterization and micromechanical modeling of damage-induced permeability variation in Beishan granite," *International Journal of Rock Mechanics and Mining Sciences*, vol. 71, pp. 64–76, 2014.

[2] J. F. Liu, X.-L. Cao, J. Xu, Q.-L. Yao, and H.-Y. Ni, "A new method for threshold determination of gray image," *Geomechanics and Geophysics for Geo-Energy and Geo-Resources*, vol. 6, no. 4, p. 72, 2020.

[3] J. Liu, S. Song, X. Cao et al., "Determination of full-scale pore size distribution of Gaomiaozi bentonite and its permeability prediction," *Journal of Rock Mechanics and Geotechnical Engineering*, vol. 12, no. 2, pp. 403–413, 2020.

[4] S. Tao, Z. J. Pan, S. D. Chen, and S. Tang, "Coal seam porosity and fracture heterogeneity of marcolithotypes in the Fanzhuang Block, southern Qinshui Basin, China," *Journal of Natural Gas Science and Engineering*, vol. 66, pp. 148–158, 2019.

[5] T. Hagengruber, M. Taha, E. Rougier, E. E. Knight, and J. C. Stormont, "Evolution of permeability in sandstone during confined Brazilian testing," *Rock Mechanics and Rock Engineering*, 2021.

[6] Y.-L. Kang and P.-Y. Luo, "Current status and prospect of key techniques for exploration and production of tight sandstone gas reservoirs in China," *Petroleum Exploration and Development*, vol. 34, no. 2, pp. 239–245, 2007.

[7] J. F. Liu, H. Y. Ni, H. Pu, Q. L. Yao, and X. B. Mao, "Test theory, method and device of gas permeability of porous media and the application," *Chinese Journal of Rock Mechanics and Engineering*, vol. 40, no. 1, pp. 137–146, 2021.

[8] W. M. Ye, Y. J. Cui, L. X. Qian, and B. Chen, "An experimental study of the water transfer through confined compacted GMZ bentonite," *Engineering Geology*, vol. 108, no. 3-4, pp. 169–176, 2009.

[9] T. Meng, X. Yongbing, J. Ma et al., "Evolution of permeability and microscopic pore structure of sandstone and its weakening mechanism under coupled thermo-hydro-mechanical environment subjected to real-time high temperature," *Engineering Geology*, vol. 280, article 105955, 2021.

[10] G. Zou, J. She, S. Peng, Q. Yin, H. Liu, and Y. Che, "Two-dimensional SEM image-based analysis of coal porosity and its pore structure," *International Journal of Coal Science & Technology*, vol. 7, no. 2, pp. 350–361, 2020.

[11] L. M. Anovitz, J. T. Freiburg, M. Wasbrough et al., "The effects of burial diagenesis on multiscale porosity in the St. Peter Sandstone: an imaging, small-angle, and ultra-small-angle neutron scattering analysis," *Marine and Petroleum Geology*, vol. 92, pp. 352–371, 2018.

[12] S. Tao, S. Chen, D. Tang, X. Zhao, H. Xu, and S. Li, "Material composition, pore structure and adsorption capacity of low-rank coals around the first coalification jump: a case of eastern Junggar Basin, China," *Fuel*, vol. 211, pp. 804–815, 2018.

[13] S. B. Song, J. F. Liu, H. Y. Ni, X. L. Cao, H. Pu, and B. X. Huang, "A new automatic thresholding algorithm for unimodal gray-level distribution images by using the gray gradient information," *Journal of Petroleum Science and Engineering*, vol. 190, pp. 107074–107077, 2020.

[14] R. Wirth, "Focused ion beam (FIB) combined with SEM and TEM: advanced analytical tools for studies of chemical composition, microstructure and crystal structure in geomaterials on a nanometre scale," *Chemical Geology*, vol. 261, no. 3-4, pp. 217–229, 2009.

[15] F. Zhang, Z. Jiang, W. Sun et al., "A multiscale comprehensive study on pore structure of tight sandstone reservoir realized by

nuclear magnetic resonance, high pressure mercury injection and constant-rate mercury injection penetration test," *Marine and Petroleum Geology*, vol. 109, pp. 208–222, 2019.

[16] B. Muench and L. Holzer, "Contradicting geometrical concepts in pore size analysis attained with electron microscopy and mercury intrusion," *Journal of the American Ceramic Society*, vol. 91, no. 12, pp. 4059–4067, 2008.

[17] S. P. S. R. Skalak, "The history of Poiseuille's law," *Annual Review of Fluid Mechanics*, vol. 25, no. 1, pp. 1–20, 1993.

WILEY | Hindawi

Research Article

A New Modified Model of the Streaming Potential Coupling Coefficient Depends on Structural Parameters of Soil-Rock Mixture

Xin Zhang [iD],[1] **Mingjie Zhao,**[1,2] **and Kui Wang** [iD][1]

[1]*Key Laboratory of Hydraulic and Waterway Engineering of the Ministry of Education, Chongqing Jiaotong University,
Chongqing 400074, China*
[2]*Engineering Research Center of Diagnosis Technology and Instruments of Hydro-Construction, Chongqing Jiaotong University,
Chongqing 400074, China*

Correspondence should be addressed to Kui Wang; anhuiwk@163.com

The streaming potential effect in soil-rock mixture (SRM) is related to the compactness and rock content, but there is no model to quantitatively describe this behavior. In this paper, the Kozeny–Carman (KC) equation is modified by using the compactness and rock content. Then, the modified KC equation is substituted into the equation of streaming potential coupling coefficient. A new modified model of streaming potential coupling coefficient that depends on the compactness, rock content, particle shape, and particle gradation is proposed. The reliability of the new modified model is tested by experiments, and the applicable scope of the model is obtained. The results show that when the rock content is 30%, the permeability coefficient prediction accuracy of the modified KC equation is higher in the range of 85–95% compactness. The new modified model of the streaming potential coupling coefficient represents well the control of the compactness (75–95%) on the coupling coefficient. When the compactness remains 85%, the permeability coefficient calculated by the modified KC equation in the range of 10–70% rock content is consistent with the experimental data. The influence of the rock content (10–90%) on the coupling coefficient is well described by the new modified model of the streaming potential coupling coefficient. The new modified model of streaming potential coupling coefficient is helpful to quantitatively evaluate the internal structure evolution of embankment dam by using streaming potential phenomenon.

1. Introduction

Embankment dams play an important role in flood control, irrigation, and power generation. However, the structural aging problem and service life prediction have become the primary concerns of embankment dams in long-term operation. Streaming potential effect is a kind of electrokinetic phenomenon, and the generation process is closely related to the seepage of porous media [1, 2]. It is often used for monitoring of water flow process and has the potential to obtain information on the structure of embankment dams [3]. At present, a large number of studies have been conducted on the streaming potential coupling coefficient model of pure rock and soil. SRM as filling material of embankment dam and the seepage

characteristics of SRM are mainly affected by structural factors such as rock content, compactness, particle shape, and grading curve [4–6]; that means the model of streaming potential coupling coefficient of SRM is different from that of rock and soil. Therefore, the existing streaming potential coupling coefficient model cannot describe the structural characteristics of the SRM.

The issue of the permeability coefficient model of SRM has received considerable critical attention. Xu and Wang [7] point out that the seepage problem of geotechnical media can be solved by means of the heat conduction problem in thermodynamics, and according to the four basic structural models of the thermal conductivity of composite materials (parallel, series, Maxwell-Eucken, and effective medium

theory), the relationship between the permeability coefficient of the SRM and the rock content is obtained (see Table 1). A variety of hybrid structural models are obtained by using the simple combination for the four basic structural models [8]. The series-and-parallel model is developed on the basis of the series model and the parallel model, and the phenomenon that the volume of the SRM will decrease after the fine particles are filled into the pores of the coarse particles is taken into account in this model; then, the model is verified by experiments and shows high accuracy [9]. As shown in Table 1, the relationship between permeability coefficient and rock content has been established in the permeability coefficient model of SRM, but the model does not depend on compactness, particle gradation, and particle shape, and it is difficult to incorporate these structural factors into the model.

The KC equation shows good performance in predicting the permeability of porous media. A large number of scholars have successfully applied the KC equation to the prediction of the permeability of coarse-grained soil [14–16]. Recently, some scholars have extended the scope of application to the permeability prediction of fine-grained soil by substituting the effective porosity into the KC equation [17–19]. Previous studies indicate that the KC equation has the potential to describe the permeability of SRM. The KC equation reveals the relationship among porosity, particle shape, and particle gradation [20]. However, the KC equation is not related to the compactness and rock content. This triggers us to consider establishing the relationship between the KC equation and compaction and rock content through porosity.

The streaming potential coupling coefficient has been the subject of many classic studies in the streaming potential phenomenon. Based on the capillary model, the Helmholtz-Smoluchowski (HS) equation for obtaining streaming potential coupling coefficient is proposed [21, 22]:

$$C = \frac{\varepsilon \zeta}{\mu \sigma_f}, \tag{1}$$

where C (V Pa^{-1}) is the streaming potential coupling coefficient, ε (F m^{-1}) is the dielectric permittivity, μ (Pa s) is the dynamic viscosity, σ_f (S m^{-1}) is the fluid conductivity, and ζ (V) is the zeta potential. The HS equation is valid when the surface conductivity is not considered. The HS equation is independent of the medium structure, so scholars have studied the streaming potential effect of a large number of different porous media materials by using the HS equation [23–26]. Revil et al. [27] derived the analytical solution of zeta potential and specific surface conduction based on the electrochemical reaction at the solid-liquid interface. Glover and Déry [28], Glover et al. [29], and Glover [30] obtained a new modified model by taking the analytical models of zeta potential and surface-specific conductance into the HS equation and studied the evolution of the streaming potential coupling coefficient at different concentrations and pH values. The relationship between the streaming potential coupling coefficient and temperature, concentration, pH, and microstructure (porosity, grain size, and formation factor) was established in the new modified model. As noted above, the HS equation does not

contain any medium structure information, and the new modified model is too complex and includes a large number of parameters, which is not convenient for field application.

Another model for calculating the streaming potential coupling coefficient is derived based on the effective excess charge density, which is dragged by the water flow in the porous medium. Revil and Leroy [31] established a theoretical system that used the effective excess charge density to describe the multifield coupling phenomenon in saturated porous media. The main idea was to extend the local Nernst-Planck and Stokes equations on the representative elementary volume scale to the macroscopic scale by the volume average approach. The streaming potential coupling coefficient was rewritten in the new theoretical system:

$$C = \frac{Q_v k}{\mu \sigma}, \tag{2}$$

where Q_v (C m^{-3}) is the effective excess charge density, k is the permeability (m^2), and σ (S m^{-1}) is the electrical conductivity. This theoretical system was extended to the derivation of multifield coupling governing equations in partially saturated porous media [32, 33]. The same formulation for streaming potential coupling coefficient was obtained in a saturated capillary model by effective excess charge density [34]. The effective excess charge density was used to be calculated by empirical relationship [35, 36]. Guarracino and Jougnot [37] proposed an analytical model of effective excess charge density, which makes the theoretical system more complete. The advantage of Equation (2) compared with the HS equation is that it takes into account the effects of the structure of the medium and surface conductivity [38]. In addition, the permeability is easy to establish relationship with other parameters.

In this work, we propose a new modified model directly relating streaming potential coupling coefficient to the compactness, rock content, particle shape, and particle gradation. The basic idea is to substitute the KC equation improved by compactness and rock content into Equation (2) to obtain a new modified model of streaming potential coupling coefficient. The new modified model is verified via comparison with laboratory data. Our goal in this study is to provide a model that quantitatively explains the effect of the compactness, rock content, particle shape, and particle gradation on the streaming potential coupling coefficient of SRM. This is of great significance to analyze and explain the failure mechanism and health status of embankment dams.

2. Model Development

The model is developed by the following method. We first calculate the porosity of SRM by the parameters of rock content and compactness, then substitute porosity into the KC equation to obtain the relationship between permeability and compaction, rock content, particle gradation, and particle shape, and finally take the permeability into Equation (2) to establish the new modified model of the streaming potential coupling coefficient of SRM.

TABLE 1: The model of permeability coefficient of SRM [7, 8].

Model	Reference	Equation	Notes
Parallel model		$K_{S-RM(p)} = C_S K_S + C_R K_R$	Layered parallel seepage direction
Series model		$K_{S-RM(S)} = \dfrac{K_S K_R}{C_S K_R + C_R K_S}$	Layered vertical seepage direction
Series-and-parallel model	[9]	$K_{S-RM(SP)} = \dfrac{n_{S-RM}^3 (1 - n_S C_S - n_R C_R)^2}{2(n_S C_S + n_R C_R)^3 (1 - n_{S-RM})^2} \left(\dfrac{K_S K_R}{C_S K_R + C_R K_S} + C_S K_S + C_R K_R \right)$	50% in series and parallel after mixing
M-E model	[10, 11]	$K_{S-RM(ME)} = \dfrac{K_S C_S + K_R C_R (3K_S/(2K_S + K_R))}{C_S + C_R (3K_S/(2K_S + K_R))}$	One continuous phase and one or more dispersed phases
EMT model	[12, 13]	$C_S \dfrac{K_S - K_{S-RM(EMT)}}{K_S + 2K_{S-RM(EMT)}} + C_R \dfrac{K_R - K_{S-RM(EMT)}}{K_R + 2K_{S-RM(EMT)}} = 0$	All phases being mutually dispersed

K_S is the permeability coefficient of soil; K_R is the permeability coefficient of rock. $K_{S-RM(p)}$ is the permeability coefficient of soil and broken rock connected in parallel, $K_{S-RM(S)}$ is the permeability coefficient of soil and broken rock connected in series, $K_{S-RM(SP)}$ is the permeability coefficient of soil and broken rock connected both in series and in parallel, $K_{S-RM(ME)}$ is the permeability coefficient of the Maxwell-Eucken model of SRM, $K_{S-RM(EMT)}$ is the permeability coefficient of effective medium model for SRM, C_S is the percentage of soil volume, C_R is the percentage of rock volume, n_S is the porosity of soil, n_R is the porosity of broken rocks, and n_{S-RM} is the porosity of SRM after blending.

2.1. Permeability Coefficient Model of SRM.

We assume that the rock is impermeable and water flows through the pores between fine particles. Figure 1 shows the sketch of three phases of SRM, which is composed of air, water, and solid (rock and soil). We set the volume of solid as $V_s = 1$ (m^3). The void ratio can be expressed by

$$e = \frac{V_v}{V_s} = \frac{V - V_s}{V_s} = \frac{V}{V_s} - 1, \tag{3}$$

where V (m^3) is the total volume of SRM and V_v (m^3) is the total void volume. The total volume of SRM is

$$V = V_s + V_v = 1 + eV_s = 1 + e. \tag{4}$$

The mass of the solid phase can be expressed by

$$m_s = G_s V_s \rho_w = G_s \rho_w, \tag{5}$$

where m_s (kg) is the mass of solid phase, G_s is the specific gravity, and ρ_w (kg m^{-3}) is the density of water. Based on the moisture content, it is defined as

$$m_w = w m_s = w G_s \rho_w, \tag{6}$$

where m_w (kg) is the mass of water and w is the moisture content. The total mass of the SRM m (kg) is

$$m = m_s + m_w = (1 + w) G_s \rho_w. \tag{7}$$

Based on Equation (7), we can get another expression of the total volume of SRM:

$$V = \frac{m}{\rho} = \frac{G_s \rho_w (1 + w)}{\rho} = \frac{G_s \rho_w}{\rho_d}, \tag{8}$$

where ρ_d (kg m^{-3}) is the dry density of SRM. Combining Equations (4) and (8), another expression of void ratio can be obtained:

$$e = \frac{G_s \rho_w}{\rho_d} - 1. \tag{9}$$

Using $n = e/(1 + e)$ and Equation (9), we obtain

$$n = 1 - \frac{\rho_d}{\rho_w G_s}. \tag{10}$$

According to the geotechnical test standard [39], the average specific gravity of SRM can be calculated by

$$G_s = \frac{1}{(P_1/G_{s1}) + (P_2/G_{s2})}, \tag{11}$$

where G_{s1} is the specific gravity of soil particles with a particle size greater than 5 mm, G_{s2} is the specific gravity of soil particles with a particle size less than 5 mm, P_1 is the percentage of the total mass of soil particles with a particle size greater than 5 mm, and P_2 is the percentage of the total mass of soil particles with a particle size less than 5 mm. In this study, the threshold value of soil and rock is referred to the 5 mm adopted by Zhou et al. [9], that is, more than 5 mm is rock and less than 5 mm is soil. The KC equation is developed by Kozeny [40] and Carman [41, 42] and widely used to describe hydraulic conductivity of porous media. The permeability k (m^2) is obtained by the KC equation:

$$k = \frac{1}{C_{K-C}} \frac{1}{S_0^2} \frac{n^3}{(1 - n)^2}, \tag{12}$$

where C_{K-C} is the KC empirical constant, with a value of 5,
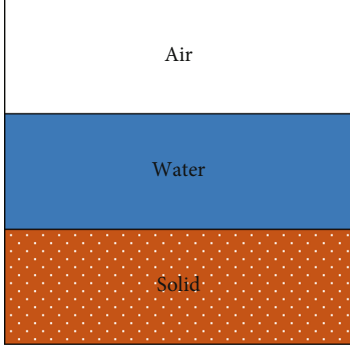
FIGURE 1: Three-phase sketch of SRM.

TABLE 2: Design of experimental scheme.

Grouping scheme	Compactness (%)	Rock content (%)
A1–A5	75, 80, 85, 90, 95	30
B1–B5	85	10, 30, 50, 70, 90

A1–A5 represent compactness 75, 80, 85, 90, and 95%. B1–B5 represent rock content 10, 30, 50, 70, and 90%. A3 and B2 are the same conditions.

and S_0 (mm^2 mm^{-3}) is the specific surface area of particles per unit volume, for uniform spherical particles, $S_0 = 6/D_{eff}$, and for the nonuniform particles, S_0 needs to be corrected:

$$ S_0 = \frac{SF}{D_{eff}}, \tag{13} $$

where SF is the shape factor [43]: rounded—6.6; medium angularity—7.5; and angular—8.4. D_{eff} (mm) is the effective particle size and can be calculated by the following equation:

$$ D_{eff} = \frac{100\%}{\sum_i \left(f_i / \left(D_{li}^{\alpha} \times D_{si}^{1-\alpha} \right) \right)}, \tag{14} $$

where f_i is the percentage of particles between the two sieves, D_{li} and D_{si} are the larger and smaller sieve sizes (mm), respectively. For well-graded grain sizes, $\alpha = 0.404$, for poorly graded grain sizes, $\alpha = 0.68$, and for gap-graded grain sizes, $\alpha = 0.9$ [44]. The permeability of the SRM can be obtained by taking Equations (10) and (11) into (12):

$$ k = \frac{1}{5} \frac{1}{S_0^2} \frac{\left[\rho_w G_{s1} G_{s2} - \rho_d (p_1 G_{s2} + p_2 G_{s1}) \right]^3}{\rho_w G_{s1} G_{s2} \rho_d^2 (p_1 G_{s2} + p_2 G_{s1})^2}. \tag{15} $$

Based on the relationship between permeability and permeability coefficient, $K = \rho_w g k / \mu$, the equation for calculating permeability coefficient of SRM can be obtained:

$$ K = \frac{\rho_w g}{5\mu} \frac{1}{S_0^2} \frac{\left[\rho_w G_{s1} G_{s2} - \rho_d (p_1 G_{s2} + p_2 G_{s1}) \right]^3}{\rho_w G_{s1} G_{s2} \rho_d^2 (p_1 G_{s2} + p_2 G_{s1})^2}. \tag{16} $$

2.2. Streaming Potential Coupling Coefficient Model of SRM.

Equation (2) has proved to be applicable to porous media with arbitrary structure and multicomponent electrolyte [45, 46]. Therefore, Equation (2) can also be used to calculate the streaming potential coupling coefficient of the SRM. We take Equation (15) into (2) to obtain the modified model of streaming potential coupling coefficient of SRM:

$$ C = \frac{1}{5} \frac{Q_v}{\eta \sigma} \frac{1}{S_0^2} \frac{\left[\rho_w G_{s1} G_{s2} - \rho_d (p_1 G_{s2} + p_2 G_{s1}) \right]^3}{\rho_w G_{s1} G_{s2} \rho_d^2 (p_1 G_{s2} + p_2 G_{s1})^2}. \tag{17} $$

The rock content (the ratio of the mass of the rock to the mass of the SRM is defined as the rock content) and dry density (compactness is equal to the ratio of dry density to maximum dry density) are substituted into the streaming potential coupling coefficient model. It has previously been observed that the effective excess charge density obviously depends on the permeability [47]. According to the empirical relationship, the effective excess charge density can be calculated [35, 36]:

$$ \log_{10} Q_v = A_1 + A_2 \log_{10}(k), \tag{18} $$

where A_1 and A_2 are constant values. We will fit these two constants by experimental data. This empirical relationship is widely used to capture water flow information and geometrical properties of media [48–50].

3. Experimental Methods

The experimental scheme is shown in Table 2. We use the self-designed device to measure the potential and water pressure when the brine flow through the SRM. The quality of material is strictly controlled, and the same test procedures are adopted. The specific experimental methodology is described by Zhang et al. [51].

The particle size distribution of SRM material (weathered broken argillaceous rock) is shown in Table 3. The SRM with $C_u \geq 5$ and $C_c = 1 - 3$ is thought to be well graded, if not, the SRM is regarded as poorly graded [52]. So we consider gradations 1 and 5 to be poorly graded, while gradations 2, 3, and 4 are well graded (see Table 4). The particle shape is angular. The X-ray diffraction tests show that the mineralogy of argillaceous rock is composed of quartz (48.8%), illite (22%), albite (17.9%), kaolinite (2.7%), chlorite (5.5%), calcite (1.8%), and hematite (1.2%). The test results indicate that the SRM is silty soil.

Figure 2 shows the new apparatus. The device is mainly composed of a water tank, PVC pipe, and acquisition system. The SRM is compacted in the middle of the water tank. The foam board is placed between the SRM and the upper cover to prevent the water flow. Arrangement of pressure sensors, Ag/AgCl nonpolarized electrodes, and moisture content meters during compaction. The pressure and potential are measured by DH3821 and DM3058, respectively. The saturation of SRM material is monitored by moisture content meters. All experiments are performed at NaCl solution of $0.01 \, mol \, L^{-1}$.

TABLE 3: Particle size distribution of different gradations.

Particle size (mm)	Gradation 1 (%)	Gradation 2 (%)	Gradation 3 (%)	Gradation 4 (%)	Gradation 5 (%)
<0.075	4	3	2	3	1
<0.25	25	12	10	6	2
<0.5	40	21	16	8	3
<1	55	32	25	10	4
<2	70	48	35	15	5
<5	90	70	50	30	10
<10	98	88	66	58	40
<20	100	100	100	100	100

The particle gradation of A1–A5 is 2. The particle gradation of B1–B5 is 1, 2, 3, 4, and 5, respectively. The minimum sieve size is 0.045 mm.

TABLE 4: Gradation characteristics.

Gradation	d_{60} (mm)	d_{30} (mm)	d_{10} (mm)	Nonuniform coefficient[a]C_u	Curvature coefficient[b]C_c
1	1.3	0.31	0.11	11.82	0.67
2	3.3	0.9	0.2	16.5	1.23
3	8.1	1.5	0.25	32.4	1.11
4	10.5	5	1	10.5	2.38
5	14	8.5	5	2.8	1.03

The d_{10}, d_{30}, and d_{60} denote the particle sizes of 10%, 30%, and 60% of the total mass on the particle size distribution curve, respectively. [a]Calculated from $C_u = d_{60}/d_{10}$ [51]. [b]Calculated from $C_c = d_{30} \cdot d_{30}/d_{10} \cdot d_{60}$ [51].

After the solution on both sides of the water tank is balanced, the static hydraulic head difference H_1 and potential U_1 are measured. The PVC pipe provides hydraulic pressure to the water tank, and the potential U_2 and hydraulic head difference H_2 are measured until the flow state is stable. The streaming potential coupling coefficient is equal to the slope of the fitting line between streaming potential $U_2 - U_1$ and hydraulic head difference $H_2 - H_1$ (see Figure 3(a)). The permeability coefficient is obtained by recording the volume of the solution per unit time. The effective excess charge density is determined by Equation (2). The relationship between effective excess charge density and permeability can be obtained by fitting the experimental data (see Figure 3(b)). We use a two-electrode device to measure the conductivity of SRM. The material properties of SRM are shown in Tables 5 and 6.

4. Results

As shown in Figure 4(a), when the compactness is 75% and 80%, there is a big difference between the predicted values of the modified KC equation and the measured values. When the compactness is greater than 80%, the calculated values of the modified KC equation are close to the measured values. Figure 4(b) shows that there is a big difference between the predicted value and the measured value when the rock content reaches 90%. The predicted value of the modified KC equation is consistent with the measured value in the range of 70% to 10% rock content.

Figure 3(b) shows that the effective excess charge density depends on the permeability of the SRM, consistent with

previous studies [47]. We obtain the coefficient $A_1 = -13.362$ and $A_2 = -1.1197$ in Equation (18), respectively. Some authors have fitted Equation (18), Jardani et al. [35] and Revil [38] obtained $A_1 = -9.23$ and $A_2 = -0.82$, and Bolève et al. [36] suggested $A_1 = -9.9956$ and $A_2 = -0.9022$. We obtain the coefficients are smaller than the fitting results of other authors.

The permeability obtained by the modified KC equation is substituted into Equation (2) to calculate the streaming potential coupling coefficient. Although there is a great difference between measured permeability and predicted permeability at 75–80% compactness and 90% rock content, but the predicted streaming potential coupling coefficient of the new modified model is consistent with the experimental data at different compactness (see Figure 5(a)). Similarly, this new modified model represents the experimental data very well when the rock content varies between 10% and 90% (see Figure 5(b)). Moreover, we use Guarracino and Jougnot's [37] model to calculate the streaming potential coupling coefficient, and the results show that this model reproduces the experimental data very well, but the new modified model is more accurate than Guarracino and Jougnot's [37] model in this study.

5. Discussion

5.1. The Modified KC Equation. At compactness 75% and 80%, the predicted permeability coefficient of the modified KC equation shows poor consistency with the experimental data. The reason for this phenomenon is that the low compactness leads to insufficient bonding of the SRM materials, and the fine particles are loose. When the hydraulic gradient is large, the fine particles are easily carried away, and the flow section becomes larger. Therefore, the measured permeability coefficient is larger than the predicted permeability coefficient. When the compactness is more than 80%, the prediction accuracy of the modified KC equation is higher due to the slight impact on the flow state at high compactness.

In the SRM with 90% rock content, the pore size and the seepage velocity are large, and the fluid is in the state of inertial laminar flow at high water head, so the measured permeability coefficient (apparent permeability coefficient) is smaller than the predicted permeability coefficient [24]. When the rock content is reduced from 70% to 10%, the measured permeability coefficient is closer to the predicted permeability coefficient.

(a)

(b)
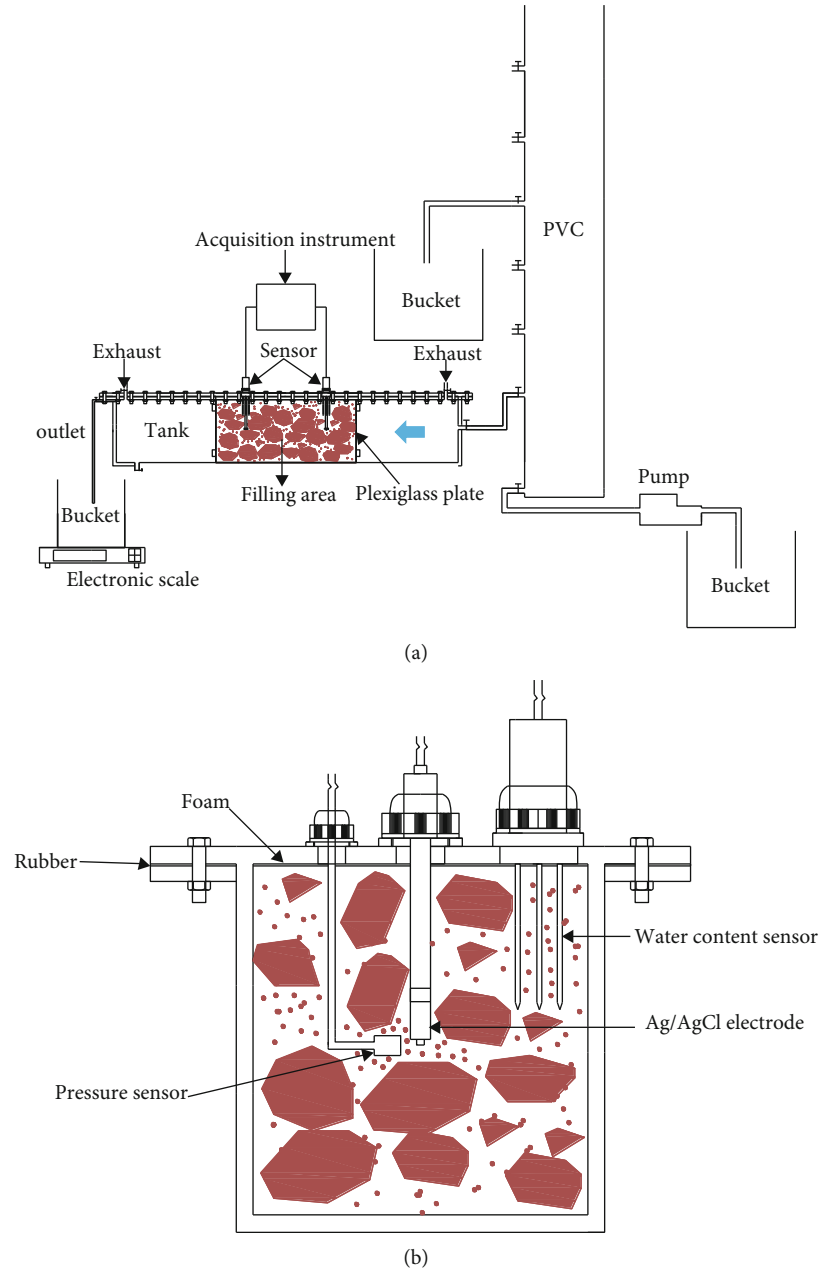
Figure 2: Sketch of the experimental apparatus. (a) The apparatus consists of a tank, PVC pipe, and data acquisition system. The blue arrow represents the direction of the water flow. (b) Cross section through the sensor.

This result can be interpreted by the macropores developed between the coarse particles are filled by the fine particles and hence the soil particles are relatively compact and the seepage velocity in the pores is low.

Compactness and rock content are the key parameters in quality management of embankment dam construction. In the project, the compactness is controlled above 90%, and the reference range of rock content is 25–75% [9]. The modified KC equation shows high prediction accuracy of permeability coefficient when the compactness varies between 85% and 95% (30% rock content) and the rock content varies between 10% and 70% (85% compactness). Therefore, the modified KC equation can be considered valid in most projects. The per-

meability coefficient of sandstone–mudstone mixture with a particle size ranges from 60 mm to 0.075 mm is successfully predicted by the KC equation [53]; it appears that the modified KC equation will have a wider application range.

At present, the height of some embankment dams has exceeded 100 meters, and the SRM materials are in complex occurrence conditions of high stress and high water level. It is necessary to establish the relationship between permeability and more parameters, such as effective stress and buried depth, so as to expand the application scope of the model. This means that the physical model for predicting permeability of SRM may become more complex. In recent years, the advantages of artificial intelligence technology in multisource
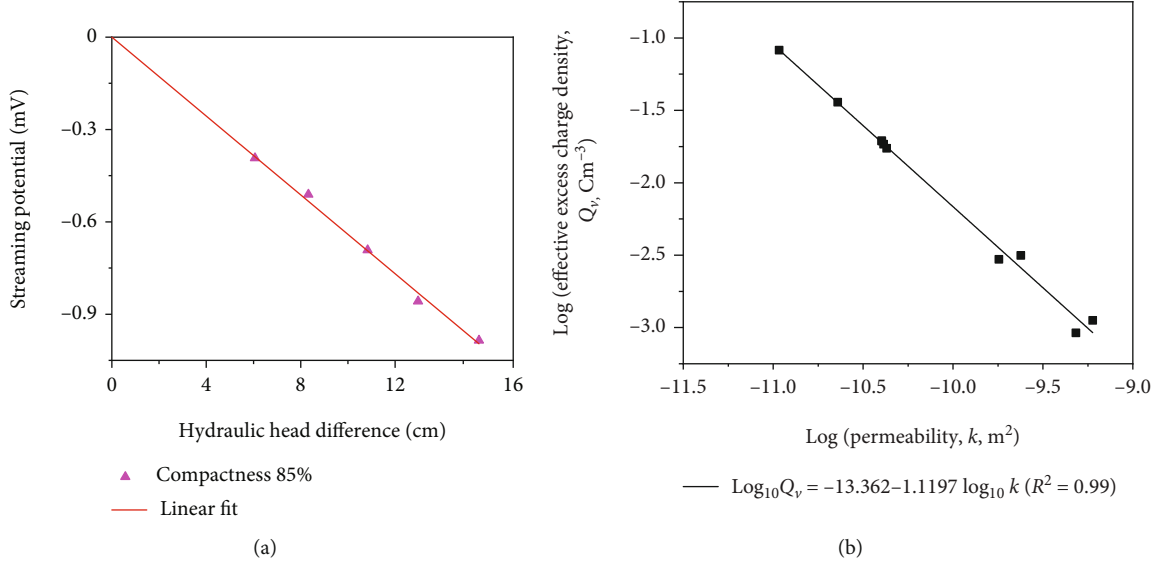
FIGURE 3: The streaming potential coupling coefficient and the effective excess charge density. (a) The streaming potential against hydraulic head difference at 85% compactness and 30% rock content. The streaming potential coupling coefficient is the slope of the regression line between streaming potential and hydraulic head difference. (b) The effective excess charge density versus permeability. The effective excess charge density is calculated by Equation (2).

TABLE 5: Properties of SRM with different compactness.

Properties	A1	A2	A3	A4	A5
Dry density ρ_d (g cm^{-3})	1.635	1.744	1.835	1.962	2.071
Effective particle size[a]D_{eff} (mm)	0.513	0.513	0.513	0.513	0.513
Specific surface area[b]S_0 (mm^2 mm^{-3})	16.361	16.361	16.361	16.361	16.361
Porosity[c]n	0.384	0.343	0.302	0.261	0.220
Conductivity σ (S m^{-1}) $\times 10^{-3}$	1.42	1.36	1.33	1.25	1.20

[a]The D_{eff} is determined from Equation (14). [b]The S_0 is determined from Equation (13). [c]The n is determined from Equation (10).

TABLE 6: Properties of SRM with different rock content.

Properties	B1	B2	B3	B4	B5
Dry density ρ_d (g cm^{-3})	1.802	1.853	1.870	1.845	1.870
Effective particle size[a]D_{eff} (mm)	0.387	0.513	0.663	0.961	2.875
Specific surface area[b]S_0 (mm^2 mm^{-3})	21.698	16.361	12.676	8.739	2.922
Porosity[c]n	0.321	0.302	0.297	0.308	0.301
Conductivity σ (S m^{-1}) $\times 10^{-3}$	1.35	1.33	1.36	1.45	1.48

[a]The D_{eff} is determined from Equation (14). [b]The S_0 is determined from Equation (13). [c]The n is determined from Equation (10).

information fusion and prediction have been rapidly developed, such as predicting the change of coal seam permeability during CO_2 geological sequestration [54] and predicting the permeability of tight carbonate rocks [55]. This provides a new idea for using multiparameters to predict the permeability of SRM.

The modified KC equation as a function of compactness, rock content, particle shape, and grading curve helps us to understand the seepage mechanism of SRM in dam projects and provides a scientific basis for the design and selection of materials for embankment dams.

5.2. The New Modified Model of the Streaming Potential Coupling Coefficient. The two coefficients are reported by other authors larger than ours. This is because the effective excess charge density and permeability are related to the specific surface area of porous media. The content of coarse particles in the SRM is high and the particle size is large, so

(a)   (b)
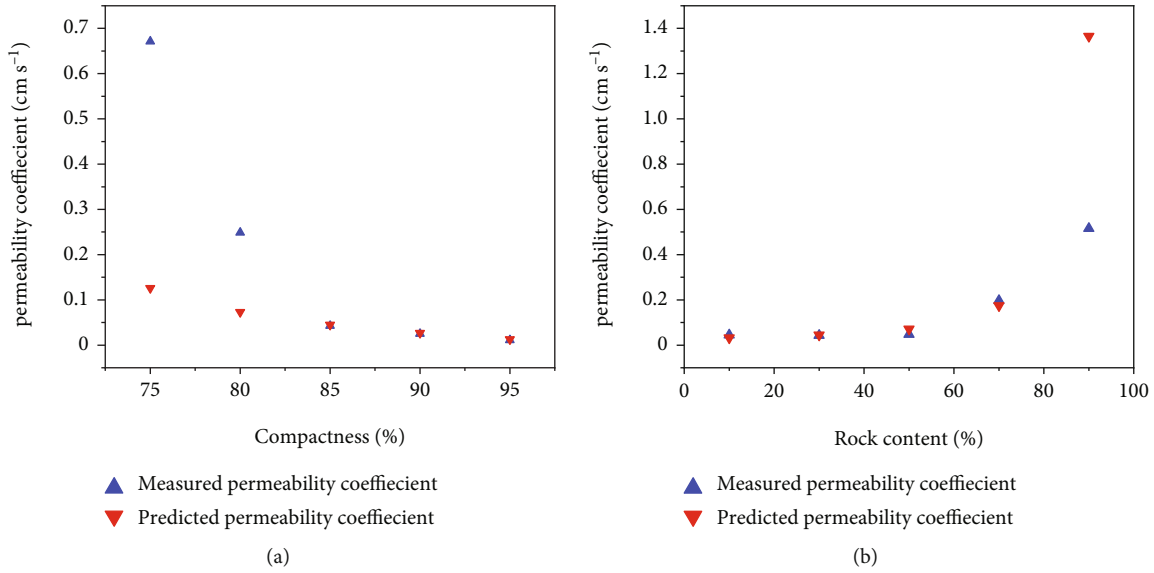
FIGURE 4: The permeability coefficient with different compactness and different rock content. (a) Predicted and measured values of permeability coefficient with different compactness. (b) Predicted and measured values of permeability coefficient with different rock content.

(a)   (b)
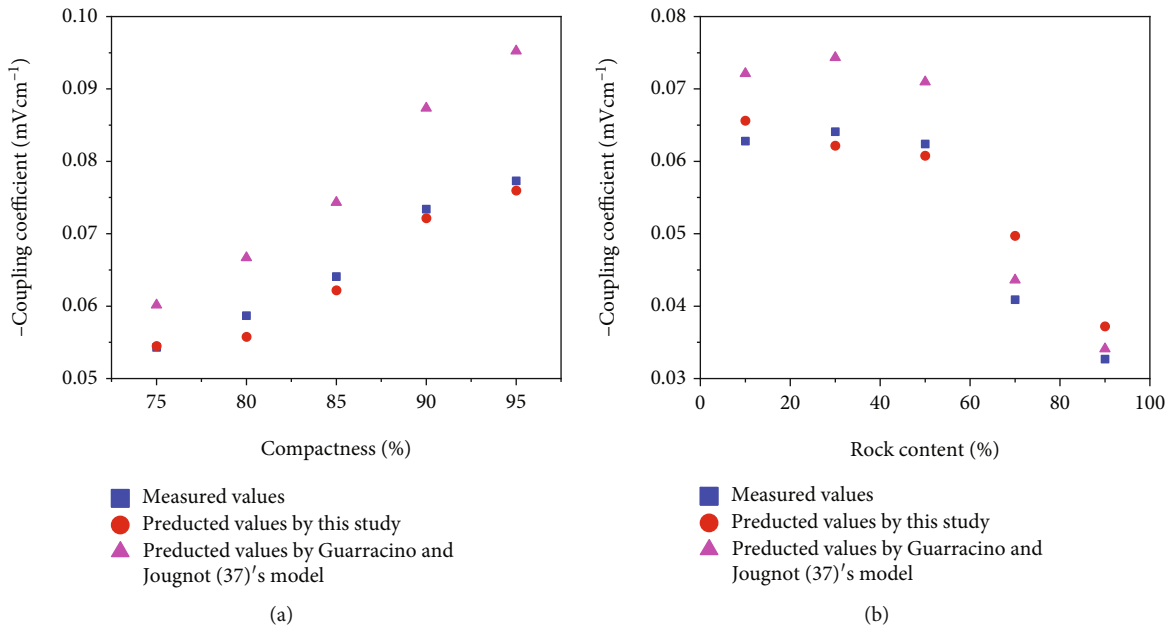
FIGURE 5: The streaming potential coupling coefficient with different compactness and different rock content. (a) Predicted and measured values of the streaming potential coupling coefficient with different compactness. (b) Predicted and measured values of the streaming potential coupling coefficient with different rock content.

the specific surface area is small. This means that the effective excess charge density dragged by the water flow in the pores decreases under the same permeability.

When the compactness is 75–80% and the rock content is 90%, the predicted permeability coefficient is not in good agreement with the measured value, but the predicted streaming potential coupling coefficient is close to the measured value. We ascribe this phenomenon to the relationship

between effective excess charge density and permeability. When the permeability of SRM increases, and the effective excess charge density decreases. It appears that this relationship can improve the difference caused by permeability.

The new modified model shows higher accuracy than Guarracino and Jougnot's [37] model. This result can be explained by the empirical relationship between effective excess charge density and permeability, which is proposed

for specific research objects. The model proposed by Guarracino and Jougnot [37] includes the porosity, permeability, tortuosity, concentration, Debye length, and zeta potential, but more influences are considered in the empirical relationship, such as complex chemical reactions on the solid-liquid surface and particle deformation. Nevertheless, Guarracino and Jougnot's [37] model still represents the experimental data very well at the different compactness and different rock content.

It should be noted that the zeta potential would not depend on the compactness and rock content of SRM as long as rock mineralogy and chemical composition of water do not change. According to the HS equation, the streaming potential coupling coefficient remains a constant. The change of flow regime leads to the deviation of streaming potential from the HS equation [56]. Therefore, the streaming potential coupling coefficient decrease at low compactness and high rock content.

The relationships between streaming potential coupling coefficient, compactness, rock content, particle shape, and grading curve reported in this study are important for monitoring the structure of embankment dam. At present, the new modified model is rarely used in embankment dams, but Guarracino and Jougnot's [37] model has verified the reliability of the new modified model, which lays the foundation for field application. In addition, Bolève et al. [24] and Soueid Ahmed et al. [57] have successfully implemented the numerical simulation of the response of the potential when the leakage path structure changes, which further promotes the application of the new modified model.

6. Conclusion

In this paper, the compactness, rock content, particle shape, and grading curve of the SRM are substituted into the formulation of the streaming potential coupling coefficient by the KC equation, and a new modified model of the streaming potential coupling coefficient depends on structural parameters of SRM is proposed. The modified KC equation and the new modified model of the streaming potential coupling coefficient are verified by the experiment. The main conclusions are as follows:

(1) Based on the relationship between the porosity, compactness, and rock content of SRM, we obtain the modified KC equation. The modified KC equation fits well with the experimental data and shows high prediction accuracy when the rock content is 30% and compactness ranges from 85% to 95%, and the compactness is 85% and the rock content ranges from 10% to 70%.

(2) By taking the modified KC equation into the streaming potential coupling coefficient model, the quantitative relationship between the structural parameters of the SRM and the streaming potential coupling coefficient is established. For the rock content remains 30% and compactness varies from 75% to 95%, and the compactness is 85% and the rock content varies from 10% to 90%, the new modified model is in good agreement with the experimental data.

(3) The modified model of streaming potential coupling coefficient provides a method for studying the mesostructure of the SRM by using the streaming potential effect. It is helpful to reveal and estimate the structural aging mechanism and service life of embankment dams.

Data Availability

The data used to support the findings of this study are available from the corresponding author upon request.

Conflicts of Interest

The authors declare that they have no conflicts of interest.

Acknowledgments

References

[1] P. W. J. Glover and M. D. Jackson, "Borehole electrokinetics," *The Leading Edge*, vol. 29, no. 6, pp. 724–728, 2010.

[2] J. Vinogradov, M. D. Jackson, and M. Chamerois, "Zeta potential in sandpacks: effect of temperature, electrolyte pH, ionic strength and divalent cations," *Colloids and Surfaces A: Physicochemical and Engineering Aspects*, vol. 553, pp. 259–271, 2018.

[3] A. Soueid Ahmed, A. Revil, A. Bolève et al., "Determination of the permeability of seepage flow paths in dams from self-potential measurements," *Engineering Geology*, vol. 268, article 105514, 2020.

[4] W. Xu, S. Wang, H. Zhang, and Z. Zhang, "Discrete element modelling of a soil-rock mixture used in an embankment dam," *International Journal of Rock Mechanics and Mining Sciences*, vol. 86, pp. 141–156, 2016.

[5] N. Zhao, Y. Wang, B. Meng, and N. Luo, "Numerical simulation on the seepage properties of soil-rock mixture," *Advances in Materials Science and Engineering*, vol. 2018, Article ID 1859319, 10 pages, 2018.

[6] W. Wu, Y. Yang, and H. Zheng, "Hydro-mechanical simulation of the saturated and semi-saturated porous soil-rock mixtures using the numerical manifold method," *Computer Methods in Applied Mechanics and Engineering*, vol. 370, article 113238, 2020.

[7] W. Xu and Y. Wang, "Meso-structural permeability of S-RM based on numerical test," *Chinese Journal of Geotechnical Engineering*, vol. 32, no. 4, pp. 542–550, 2010.

[8] J. Wang, J. K. Carson, M. F. North, and D. J. Cleland, "A new structural model of effective thermal conductivity for heterogeneous materials with co-continuous phases," *International*

Journal of Heat and Mass Transfer, vol. 51, no. 9–10, pp. 2389–2397, 2008.

[9] Z. Zhou, H. Yang, X. Wang, and B. Liu, "Model development and experimental verification for permeability coefficient of soil–rock mixture," *International Journal of Geomechan-ics*, vol. 17, no. 4, article 04016106, 2017.

[10] J. C. Maxwell, *A Treatise on Electricity and Magnetism*, Dover Publications Inc., New York, third ed. edition, 1954.

[11] A. Eucken, "Allgemeine Gesetzmäßigkeiten für das Wärme-leitvermögen verschiedener Stoffarten und Aggregatzustände," *Forschung Gabiete Ingenieur*, vol. 11, no. 1, pp. 6–20, 1940.

[12] C. J. F. Böttcher, *Theory of Electric Polarization*, Elsevier, Houston, 1952.

[13] R. Landauer, "The electrical resistance of binary metallic mix-tures," *Journal of Applied Physics*, vol. 23, no. 7, pp. 779–784, 1952.

[14] T. T. Nguyen and B. Indraratna, "The role of particle shape on hydraulic conductivity of granular soils captured through Kozeny–Carman approach," *Géotechnique Letters*, vol. 10, no. 3, pp. 398–403, 2020.

[15] J. Song, X. Chen, C. Cheng, D. Wang, S. Lackey, and Z. Xu, "Feasibility of grain-size analysis methods for determination of vertical hydraulic conductivity of streambeds," *Journal of Hydrology*, vol. 375, no. 3–4, pp. 428–437, 2009.

[16] K. Urumović and K. Urumović Sr., "The referential grain size and effective porosity in the Kozeny–Carman model," *Hydrol-ogy and Earth System Sciences*, vol. 20, no. 5, pp. 1669–1680, 2016.

[17] B. Hong, X. Li, L. Wang, L. Li, Q. Xue, and J. Meng, "Using the effective void ratio and specific surface area in the Kozeny–Carman equation to predict the hydraulic conductivity of loess," *Water*, vol. 12, no. 1, p. 24, 2020.

[18] X. Ren, Y. Zhao, Q. Deng, J. Kang, D. Li, and D. Wang, "A rela-tion of hydraulic conductivity – void ratio for soils based on Kozeny- Carman equation," *Engineering Geology*, vol. 213, pp. 89–97, 2016.

[19] F. Dang, H. Liu, X. Wang, H. Xue, and Z. Ma, "Empirical for-mulas of permeability of clay based on effective pore ratio," *Chinese Journal of Rock Mechanics and Engineering*, vol. 34, no. 9, pp. 1909–1917, 2015.

[20] W. D. Carrier III, "Goodbye, Hazen; hello, Kozeny-Carman," *Journal of Geotechnical and Geoenvironmental Engineering*, vol. 129, no. 11, pp. 1054–1056, 2003.

[21] H. V. Helmholtz, "Studien über electrische Grenzschichten," *Annalen der Physik*, vol. 243, no. 7, pp. 337–382, 1879.

[22] M. von Smoluchowski, "Contribution to the theory of electro-osmosis and related phenomena," *Bulletin International de l'Academie des Sciences de Cracovie*, vol. 3, pp. 184–199, 1903.

[23] E. Walker and P. W. J. Glover, "Measurements of the relation-ship between microstructure, pH, and the streaming and zeta potentials of sandstones," *Transport in Porous Media*, vol. 121, no. 1, pp. 183–206, 2018.

[24] A. Bolève, A. Crespy, A. Revil, F. Janod, and J. L. Mattiuzzo, "Streaming potentials of granular media: influence of the Dukhin and Reynolds numbers," *Journal of Geophysical Research: Solid Earth*, vol. 112, no. B8, 2007.

[25] E. Walker, P. W. J. Glover, and J. Ruel, "A transient method for measuring the DC streaming potential coefficient of porous and fractured rocks," *Journal of Geophysical Research: Solid Earth*, vol. 119, no. 2, pp. 957–970, 2014.

[26] A. Alroudhan, J. Vinogradov, and M. D. Jackson, "Zeta poten-tial of intact natural limestone: impact of potential-determining ions Ca, Mg and SO$_4$," *Colloids and Surfaces A: Physicochemical and Engineering Aspects*, vol. 493, pp. 83–98, 2016.

[27] A. Revil, P. A. Pezard, and P. W. J. Glover, "Streaming poten-tial in porous media: 1. Theory of the zeta potential," *Journal of Geophysical Research: Solid Earth*, vol. 104, no. B9, pp. 20021–20031, 1999.

[28] P. W. J. Glover and N. Déry, "Streaming potential coupling coefficient of quartz glass bead packs: dependence on grain diameter, pore size, and pore throat radius," *Geophysics*, vol. 75, no. 6, pp. F225–F241, 2010.

[29] P. W. J. Glover, E. Walker, and M. D. Jackson, "Streaming-potential coefficient of reservoir rock: a theoretical model," *Geophysics*, vol. 77, no. 2, pp. D17–D43, 2012.

[30] P. W. J. Glover, "Modelling pH-dependent and microstructure-dependent streaming potential coefficient and zeta potential of porous sandstones," *Transport in Porous Media*, vol. 124, no. 1, pp. 31–56, 2018.

[31] A. Revil and P. Leroy, "Constitutive equations for ionic trans-port in porous shales," *Journal of Geophysical Research: Solid Earth*, vol. 109, no. B3, 2004.

[32] A. Revil, N. Linde, A. Cerepi, S. Matthäi, S. Finsterle, and S. Finsterle, "Electrokinetic coupling in unsaturated porous media," *Journal of Colloid and Interface Science*, vol. 313, no. 1, pp. 315–327, 2007.

[33] N. Linde, D. Jougnot, A. Revil et al., "Streaming current gener-ation in two-phase flow conditions," *Geophysical Research Let-ters*, vol. 34, no. 3, 2007.

[34] A. Revil, W. F. Woodruff, and N. Lu, "Constitutive equations for coupled flows in clay materials," *Water Resources Research*, vol. 47, no. 5, 2011.

[35] A. Jardani, A. Revil, A. Bolève et al., "Tomography of the Darcy velocity from self-potential measurements," *Geophysical Research Letters*, vol. 34, no. 24, 2007.

[36] A. Bolève, J. Vandemeulebrouck, and J. Grangeon, "Dyke leak-age localization and hydraulic permeability estimation through self- potential and hydro-acoustic measurements: self-potential 'abacus' diagram for hydraulic permeability esti-mation and uncertainty computation," *Journal of Applied Geo-physics*, vol. 86, pp. 17–28, 2012.

[37] L. Guarracino and D. Jougnot, "A physically based analytical model to describe effective excess charge for streaming poten-tial generation in water saturated porous media," *Journal of Geophysical Research: Solid Earth*, vol. 123, no. 1, pp. 52–65, 2018.

[38] A. Revil, "Transport of water and ions in partially water-saturated porous media. Part 1. Constitutive equations," *Advances in Water Resources*, vol. 103, pp. 119–138, 2017.

[39] Ministry of Water Resources of the People's Republic of China, *Standard for Soil Test Method*, China Hydroelectricity Press, Beijing, 1999.

[40] J. Kozeny, "Uber kapillare leitung der wasser in boden," *Royal Academy of Science, Vienna, Proceedings Class I*, vol. 136, pp. 271–306, 1927.

[41] P. C. Carman, "Permeability of saturated sands, soils and clays," *The Journal of Agricultural Science*, vol. 29, no. 2, pp. 262–273, 1939.

[42] P. C. Carman, *Flow of Gas through Porous Media*, Butter-worths Scientific Publications, London, 1956.

[43] A. G. Loudon, "The computation of permeability from simple soil tests," *Geotechnique*, vol. 3, no. 4, pp. 165–183, 1952.

[44] W. Zheng and D. D. Tannant, "Improved estimate of the effective diameter for use in the Kozeny–Carman equation for permeability prediction," *Géotechnique Letters*, vol. 7, no. 1, pp. 1–5, 2017.

[45] A. Revil and N. Linde, "Chemico-electromechanical coupling in microporous media," *Journal of Colloid and Interface Science*, vol. 302, no. 2, pp. 682–694, 2006.

[46] A. Revil, P. Leroy, and K. Titov, "Characterization of transport properties of argillaceous sediments: application to the Callovo-Oxfordian argillite," *Journal of Geophysical Research: Solid Earth*, vol. 110, no. B6, 2005.

[47] D. Jougnot, A. Mendieta, P. Leroy, and A. Maineult, "Exploring the effect of the pore size distribution on the streaming potential generation in saturated porous media, insight from pore network simulations," *Journal of Geophysical Research: Solid Earth*, vol. 124, no. 6, pp. 5315–5335, 2019.

[48] A. Bolève, F. Janod, A. Revil, A. Lafon, and J. J. Fry, "Localization and quantification of leakages in dams using time-lapse self- potential measurements associated with salt tracer injection," *Journal of Hydrology*, vol. 403, no. 3–4, pp. 242–252, 2011.

[49] J. Bolèkve, A. Revil, F. Janod, J. L. Mattiuzzo, and J. J. Fry, "Preferential fluid flow pathways in embankment dams imaged by self-potential tomography," *Near Surface Geophysics*, vol. 7, no. 5–6, pp. 447–462, 2009.

[50] A. Soueid Ahmed, A. Jardani, A. Revil, and J. P. Dupont, "Hydraulic conductivity field characterization from the joint inversion of hydraulic heads and self-potential data," *Water Resources Research*, vol. 50, no. 4, pp. 3502–3522, 2014.

[51] X. Zhang, M. Zhao, and K. Wang, "Experimental study on the streaming potential phenomenon response to compactness and salinity in soil–rock mixture," *Water*, vol. 13, no. 15, p. 2071, 2021.

[52] X. R. Liu, Y. L. Tu, P. Wang, Z. L. Zhong, W. B. Tang, and L. B. Du, "Particle breakage of soil-rock aggregate based on large-scale direct shear tests," *Chinese Journal of Geotechnical Engineering*, vol. 39, no. 8, pp. 1425–1434, 2017.

[53] Z. Qiu and J. Wang, "Experimental study on the anisotropic hydraulic conductivity of a sandstone–mudstone particle mixture," *Journal of Hydrologic Engineering*, vol. 20, no. 11, article 04015029, p. 9, 2015.

[54] H. Yan, J. Zhang, S. S. Rahman, N. Zhou, and Y. Suo, "Predicting permeability changes with injecting CO_2 in coal seams during CO_2 geological sequestration: a comparative study among six SVM-based hybrid models," *Science of the Total Environment*, vol. 705, article 135941, 2020.

[55] H. Al Khalifah, P. W. J. Glover, and P. Lorinczi, "Permeability prediction and diagenesis in tight carbonates using machine learning techniques," *Marine and Petroleum Geology*, vol. 112, article 104096, 2020.

[56] T. Watanabe and Y. Katagishi, "Deviation of linear relation between streaming potential and pore fluid pressure difference in granular material at relatively high Reynolds numbers," *Earth, Planets and Space*, vol. 58, no. 8, pp. 1045–1051, 2006.

[57] A. Soueid Ahmed, A. Revil, B. Steck, C. Vergniault, A. Jardani, and G. Vinceslas, "Self-potential signals associated with localized leaks in embankment dams and dikes," *Engineering Geology*, vol. 253, pp. 229–239, 2019.

WILEY | Hindawi

Research Article

Experimental Investigation of the Effects of the Gangue Particle Size on the Evolution Rules of Key Seepage Parameters

Lihua Wang [ID],[1] **Jixiong Zhang** [ID],[1,2] **Yongqi Wei**,[3] **Cunli Zhu** [ID],[1,2] and **Gaolei Zhu** [ID][1,2]

[1]*School of Mines, China University of Mining and Technology, Xuzhou, 221116 Jiangsu, China*
[2]*State Key Laboratory of Coal Resources and Safe Mining, Xuzhou, 221116 Jiangsu, China*
[3]*Yanzhou Coal Mining Co. Ltd., Jining 272100, China*

Correspondence should be addressed to Cunli Zhu; cumtzhucunli@163.com

In order to deal with solid wastes and protect the fragile ecological environment on the ground, using gangues as the filling materials in the underground goaf can not only achieve favorable waste disposal but also alleviate surface subsidence and protect surface buildings and the ecological environment, with great practical significance and application prospects. During the water seepage process, the evolution rules of inner seepage channels in the bulk filling materials are the theoretical foundation for the realization of water-preserved mining. In order to gain clear knowledge of the seepage characteristics of the bulk filling gangues with different sizes, the evolution rules of some seepage parameters mainly including the displacement, the porosity, and the permeability of gangues and hydraulic pressure were analyzed via COMSOL numerical simulation. The evolution rules of the seepage characteristics of the bulk filling materials with different sizes were revealed by combining the present experimental and numerical results. Moreover, the present seepage experiment was proved to be reliable by comparing with numerical simulation results. This work can provide theoretical foundation for investigating the evolution characteristics of inner seepage paths in the bulk filling materials and selecting appropriate bulk filling materials under different stress and seepage environments.

1. Introduction

Coal mining has imposed serious effect on the balance of the underground water and surface water system in China [1–4]. During coal mining especially the modern mining process, original overlying strata are severely damaged under intense mining in the underground working face, thereby forming a lot of water-diversion fractures [5–8]. When the water-diversion fractures are connected with the aquifer, underground water can flow to the working face along the water-diversion channels formed by fractures, which can pose serious threat to safety production in mines, accompanied with the decline in the underground water level and the pollution of water quality [9–12]. According to the statistics, approximately $2.54m^3$ underground water is polluted for the mining of 1 ton of coal [13–15]. Therefore, how to achieve adequate protection of water resources in coal mining is the problem demanding prompt solution in the coal mining industry.

Mining with filling or backfill mining is an effective measure for inhibiting the development height of the mining-induced water-diversion fractured zone and protecting the aquifer. Gaining in-depth knowledge of the seepage rules of bulk filling materials with different particle sizes in a complex underground water environment can lay solid theoretical foundation for achieving water-preserved mining [16–19]. Currently, scholars from all over the world have conducted a great deal of research on the seepage rules of bulk filling materials. By combining laboratory test, theoretical analysis, and field application, Ma et al. examined non-Darcy hydraulic characteristics and deformation behaviors of bulk gangues and concluded that both porosity and permeability of gangues increased with the increase of the original GSG and the decrease of the stress rate [20]. Raziperchikolaee et al. focused on the relation between permeability of the deformed rock joints and seismic source response, established the fluid flow-geomechanics-seismicity

model at microscale, and investigated the displace response and failure mechanisms of microfractures in the sandstone samples that were developed along the joint during the development [21]. Li et al. investigated the effects of the particle size on compressive deformation and particle damage of the filling gangues in the goaf and analyzed the compressive deformation, particle clustering distribution, and gauge bulk shape change rules of the filling gangues [22]. Minh et al. explored the effects of the elasticity of pores on the solute transport process in viscous unstable aquifers and constructed a coupled flow, migration, and geomechanics framework for simulating the diffusion, mixing, and deformation mechanisms of stress-sensitive aquifers in the fingering process [23]. Zhang et al. investigated pore pressure evolution rules and energy loss characteristics during the seepage process of different sizes of gangues and performed tests on the permeability, mass loss, and pore pressure of gangues in the seepage process [24]; according to their test results, the mass loss of fractured gangues increased with the disproportionate increase of the large particle size. Conclusively, despite of substantial laboratory tests on the permeability of bulk filling materials, scholars [25–28] mainly focused on basic seepage parameters and fundamental physical/mechanical characteristics of bulk filling materials while neglecting the effects of the particle sizes of bulk filling materials on the seepage characteristics and the inner seepage evolution rules.

In this work, the goaf was filled with different sizes of solid wastes as the bulk filling materials. Under the complex stope environment, water in upper and lower adjacent artesian aquifers seeps constantly into the goaf through the water-diversion fractured zone and different geologic structures; accordingly, bulk filling materials are always in infiltrative mines. The compact filling body changes under coupled crustal stress and underground water flow. The bulk materials are constantly compacted when being subjected to the crustal stress, and the particles are gradually crushed and refined, accompanied with constant changes of pores among particles and the fluid's seepage channels. Next, as the size particle of bulk filling materials changes, the confined water enters into the filling body in the goaf via the water-diversion fractured zone; as the seepage pressure increases, pore channels in the filling body change gradually and the bulk filling materials with different sizes vary in seepage channels and rules. Investigating the seepage characteristics of bulk filling materials with different sizes is the key scientific problem in water-preserved mining.

In this study, based on laboratory test and numerical simulation, the effects of the filling gangues with different particle size ranges (0 ~ 5 mm, 5 ~10 mm, 10~15 mm and 15~20 mm) on seepage discharge and permeability parameters were investigated in depth. The evolution rules of displacement, porosity, permeability of gangues and hydraulic pressure after the filling were simulated using COMSOL numerical simulation software. Finally, the evolution rules of various seepage parameters after the filing of different sizes of materials were revealed by above laboratory and simulation data. Meanwhile, the reliability of the experimental results was validated by the present numerical simulation data. This work can provide theoretical foundation for examining the

evolution characteristics of inner seepage paths of the bulk filling materials and selecting appropriate bulk filling materials under different stress and seepage environments.

2. Materials and Methods

The filling materials mainly consisting of different sizes of gangues are essentially a kind of discontinuous media [29–32], which themselves change in the compaction process.

2.1. Experimental Materials.

The bulk filling materials in this work are mainly composed of different sizes of gangues. The gangues were directly collected from mines and the specimens with different size ranges were prepared, as shown in Figure 1.

Before the experiment, large gangues were collected and crushed. To be specific, large gangues were artificially crushed to the fragments with a size range of 200~300 mm so that the gangue fragments can smoothly pass through the inlet of the crusher; next, small gangues passed through the square hole sieves for step-by-step screening so as to obtain small gangues with different size ranges (0~5 mm, 5~10 mm, 10~15 mm, and 15~20 mm). Figure 1 shows the gangues with different sizes after crushing.

2.2. Experimental Method and Devices

2.2.1. Axial Loading.

As shown in Figure 2, the experimental loading system was used to offer the axial force for material compaction. Using the WAW-1000D Electro-Hydraulic Servo Universal Tester, the loading was applied in a displacement mode at a rate of 0.5 mm/min. The tester can display the measurement process and experiment results in real time. The tester with a maximum experimental force of 1000 kN can automatically measure the material's feature points and plot stress/strain and stress/displacement curves. When investigating the seepage characteristics of different sizes of gangues under axial compressive stress, the axial loading force was set as 4 MPa, 6 MPa, 8 MPa, 10 MPa, 16 MPa, and 20 MPa.

2.2.2. Seepage System.

The seepage characteristics of different sizes of gangues were investigated at a hydraulic pressure of 2 MPa, 3 MPa, 4 MPa, 5 MPa, 6 MPa, 7 MPa, and 8 MPa. In order to achieve water permeation in bulk filling materials, constant hydraulic pressure was steadily applied on the bottom of the materials under the stress, thereby generating pressure difference between the upper atmospheric pressure. Accordingly, water can freely flow in from one end of the bulk filling materials and out from the upper end. The pressure at the inlet of the bulk filling materials was controlled by the hydraulic power unit so as to provide different inlet pressures for the bulk filling materials.

Figure 3 shows the experimental seepage system, which mainly consists of the permeameter, the hydraulic-pressure control system, and the data acquisition instrument. In the present study, the permeameter was horizontally placed on the loading platform, whose bottom was in contact with the loading platform. The cylinder tube was placed on the bottom and sealed by O-shaped rubber seal rings. The porous plates were placed on the bottom of the cylinder

0~5 mm

5~10 mm

10~15 mm

15~20 mm
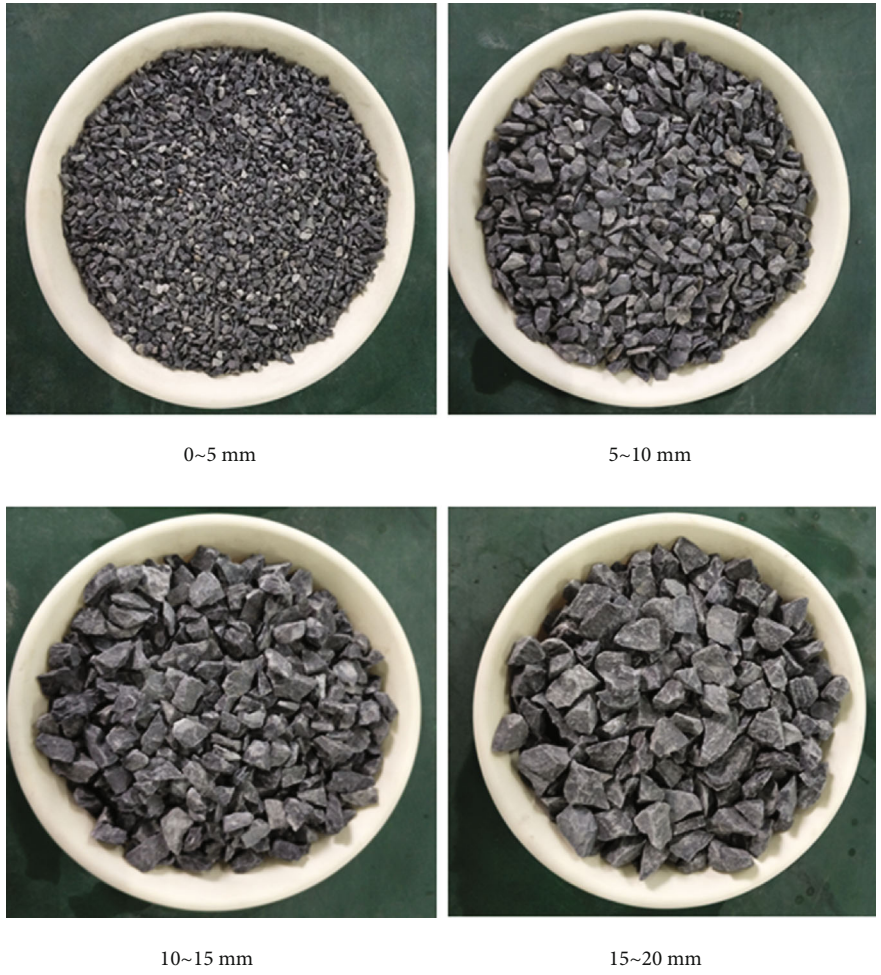
FIGURE 1: Pictures of the gangues with different sizes.
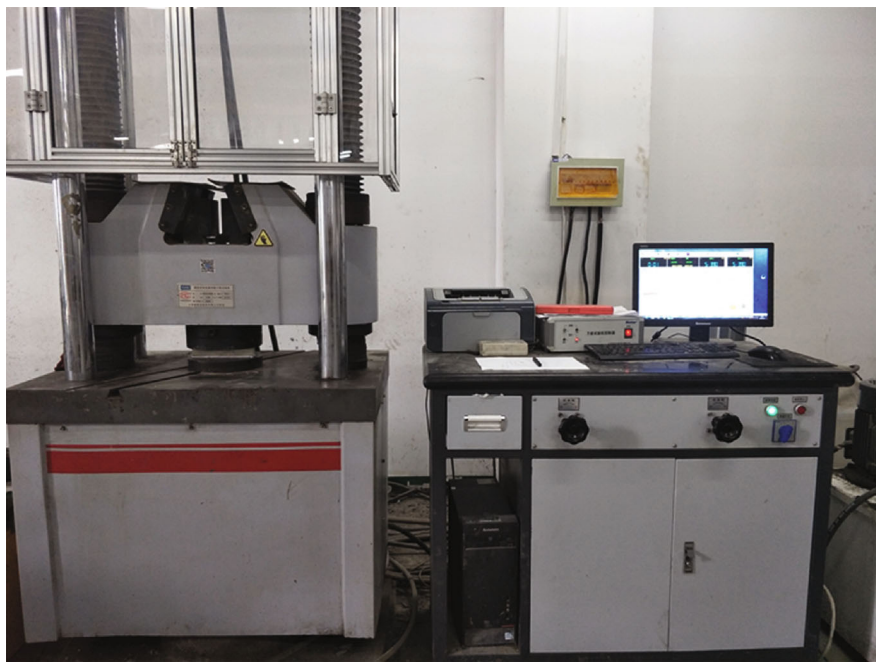
FIGURE 2: Picture of the experimental loading system.

(a) Permeameter

(b) Cylinder tube

(c) Bottom support

(d) Piston

(e) Porous plate

(f) Sealing ring

(g) Balance structure

(h) Bearing column

(i) Overflow barrel

FIGURE 3: Picture of the experimental seepage system.

tube. The cylinder tube was filled with bulk filling specimen with the piston on the surface. The piston was connected with the bearing column, the balance structure, and the overflow barrel. Finally, vertical axial stress can be applied on the bulk filling materials by the load of the tester via the overflow barrel cover, the overflow barrel, and the piston.

2.3. Measuring Principle of the Seepage Test. The present experimental system was used for measuring seepage characteristics of bulk filling materials with the steady method. In order to simulate the effects of the crustal stresses at different burial depths on the seepage characteristics of bulk filling materials, the seepage behaviors under different axial
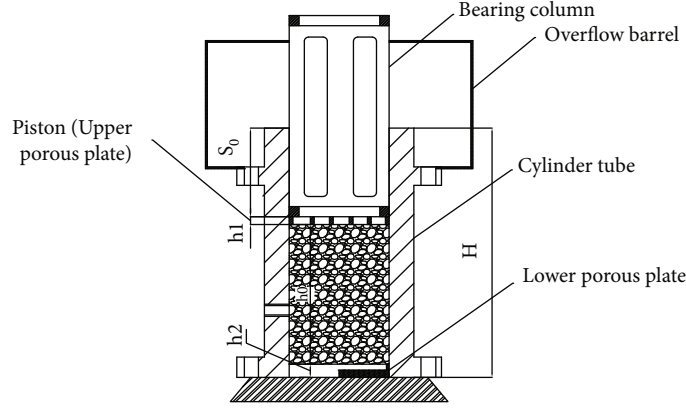
FIGURE 4: Illustration of the loading process of the permeameter.

TABLE 1: Test scheme.

Test order	Particle size of gangues (mm)	Axial load (MPa)	Hydraulic pressure (MPa)
i-1	0~5	4, 6, 8, 10, 16, 20	2, 3, 4, 5, 6, 7, 8
i-2	5~10	4, 6, 8, 10, 16, 20	2, 3, 4, 5, 6, 7, 8
i-3	10~15	4, 6, 8, 10, 16, 20	2, 3, 4, 5, 6, 7, 8
i-4	15~20	4, 6, 8, 10, 16, 20	2, 3, 4, 5, 6, 7, 8

stresses were tested with the axial stress control method. According to the mining engineering environment, the axial stress in preliminary design was set in the range of 4~20 MPa. The axial stress was uniformly increased and the displacement under each axial stress (S_0) was recorded. Meanwhile, the residual height can be calculated by the initial filling height and the thicknesses of the upper and the lower porous plates, i.e., $h = H - S_0 - h_1 - h_2$, as the principle shown in Figure 4.

The hydraulic pressure at 4 levels or above was injected from the bottom of the bulk materials via the hydraulic pump. Based on practical engineering background and the current test condition, the hydraulic pressure was preliminarily designed within 1~7 MPa. Next, the value when the flow reached stability at each level of hydraulic pressure was read, i.e., the velocity at the steady state, denoted as v, can be obtained. The corresponding pressure gradient G_P corresponding to each level of hydraulic pressure equals to the ratio of the difference between the pressure at the outlet and the hydraulic pressure at the inlet to the height of the bulk materials, i.e., $G_P = -P/h$. Next, the scatter diagrams can be plotted given each level of pressure gradient and the corresponding steady-state seepage velocity and the permeability k and non-Darcy factor β at the axial pressure can be obtained via fitting formula (1) as follows:

$$G_P = -\frac{\mu}{k} - \rho\beta v^2. \tag{1}$$

3. Experimental Schemes and Proportions

3.1. Proportion Settings.
In order to explore the seepage characteristics of different sizes of gangue filling materials under different axial loads and confining pressures, the gangue par-

ticle size range was set as 0~5 mm, 5~10 mm, 10~15 mm, and 15~20 mm and the axial load was set as 4 MPa, 6 MPa, 8 MPa, 10 MPa, 16 MPa, and 20 MPa, while the hydraulic pressure was set as 2 MPa, 3 MPa, 4 MPa, 5 MPa, 6 MPa, 7 MPa, and 8 MPa, respectively; the test scheme is shown in Table 1.

The axial load was set at 4~20 MPa so as to simulate the crustal stress from a shallow-buried coal seam to a deep well at a depth of several kilometers. Table 2 shows the axial load and corresponding oil pressure via calculation. The hydraulic pressure was set within a range of 2 MPa to 8 MPa, which can almost satisfy the pressure range of underground confined water. The axial load was cyclically applied, i.e., the axial load at the next level was applied for seepage after the load of each level of axial load. If no water passed at a hydraulic pressure of 7 MPa (i.e., water flow at a steady state equaled to 0), the loading stopped. It should be noted that steady state refers to flow reaching a stable value within a short time.

3.2. Testing Process.
The screened gangues with different sizes were soaked in water for 24 hours. Next, the gangues within same particle size range after soaking were put into the permeameter. The axial loads at 4 MPa, 6 MPa, 8 MPa, 10 MPa, 16 MPa, and 20 MPa were loaded on the WAW-1000D Electro-Hydraulic Servo Universal Tester. Under each level of axial load, the hydraulic pressure was increased step by step and the flow readings under different hydraulic pressures were read. Figure 5 illustrates the detailed testing process.

4. Experimental Results

4.1. Measured Results of Physical Characteristics

TABLE 2: Conversion between axial stress and oil pressure.

P (MPa)	1.5	2	4	6	8	10	16	20
S (m^2)	0.00785	0.00785	0.00785	0.00785	0.00785	0.00785	0.00785	0.00785
F (N)	11775	15700	31400	47100	62800	78500	125600	157000
Oil pressure (KN)	11.775	15.7	31.4	47.1	62.8	78.5	125.6	157
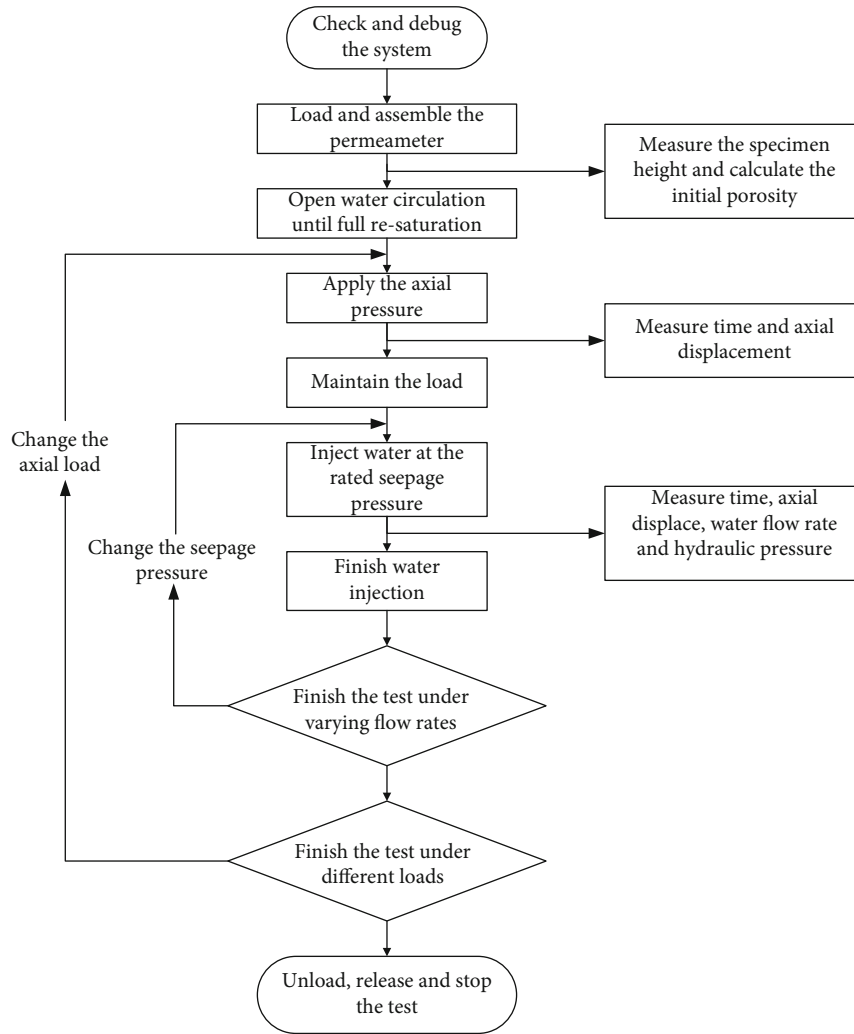
FIGURE 5: Illustration of the present testing process.

TABLE 3: Densities of the gangue specimens with different sizes.

Materials	Natural density	Saturated density	Accumulation density (g/cm^3)			
			0~5	5~10	10~15	15~20
Gangue specimen	2.08	2.12	1.475	1.409	1.398	1.395

TABLE 4: Initial porosities of different sizes of gangues.

Material	0~5 mm	5~10 mm	10~15 mm	15~20 mm
Gangue	0.34	0.42	0.43	0.47

TABLE 5: Seepage discharges of different sizes of gangues.

Particle size (mm)	Axial load (MPa)	Hydraulic pressure (MPa)							
		0~2	2	3	4	5	6	7	8
0~5	4	6.741	7.638	9.261	12.316	14.427	—	—	—
	6	3.59	5.78	6.93	7.57	8.505	—	—	—
	8	0	0	0	0	0.504	3.39	5.04	6.21
	10	0	0	0	0	0	0	0	0
5~10	4	62.43	—	—	—	—	—	—	—
	6	—	5.67	8.379	11.214	12.97	14.679	—	—
	8	—	6.237	7.632	8.26	8.31	—	—	—
	10	—	0	0	0	0.315	1.157	1.796	4.898
	16	0	0	0	0	0	0	0	0
10~15	4	62.43	—	—	—	—	—	—	—
	6	—	7.501	16.52	26.42	34.43	—	—	—
	8	—	6.237	7.632	8.26	8.31	—	—	—
	10	0	0	0	0	0	0	0	0
15~20	4	62.43	—	—	—	—	—	—	—
	6	13.549	62.43	—	—	—	—	—	—
	8	6.77	7.371	7.632	12.66	20.16	24.61	—	—
	10	0	2.16	3.41	3.59	5.66	—	—	—
	16	0	0	0	0	0	0	0	0

Because of limited range of the flowmeter, the flow rate of large-size gangues exceeded the measuring range, and simultaneously, small-size gangues were tightly compacted under large axial load, whose flow rates were fixed at 0 at different hydraulic pressures. Therefore, the permeability at that axial load condition can not be monitored.

4.1.1. Measurement of Gangue Density. This study selected a natural gangue, some bulk filling materials under a natural state, or saturated bulk filling materials after 24-hour soaking for measurement. The mass and the volume were weighed by the electronic balance and appropriate measuring glass so as to calculate the density. It should be noted that the experimenters should look at the front of the measuring glass as horizontally as possible so as to obtain accurate readings. Finally, the calculated results were averaged as the mean density of the bulk filling material. The specific calculation formula is shown in formula (2) as follows:

$$\rho_s = \frac{1}{k}\sum_{i=1}^{n}\rho_i = \frac{1}{k}\sum_{i=1}^{n}\frac{m_i}{V_i}, \qquad (2)$$

where ρ_s denotes the specimen density, k denotes the selected number of measurements, ρ_i denotes the specimen density in the ith measurement, m_i denotes the specimen mass in the ith measurement, and V_i denotes the specimen volume in the ith measurement.

As described above, the filling gangues are a kind of discontinuous media. The accumulation density is a quite important parameter for determining the consumption of the filling materials in the goaf. A certain mass of gangue blocks within a same particle size range was randomly selected and placed into the circular cylinder tube. The volume of the crushed gangue blocks can thus be determined by measuring the loading height and the cylinder tube size. In combination with the total mass of the gang-

ues, the packing density calculation formula is shown in formula (3) as follows:

$$\rho_b = \frac{m_b}{V_b} = \frac{4m_b}{\pi d^2 h_b}, \qquad (3)$$

where "ρ_b" denotes the accumulation density of the gangue specimen, "m_b" denotes the total mass of the gangue specimen in the tube, "V_b" denotes the volume of the gangue specimen in the tube, "d" denotes the inner diameter of the tube, and "h_b" denotes the height of the gangue specimen in the tube.

According to above measurement methods and computational formulas, natural densities, saturated densities, and accumulation densities of the filing gangues with different sizes were calculated, as the results shown in Table 3.

4.1.2. Initial Porosity of the Gangue Specimen. Porosity refers to the ratio of the pore volume between blocks to the accumulation volume when the crushed gangues were packed, which can directly reflect the compaction degree of the filling gangues. A higher porosity is indicative of a lower compaction degree, which is conductive for the water flow; contrarily, water can more hardly pass through the specimen with lower porosity. The porosity calculation formula is shown in formula (4) as follows:

$$\phi_o = \frac{V_b - V_e}{V_b} = 1 - \frac{V_e}{V_b} = 1 - \frac{4m_b}{\pi d^2 h_b \rho_s}, \qquad (4)$$

(a) 0~5 mm

(b) 5~10 mm

(c) 10~15 mm

(d) 15~20 mm
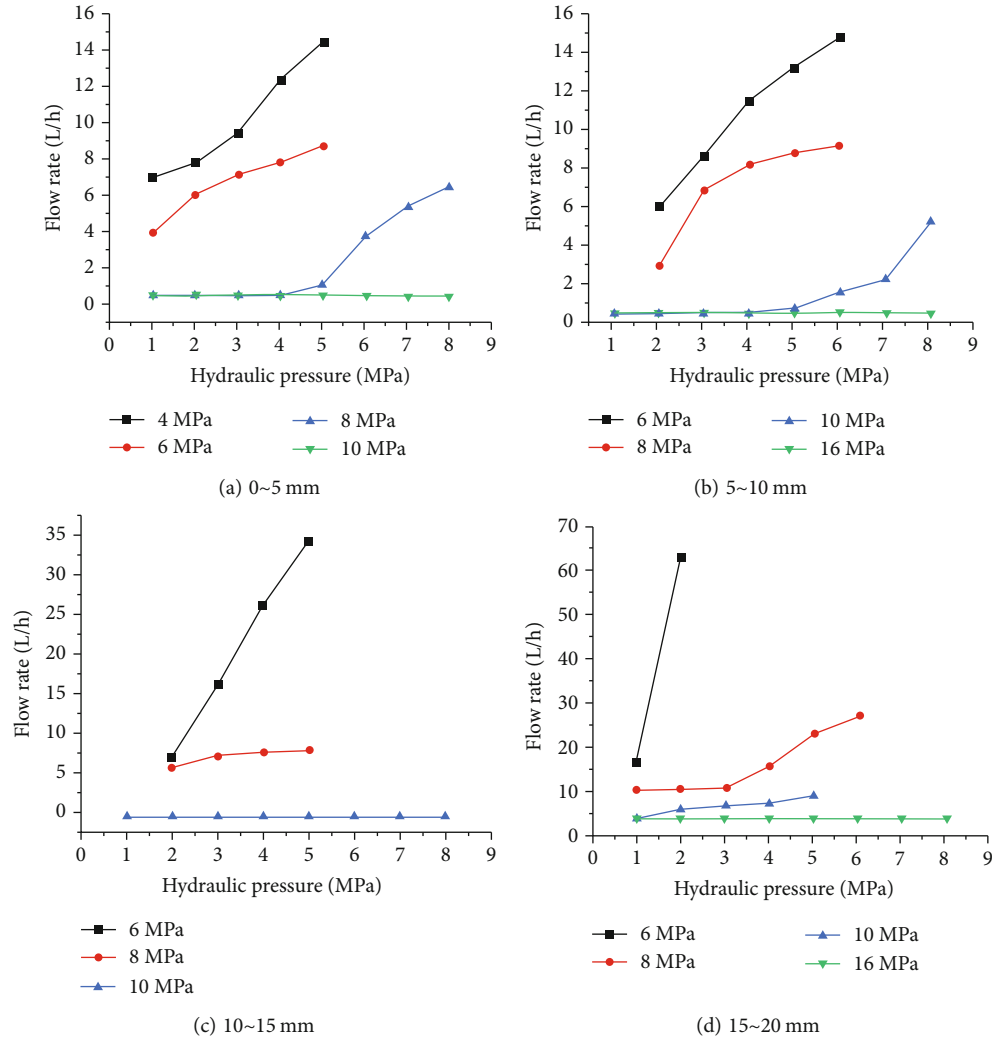
FIGURE 6: Relations between the flow rate and hydraulic pressure for the filling gangues with different size ranges.

where ϕ_o denotes the original porosity of the gangue specimen and denotes the protolith volume. Table 4 lists the measured porosities of different sizes of filling gangues.

4.2. Effect of the Particle Size on the Flow Rate and Permeability Parameters. In order to clarify the effects of the particle size on the flow rate and permeability parameters, the gangues with different size ranges (0~5 mm, 5~10 mm, 10~15 mm, and 15~20 mm) were selected for seepage experiments under an axial load of 4 MPa, 6 MPa, 8 MPa, 10 MPa, and 16 MPa, respectively. Table 5 lists the seepage discharges of different sizes of gangues at a same axial load but different hydraulic pressures.

As listed in Table 5, when the seepage discharge equaled to 0, the loading on the bulk filling materials stopped. At a fixed axial load, the seepage discharges of different sizes of gangues increased gradually with the increasing hydraulic pressure. This can be attributed to the discontinuity of bulk filling materials. As the hydraulic pressure increased, more water-diversion fractures appeared in the filling materials,

accompanied with a larger number of water-diversion fracture zones throughout the filling materials. Figure 6 shows the variations of seepage discharge and hydraulic pressure with the axial load for different sizes of gangues.

It can be observed in Figure 6 that seepage discharge dropped with the axial load at a decreasing rate. Meanwhile, the flow rate at a fixed axial load showed no change and approached to 0. This is mainly due to the fact that the bulk filling materials were gradually compacted under increasing axial load, accompanied with gradual compaction of water-diversion channels in the filling materials. When the axial load increased to a certain value, the pores in the bulk filling materials were gradually compacted and water cannot be infiltrated into the filling materials; at that moment, the seepage discharge of the bulk filling materials equaled to 0. When the particle size of bulk filling materials increased steadily, the seepage discharge of water increased with the increasing hydraulic pressure at a fixed axial load. On account of a low bonding degree, water channels were generally large in large-size gangues. In

(a)

(b)

FIGURE 7: Continued.

$$G_p = 1.09319E\text{-}15V^2 - 5.48295E11V$$

R2=0.95 = 0.95

(c)
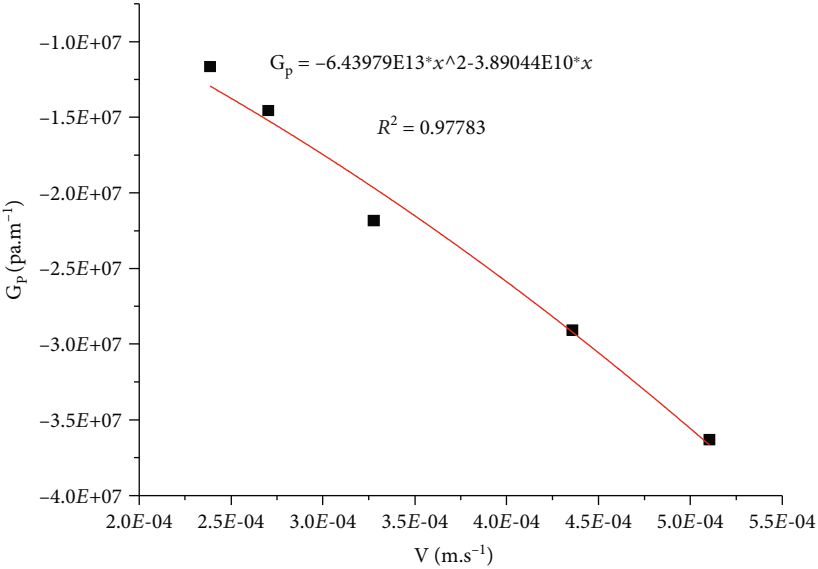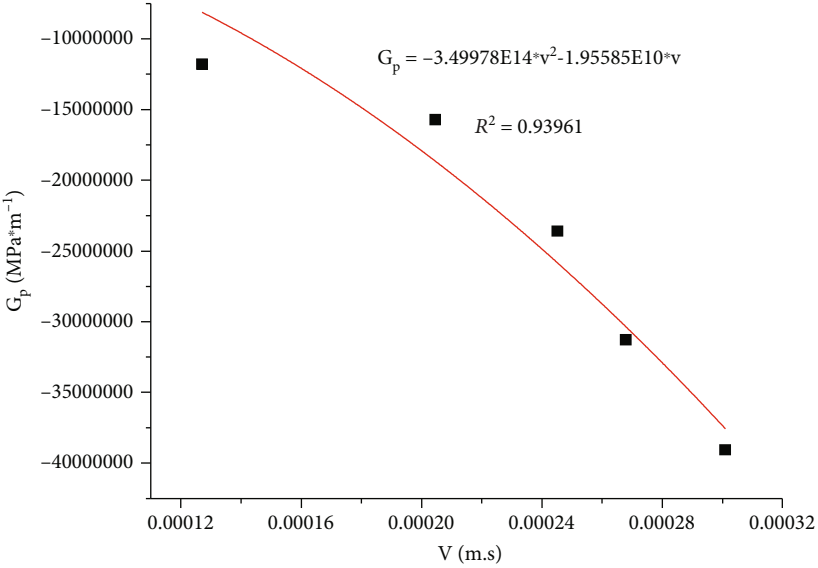
FIGURE 7: Fitted curves between G_p and V of the filling gangues with a particle size of 0~5 mm at different axial loads: (a) 4 MPa, (b) 6 MPa, and (c) 8 MPa.

the meantime, the inner channels in the bulk filling materials also changed under changing axial load and the inner water-diversion fracture channels underwent dynamic change. This can lay foundation for investigating the seepage characteristics of the bulk filling materials with different particle sizes.

By fitting the pressure gradient generated under different hydraulic pressures G_P and the seepage velocity V at a fixed axial load with non-Darcy Law that satisfies the Forchheimer formula, the permeability k and the non-Darcy permeability factor β in the formula can be obtained, as the fitted curves shown in Figures 7–10.

Figures 5–10 show the fitted curves between the pressure gradient under different hydraulic pressures G_P and the seepage velocity V for different sizes of gangues at different axial loads. Because of the limited measuring range of the flowmeter in the present experiment, the flow rate of large-size gangues at a small axial load exceeded the measuring range, while small-size gangues were compacted under a large axial load, resulting in 0 flow rate at different hydraulic pressures. Therefore, the permeability parameters cannot be obtained via fitting. Permeability parameters of gangue with different particle sizes are shown in Table 6.

In consideration of the restriction in the measuring range of the flowmeter, some seepage characteristics cannot be quantitatively analyzed but qualitatively measured. According to the practical condition in the field, the flow rate still equaled to 0 at a hydraulic pressure of 5~7 MPa, suggesting excellent water-resisting performance.

It can also be observed in Figures 5–10 that the pressure gradient and the flow velocity at a low axial load approximately followed linear relation. Moreover, nonlinearity was enhanced with the increasing axial load. At the beginning

of axial load, the bulk filling materials were loose with large seepage discharge. Next, as the axial load increased gradually, the compaction velocity of pores in the bulk filling materials was great; accordingly, the change of pressure gradient can be described in a quadratic pattern. For the gangues within a same size range, the permeability dropped steadily with the increasing axial load. To be specific, the permeability remained between $10E - 14 \text{ m}^2$ and $10E - 15$ m^2 at an axial load of 4~10 MPa.

Next, it can be observed from the fitted curves between G_P and V that the non-Darcy permeability factor can be negative or positive, with constantly increasing the absolute value in the range of $10E10 \sim 10E12 \text{ m}^{-1}$. The non-Darcy factor is more inclined to be positive for small-size gangues. As the particle size increased, the non-Darcy factor dropped to be negative. Since the compaction degree of small-size gangues is high, the flow increased slowly with the increase of hydraulic pressure gradient. The large-size gangues showed a low compaction degree, in which pores were great and new seepage channels were easily formed with the increasing hydraulic pressure, thereby generating large seepage velocity. After the experiments, the pictures were taken from the bottom of the filling body, as the pictures shown in Figure 11.

As shown in Figure 11, small-size gangues were more tightly compacted after loading, accompanied with more uniform pore distribution. By contrast, large-size gangues showed poor compaction effect after loading, accompanied with nonuniform pore distribution. It can also be found in the unloading process that the gangues in the upper part were small in size but were great in the lower part. Additionally, the crushing degree of the lower gangues was low. Next, the permeability should be below $10E - 15$ and non-Darcy factors should be above $10E12$ so as to achieve favorable water-resisting performance.
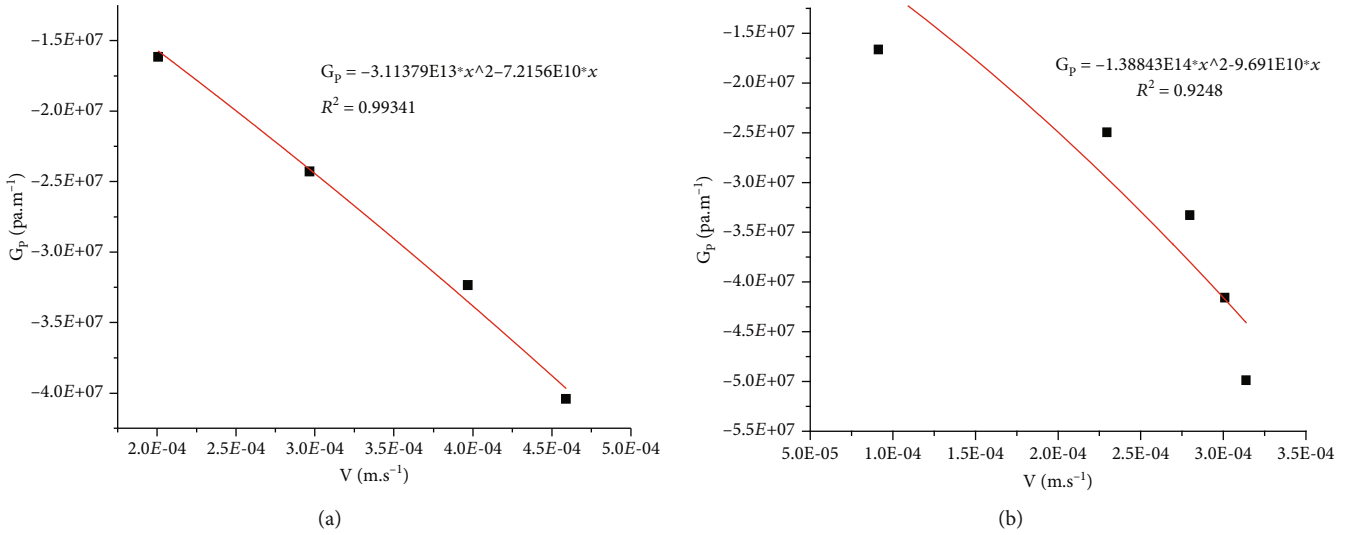
FIGURE 8: Fitted curves between G_p and V of the filling gangues with a particle size of 5~10 mm at different axial loads: (a) 6 MPa and (b) 8 MPa.
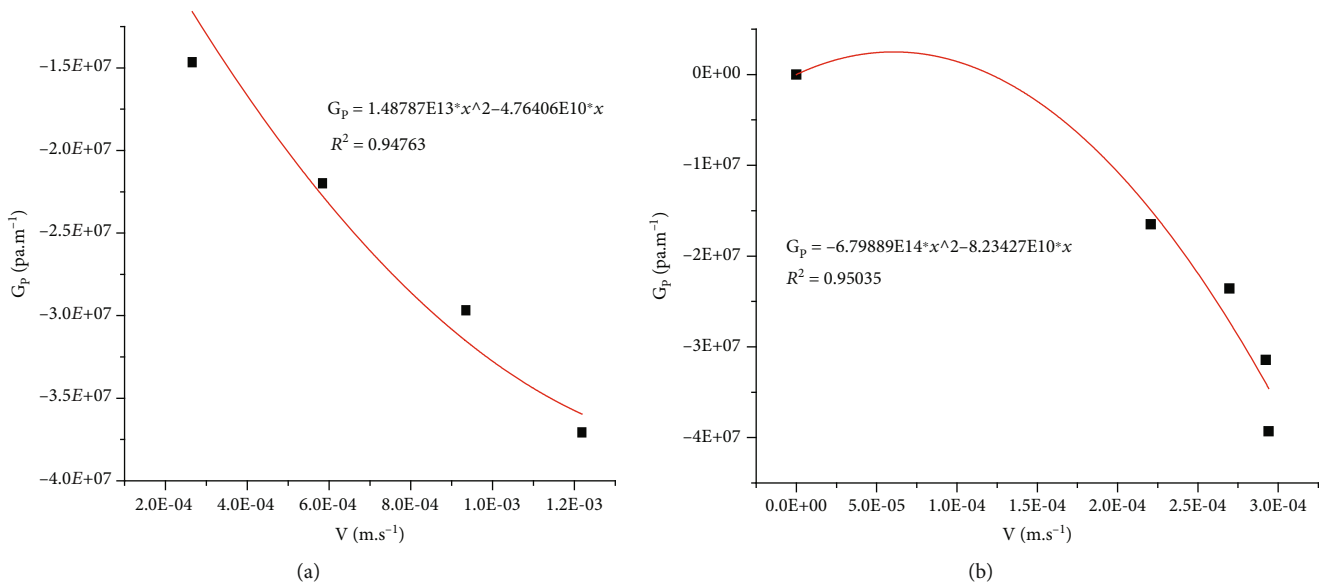
FIGURE 9: Fitted curves between G_p and V of the filling gangues with a particle size of 10~15 mm at different axial loads: (a) 6 MPa and (b) 8 MPa.

5. Discussions

As stated above, the effects of the particle size of gangues on seepage discharge and permeability parameters under different axial loads and hydraulic pressures were examined in depth. Next, the seepage rules in different sizes of gangues (0~5 mm, 5~10 mm, 10~15 mm, and 15~20 mm) under an axial load of 6 MPa and a hydraulic pressure of 4 MPa were simulated for gaining in-depth knowledge of the effect of the particle size on seepage behaviors. Meanwhile, the variations of displacement, porosity, permeability, and flow velocity of different sizes of gangues and hydraulic pressure in the seep-

age process were simulated. The detailed simulation process is described below.

According to the present simulation results, under an axial load of 6 MPa and a hydraulic pressure of 4 MPa, the equivalent Young modulus and the Poisson's ratio of the filling gangues with a size range of 0~5 mm equaled to 0.6 GPa and 15, respectively.

When the axial load and the hydraulic pressure were fixed at 6 MPa and 4 MPa, the equivalent Young modulus and the Poisson's ratio of the filling gangues with a size range of 5~10 mm in this simulation equaled to 0.5 GPa and 16, respectively. The cloud charts of the changes of
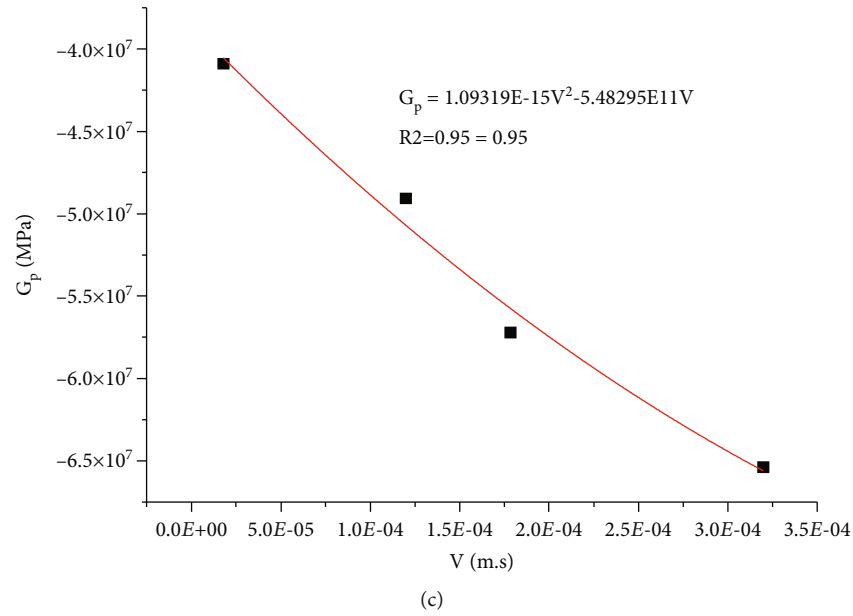
(a)

(b)
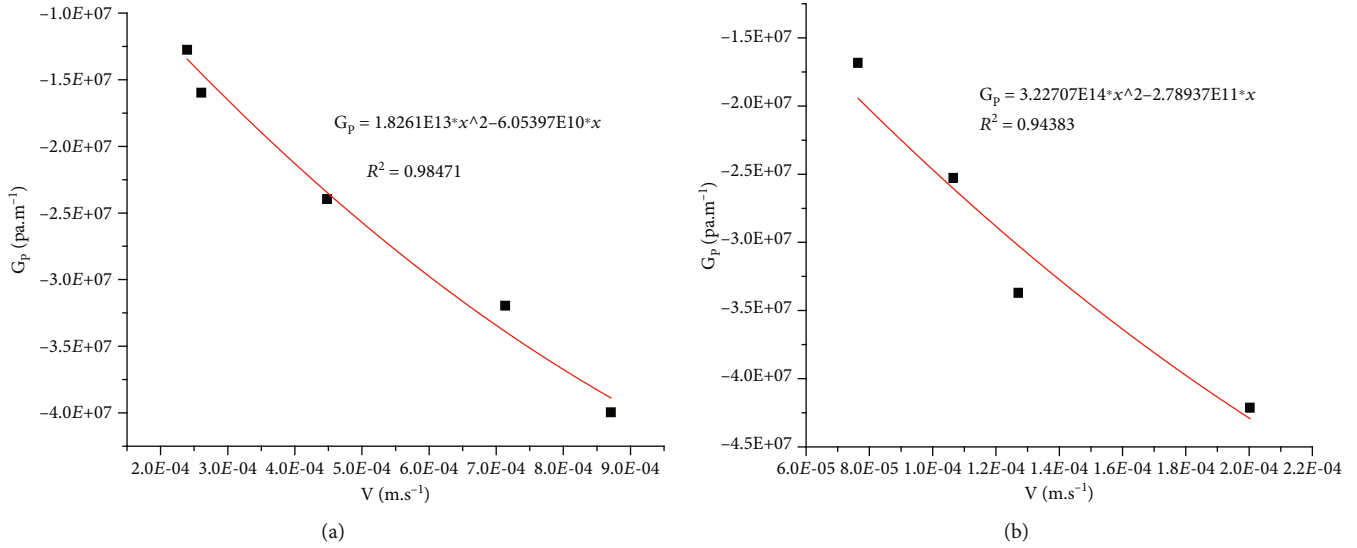
FIGURE 10: Fitted curves between G_p and V of the filling gangues with a particle size of 0~5 mm at different axial loads: (a) 8 MPa and (b) 10 MPa.

TABLE 6: Permeability parameters of the filling gangues with different sizes.

Particle size (mm)	Permeability parameters	Axial load (MPa)				
		4	6	8	10	16
0~5	Permeability (m²)	$2.57E-14$	$1.11E-14$	$1.82E-15$	—	—
	Non-Darcy factor (m⁻¹)	$6.44E+10$	$3.50E+11$	$-1.09E+12$	—	—
5~10	Permeability (m²)	—	$1.75E-14$	$1.02E-14$	$2.30E-15$	—
	Non-Darcy factor (m⁻¹)	—	$6.83E+10$	$1.41E+11$	$1.46E+12$	—
10~15	Permeability (m²)	—	$2.10E-14$	$1.21E-14$	—	—
	Non-Darcy factor (m⁻¹)	—	$-1.49E+10$	$6.80E+11$	—	—
15~20	Permeability (m²)	—	—	$1.65E-14$	$3.78E-15$	—
	Non-Darcy factor (m⁻¹)	—	—	$-1.83E+10$	$-2.65E+11$	—

FIGURE 11: Pictures after the seepage in different sizes of gangues.

displacement, porosity, permeability, flow velocity, and hydraulic pressure under the stress and particle size conditions were plotted, as shown in Figure 12.

For the gangues with a size range of 10~15 mm, when the axial load and the hydraulic pressure were fixed at 6 MPa and 4 MPa, the equivalent Young modulus and the Poisson's ratio were 0.7 GPa and 26.5, respectively. Based on COMSOL simulation results, the cloud charts of the changes of displacement, porosity, permeability, flow velocity, and hydraulic pressure under the stress and particle size conditions were plotted, as shown in Figure 13.

Similarly, the simulation was performed on the gangues with a size range of 15~20 mm at an axial load of 6 MPa and a hydraulic pressure of 4 MPa. According to the simulation results, the equivalent Young modulus and the Poisson's ratio equaled to 0.75 GPa and 28, respectively. Figure 14 reflects the changes of displacement, porosity, permeability, flow velocity, and hydraulic pressure during the seepage process in the gangues with a size range of 15~20 mm.

(a) Displacement

(b) Porosity

(c) Permeability

(d) Flow velocity

(e) Hydraulic pressure
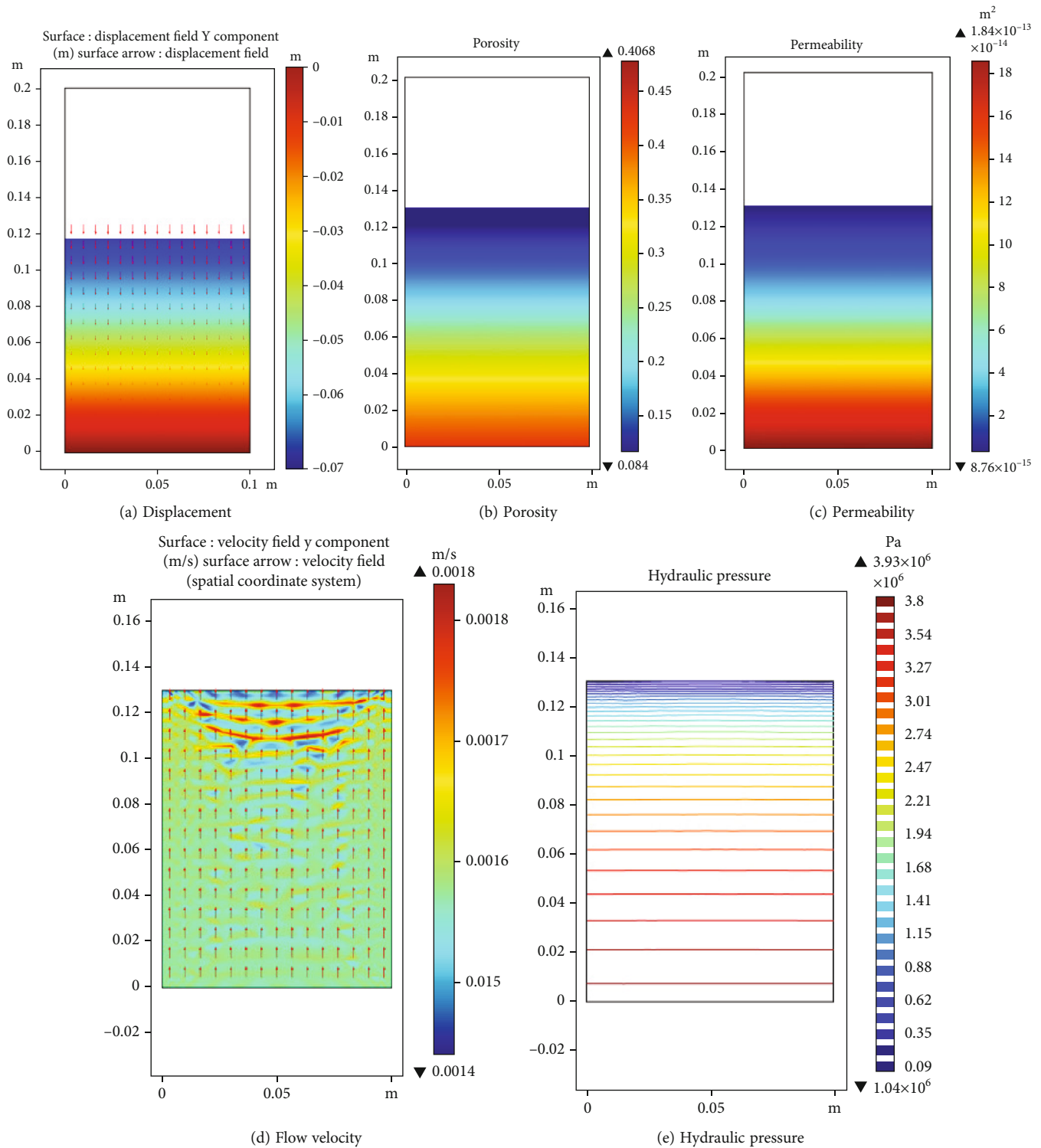
FIGURE 12: Seepage rules in the gangues with a size range of 5~10 mm.

As shown in Figures 14–15, the gangues with a larger particle size underwent less displacement. The displacement of the gangues with a particle size range of 5~10 mm reached a maximum of 84.8 mm, while the displacements of the gangues within the other size ranges were 63 mm, 75.22 mm, and 75.9 m, respectively. Under a same axial load,

the porosity of the gangues with larger particle size was greater. The porosity of the gangues with a particle size range of 15~20 mm was greatest, accompanied with the greatest permeability. Accordingly, the distribution of hydraulic pressure in the gangues with a larger size was more uniform. The simulation results with COMSOL software fit

(a) Displacement

(b) Porosity

(c) Permeability

(d) Flow velocity

(e) Hydraulic pressure
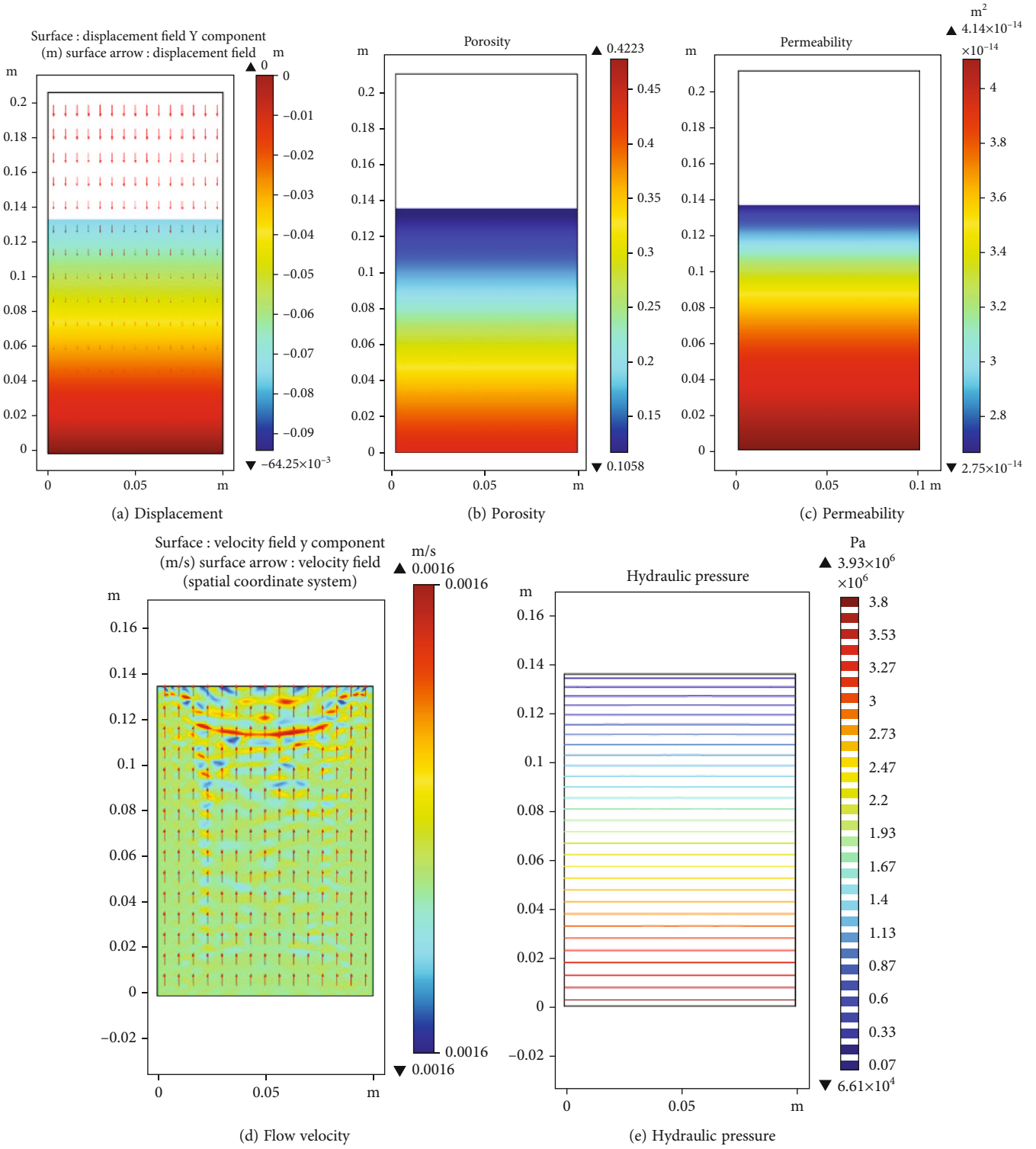
FIGURE 13: Seepage rules in the gangues with a size range of 10~15 mm.

(a) Displacement

(b) Porosity

(c) Permeability

(d) Flow velocity

(e) Hydraulic pressure
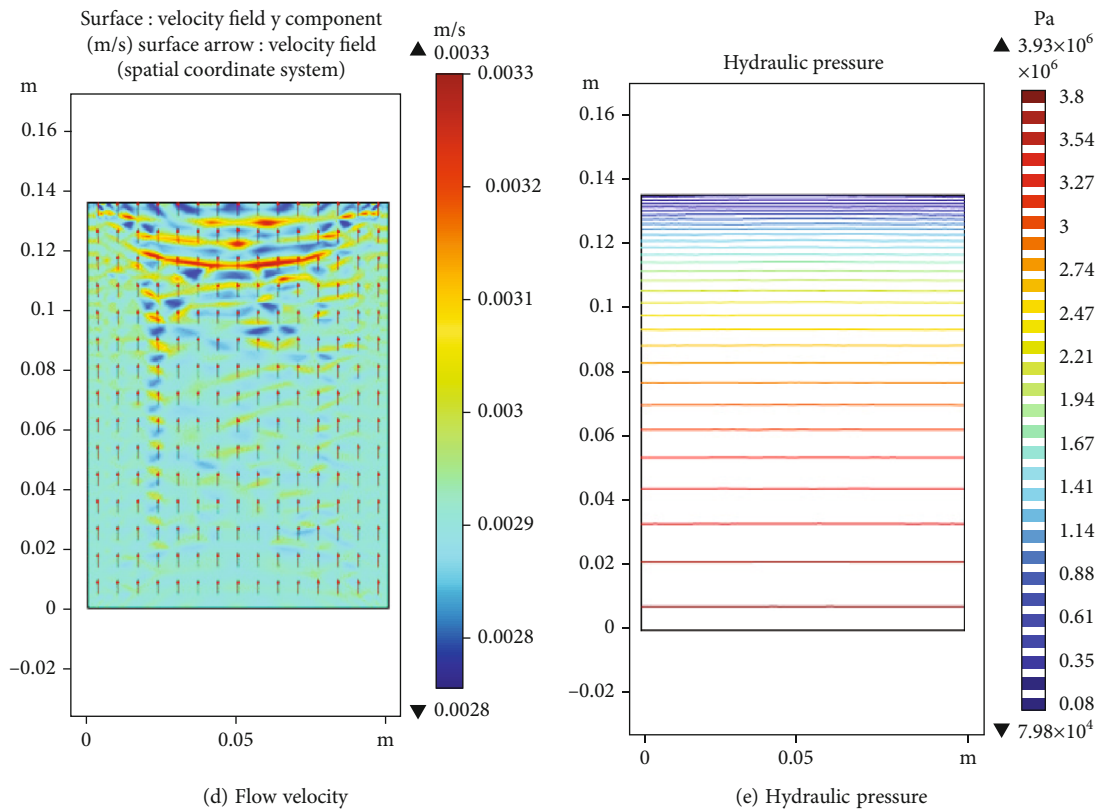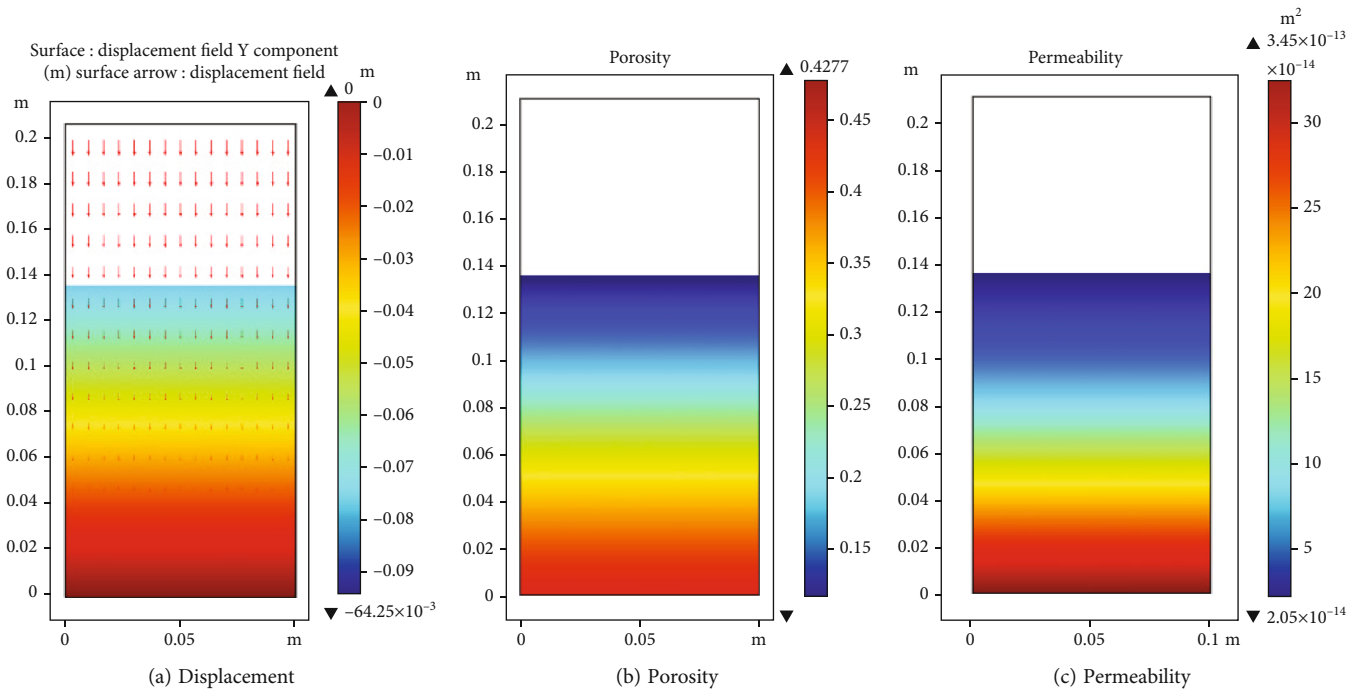
FIGURE 14: Seepage rules in the gangues with a size range of 15~20 mm.

(a) Displacement

(b) Porosity

(c) Permeability

(d) Flow velocity

(e) Hydraulic pressure
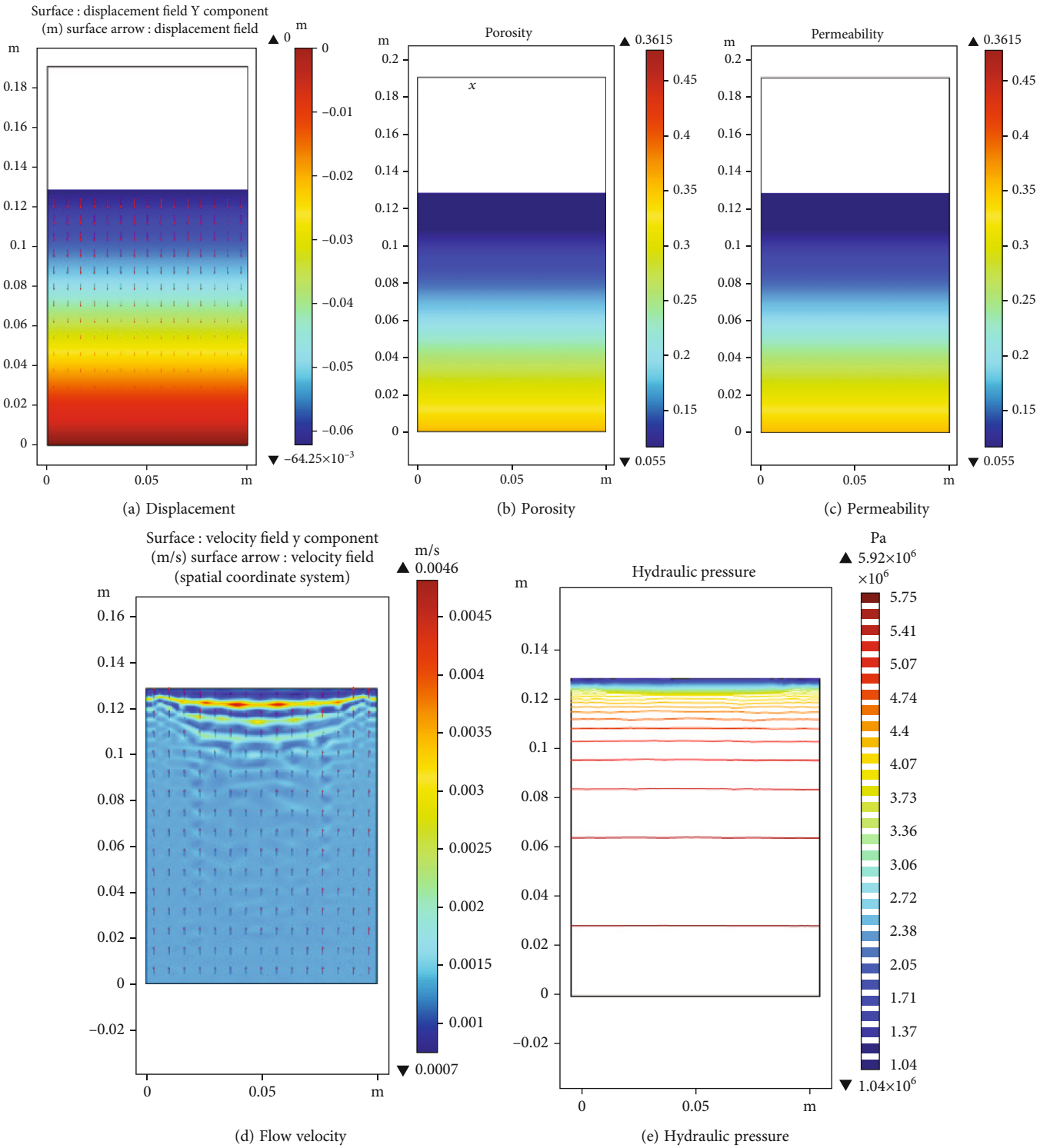
FIGURE 15: Seepage rules in the gangues with a size range of 0~5 mm.

(a) Porosity

(b) Permeability

(c) Seepage velocity
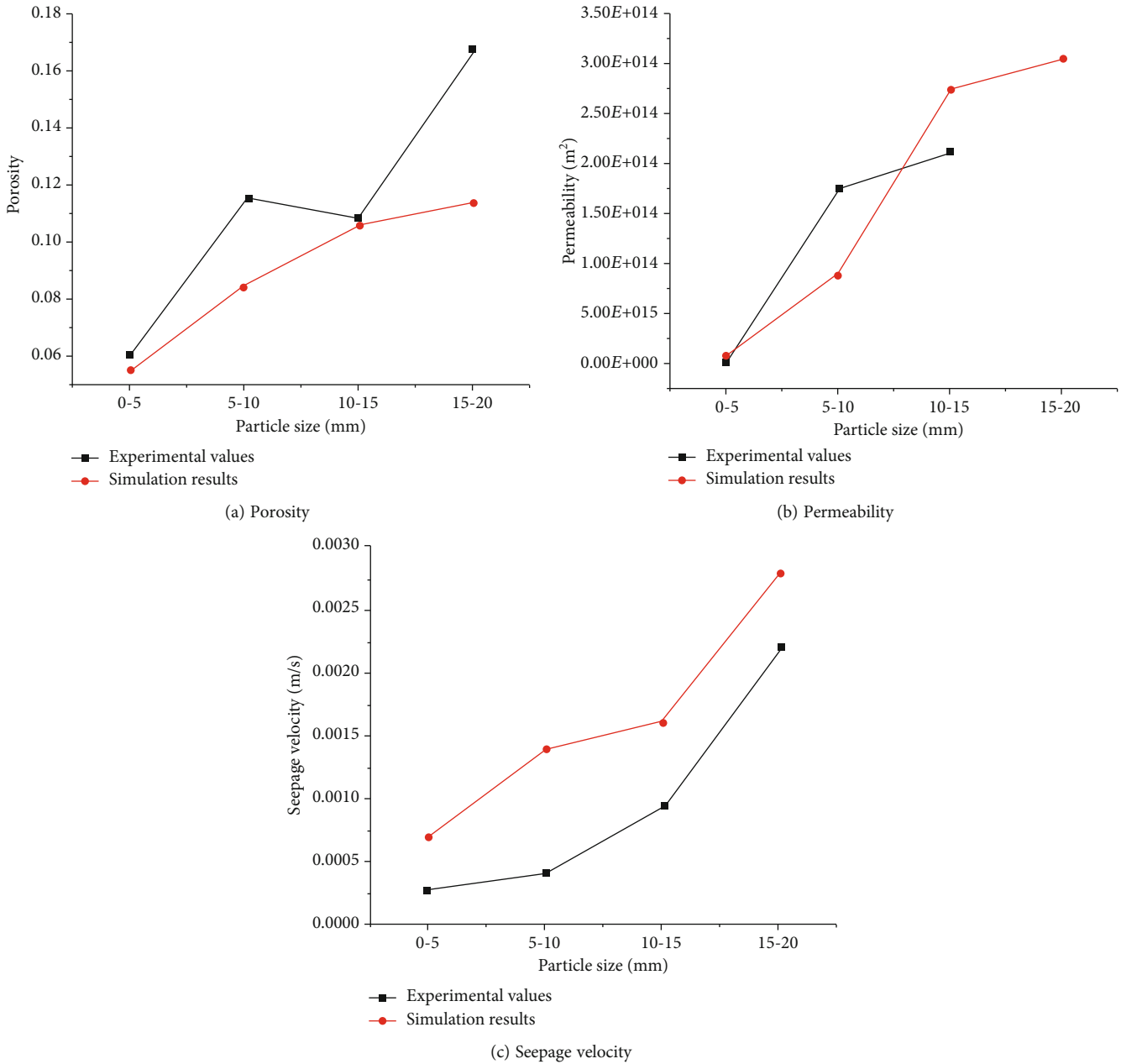
FIGURE 16: Comparison between the experimental and numerical simulation data for different sizes of gangues.

well with the data in seepage experiment, validating the reliability of the present experiment.

Figure 16 compares the experimentally measured porosities, permeabilities, and seepage velocities of different sizes of gangues with the numerical simulation data.

Apparently, the seepage velocity curves between experimental and the simulation results show higher coincidence than the other two curves. Moreover, the porosity, the permeability, and the seepage velocity of the gangues increased gradually with the increasing particle size.

6. Conclusions

This study experimentally investigated the fundamental physical and mechanical properties of gangues and the effects of the particle size on the seepage discharge and the permeability parameters in the gangues with different sizes under different axial loads and hydraulic pressures and revealed the variations of the flow rate with axial load and hydraulic pressure in the gangues within a same size range. Finally, the effects of the particle size on the seepage rules of gangues were concluded via COMSOL numerical simulation for validating the reliability of the present experiment. The following conclusions can be drawn.

(1) Firstly, some fundamental physical and mechanical properties of the bulk filling materials were measured. The density of the bulk filling gangues under natural condition was 2.08 g/cm^3; after soaking, the saturated density changed to be 2.12 g/cm^3. The accumulation

densities of the filling gangues with different size ranges (0~5 mm, 5~10 mm, 10~15 mm, and 15~20 mm) were 1.475 g/cm^3, 1.409 g/cm^3, 1.398 g/cm^3, and 1.395 g/cm^3, respectively. Meanwhile, the initial porosities of the filling gangues with different size ranges were 0.34, 0.42, 0.43, and 0.47, respectively. The above analysis of fundamental physical and mechanical properties of gangues can provide insightful reference for later investigation of basic physical and mechanical behaviors during water seepage in the filling materials

(2) The effects of the particle size of gangues on water seepage discharges and permeability parameters at different axial loads and hydraulic pressures were also investigated in the laboratory. Considering that the bulk filling gangues are a kind of discontinuous media, the bulk filling materials were gradually compacted under increasing axial load, accompanied with the change of inner seepage channels. Meanwhile, as the hydraulic pressure increased steadily, water-diversion channels in the bulk filling materials increased, which also increased water seepage discharge. Under varying axial load and hydraulic pressure, the seepage trajectories of water in the bulk filling materials changed, which can provide reference for investigating the seepage characteristics in the bulk filling materials with different sizes

(3) Finally, the effects of the particle size on water seepage behaviors were simulated with COMSOL numerical simulation software. The seepage behaviors in gangues can be characterized by the displacement, the porosity, and the permeability of gangues as well as water flow velocity and hydraulic pressure. For the gangues with a size range of 5~10 mm, the displacement of gangues reached a maximum of 84.8 mm; moreover, hydraulic pressure distribution became more uniform with the increasing particle size, accompanied with a steady increase of porosity and permeability of gangue. The numerical simulation results with COMSOL fit well with the present experimental data, validating the reliability of the seepage experiment

Data Availability

The latest data used to support the findings of this study are included within the article.

Conflicts of Interest

None of the authors have any conflicts of interest.

Acknowledgments

References

[1] H. J. Li, R. Y. Long, and H. Chen, "Economic transition policies in Chinese resource-based cities: an overview of government efforts," *Energy Policy*, vol. 55, pp. 251–260, 2013.

[2] J. T. Chen, L. M. Yin, W. B. Sun, C. Lu, S. C. Zhang, and X. Z. Sun, "Development and application for new solid-fluid coupling similar material of deep floor aquifer," *Chinese Journal of Rock Mechanics and Engineering*, vol. 34, no. 2, pp. 3956–3964, 2015.

[3] H. Zhang, Y. Wang, R. X. Yang, and R. Z. Ye, "Modeling the effects of phosphate mining on groundwater at different stages of mine development," *Mine Water and the Environment*, vol. 37, no. 3, pp. 604–616, 2018.

[4] P. Y. Li, "Mine water problems and solutions in China," *Mine Water and The Environment*, vol. 37, no. 2, pp. 217–221, 2018.

[5] D. Ma, X. X. Miao, H. B. Bai et al., "Effect of mining on shear sidewall groundwater inrush hazard caused by seepage instability of the penetrated karst collapse pillar," *Natural Hazards*, vol. 82, no. 1, pp. 73–93, 2016.

[6] H. Bouwer, "Land subsidence and cracking due to groundwater depletiona," *Groundwater*, vol. 15, no. 5, pp. 358–364, 1977.

[7] Y. Xue, J. Liu, P. G. Ranjith, X. Liang, and S. Wang, "Investigation of the influence of gas fracturing on fracturing characteristics of coal mass and gas extraction efficiency based on a multi-physical field model," *Journal of Petroleum Science and Engineering*, vol. 206, article 109018, 2021.

[8] K. Ma, L. M. Yin, J. T. Chen, M. Chen, Z. Q. Wang, and B. Q. Cui, "Theoretical analysis on failure of water-resisting key strata in the floor by local high confined water in deep mining," *Rock and Soil Mechanics*, vol. 39, no. 9, pp. 3213–3222, 2018.

[9] D. Ma, H. Duan, W. Liu, X. Ma, and M. Tao, "Water–Sediment two-phase flow inrush hazard in rock fractures of overburden strata during coal mining," *Mine Water and the Environment*, vol. 39, no. 2, pp. 308–319, 2020.

[10] A. Karaman, P. J. Carpenter, and C. J. Booth, "Type-curve analysis of water-level changes induced by a longwall mine," *Environmental Geology*, vol. 40, no. 7, pp. 897–901, 2001.

[11] Y. Xue, T. Teng, F. Dang, Z. Ma, S. Wang, and H. Xue, "Productivity analysis of fractured wells in reservoir of hydrogen and carbon based on dual-porosity medium model," *International Journal of Hydrogen Energy*, vol. 45, no. 39, pp. 20240–20249, 2020.

[12] R. Gao, H. Yan, F. Ju, X. Mei, and X. Wang, "Influential factors and control of water inrush in a coal seam as the main aquifer," *International Journal of Mining Science and Technology*, vol. 28, no. 2, pp. 187–193, 2018.

[13] J. F. Hou, Z. P. Guo, W. Z. Liu, H. Yang, and W. W. Xie, "Study on damage model and damage evolution characteristics of backfill with prefabricated fracture under seepage-stress coupling," *Advances in Materials Science and Engineering*, vol. 2020, 11 pages, 2020.

[14] J. M. Li, Y. L. Huang, and M. Qiao, "Effects of water soaked height on the deformation and crushing characteristics of loose gangue backfill material in solid backfill coal mining," *Processes*, vol. 6, no. 6, p. 64, 2018.

[15] J. Li, S. Zhang, Q. Wang et al., "Feasibility of using fly ash-slag-based binder for mine backfilling and its associated leaching risks," *Journal of Hazardous Materials*, vol. 400, article 123191, 2020.

[16] J. Wu, Q. Yin, Y. Gao, B. Meng, and H. Jing, "Particle size distribution of aggregates effects on mesoscopic structural evolution of cemented waste rock backfill," *Environmental Science and Pollution Research*, vol. 28, no. 13, pp. 16589–16601, 2021.

[17] R. D. Lokhande, A. Prakash, K. B. Singh, and K. K. K. Singh, "Subsidence control measures in coalmines: a review," *Journal of Scientific and Industrial Research*, vol. 64, pp. 323–332, 2005.

[18] J. Roser, D. Potocnik, and M. Vulic, "Analysis of dynamic surface subsidence at the underground coal mining site in Velenje, Slovenia through modified sigmoidal function," *Minerals*, vol. 8, no. 2, p. 74, 2018.

[19] Z. Bian, X. Miao, S. Lei, S. E. Chen, W. Wang, and S. Struthers, "The challenges of reusing mining and mineral-processing wastes," *Science*, vol. 337, no. 6095, pp. 702-703, 2012.

[20] D. Ma, H. Duan, X. Li, Z. Li, Z. Zhou, and T. Li, "Effects of seepage-induced erosion on nonlinear hydraulic properties of broken red sandstones," *Tunnelling and Underground Space Technology*, vol. 91, article 102993, 2019.

[21] S. Raziperchikolaee, V. Alvarado, and S. Yin, "Microscale modeling of fluid flow-geomechanics-seismicity: relationship between permeability and seismic source response in deformed rock joints," *Journal of Geophysical Research-Solid Earth*, vol. 119, no. 9, pp. 6958–6975, 2014.

[22] M. Li, A. Li, J. Zhang, Y. Huang, and J. Li, "Effects of particle sizes on compressive deformation and particle breakage of gangue used for coal mine goaf backfill," *Powder Technology*, vol. 360, pp. 493–502, 2020.

[23] T. Minh and J. Birendra, "Coupling between transport and geomechanics affects spreading and mixing during viscous fingering in deformable aquifers," *Advances in Water Resources*, vol. 136, article 103485, 2020.

[24] J. Zhang, Y. Liu, N. Zhou, and M. Li, "Pore pressure evolution and mass loss of broken gangue during the seepage," *Royal Society Open Science*, vol. 5, no. 10, article 180307, 2018.

[25] Z. Huang, S. Li, K. Zhao, Y. Wu, W. Zeng, and H. Xu, "Estimating the hydraulic conductivity of deep fractured rock strata from high-pressure injection tests," *Mine Water and The Environment*, vol. 39, no. 1, pp. 112–120, 2020.

[26] W. Zeng, Z. Huang, Y. Wu, S. Li, R. Zhang, and K. Zhao, "Experimental investigation on mining-induced strain and failure characteristics of rock masses of mine floor," *Geomatics Natural Hazards & Risk*, vol. 11, no. 1, pp. 491–509, 2020.

[27] L. Xiao, Q. Wu, C. Niu et al., "Application of a new evaluation method for floor water inrush risk from the Ordovician fissure confined aquifer in Xiayukou coal mine, Shanxi, China," *Carbonates and Evaporites*, vol. 35, no. 3, pp. 1–16, 2020.

[28] W. Perl, "A friction coefficient, series-parallel channel model for transcapillary flux of nonelectrolytes and water," *Microvascular Research*, vol. 6, no. 2, pp. 169–193, 1973.

[29] Y. B. Wang, D. W. Yin, S. J. Chen, L. Zhang, D. Liu, and Y. Sun, "Experimental study on properties of rock-cemented coal gangue-Fly ash backfill bimaterials with different coal gangue particle sizes," *Advances in Civil Engineering*, vol. 2020, 12 pages, 2020.

[30] J. Hou, Z. Guo, W. Liu, and Y. Zhang, "Mechanical properties and meso-structure response of cemented gangue-fly ash backfill with cracks under seepage- stress coupling," *Construction and Building Materials*, vol. 250, article 118863, 2020.

[31] C. Wang, B. Shen, J. Chen et al., "Compression characteristics of filling gangue and simulation of mining with gangue backfilling: an experimental investigation," *Geomechanics and Engineering*, vol. 20, no. 6, pp. 485–495, 2020.

[32] J. Y. Li and J. M. Wang, "Comprehensive utilization and environmental risks of coal gangue: a review," *Journal of Cleaner Production*, vol. 239, article 117946, 2019.

WILEY | Hindawi

Research Article

Control of Water Inrush from Longwall Floor Aquifers Using a Division Paste Backfilling Method

Qingliang Chang, Xingjie Yao, Shiguo Ge [ID], Ying Xu [ID], and Yuantian Sun [ID]

School of Mines, Key Laboratory of Deep Coal Resource Mining of the Ministry of Education, China University of Mining and Technology, Xuzhou, Jiangsu 221116, China

Correspondence should be addressed to Shiguo Ge; ts20020015a31@cumt.edu.cn and Ying Xu; kdxuying@163.com

Aiming at the problem of the safety mining problems of longwall paste filling working face under buildings on high confined water in the Daizhuang Coal Mine, the paste filling mining method was used. A series of theoretical analyses, numerical simulations, and field measurements were applied. The results showed that when the filling interval of the working face increases from 1.2 m to 3.6 m, no significant change is found in the depth of the perforated plastic zone of the floor strata. According to the types of water-conducting cracks in the floor strata of the working face 11607, the floor strata are divided into the floor intact area, the structure developed area, and the floor weak area. Based on that, the measures for preventing and controlling the floor failure in the paste filling working face are proposed. Furthermore, the failure depth of the floor of the test working face was detected by the on-site water injection method, and the results showed that the maximum failure depth of the floor of the test working face was about 3 m.

1. Introduction

Researchers in many countries have conducted a lot of theoretical research and practical applications on the prevention and treatment of coal mining under confined water by the backfill mining method [1–6]. To study and analyze the destruction depth and law of the underlying coal and rock during the mining process of the working face, water inrush from the underlying aquifer was studied by numerical modeling. The most dangerous position is in the section where the working face passes through the fault zone [7–10]. The underlying coal and rock layers were regarded as brittle rock masses, and the underlying water-conducting and nonconducting fracture surfaces were constructed. The probability of fracture and water inrush of the underlying coal seam increases with the increase of coal mining depth. The water inrush from the floor is directly related to the pressure of the mine [11–16].

Three-dimensional in situ stress was measured on-site, and according to the Mohr-Coulomb criterion, the results were obtained through FLAC3D numerical simulation analysis, to study and analyze the failure depth [17–20]. The plastic

failure zone and stress field distribution law of the underlying coal strata at different coal mining stages are investigated. The on-site geophysical prospecting and drilling were used to study the damage depth of the underlying coal and rock during the mining process of coal seam faces in North China [21–23]. By detecting the displacement, deformation, and failure characteristics and stress field distribution of the underlying coal and rock layers before and after coal mining in the working face, the depth of deformation and failure of rock layers are obtained [24–26].

Aiming at the safe mining of the No. 16 coal seam in Daizhuang Coal Mine under buildings and high confined water conditions, the paste is used to fill the goaf area so that the filling body and the top and bottom of the goaf form a supporting system of the top plate-filling body-bottom plate. This technology can control the depth of the bottom plate damage and can play a better role in groundwater resources [27–30]. The protective effect of the coal mine, especially under the condition of coal mining under confined water, can significantly improve the safe production conditions of coal mines [31–34]. Furthermore, this technology can effectively control the surface subsidence and

deformation to achieve nonrelocation of coal mining, which can greatly improve coal resources. Also, the use of mine solid waste as a filling material can greatly improve the ecological environment of the mining area.

2. Project Overview

Daizhuang Coal Mine is located in Jining City, Shandong Province (Figure 1). It belongs to the conditions of coal mining under typical buildings and close-distance high-pressure water. There are 78 surface villages in the minefield. The mine is divided into the upper group of coal at the -410 m level and the lower group of coal at the -580 m level. The -410 m level mainly mines 3 upper and 3 lower coal seams, and the -580 m level mainly mines 16 and 17 coal seams.

According to the geological and hydrological drilling of the mine (Figure 2), it is proved that the distance between the No. 16 coal seam and the floor is 21.6 m on average, and the average distance from the Ordovician ash of the floor is 61.1 m. The positional relationship between the coal seam and the aquifer is shown in Figure 2. The maximum water inrush coefficient of the Ordovician ash aquifer in the No. 16 coal seam floor is about 0.12 MPa/m. The floor elevation of the working face is between -443.5 m and -516.9 m, and the average elevation is -501.3 m. The buried depth of the working face is between 480.6 and 558.3 m, with an average buried depth of 541.6 m. The thickness of the No. 16 coal seam in the working face is between 1.65 m and 2.35 m.

3. Analysis of Floor Failure Mechanism in Paste Filling Mining

3.1. Theoretical Analysis of Equivalent Roadway. When the working face is not filled with mining, as the working face continues to advance, the roof will undergo initial breakage and periodic breakage, and the pressure of the mine will appear stronger and obvious. When using filling mining, because the goaf behind the working face is continuously filled with paste, the timely support effect on the roof and floor can be used to look at the equivalent roadway that is continuously advancing, as shown in Figure 3. Therefore, the destruction depth of the underlying coal strata in backfill mining can be theoretically calculated using the equivalent roadway theory. For the exploration of the equivalent of the paste-filled working face into a moving roadway (or short-wall working face), the key question is how to determine the space effect and time effect of the equivalent moving roadway.

3.2. Spatial Effect on Equivalent Roadway Width. The width of the equivalent roadway is not the working face control roof distance, but it should be the distance from the coal wall to the filling body at a certain position behind the working face. The filling body at this position should meet certain requirements in terms of strength. With the difference in the paste filling process, the width of the equivalent roadway will also change. Parameters such as the solidification speed of the filling body, the daily footage of the working face, the filling step, and the roof control distance all affect the equivalent roadway.

(1) Before the coal mining machine cuts the coal after the open cut in the working face, the impact of mining on the working face is only the open cut, and the previous analysis has analyzed the open cut as an equivalent moving roadway, and the width of the roadway is the open cut. The width of the cut eye is L cut

(2) When the coal cutting footage of the working face is 1 filling step, it is widened compared to the equivalent moving roadway. Before the filling body solidifies and condenses, the width of the equivalent roadway is L branch + L step (where L step is a filling step, and L branch is the length of the top beam of the support), as shown in Figure 4(a)

(3) As the working face continues to cut coal forward when the coal cutting footage of the working face reaches 2 filling steps, it continues to expand and widen relative to the equivalent moving roadway. The age of the first filling zone in this period is 1 d; then, the width of the equivalent roadway at this time is $(L_{branch} + L_{step}) \sim (L_{branch} + 2 L_{step})$. According to the practice of field engineering application, to ensure the safety of the calculation of the destruction depth value of the underlying coal strata, the width of the equivalent roadway is the largest $(L_{branch} + 2 L_{step})$, as shown in Figure 4(b)

(4) After the goaf is filled with paste material, as the filling body condenses and solidifies, its strength continues to increase, supporting the roof and floor of the goaf. When the strength of the filling body is sufficient to transmit the overlying rock layer's self-weight load, the filling body at this position is regarded as a bunch of equivalents. At this time, the width of the equivalent roadway is $L_{branches} + nL_{steps}$ (the number of days for the filling body to reach the hydraulic pressure resistance is n), as shown in Figure 4(c)

(5) The distance between the coal wall and the filling zone of the working face after mining is the width of the final equivalent roadway. At this time, the maximum equivalent roadway width of the paste filling working face is $L_{cut} + nL_{steps}$. The minimum width is the open-cut eye width L_{cut}. The equivalent roadway width of the paste-filled working face in different states is different. The width of the equivalent roadway is $L_{branch} + n \times L_{steps}$, and the floor damage depth is the largest at this time

3.3. Time Effect on Equivalent Roadway Action. According to the observation results of general roadway deformation, it takes 30-40 days for a stable deformation. After the goaf is filled, the strength of the filling body gradually increases. The filling body prevents the top plate from continuing to sink and transmits the top plate load to the bottom plate. The time is taken by the floor from "excavation-support, support-exposed, filled area-backfill support" which is the time equivalent to the action of the mine pressure on the roadway. The calculation formula is as follows:

Figure 1: The location of Daizhuang Coal Mine.
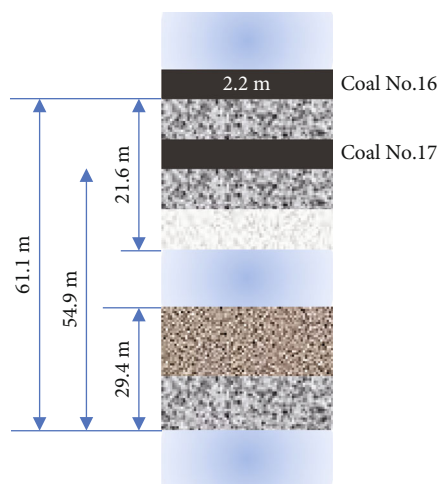
Figure 2: Location relationship between coal seam and aquifer.

$$T = \frac{L_{\text{branch}} + tL_{\text{step}}}{v}, \qquad (1)$$

where L branch is the length of the support, m; T is the equivalent roadway action time, d; v is the advancing speed of the working face, m/d; and t is the time for the filling body to reach the water pressure resistance strength, d.

3.4. Bottom Failure Depth Analysis. Based on the equivalent roadway theory [35–38], the shape of the plastic failure zone of the working face floor with paste filling is shown in Figure 5. When the working face floor is damaged and the plastic failure range occurs, the plastic failure range of the working face floor is divided into the active limit range (such as area I in Figure 5), transition range (area II in Figure 5), and passive limit range (area III in Figure 5); the calculation formula of the floor failure depth can be derived from the theory of plastic slip line field:

$$h_{\text{po}} = \frac{l_a \cos \phi}{2 \cos (\pi/4 + \phi/2)} \exp \left[\left(\frac{\pi}{4} + \frac{\phi}{2} \right) \tan \phi \right]. \qquad (2)$$

Direction of
working face

Solidified filling   Filling pipe   Unmined coal
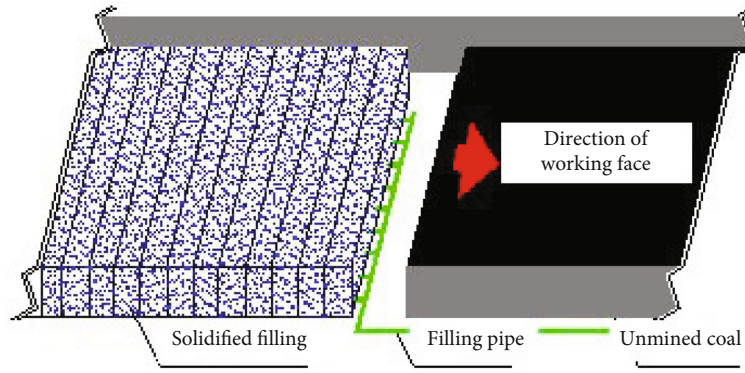
FIGURE 3: Schematic diagram of longwall paste filling working face.

Original opening width

L_q

Advance one filling step

(a) Fill in one step

Original opening width

L_q

Advance one filling step

Advance two filling step

(b) Fill in 2 steps

Equivalent moving roadway width

L_t

Fillings

h_p

h_{p0}

Equivalent moving
roadway floor
failure depth

Advance n filling steps

Original static roadway failure depth

(c) Fill n steps
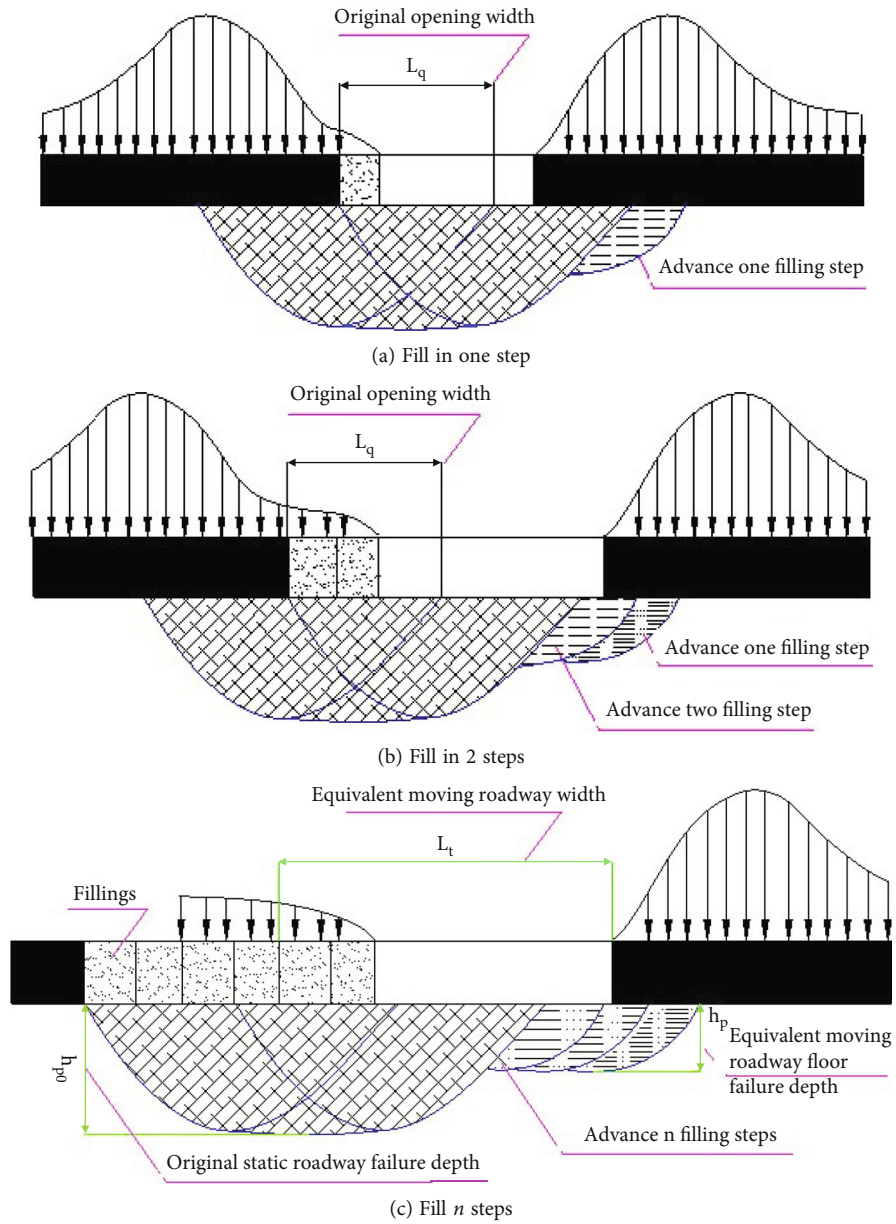
FIGURE 4: The relationship between equivalent roadway width and floor failure depth.
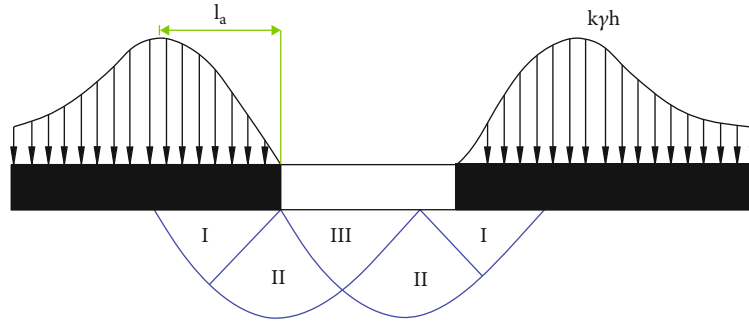
FIGURE 5: Calculation model of equivalent roadway floor failure depth.
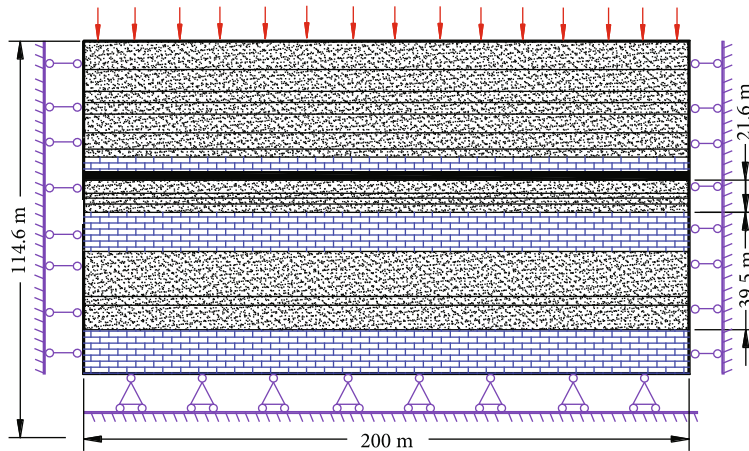
FIGURE 6: Numerical simulation models and boundary conditions.

In the formula, h_{po} is the depth of coal and rock failure under the paste filling face, m; l_a is the width of the plastic zone on the two sides of the roadway, m; and φ is the internal friction angle of the coal seam floor.

4. Numerical Simulation Analysis of Floor Failure

4.1. Model Construction and Program Design. The simulation uses FLAC numerical simulation software. Combining the comprehensive histogram of the 11607 working face on the Daizhuang Coal Mine site and the actual conditions of the four geological boreholes L10-2, L10-4, 11607-2, and 15-2 in the underlying coal seam, the numerical simulation is based on the lower part of the 11607 working face. The height and width of the constructed model are 114.6 m and 200 m, respectively. The cutting height of the 11607 working face is 2 m. The distance between the No. 16 coal seam and the uppermost boundary of the model is 39.6 m, and the distance from the bottom boundary of the model is 75 m. The upper bound of gray is 61.1 m away, and the distance from the upper thirteenth upper bound of the lower part is 21.6 m. The numerical simulation model is shown in Figure 6. In the design model, the inclined length of the 11607 paste filling working face is 120 m, and an open cut is arranged at the left end of the model 50 m, and the mining advances from the left end of the model to the right. The width between the left and right boundaries of the design model is 200 m. The rock mass parameters are given in Table 1.

This simulation is mainly aimed at the research and analysis of the relationship between the different filling process parameters of the paste filling working face and the floor failure depth under the conditions of different filling body strength, filling step, and filling rate at 11607 paste filling working face. First, the coal mining operation is carried out, the goaf is followed by the filling operation, and finally, the working face is overhauled. At the same time, the paste filling body is solidified, and the goaf is filled. The step distance is consistent with the daily footage of the working face, and the numerical simulation plan is designed according to the site conditions: (1) the simulation setting 11607 working face goaf is 98% filling rate, filling step 2.4 m/d, and simulation. The 28 d strength of the filling body is 3 MPa, 4 MPa, 5 MPa, and 7 MPa; (2) the strength (28 d strength) of the paste filling body in the goaf area of 11607 working faces is set to 5 MPa, and the filling rate is 98%. Then, the filling step distance distribution of the simulated paste filling body is 1.2 m, 2.4 m, and 3.6 m.

4.2. Analysis of the Results of Numerical Simulations. According to the simulation results of numerical simulation plan 1 and plan 2, under the conditions of different filling strength parameters, the simulation results of the failure depth of the

TABLE 1: The rock mass properties.

No.	Lithology	Density (kg/m³)	Bulk modulus (GPa)	Shear modulus (GPa)	Cohesion (MPa)	Friction angle (°)	Tensile strength (MPa)
1	Grit stone	2450	31.37	23.51	8.61	44	9.12
2	Fine stone 11 sandstone	2600	19.71	14.62	6.52	37	6.94
3	Medium stone	2550	31.35	20.51	6.80	42	7.61
4	Siltstone	2650	16.35	12.24	4.69	31	2.36
6	Coal	1450	0.78	0.45	2.21	22	0.41
7	Mudstone	2250	7.11	3.98	3.45	35	0.89

(a)

(b)

(c)

(d)
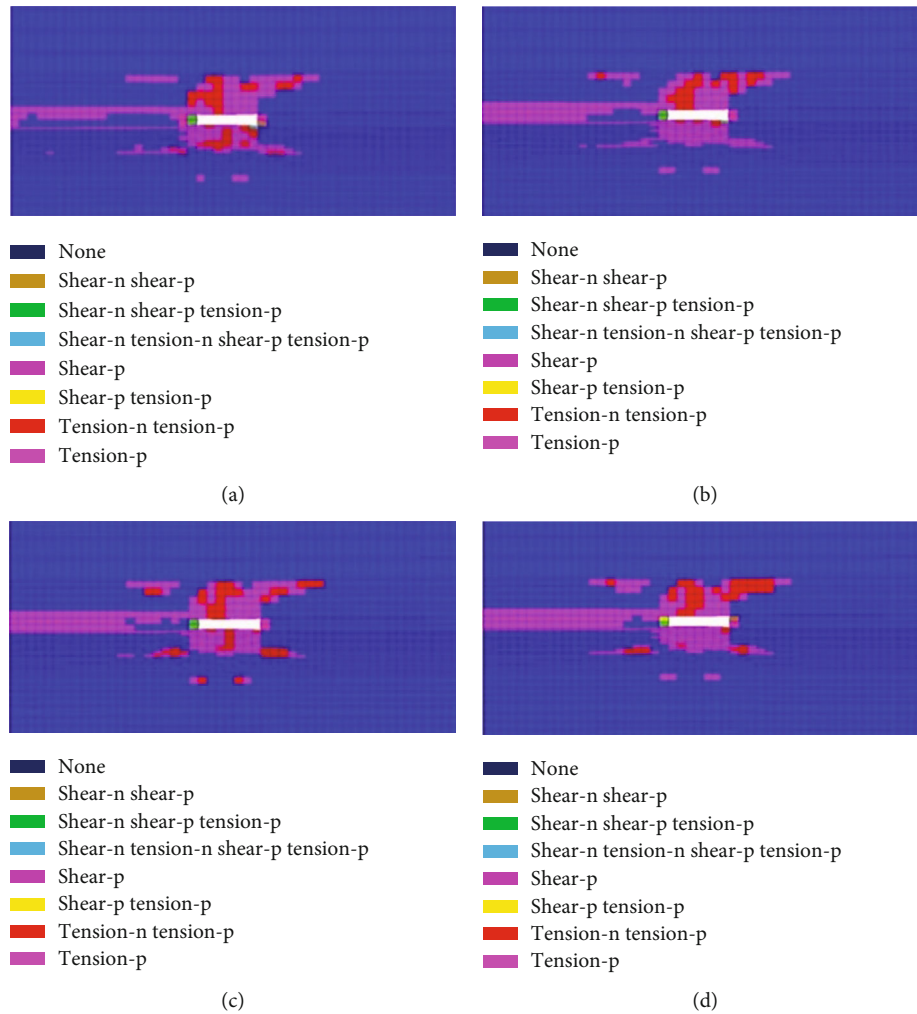
FIGURE 7: Numerical simulation of the plastic zone of 28 d strength of the different paste: (a) 3 MPa, (b) 4 MPa, (c) 5 MPa, and (d) 7 MPa.

floor of the paste filling working face, the deformation of the rock formation, and the distribution of the plastic zone are shown in Figures 7 and 8 (A section is taken at the middle of the advancing direction of the 11607 working face).

It can be seen from the analysis in Figure 7 that when the 28 d strength of the filling paste on the 11607 working face

increases from 3 MPa to 7 MPa, the peak subsidence of the overlying coal strata on the working face also shows a downward trend, and the peak subsidence drops from 250 mm to 200 mm. The bottom heave of the working face has no obvious deformation. When the 28 d strength of the filling paste on the 11607 working face increased from 3 MPa to 7 MPa, no

(a)

(b)

(c)
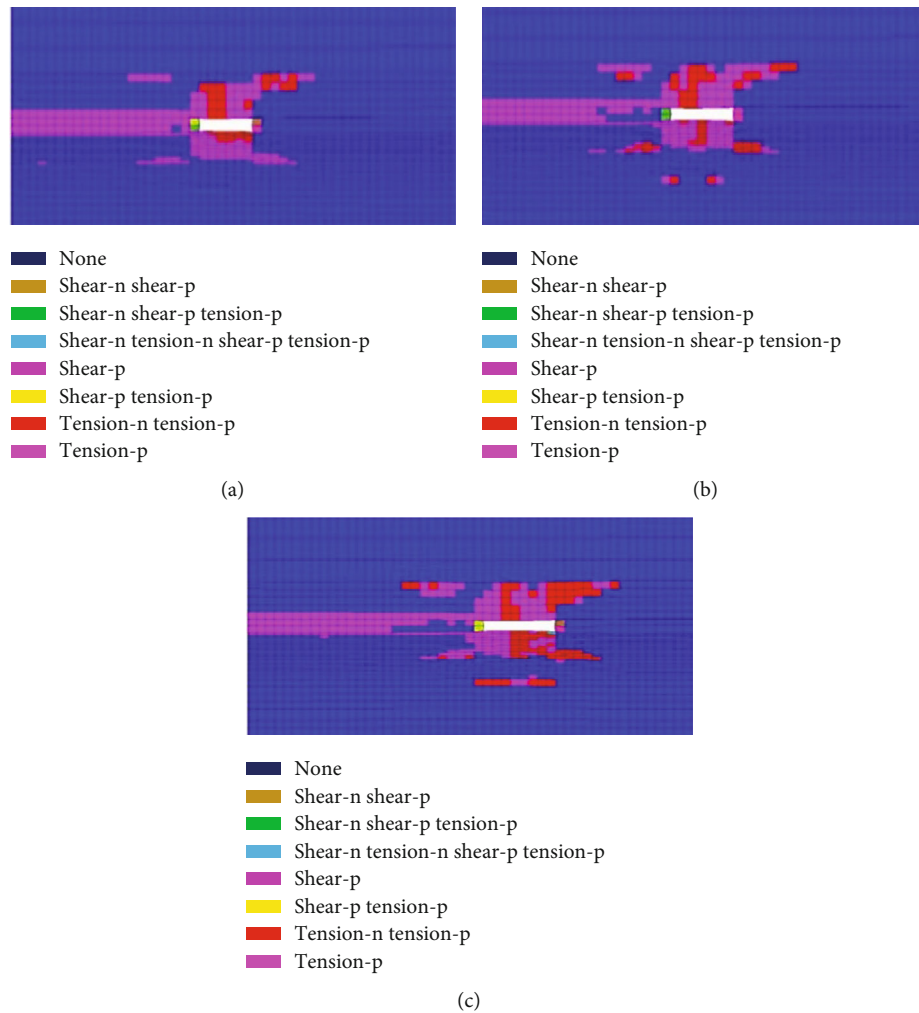
Figure 8: The plastic zone is numerically simulated with different filling steps: (a) 1.2 m, (b) 2.4 m, and (c) 3.6 m.

significant change was found in the depth of the penetrated plastic zone of the coal and rock layer beneath the working face, and only its range slightly decreased.

It can be seen from Figure 8 that when the filling step of the 11607 working face increases from 1.2 m to 3.6 m, the peak subsidence of the overlying coal strata on the working face also shows an upward trend, and the peak subsidence rises from 180 mm to 250 mm. Obvious deformation of the bottom drum of the working face occurs, and the peak value of the bottom drum rises from 180 mm to 200 mm. When the filling step of the 11607 working face was increased from 1.2 m to 3.6 m, no significant change was found in the depth of the penetrated plastic zone of the coal and rock layer beneath the working face. When the filling steps are 1.2 m, 2.4 m, and 3.6 m, the depth of the plastic zone penetrated by the coal strata beneath the working face is approximately 3.6 m, and the coal strata beneath the working face penetrate to the bottom mudstone and fine-grained sandstone. Floor. The plastic zone of the coal and rock layer beneath the working face presents a process from layered failure to final penetration. When the filling step is 2.4 m, the plastic zone in the lower coal layer of the working face extends to the siltstone layer at a distance of about 6.3 m; when the filling step is 3.6 m, the depth of the

plastic zone in the lower coal layer of the working face is still at the lower distance The siltstone layer is about 6.3 m away, but the extent of the plastic zone tends to further increase.

Based on the above analysis, it can be concluded that after the open-cut hole is excavated in the paste filling face, as the face continues to advance coal mining, paste fill the mined area in the goaf behind the face, and the roof of the mined area is no longer. The initial collapse and periodic collapse occur, which is equivalent to the continuous advancement of the open cut in the coal mining process, and the open cut is a special roadway, so the paste filling face is equivalent to the mine pressure generated by the special roadway that is continuously advancing which has a low degree of disturbance to the stress field of the surrounding rock of the roof and floor. The appearance of the mine pressure is very similar to that of the excavation roadway. The difference lies in the maximum vertical stress and plasticity of the filling body in the goaf. The area is smaller than that near the coal wall, and the maximum vertical displacement near the backfill is larger than that near the coal wall. Based on the analysis of the numerical simulation results and the previous theoretical calculations, combined with the actual on-site mining of the 11607 paste filling face of Daizhuang
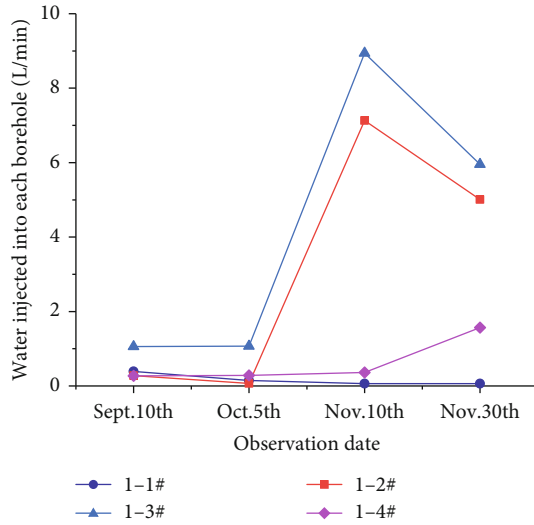
Figure 9: 1# water injection into each borehole at test point.
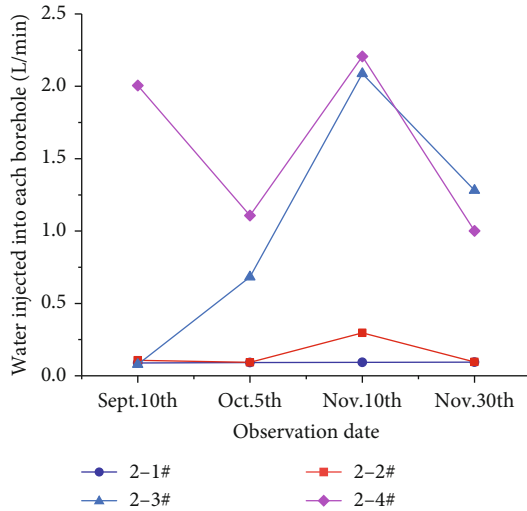
Figure 10: Water injection test results of 1# station.

Coal Mine, and referring to mining practical experience, it is theoretically estimated that the 11607 working face adopts the paste filling technology and then the underlying coal. The depth of rock failure is between 4.6 m and 8.4 m.

5. Field Engineering Application

5.1. Parameter Design. According to the geological report and on-site investigation of the 11607 working face of Daizhuang Coal Mine in the early stage, and according to the types of water-conducting cracks in the underlying coal and rock layers of the working face, the underlying coal and rock layers of the 11607 working face are roughly classified into the following three categories: (1) complete floor area, (2) tectonic development zone, and (3) weak floor zone. The technical measures and safety guarantee methods for the prevention and control of water inrush from the floor are proposed for different areas such as the complete block of the floor, abnor-

mal hydrological detection or high pressure, and weak floor or structurally developed blocks:

(1) Only paste is used to fill the goaf in the complete area of the 11607 working face floor, and the floor is not treated. The design mass concentration of the paste material to fill the goaf is 78%, and the amount of coal gangue, fly ash, and cement is, respectively, $1600 \, \text{kg/m}^3$, $400 \, \text{kg/m}^3$, and $60 \, \text{kg/m}^3$. (2) Weak floor area, combined with simulation and on-site paste filling working face mine pressure influence range, initially determines the weak area to be 50 m outward for floor grouting transformation. (3) The fault-affected area, combined with the simulation and the on-site paste-filling working face's underground pressure influence range, it is preliminarily determined that the F11605-2, F11605-3, and DF16 faults will be reinforced and plugged by floor grouting within 50 m outwards. For small faults exposed in the working face, it is necessary to consider the actual situation of on-site drilling and comprehensive analysis to consider whether to carry out floor grouting reinforcement and plugging reconstruction. (4) High water pressure areas and detection of hydrological abnormal areas, 11607 working face adopts paste filling. After the mined-out area technology, the impact range of the mine pressure around the stope is less than 50 m, so the preliminary design is carried out on the proven high water pressure area of the underlying coal and rock layer (water pressure greater than 4.4 MPa) and the area where hydrological anomalies have been detected at the working face. For dredging treatment, the dredging range is within 100 m from the left to the right and the front and back of the working face.

5.2. Field Application Effect Analysis. Through on-site investigation of the mining practice of Daizhuang Coal Mine 11607 working face, water injection tests were carried out in the track lane of 11607 working face to observe the destruction depth of the underlying coal and rock layers. It is selected to be carried out at a position 150 m away from the stop line of 11607 working face, and two detection points numbered 1# and 2# are arranged. The distance between the two detection points is about 15 m, and both detection points 1# and 2# are arranged 4 water injection test boreholes for observing the destruction depth of the underlying coal and rock layers, and the distance between the water injection test boreholes is 2 m. The elevation and depression angles of the water injection boreholes arranged in the 1# detection point and the No. 16 coal seam are both 60°, and the destruction depths of the underlying coal strata are observed to be 2 m, 3 m, 5 m, and 7 m in sequence. The water injection boreholes arranged in the 2# detection point are perpendicular to the No. 16 coal seam, and the destruction depth of the underlying coal strata is observed to be 2 m, 3 m, 5 m, and 7 m in order. The detection results are as follows:

The water injection volume change curve of each borehole at 1# detection point is shown in Figure 9. Through analysis, it can be seen that the water injection volume of the 1-2# borehole with a depth of 3 m and the 1-3# borehole with a depth of 5 m has relatively large changes. The fluctuation changes are more obvious, while the 1-1# drill hole with a depth of 2 m and the drill hole 1-4# with a depth of 7 m injected lower water volume, and the fluctuation change is not obvious,

indicating that the depth of the underlying coal strata at the working face is 3~ coal, and rock mass cracks within 5 m are more developed, and the depth is greater than that of the coal and rock mass underneath the working face. The degree of development of the cracks is relatively low. Based on the above analysis, the depth of the floor is less than 3~5 m after adopting the paste filling technology in the 11607 working face.

The water injection volume change curve of each borehole at the 2# detection point is shown in Figure 10. The analysis shows that the water injection volume of the four boreholes 2-1#, 2-2#, 2-3#, and 2-4# is relative to that of 1#. The boreholes at the detection points are relatively small, and the water injected into the 2-2# borehole with a depth of 2 m and the 2-4# borehole with a depth of 8 m is 0 L/min, indicating that the depth of the underlying coal strata at the working face is 2 m. The cracks in the coal and rock masses are relatively developed, and the depth is greater than that of the coal and rock masses under the working face. The degree of development of the cracks in the coal and rock masses underneath the working face is relatively low. The destruction depth is about 2 m.

6. Conclusion

(1) Based on the equivalent roadway theory, when the advancing speed of the working face is 1.2~3.6 m/d and the water pressure resistance of the filling body does not exceed 2 d, the failure depth of the floor of the paste filling working face is 4.6~8.4 m

(2) According to the geological report and field survey of the 11607 working face, the floor coal and rock layers of the 11607 working face are divided into three regions. According to the different zones of the floor, technical measures and safety guarantee methods for the prevention and control of water inrush from the floor are proposed

(3) Detect by using the water injection test method onsite, it is concluded that the maximum damage depth of the bottom plate is about 3 m

Data Availability

The Microsoft Excel Worksheet data used to support the findings of this study are available from the corresponding author upon request.

Conflicts of Interest

The authors declare that they have no competing interests.

Acknowledgments

References

[1] X. Shi, H. Zhou, X. Sun, Z. Cao, and Q. Zhao, "Floor damage mechanism with cemented paste backfill mining method," *Arabian Journal of Geosciences*, vol. 14, no. 2, pp. 1–9, 2021.

[2] Q. Sun, G. Meng, K. Sun, and J. Zhang, "Physical simulation experiment on prevention and control of water inrush disaster by backfilling mining under aquifer," *Environmental Earth Sciences*, vol. 79, no. 18, pp. 1–17, 2020.

[3] W. Sun, S. Zhang, W. Guo, and W. Liu, "Physical simulation of high-pressure water inrush through the floor of a deep mine," *Mine Water and the Environment*, vol. 36, no. 4, pp. 542–549, 2017.

[4] Y. Sun, G. Li, J. Zhang, J. Sun, and J. Xu, "Development of an ensemble intelligent model for assessing the strength of cemented paste backfill," *Advances in Civil Engineering*, vol. 2020, 6 pages, 2020.

[5] S. Yu, J. Xu, W. Zhu, S. Wang, and W. Liu, "Development of a combined mining technique to protect the underground workspace above confined aquifer from water inrush disaster," *Bulletin of Engineering Geology and the Environment*, vol. 79, no. 7, pp. 3649–3666, 2020.

[6] Q. Bai, S. Tu, C. Zhang, and D. Zhu, "Discrete element modeling of progressive failure in a wide coal roadway from water-rich roofs," *International Journal of Coal Geology*, vol. 167, pp. 215–229, 2016.

[7] J. Liu, G. Li, S. Yang, and J. Huang, "Prediction models for evaluating the strength of cemented paste backfill: a comparative study," *Minerals*, vol. 10, no. 11, p. 1041, 2020.

[8] H. Rong, G. Li, D. Liang, C. Sun, S. Zhang, and Y. Sun, "Numerical investigation on the evolution of mechanical properties of rock affected by micro-parameters," *Applied Sciences*, vol. 10, no. 14, p. 4957, 2020.

[9] Y. Sun, G. Li, J. Zhang, B. Yao, D. Qian, and J. Huang, "Numerical investigation on time-dependent deformation in roadway," *Advances in Civil Engineering*, vol. 2021, 7 pages, 2021.

[10] J. Zhao, J. Chen, X. Zhang, J. Ning, and Y. Zhang, "Distribution characteristics of floor pore water pressure based on similarity simulation experiments," *Bulletin of Engineering Geology and the Environment*, vol. 79, no. 9, pp. 4805–4816, 2020.

[11] Q. Bai and S. Tu, "A general review on longwall mining-induced fractures in near-face regions," *Geofluids*, vol. 2019, Article ID 3089292, 22 pages, 2019.

[12] C. Eriksson and A. Nyström, "Garpenberg mine–10 years of mining with paste backfill," in *Proceedings of the 21st International Seminar on Paste and Thickened Tailings*, pp. 323–336, Perth, Australia, 2018.

[13] G. Li, Z. Jiang, C. Lv, C. Huang, G. Chen, and M. Li, "Instability mechanism and control technology of soft rock roadway affected by mining and high confined water," *International Journal of Mining Science and Technology*, vol. 25, no. 4, pp. 573–580, 2015.

[14] W. Liu, D. Mu, X. Xie, L. Yang, and D. Wang, "Sensitivity analysis of the main factors controlling floor failure depth and a risk evaluation of floor water inrush for an inclined coal seam," *Mine Water and the Environment*, vol. 37, no. 3, pp. 636–648, 2018.

[15] K. Ma, X. Sun, C. Tang, F. Yuan, S. Wang, and T. Chen, "Floor water inrush analysis based on mechanical failure characters and microseismic monitoring," *Tunnelling and Underground Space Technology*, vol. 108, article 103698, 2021.

[16] W. Song, Z. Liang, and C. Zhao, "Mechanical failure characteristics of mining floor along working face inclination above confined water," *Chinese Journal of Rock Mechanics and Engineering*, vol. 37, no. 9, pp. 144–156, 2018.

[17] M.-K. Bo, "Analysis on reverse fault activation and water inrush possibility for coal mining above confined aquifer in a mining area," *Journal of China Coal Society*, vol. 36, no. 7, pp. 1177–1183, 2011.

[18] J. Chen, J. Zhao, S. Zhang, Y. Zhang, F. Yang, and M. Li, "An experimental and analytical research on the evolution of mining cracks in deep floor rock mass," *Pure and Applied Geophysics*, vol. 177, no. 11, pp. 5325–5348, 2020.

[19] J. Zhang, "Investigations of water inrushes from aquifers under coal seams," *International Journal of Rock Mechanics and Mining Sciences*, vol. 42, no. 3, pp. 350–360, 2005.

[20] S. Zhang, W. Guo, and Y. Li, "Experimental simulation of water-inrush disaster from the floor of mine and its mechanism investigation," *Arabian Journal of Geosciences*, vol. 10, no. 22, pp. 1–11, 2017.

[21] H. Gui, X. Song, and M. Lin, "Water-inrush mechanism research mining above karst confined aquifer and applications in north China coalmines," *Arabian Journal of Geosciences*, vol. 10, no. 7, p. 180, 2017.

[22] Y. Hu, W. Li, Q. Wang, S. Liu, and Z. Wang, "Evolution of floor water inrush from a structural fractured zone with confined water," *Mine Water and the Environment*, vol. 38, no. 2, pp. 252–260, 2019.

[23] Y. Sun, R. Bi, Q. Chang et al., "Stability analysis of roadway groups under multi-mining disturbances," *Applied Sciences*, vol. 11, no. 17, p. 7953, 2021.

[24] N. J. Koupouli, T. Belem, P. Rivard, and H. Effenguet, "Direct shear tests on cemented paste backfill-rock wall and cemented paste backfill-backfill interfaces," *Journal of Rock Mechanics and Geotechnical Engineering*, vol. 8, no. 4, pp. 472–479, 2016.

[25] Z. Liang, W. Song, and W. Liu, "Theoretical models for simulating the failure range and stability of inclined floor strata induced by mining and hydraulic pressure," *International Journal of Rock Mechanics and Mining Sciences*, vol. 132, article 104382, 2020.

[26] S. Liu, W. Liu, and J. Shen, "Stress evolution law and failure characteristics of mining floor rock mass above confined water," *KSCE Journal of Civil Engineering*, vol. 21, no. 7, pp. 2665–2672, 2017.

[27] M. He, P. Guo, J. Wang, and H. Wang, "Experimental study on gob-side entry formed by roof cut of broken roof at shallow depth of hecaogou no. 2 coalmine," *Chinese Journal of Geotechnical Engineering*, vol. 40, no. 3, pp. 391–397, 2018.

[28] W. Li, Y. Liu, W. Qiao, C. Zhao, D. Yang, and Q. Guo, "An improved vulnerability assessment model for floor water bursting from a confined aquifer based on the water inrush coefficient method," *Mine Water and the Environment*, vol. 37, no. 1, pp. 196–204, 2018.

[29] V. Odintsev and N. Miletenko, "Water inrush in mines as a consequence of spontaneous hydrofracture," *Journal of Mining Science*, vol. 51, no. 3, pp. 423–434, 2015.

[30] Y. Sun, G. Li, J. Zhang, J. Sun, J. Huang, and R. Taherdangkoo, "New insights of grouting in coal mass: from small-scale experiments to microstructures," *Sustainability*, vol. 13, no. 16, p. 9315, 2021.

[31] G. Li, Y. Sun, J. Zhang et al., "Experiment and application of coalcrete on roadway stability: a comparative analysis," *Advances in Materials Science and Engineering*, vol. 2020, 14 pages, 2020.

[32] M. Li, J. Zhang, W. Zhang, A. Li, and W. Yin, "Experimental investigation of water-inrush risk based on permeability evolution in coal mine and backfill prevention discussion," *Geofluids*, vol. 2019, Article ID 3920414, 9 pages, 2019.

[33] N. Niroshan, L. Yin, N. Sivakugan, and R. L. Veenstra, "Relevance of sem to long-term mechanical properties of cemented paste backfill," *Geotechnical and Geological Engineering*, vol. 36, no. 4, pp. 2171–2187, 2018.

[34] A. N. Pan, M. W. Grabinsky, and L. Guo, "Shear properties of cemented paste backfill under low confining stress," *Advances in Civil Engineering*, vol. 2021, Article ID 561977, 11 pages, 2021.

[35] S. Ning, W. Zhu, X. Yi, and L. Wang, "Evolution law of floor fracture zone above a confined aquifer using backfill replacement mining technology," *Geofluids*, vol. 2021, Article ID 8842021, 14 pages, 2021.

[36] K. Polak, K. Różkowski, and P. Czaja, "Causes and effects of uncontrolled water inrush into a decommissioned mine shaft," *Mine Water and the Environment*, vol. 35, no. 2, pp. 128–135, 2016.

[37] M. Sheshpari, "A review of underground mine backfilling methods with emphasis on cemented paste backfill," *Electronic Journal of Geotechnical Engineering*, vol. 20, no. 13, pp. 5183–5208, 2015.

[38] Y. Sun, G. Li, N. Zhang, Q. Chang, J. Xu, and J. Zhang, "Development of ensemble learning models to evaluate the strength of coal-grout materials," *International Journal of Mining Science and Technology*, vol. 31, no. 2, pp. 153–162, 2021.

WILEY | Hindawi

Research Article

Surrounding Rock Control Technology When the Longwall Face Crosses Abandoned Roadways: A Case Study

Zhenpeng Jiang,[1] Fangtian Wang [1], Kaijun Miao,[1] and Qinghua Cao[2]

[1]*School of Mines, Key Laboratory of Deep Coal Resource Mining, Ministry of Education of China, China University of Mining and Technology, Xuzhou, Jiangsu 221116, China*
[2]*Juji Coal Mine of Henan Longyu Energy Co., Ltd., Yongcheng, Henan 476600, China*

Correspondence should be addressed to Fangtian Wang; wangfangtian111@163.com

When a working face is crossing the abandoned roadways, problems such as roof subsidence, rock fracture, and instability will occur, resulting in widespread roof fall and rib spalling, which seriously affect safe and efficient mining on the working face. In this paper, the no. 23 coal pillar working face of Juji coal mine is taken as the engineering background, a mechanical model of crossing the abandoned roadways is constructed aimed at the problem of the working face crossing the abandoned roadway group, the collapse of the abandoned roadway roof is analyzed, a scheme of crossing the abandoned roadways is designed, and the development law of the stress and plastic zone after the reinforcement scheme is stimulated and analyzed. The results show that when the working face advances to the abandoned roadway, key block B crosses the abandoned roadway and the solid coal to form a "cross-roadway long key block." It is calculated that the minimum support resistance required for the abandoned roadway is 6700 kN. Based on the results of numerical comparison, it is concluded that filling wood pile when the working face passes through the roof abandoned roadway and adding anchor cables for reinforcement support when the working face crosses the coal seam abandoned roadway effectively reduce the stress concentration of surrounding rocks, decrease the development of the plastic zone, and achieve safe and efficient mining when the working face crosses the abandoned roadways.

1. Introduction

In the process of coal mine production, in order to save coal resources and ensure smooth replacement of the working face, the reserved coal pillar is often recovered and mined. In the coal pillar mining, the coal pillar working face often passes through abandoned roadways, which are usually abandoned roadways that exist before the working face mining and lose their functions. As the mining of the coal pillar working face is subject to the goaf and the abandoned roadway, the movement law of the overburden strata on the working face is different from that of conventional coal mining [1–3]. The main problems faced in coal pillar mining include the following: (1) the occurrence conditions of the coal seam are complex, both sides of the coal pillar working face are goafs, and abandoned roadways can exist in the coal

seams. (2) Rock burst appears violent. The existence of abandoned roadways leads to roof fracture in the working face, to form a "cross-roadway long key block." Therefore, the pressure strengthens. Affected by the abandoned roadways and the goafs, the surrounding rock stress on the working face is redistributed, and the periodic pressure is irregular. (3) The hydraulic support bears uneven stress and needs to bear the impact load caused by roof fracture.

A large number of studies have been made by scholars domestically and internationally on the safety guarantee technology of the working face passing through abandoned roadways. Bai and Hou [4] established a mechanical model of the working face through abandoned roadways and adopted the new technology of high water material filling to ensure the stability of the surrounding rocks of abandoned roadways. Feng et al. [5] developed the technology

of ultrahigh water material filling, which fills the abandoned roadways with high water materials and achieves the strength required in practical projects with different ratios. Zhou and Huang [6, 7] studied the instability mechanism of abandoned roadways and the law of the main roof fracture when the working face passes through the abandoned roadway group and put forward the scheme of the fully mechanized mining face quickly crossing the large-section abandoned roadway group, which can avoid roof fall accidents. Liu et al. [8] analyzed the failure mechanism of surrounding rocks on the fully mechanized mining face by multiple means and determined the support mode of filling the wood stack connection with coal powder and cement, which effectively ensures normal advancement of the fully mechanized mining face. Xu et al. [9] established a mechanical model of the main roof of an abandoned roadway, revealed the stability mechanism of the abandoned roadway roof, and determined the minimum support resistance to maintain the stability of the abandoned roadway roof. Yin et al. [10] applied catastrophe theory to analyze the instability mechanism of the coal pillar between the working face and the front abandoned roadway from the perspective of potential energy accumulation and applied the theory of elastic thin plate to study the stress state and fracture position of the main roof after the coal pillar loses stability. Zorkov et al. [11] studied the classification of the working face entering the predriven coal mining face (PDRR), simulated the process of the working face passing through abandoned roadways under the condition of a thick hard roof, and evaluated the load of the working face support. Tadolini et al. [12] applied the technology of fiber-reinforced shotcrete to roadway support, which helps alleviate the deformation and failure of the roadway caused by cyclic load. Esterhuizen et al. [13] monitored the rock mass displacement, rock support, and stress changes behind the working face and verified the numerical modeling program developed for evaluating the entry into the support system, based on the corresponding data of rock bolt in calibration modeling.

Based on the studies above, different support technologies for crossing abandoned roadways should be adopted in different mine geological environments and mining conditions. At present, the support technologies for crossing abandoned roadways mainly include [14–16] pseudoslope adjustment of the working face, strengthening roof management, concrete grouting, roof fall prevention by isobaric mining, and high water material filling. However, there are few relevant studies on the coal pillar working face crossing abandoned roadways in a deep well and a lack of similar experience of crossing abandoned roadways. Therefore, the abandoned roadway crossing mode should be reasonably selected in combination with the actual geological mining conditions in the technical study of the working face crossing abandoned roadways. In this paper, the no. 23 coal pillar working face in Juji coal mine is taken as the research background, with the methods of theoretical analysis, numerical simulation, and field measurement, the deformation control characteristics of surrounding rocks in the mining in the coal pillar working face in a deep well is studied, and the support scheme for crossing abandoned roadways and the

reinforcement support of the weak roof are designed, which ensures that the stope face crosses abandoned roadways smoothly.

2. Engineering Background

The no. 23 coal pillar working face of Juji coal mine is located at a level of -850 m, the ground elevation is +31.3 m to +32.5 m, the working face is 250 m wide, and the advancing length is about 270 m. The working face is located at the lower part of the north wing of the no. 23 mining area, with no. 2312, no. 2314, and no. 2316 goafs in the north, the protective coal pillar at the lower section of the no. 23 headentry in the south, the no. 23 middle water bunker and winch room in the west, and the no. 23 lower water bunker in the east. In the working face, there are many abandoned roadways, of which three are typical, namely, the track roadway, the headentry, and the return airway. The layout of the working face is shown in Figure 1.

The coal seam mined in the working face is the no. 2 coal seam, with a thickness of 2.0-4.1 m, an average thickness of 2.9 m, an inclination of 10-20°, and an average angle of 15°. Thus, it is a stable coal seam. The geological histogram of the no. 23 coal pillar working face is shown in Figure 2.

There will be some problems when the working face is passing through the abandoned roadways: sharp increase in the stress of the abandoned roadways, serious deformation of the surrounding rocks, roof sinking, and rib spalling. Therefore, the borehole peering instrument was used to detect the development of roadway fractures near the abandoned roadways, so as to analyze the impact of the abandoned roadway group on the gateway. The peering image of the vertical roof borehole near the abandoned roadway side is shown in Figure 3.

As observed, the fracture development at 0.8 m of the rock mass in the borehole is relatively obvious, the fracture area is large, and the fracture extends internally. The circumferential fracture development at 1.7-3.0 m is obvious. With the increase in depth, the degree of fracture decreases. When the depth exceeds 6.5 m, the internal structure is clear and complete, and almost no fracture development appears. From the peering result, near the abandoned roadway, the roof fracture can develop to 5.7 m, and some areas can run through the direct roof. Therefore, a mechanical model should be established to analyze the roof support conditions and structural change characteristics when the working face passes through abandoned roadways.

3. Analysis of Mechanical Characteristics When the Working Face Crosses the Abandoned Roadway

3.1. Establishment of the Mechanical Model of the Working Face Crossing the Abandoned Roadway. When the working face advances towards the abandoned roadway, the initial advancing working face is far from the abandoned roadway, the coal pillar stress is distributed along a saddle curve, and the stress is at a stable level. The breaking process is shown in Figure 4.
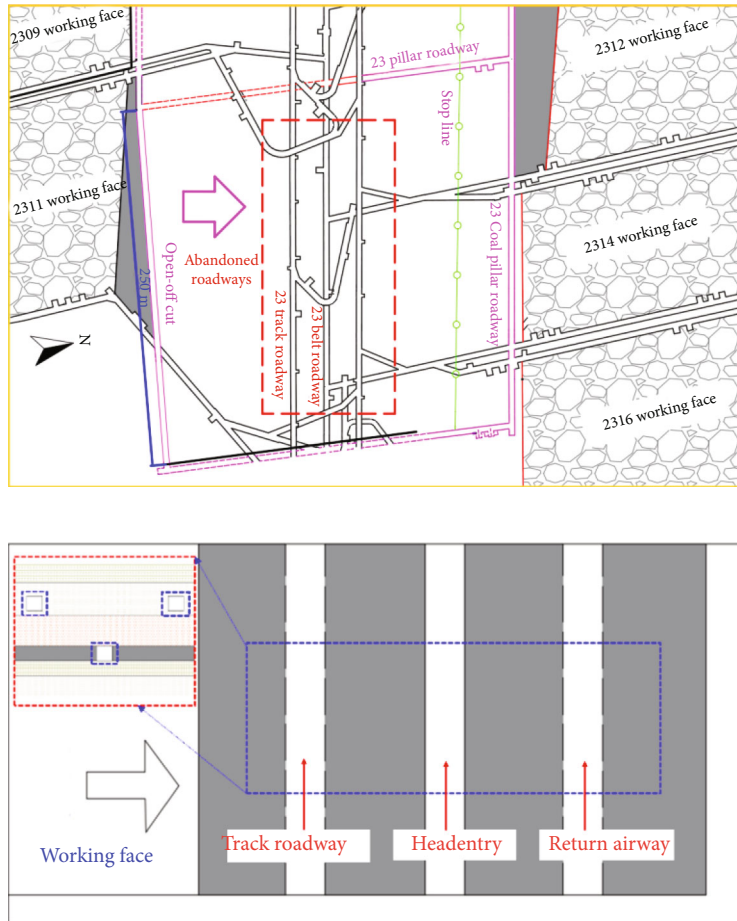
Figure 1: Layout of the no. 23 coal pillar working face.

Order	Histogram		Depth (m)	Thickness (m)	Rock structure	Lithology
1			721.60 m	2.90 m	Main roof	Fine grained sandstone
2			729.70 m	8.10 m		Sandy mudstone
3			730.42 m	0.72 m	Immediate roof	Carbonaceous mudstone
4			735.62 m	5.20 m		Siltstone
5			737.52 m	2.90 m	Coal seam	Coal
6			741.46 m	2.94 m	Immediate floor	Mudstone
7			750.06 m	8.60 m	Main floor	Fine grained sandstone
8			754.46 m	4.40 m		Sandy mudstone

Figure 2: Geological histogram.

(a) 0.8 m

(b) 1.7 m

(c) 2.6 m

(d) 4.6 m

(e) 5.7 m

(f) 6.5 m
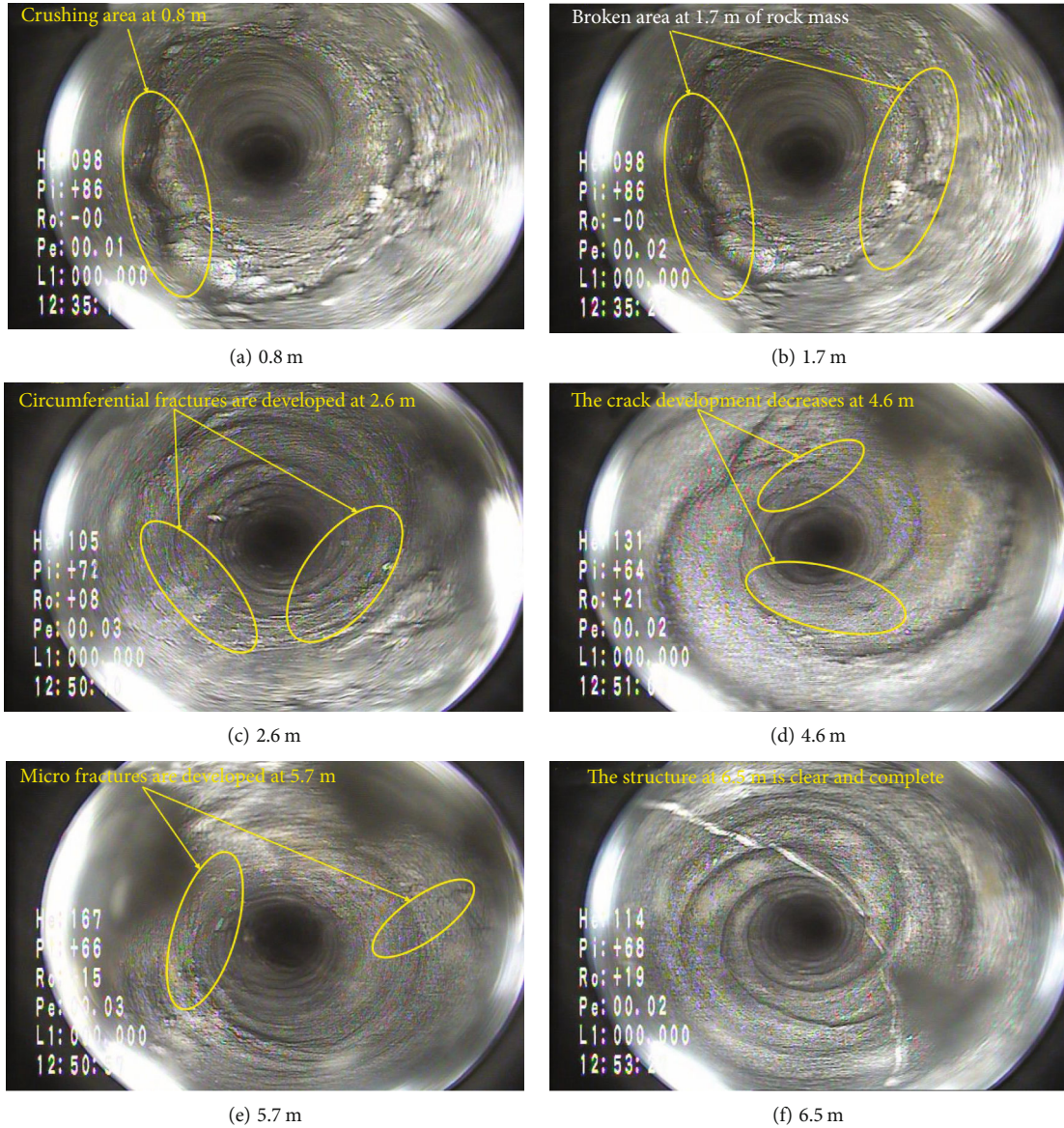
FIGURE 3: Peering image of the vertical roof borehole near the abandoned roadway side.
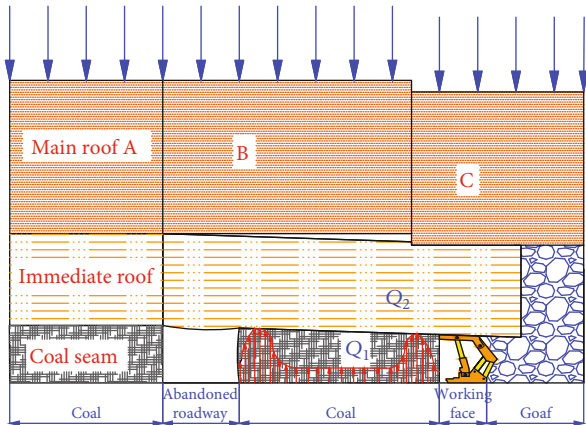
FIGURE 4: Schematic diagram of crossing the abandoned roadway during initial mining.

When advancement continues and affected by the abandoned roadway, the main roof breaks into key blocks, the coal pillar stress is distributed in double-saddle shape, and the bearing capacity of the coal pillar gradually decreases. The further breaking process is shown in Figure 5.

When the working face advances close to the abandoned roadway, the coal pillar before the abandoned roadway is broken and loses its stability and bearing capacity. The roof is broken into a masonry beam structure. The key block rotates in advance, and the stress of solid coal is redistributed. Key block B crosses the roadway and solid coal to form a "cross-roadway long key block" [17–21]. The block is broken in front of the abandoned roadway. The model diagram of crossing the abandoned roadway is shown in Figure 6.

The stress analysis of key blocks B and C when the working face passes through the abandoned roadway is shown in Figure 7.
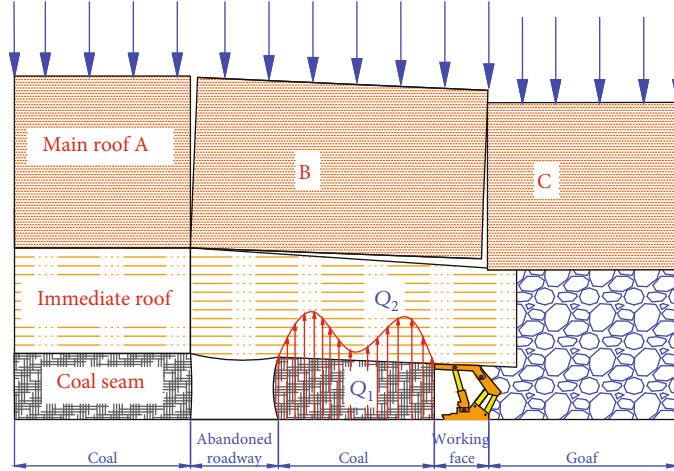
FIGURE 5: Schematic diagram of crossing the abandoned roadway during medium-term mining.
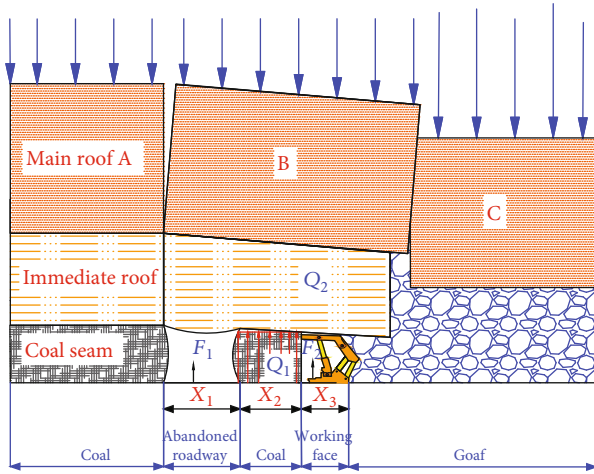
FIGURE 6: Schematic diagram of roadway crossing close to the abandoned roadway.

After analyzing the stress state of key blocks B and C, the balance equation is obtained:

$$\frac{2R_1(x_1 + x_2 + x_3)}{3 + T(h - \Delta - a) - (P_1 L \cos \theta_1)/2} = 0, \quad (1)$$

$$P_1 = R_1 + Q_A. \quad (2)$$

The simultaneous equation of (1) and (2) is

$$T = \frac{P_1 L \cos \theta_1}{2(h - \Delta - a)} - \frac{2R(x_1 + x_2 + x_3)}{3(h - \Delta - a)}. \quad (3)$$

To prevent the key block of the main roof from sliding and losing stability at point A', the following conditions shall be met:

$$T \tan \varphi \geq Q_{A'}. \quad (4)$$

By introducing formula (4) into (1)–(3), we can get

$$\begin{cases} R_1 \geq P_1 \left[\dfrac{3L \cos \theta_1 \tan \varphi - 6(h - \Delta - a)}{4 \tan \varphi (x_1 + x_2 + x_3) - 6(h - \Delta - a)} \right], \\[2mm] P_1 = bL(q + h\gamma_2), \\[2mm] \theta_1 = \dfrac{\arcsin [M - (K_P - 1)\sum h]}{L}, \\[2mm] a = \dfrac{h - \Delta}{2}. \end{cases} \quad (5)$$

In the formula, T is the horizontal force on the key block (kN), a is the length of the contact surface pressed between key blocks B and C (m), R_1 and R_2 are the supporting forces of the immediate roof and the gangue on key blocks B and C (kN), Q_A and Q_B are the shear forces on the key blocks (kN), P_1 and P_2 are the self-weight and load borne of key blocks B and C (MPa), L and l are the lengths of key blocks B and C (m), θ_1 and θ_2 are the rotation angles of key blocks B and C (°), h is the thickness of key block B (m), γ_2 is the unit weight of the immediate roof (kN/m³), Δ and q are the rotation sinking value (m) and load borne of key block B (MPa), K_P is the rock dilatancy coefficient, b is the width of the hydraulic support (m), and Σh is the thickness of the immediate roof (m).

Based on the above parameters, F_1, the critical support resistance of the abandoned roadway roof, is calculated:

$$\frac{F_1 x_1}{2} + F_2 \left(x_1 + x_2 + \frac{x_3}{3} \right) \\ - \frac{2(Q + R_1)(x_1 + x_2 + x_3)}{3} = 0, \quad (6)$$

$$F_1 + F_2 = Q + R_1, \quad (7)$$

$$F_1 = \frac{2x_1 + 2x_2 - 2x_3}{3x_1 + 6x_2 + 2x_3}(Q + R_1). \quad (8)$$

The simultaneous equations (5)–(8) are obtained to substitute the relevant parameters of Juji coal mine: the main
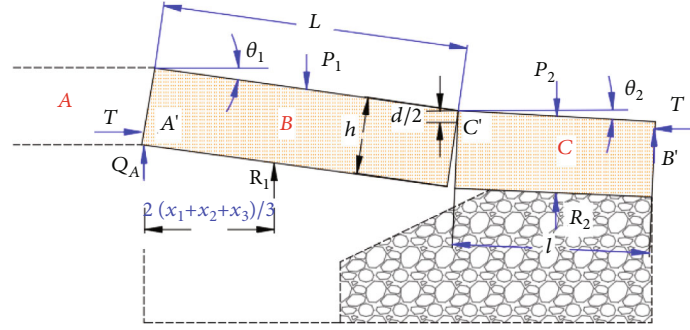
FIGURE 7: Stress state of key blocks B and C.

TABLE 1: Physical mechanical parameters of coal rock in the established model.

Lithology	Bulk modulus (GPa)	Shear modulus (GPa)	Internal friction angle (°)	Cohesion (MPa)	Tensile strength (MPa)	Density (kg·m^{-3})
Main roof	3.2	1.8	33.82	7.27	5.66	2600
Immediate roof	4.3	2.6	34.99	10.79	8.41	2400
II2 coal	1.7	1.0	32.21	2.08	0.77	1400
Immediate floor	4.5	3.1	34.21	10.70	6.21	2400
Main floor	8.0	4.0	36.50	9.89	9.30	2500

roof thickness of the no. 23 coal pillar working face $h = 11.0$ m, the immediate roof thickness $\Sigma h = 5.92$ m, the internal friction angle in the rock stratum $\varphi = 34°$, the unit weight of the rock stratum $\gamma_2 = 26$ kN/m^3, the coal thickness $M = 2.9$ m, the unit weight of coal seam $\gamma_1 = 14$ kN/m^3, and the roof control distance $x_3 = 3.51$ m. It is calculated that the minimum support resistance required for the abandoned roadway is $F_1 = 6700$ kN.

However, the geological conditions of the no. 23 coal pillar working face are complex. There are many abandoned roadways located in the roof and coal seams, and around the coal pillar are goafs. Further analysis should be made on the distributions of the surrounding rock stress and plastic zone of the abandoned roadways in the mining process, to ensure that the working face passes through the abandoned roadways safely.

3.2. Characteristics of Mining When the Working Face Crosses the Abandoned Roadways. The FLAC3D software was applied to simulate and study the working face crossing the abandoned roadways, thus simulating and analyzing the maximum vertical stress and the development law of the plastic zone when the working face crosses the abandoned roadways. The Mohr-Coulomb failure criterion was adopted for the model. The *x*-axis represents the advancing direction of the working face. The *x*-axis is taken as 400 m, the *y*-axis is taken as 300 m, the *z*-axis is taken as 60 m, and the ground stress is taken as 20 MPa. The physical mechanical parameters of coal rock in the established model are shown in Table 1.

The model limits the lateral and bottom displacements, applies corresponding stress compensation on the upper boundary, and scales to a certain extent. The designed working face extends a length of 200 m and a width of 110 m.

Goafs were arranged on both sides of the working face. In the middle part of the working face, three abandoned roadways were arranged, namely, the track roadway, the headentry, and the return airway. The roadway widths were 4 m, the heights were 3 m, and the adjacent spacings were 20 m. The track roadway and the return airway were located at 5 m above the coal seam, and the headentry was located in the coal seam. The stress and the development law of the plastic zone when the stimulation working face passes through the three abandoned roadways are shown in the model in Figure 8.

The variation law of vertical stress distribution when the working face passes through the track roadway, the return airway, and the headentry is shown in Figure 9.

According to the results in Figure 9:

(1) In the mining process from 50 m to 100 m in the working face, the peak stresses are 54.6, 55.3, 54.9, 21.3, 57.4, and 54.6 MPa, respectively. When the working face is mined to 75 m, there is only 5 m coal pillar between the working face and the headentry, and the coal pillar loses its bearing capacity

(2) When the working face passes through the roof abandoned roadway, the leading stress peak shifts to the abandoned roadway and overlaps with the stress at the abandoned roadway. The stress peak increases continuously, and the stress intensively and gradually extends to the upper abandoned roadway, with a large degree of concentration

(3) When the working face passes through the abandoned roadway of the coal seam, the peak stress gradually shifts to the abandoned roadway. As the working face advances, the width of the solid coal
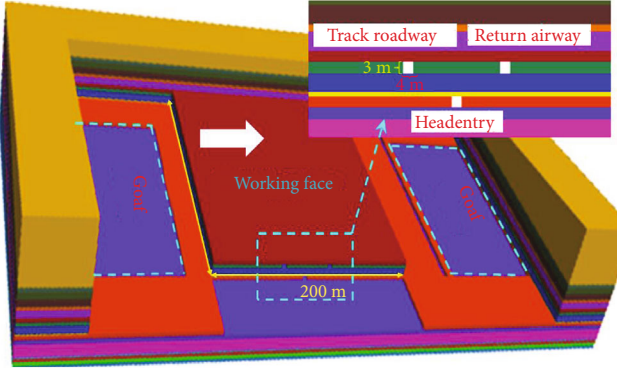
FIGURE 8: Numerical model of crossing the abandoned roadways.

pillar between the abandoned roadway and the working face decreases continuously, and its bearing capacity also decreases. When it is shortened to the limit width of the coal pillar, it will lose its bearing capacity and fully reach plastic failure

The development law of the coal seam and roadway plastic zone when the coal pillar working face passes through the track roadway, the return airway, and the headentry is shown in Figure 10.

As shown in Figure 10, the development law of the plastic zone is as follows: when the working face passes through the roof roadway, the front coal wall on the initial advancing working face is affected by the advanced stress. The development depth in the plastic zone is 6.2 m, and the development depth in the plastic zone on the sidewall of the abandoned roadway near the working face is 2.4 m. Plastic deformation occurs on the roof and the sidewall. The development of solid coal between the working face and the track roadway is distributed as "plastic zone-elastic zone-plastic zone." When the working face continues to advance, the development of the coal pillar plastic zone between the working face and the abandoned roadway is gradually connected.

In the actual mining process, the roof thickness changes with the strike of strata, and the thickness distribution of the immediate roof on the working face is uneven. Therefore, the weak part of the immediate roof requires additional reinforcement.

3.3. Analysis of the Position of the Weak Roof in the Working Face. The safe rock pillar thickness refers to the minimum rock pillar thickness when the roof can bear the concentrated stress caused by coal mining and the support does not collapse as it moves downwards. The section where the thickness of the abandoned roadway and the roof rock pillar on the working face is less than or equal to the safe rock pillar thickness is the short-distance cross-mining section, and the mining of this section needs to be strengthened.

The thickness of the safe rock pillar (T) is composed of the maximum depth of plastic failure on the panel roof (T_1), the thickness of the effective bearing rock stratum (T_2), and the maximum height of roof failure in the underlying roadway (T_3), that is, $T = T_1 + T_2 + T_3$.

(1) Calculation of the maximum depth of roof failure on the working face (T_1)

$$T_1 = \frac{L \sin \varphi}{2 \cos ((\pi/4) + (\varphi/2))} \times \exp\left[\cos\left(\frac{\pi}{4} + \frac{\varphi}{2}\right) \tan \varphi\right].$$ (9)

In the formula, L is the distance from the peak bearing pressure to the coal wall (taken as 5 m) and ψ is the internal friction angle of roof rock (34° for sandy mudstone).

(2) Calculation of bearing stratum thickness (T_2)

The thickness of the bearing rock stratum shall be greater than the minimum thickness when shear or tensile failure occurs, i.e., $T_2 > \text{Max} \{T_{2S}, T_{2T}\}$. T_{2S} is the minimum thickness of the bearing stratum in the case of shear failure, and T_{2T} is the minimum thickness of the bearing stratum in the case of tensile failure.

$$T_{2S} = \frac{3q(L_1 + L_2)}{8R_S},$$
$$T_{2T} = \sqrt{\frac{3q(L_1 - L_2)^2}{16EIR_T}}.$$ (10)

In the formula, q_1 is the uniform load of bearing pressure on the working face (taken as 0.67 MPa), R_S is the shear strength of the roof rock beam (10.35 MPa), L_1 is the length of the hydraulic support (4.7 m), L_2 is the roadway width (4.0 m), EI is the product of elastic modulus and inertia distance of the roof rock (4 MPa, m⁴), and R_T is the tensile strength of the roof rock beam (5.6 MPa).

(3) Calculation of the height of roadway roof failure (T_3)

Within the normal range, the height of roadway roof failure should not exceed the caving arch height of the roadway roof. The value is related to the roadway width and the firmness coefficient of roof rock.

$$T_3 = \frac{L_2}{2f} \leq T_M.$$ (11)

In the formula, T_M is the carving arch height of the roadway roof (m), f is the firmness coefficient (taken as 3.3), and L_2 is the roadway width (4.0 m).

Through calculation, the thickness of the safety rock column is $T = 3.61$ m (taken as 4 m). It is understood that the short-distance cross-mining position is the section where the thickness of the slate pillar of the roadway and the coal seam roof is not greater than 4 m. In the roof roadway, reinforcement measures can be taken for the roadway section within 4 m above the coal seam. The area to be reinforced in the no. 23 pillar working face is shown in Figure 11. In the abandoned roadways of the internal roof on the working face, there are 12 roof tunnels in which roof reinforcement is required.

(a) Backstoping 50 m   (b) Backstoping 60 m   (c) Backstoping 70 m

(d) Backstoping 75 m   (e) Backstoping 80 m   (f) Backstoping 100 m
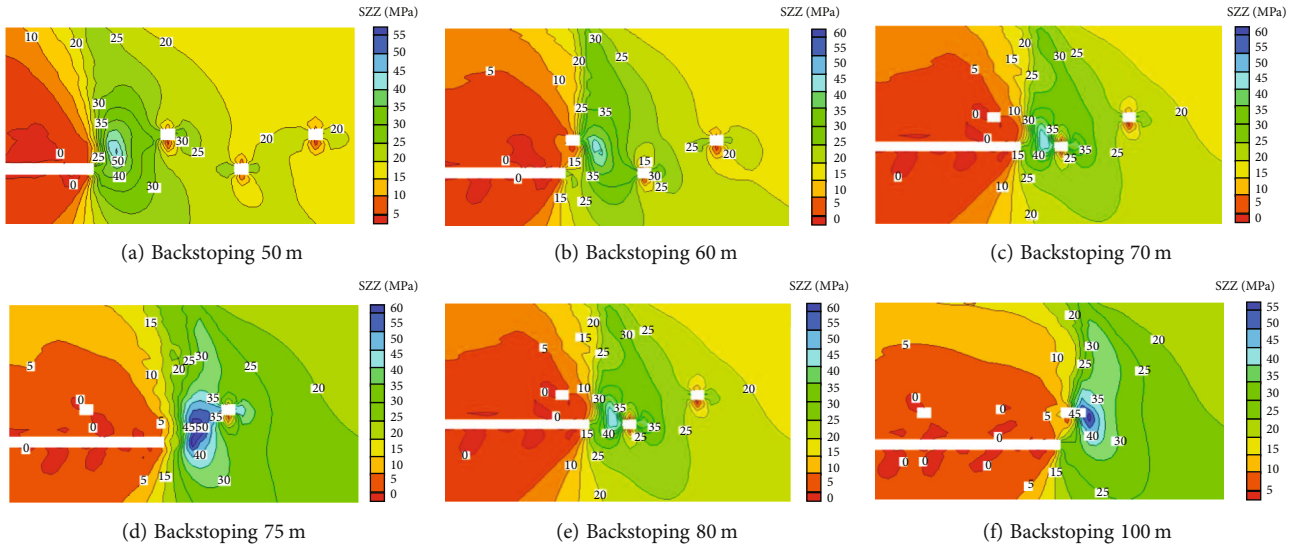
FIGURE 9: Stress distribution at different positions when the working face passes through the abandoned roadways.

(a) Backstoping 50 m   (b) Backstoping 60 m   (c) Backstoping 70 m

(e) Backstoping 75 m   (d) Backstoping 80 m   (f) Backstoping 100 m
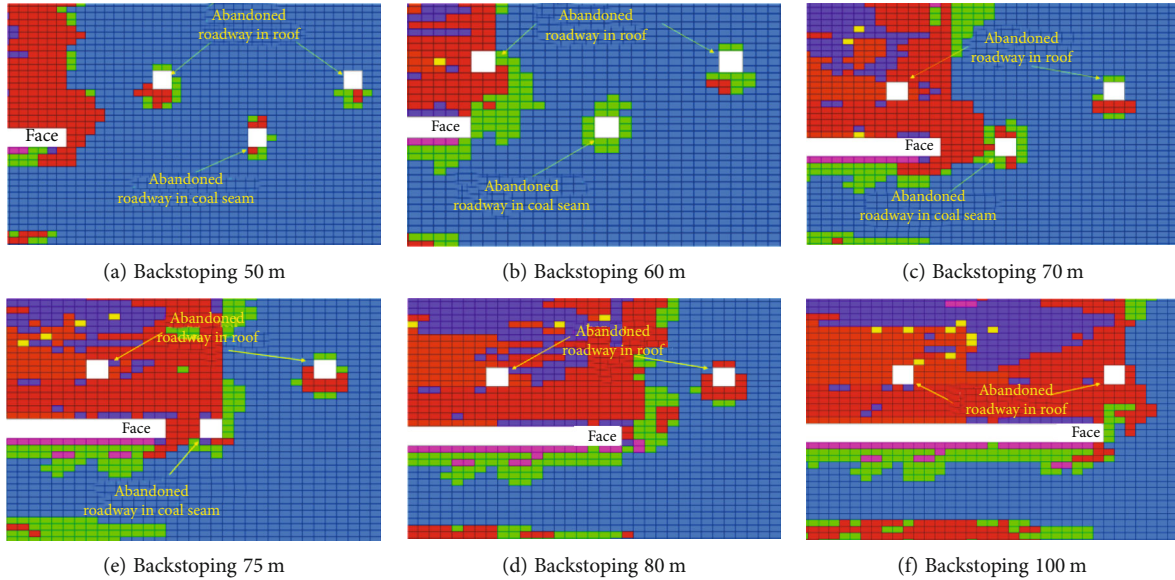
FIGURE 10: Development of plastic zones at different positions when the working face passes through the abandoned roadways.

4. Reinforcement Support Scheme and Effect for the Working Face Crossing the Abandoned Roadway

4.1. Reinforcement Support Measures for the Working Face Crossing the Abandoned Roadway. As the roadway is located in the coal seam, with long support length and time, the design is to carry out pseudoinclined mining in the working face and to add anchor cable to the coal seam abandoned roadway to reinforce the support. In the no. 23 mining area, the inclined coal outlet of roadway 2311 and the combined coal outlet of roadway 2311, roadway 2314, and roadway 2312 are coal roadways. The reinforcement scheme is to construct two rows of anchor cables along the lines on the left and right from the roadway centerline, with an anchor cable spacing of 1.6 m. The specification of the anchor cable

is $\Phi21.6 \times 9200$ mm, equipped with a 300×300 mm anchor cable tray. The reinforcement support by means of the anchor cable is adopted to improve the roadway support strength and achieve the support resistance of crossing the empty roadway. The layout of the anchor cable for the reinforcement roof in the headentry is shown in Figure 12.

4.2. Reinforcement Measures for the Weak Roof in the Working Face Crossing the Abandoned Roadway. In the previous reinforcement measures for the abandoned roadway roof, both the wood pile supporting and filling technologies can strengthen the roof support capacity. Also, when used as a false roof, they allow the hydraulic support to hold the wood pile or filling body above when the roof collapses, so that there is no empty roof above the support. The supporting effect is relatively excellent [22–25].
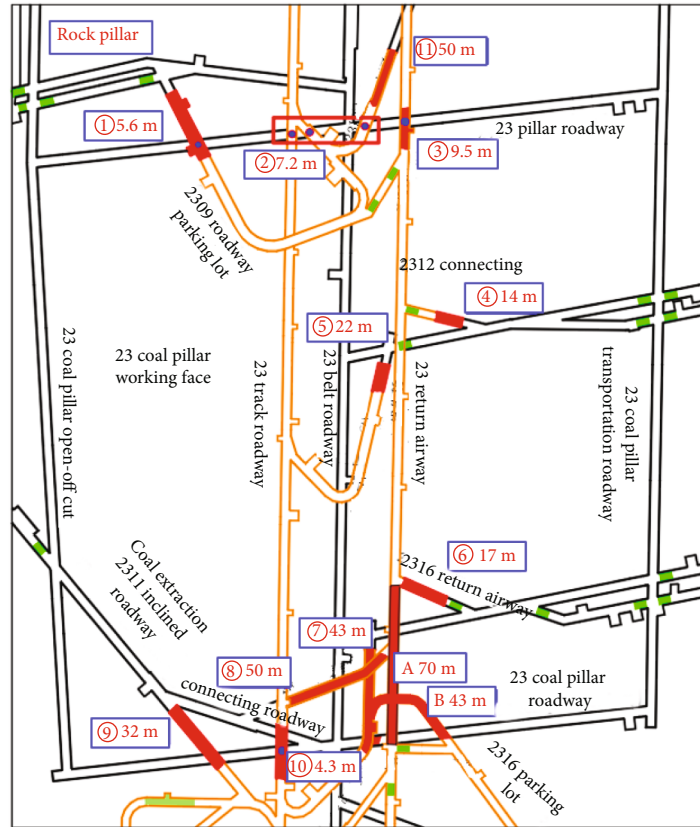
Figure 11: Positions requiring to be reinforced when the working face passes through the roof abandoned roadway.
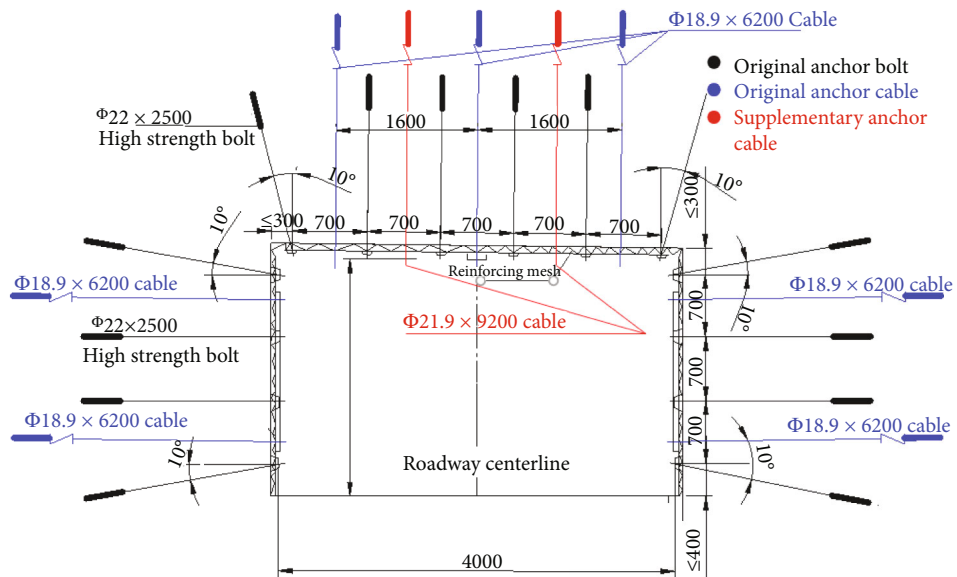
Figure 12: Layout of anchor cables for the reinforcement roof in the headentry.

The no. 23 working face contains many abandoned roadways, each of which needs a small support area. If the filling technology is adopted, the construction process is complex and the cost is high. The wooden pile supporting process is simple, and the mining period of the working face is short; thus, it can meet the supporting requirements and can be a reasonable choice for the no. 23 coal pillar crossing the working face. The design scheme for strengthening the weak roof with wooden pile support is as follows:

(1) At no. 2, no. 3, and no. 10 reinforcement points, the rock columns exceed 4 m, and there is no risk of roof
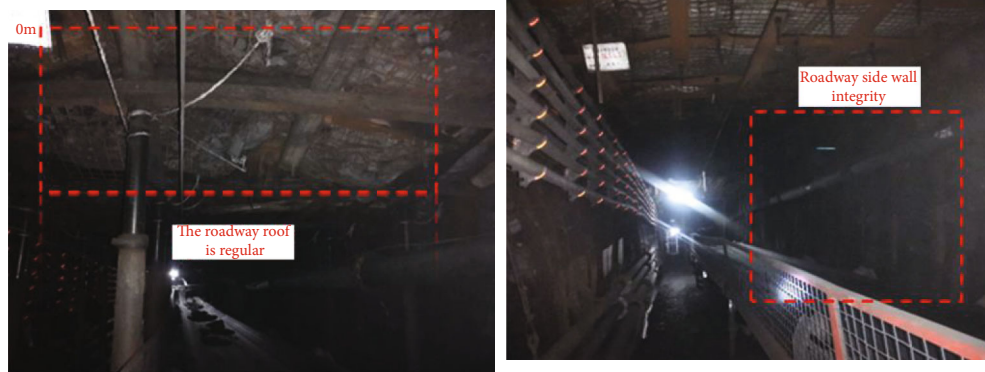
FIGURE 13: Field support effect on the working face.

fall in passing through the roadway normally; thus, no reinforcement measures are required. At the no. 1 point, the rock pillar is 5.6 m, and the roadway in this section needs to be reserved along the goaf. Therefore, the spatial intersection in the roadway at the no. 1 point needs to be reinforced, to ensure the roadway supporting effect during roadway retention. The roadway reinforcement length is 5 m, and the reinforcement method is to set up wooden stacks connecting the top to the bottom, which are bound firmly to prevent collapse

(2) No. 4 to no. 9 reinforcement points are all the junctions of the coal roadway and the rock roadway, with the highest risk of roof fall during backstoping; thus, key reinforcement is required. The reinforcement length is 14 m at the no. 4 point, 22 m at the no. 5 point, 17 m at the no. 6 point, 43 m at the no. 7 point, 50 m at the no. 8 point, and 32 m at the no. 9 point. The reinforcement method is to arrange a layer of wood beams at an interval of 1 m along the disposal and roadway side on the bottom plate, arrange a layer of reinforcement mesh on the wood beam 2 m before the junction of coal and rock, and then set wood cribs on the wood beam to connect the top and bind them together to form a whole

(3) The reinforced sections A and B are both rock roadways near the coal seam, where the rock pillar is less than 4 m and the minimum rock pillar is 1.8 m. They are locations with high risks of roof fall during backstoping and need to be reinforced. The reinforcement length is 70 m for section A and 43 m for section B

4.3. Support Effect of the Working Face Crossing the Abandoned Roadway. After the support scheme is implemented, when the working face passes through the coal seam abandoned roadway, all the coal pillars between the coal seam abandoned roadway and the working face have undergone plastic failure. With the continuous reduction of the coal pillar width and under the mining impact, the plastic zone of the surrounding rock in the abandoned roadway extends to the deeper part, the shear failure state develops

to tensile failure, and the coal pillar loses its bearing capacity. After the working face is strengthened by wood pile classified and anchor cable reinforcement, the stress concentration is reduced, the stress of surrounding rock declines, and the impact of the abandoned roadway on the working face mining is reduced. The effect after abandoned roadway support is shown in Figure 13.

After the reinforcement measures are taken, the roadway support effect is good. Therefore, the reinforcement measures are feasible.

In the mining process, the hydraulic support resistance on the working face was monitored. The monitored objects were the three abandoned roadways in the middle part of the working face, namely, the track roadway, the transit roadway, and the return airway. The headentry was taken as the 0 position on the working face, the support resistance was tested and collected within 100 m before and after the transit roadway, and the characteristics of the working resistance of hydraulic support were at different positions when the working face was pushed to the abandoned roadways. The average support resistances were drawn into a curve, as shown in Figure 14. The impact on the support resistance on the working face in passing through the abandoned roadways is analyzed.

As shown in Figure 14:

(1) In the advancement of the working face, the influence range of the abandoned roadway is 50 m. Beyond 50 m, the support resistance remains 29.4 MPa, basically not affected by the abandoned roadway. Within 50 m and nearing the abandoned roadway, the influence degree gradually increases. When the working face is pushed to the roof abandoned roadway, the working resistance reaches the peak

(2) When the working face advances to the track roadway, the headentry, and the return airway, the working resistances reach the peak values 39.3, 40.6, and 39.6 MPa, respectively. After the working face passes through the track roadway, the support resistance, under the overlapped impact of the track roadway and the transit roadway simultaneously, first decreases and then increases. But the resistance peak is still within the pressure range of the support safety
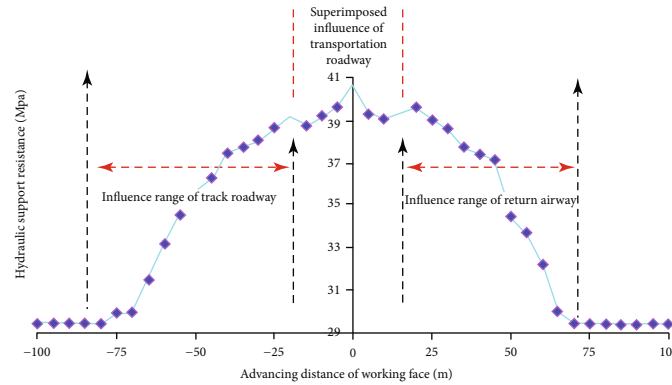
FIGURE 14: Support resistances when the working face is pushed to different positions in the abandoned roadway.

valve, and the hydraulic support can continue to work normally

The monitoring of hydraulic support resistance shows that the methods of wood pile reinforcement and anchor cable reinforcement on the working face are effective. The hydraulic support can operate normally, which ensures safe mining on the no. 23 coal pillar working face.

5. Discussions

The working face crossing the abandoned roadway under complex stress conditions in deep mining is a complicated engineering issue. Before the support design scheme was made, a large number of field researches and knowledge were made, a mechanical model was established for the characteristics of the main roof fracture, and its characteristics of fracture were analyzed. A numerical simulation analysis was carried out on the characteristics of the surrounding rock stress and the plastic area changes when the working face passed through the abandoned roadway group. A support scheme is designed for the working face crossing several abandoned roadways as per different roadway positions in the working face, and the characteristics of working resistance change as the working face hydraulic support advances are monitored throughout the process, to verify the feasibility of the support scheme. The support scheme designed in this paper is the final result of a series of work above.

The working face is buried deep, the immediate roof is thick, and the rock pressure is not obvious. Even in the same mine, the surrounding rock structure changes greatly and has different characteristics. The support scheme required still needs to be reevaluated and designed. The mechanical model established herein is not perfect in details. The establishment of the model is considered from the view of the main roof but the influence when the immediate roof contains two layers of rocks with an accumulative thickness of 5.92 m. The monitoring result of the support resistance on the hydraulic support shows that the fluctuations are as we expected. If the surrounding rock control theory is optimized, the simulation effect of the mechanical model can be closer to the engineering practices, and the error can even be limited within a range, so that the utilization rate of mine

resources will be improved. Therefore, more relevant practices and researches are required in the future.

6. Conclusions

(1) The mechanical model of the coal pillar working face crossing the abandoned roadway is constructed. The process of fracture when the working face crosses the abandoned roadway is analyzed, which mainly shows that key block B crosses the abandoned roadway and the solid coal, forming the "cross-roadway long key block." It is calculated that the minimum support resistance required for the abandoned roadway is 6700 kN

(2) The stress distribution when the working face passes through the abandoned roadway is simulated and analyzed. The results show that when the working face passes through the roadway, the stress gradually increases, stress concentration appears, the plastic zone gradually extends to the deeper part, and the plastic zones of surrounding rocks of the abandoned roadway are connected, which affect the normal mining of the no. 23 coal pillar working face

(3) The support scheme of the working face crossing the abandoned roadway is proposed. According to the roof abandoned roadway, the thickness of the safe rock column is calculated to be 4 m, and wood pile filling is applied to strengthen reinforcement. The coal seam abandoned roadway is used for pseudoinclined mining and anchor cable reinforcement support on the working face. The field observation shows good supporting effect

(4) The monitoring scheme of working resistance on the hydraulic support in the working face is put forward. When the working face advances to the headentry, under the overlapped impact of the headentry abandoned roadway group, the support resistance reaches the peak value of 40.6 MPa, which is still within the normal range of the safety valve. The wood pile classified reinforcement and anchor cable reinforcement scheme can ensure that the working face passes through the abandoned roadways safely

Data Availability

The data used to support the findings of this study are included within the article.

Conflicts of Interest

The authors declare no conflicts of interest.

Acknowledgments

References

[1] M. G. Qian and P. W. Shi, "*Mine pressure and strata control*," China University of Mining and Technology Press, 2003.

[2] M. G. Qian, X. X. Miao, and F. He, "Analysis of key block in the structure of voussoir beam in longwall mining," *Journal of China Coal Society*, vol. 19, no. 6, pp. 557–563, 1994.

[3] J. L. Xu and J. F. Ju, "Structural morphology of key stratum and its influence on strata behaviors in fully-mechanized face with super-large mining height," *Chinese Journal of Rock Mechanics and Engineering*, vol. 30, no. 8, pp. 1547–1556, 2011.

[4] J. B. Bai and C. J. Hou, "Research on principle of roof stability of abandoned workings and supporting technology," *Journal of China Coal Society*, vol. 30, no. 1, pp. 8–11, 2005.

[5] G. M. Feng, K. J. Jia, and B. B. Shang, "Application and prospect of ultra-high water filling materials in mining engineering," *Coal Science and Technology*, vol. 43, no. 1, pp. 5–9, 2015.

[6] H. F. Zhou and Q. X. Huang, "Study on the law of roof breakage and mine pressure passing large cross-section gob group in the fully-mechanized face with high mining height," *Coal Science and Technology*, vol. 48, no. 2, pp. 70–79, 2020.

[7] H. F. Zhou, "Roof cutting mechanism and control technology of high cutting coal mining face passing through large cross section abandoned gateway," *Coal Science and Technology*, vol. 42, no. 2, pp. 120–123, 2014.

[8] B. Q. Liu, Z. J. Li, S. C. Dai, X. H. Yuan, and X. D. Xing, "The failure mechanism and control technology of the surrounding rock of the coal pillar crossing abandoned roadway," *Coal Science and Technology*, vol. 48, no. 2, pp. 1–11, 2020.

[9] Q. Y. Xu, Z. X. Ning, R. S. Zhu, and K. S. Zeng, "Study on instability mechanism and top control of overfilled roof in fully mechanized caving face," *Journal of Mining & Safety Engineering*, vol. 36, no. 3, pp. 505–512, 2019.

[10] C. Y. Yin, G. M. Feng, P. Gao, and Y. Zhao, "Research on instability mechanism of surrounding rock in stage of working face passing abandoned roadway," *Journal of Mining & Safety Engineering*, vol. 35, no. 3, pp. 457–464, 2018.

[11] D. Zorkov, A. Renev, K. Filimonov, and R. Zainulin, "The roof support load analysis for pre-driven recovery room parameters design," *E3S Web of Conferences*, vol. 174, no. 10, 2020.

[12] C. S. Tadolini, S. P. Mills, and R. D. Burkhard, "Tekcrete Fast®: fiber-reinforced, rapid-setting sprayed concrete for rib and surface control," *International Journal of Mining Science and Technology*, vol. 28, no. 1, pp. 29–34, 2018.

[13] G. S. Esterhuizen, D. F. Gearhart, and I. B. Tulu, "Analysis of monitored ground support and rock mass response in a longwall tailgate entry," *International Journal of Mining Science and Technology*, vol. 28, no. 1, pp. 43–51, 2018.

[14] W. Yu and K. Li, "Deformation mechanism and control technology of surrounding rock in the deep-buried large-span chamber," *Geofluids*, vol. 2020, Article ID 8881319, 22 pages, 2020.

[15] C. Liu, P. L. Gong, K. Wang, X. Q. Zhang, and Y. D. Liu, "Roof stability for repeated mining workface passing through abandoned parallel gateway," *Journal of China Coal Society*, vol. 40, no. 2, pp. 314–322, 2015.

[16] C. Liu, J. W. Zhang, Z. Q. Yang et al., "Mechanism of advance fracture of main roof and its control technology when workface crossing abandoned roadway," *Rock and Soil Mechanics*, vol. 39, no. 44, pp. 1411–1421, 2018.

[17] C. Liu, Z. Q. Yang, P. L. Gong et al., "Mechanism and control technology of supports crushing induced by main roof breaking ahead of workface crossing abandoned roadway," *Journal of China Coal Society*, vol. 40, no. 2, pp. 314–322, 2015.

[18] X. N. He, Y. Chen, and Y. Z. Qin, "Application and study on technology of fully-mechanized top coal caving mining face passing through mine abandoned roadway," *Coal Science and Technology*, vol. 45, no. 6, pp. 124–130, 2017.

[19] H. P. Kang, H. Lv, X. Zhang, F. Gao, Z. Wu, and Z. Wang, "Evaluation of the ground response of a pre-driven longwall recovery room supported by concrete cribs," *Rock Mechanics and Rock Engineering*, vol. 49, no. 3, pp. 1025–1040, 2016.

[20] W. Fangtian, Z. Cun, W. Shuaifeng, Z. Xiaogang, and G. Shenghua, "Whole section anchor-grouting reinforcement technology and its application in underground roadways with loose and fractured surrounding rock," *Tunnelling and Underground Space Technology*, vol. 51, no. 1, pp. 133–143, 2016.

[21] W. Yu, K. Li, Z. Liu, B. An, P. Wang, and H. Wu, "Mechanical characteristics and deformation control of surrounding rock in weakly cemented siltstone," *Environmental Earth Sciences*, vol. 80, no. 9, pp. 33–48, 2021.

[22] B. Zhao, F. T. Wang, N. N. Liang, and W. L. Wang, "Reasonable segment pillar width and its control technology for fully mechanized top-coal caving face with high stress," *Journal of Mining & Safety Engineering*, vol. 35, no. 1, pp. 19–26, 2018.

[23] B. Zhao, N. N. Liang, F. T. Wang, and Z. X. Liu, "Surrounding rock broken zone evolution law of high-intensity mining affected roadway in shallow coal seam," *Coal Science and Technology*, vol. 46, no. 5, 2018.

[24] Z. Z. Zhang, J. B. Bai, Z. T. Han, X. Y. Wang, Y. Xu, and M. Wang, "Roof mechanics analysis and backfill technology for abandoned roadway," *Journal of Mining & Safety Engineering*, vol. 30, no. 2, pp. 194–198, 2013.

[25] H. Yu, Z. Y. Niu, L. G. Kong, C. C. Hao, and P. Cao, "Mechanism and technology study of collaborative support with long and short bolts in large-deformation roadways," *International Journal of Mining Science and Technology*, vol. 25, no. 4, pp. 587–593, 2015.

WILEY | Hindawi

Research Article

Shock and Vibration of Rainfall on Rotational Landslide and Analysis of Its Deformation Characteristics

Li Weiguo [ID],[1,2] **Liu Yali,**[1] **Chen Yanhong,**[1] **and Yang Libing**[1]

[1]*School of Land Science and Space Planning, Hebei GEO University, China*
[2]*Department of Geoinformatics, Faculty of Mining and Geology, VŠB-Technical University of Ostrava, 17. Listopadu 15/2172, 708 00 Ostrava-Poruba, Czech Republic*

Correspondence should be addressed to Li Weiguo; weiguo.li.st@vsb.cz

Earthquake, flood, human activity, and rainfall are some of the trigger factors leading to landslides. Landslide monitoring data analysis indicates the deformation characteristics of landslides and helps to reduce the threat of landslide disasters. There are monitoring methods that enable efficient acquisition of real-time data to facilitate comprehensive research on landslides. However, it is challenging to analyze large amounts of monitoring data with problems like missing data and outlier data during data collection and transfer. These problems also hinder practical analysis and determination concerning the uncertain monitoring data. This work analyzes and processes the deformation characteristics of a rainfall-induced rotational landslide based on exploratory data analysis techniques. First, we found that the moving average denoising method is better than the polynomial fitting method for the repair and fitting of monitoring data. Besides, the exploratory data analysis of the Global Navigation Satellite System (GNSS) monitoring data reveals that the distribution of GNSS monitoring points has a positive correlation with the deformational characteristics of a rotational landslide. Our findings in the subsequent case study indicate that rainfalls are the primary trigger of the Zhutoushan landslide, Jiangsu Province, China. Therefore, this method provides support for the analysis of rotational landslides and more useful landslide monitoring information.

1. Introduction

A landslide is a common geological hazard that seriously threatens life and property globally [1–3]. Like an earthquake, rainfall is also one of the most recognized trigger factors for landslides [4, 5]. Researchers have proposed rainfall thresholds and established relevant models to forecast the landslide occurrence [6, 7], and some have developed early warning systems for all kinds of landslides [8]. However, researchers have also suggested that rainfall information alone is not enough for predicting landslides because it does not consider soil moisture conditions [9]. Therefore, a single-factor monitoring method is not enough to predict landslides accurately. At present, there are various hydrological, geological, and surface monitoring methods. Setting alarm thresholds for multiple parameters is reasonable

[10]. However, rainfall can cause changes in other monitoring parameters of landslides.

Exploratory data analysis (EDA) is a technique or method for analyzing and processing data sets for summarizing their main characteristics, usually by visualization, and it plays a paramount role in obtaining valuable information from data [11]. This method has been effectively applied to a variety of aspects [12], such as computer graphics [13], bioinformatics [14, 15], meteorology [16], traffic [17], and crops [18]. According to the soil or rock mass movement principle and reason, for landslides, Qarinur [19] focused on determining the correlations between the sliding distance of landslide against high, slope, and volume by using the EDA method. It was reported to be the first time EDA was implemented to describe the relationship between the location of GPS monitoring points and the trend of their
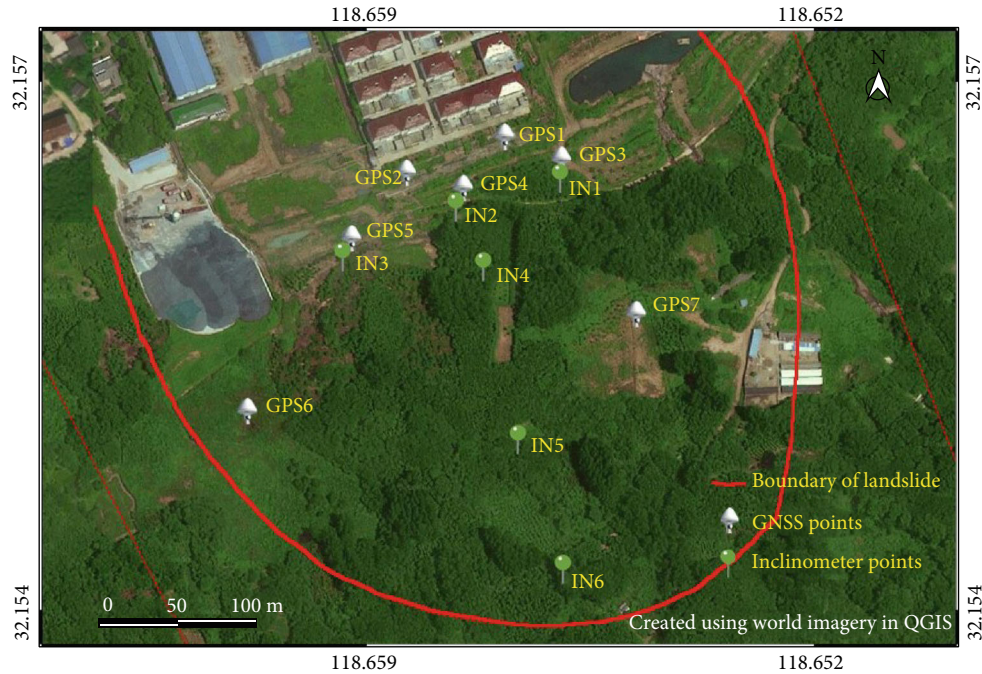
FIGURE 1: Location of the Zhutoushan landslide.

displacements. He detected the outliers from the raw data and verified the deformation characteristics of a rotational landslide using 3D graphs.

It is necessary to know the steps of the EDA process. First, the project-related data, their types, and the category of variables should be prepared and identified; second, outliers should be detected or fixed using mathematical models if necessary [20]. There are two types of causes of outliers: artificial and natural [21]. Second, different methods should be considered to solve different situations due to the different outliers, such as monitoring, data processing, and sampling errors. Third, outliers should be removed or fixed by using statistical methods [22]. Fourth, the connections between each variable and its target should be surveyed. Finally, data should be analyzed from different dimensions to get the internal relationship among various data.

Mathematical models are often employed for the landslide early warning to predict landslides and achieve good results [23, 24]. However, the precondition of establishing a mathematical model is to ensure the integrity and validity of monitoring data. In the process of landslide monitoring, the loss or abnormality of monitoring data caused by monitoring equipment failure or external factors is inevitable [25]. It is essential for irregular data to know whether it is caused by disturbance, gear disappointment, or avalanche distortion to avoid triggering a false alarm. This requires data analysis and research to reduce the uncertainty impact of big data [26, 27].

Owing to the complex geologic structure of the landslides, the deformation of the monitored points at different locations is closely related to the geological features of those locations [25]. This paper provides insights into the types of

landslides and the relationship between rainfall and other monitoring data through the analysis of the Zhutoushan landslide monitoring data in China and explores how to evaluate the outlier data using EDA.

2. Material and Methodology

The Zhutoushan lies above the residential area of Yongning Town, Nanjing, Jiangsu Province, China. The central areas are located at the $118°39'37''$E and $32°09'24''$N (see Figure 1).

The study area is located on one side of the Zhutoushan Range, and there are many prominent fault zones. The geological structure is composed of sandstone, marlite, and loose soil. In the 1970s, large-scale mining activities took place at the base of Zhutoushan and unreasonable excavations led to many landslide disasters. Houses were destroyed at the foot of the slope, resulting in a significant loss of life and property.

An early warning and automatic deformation monitoring system based on GNSS is adopted to monitor the surface deformation of the Zhutoushan landslide. The system integrates technologies are composed of GNSS high-precision positioning, General Packet Radio Service (GPRS) communication, wireless communication, database technology, and all kinds of sensors, being able to monitor the deformation of the landslide immediately and analyze and compare the monitoring results.

According to the design requirements and field survey, this system comprises one GNSS reference station located outside of the landslide, eight GNSS monitoring stations (Figure 1) (the GPRS is outside the area affected by landslide deformation), six inclinometer monitoring points in which
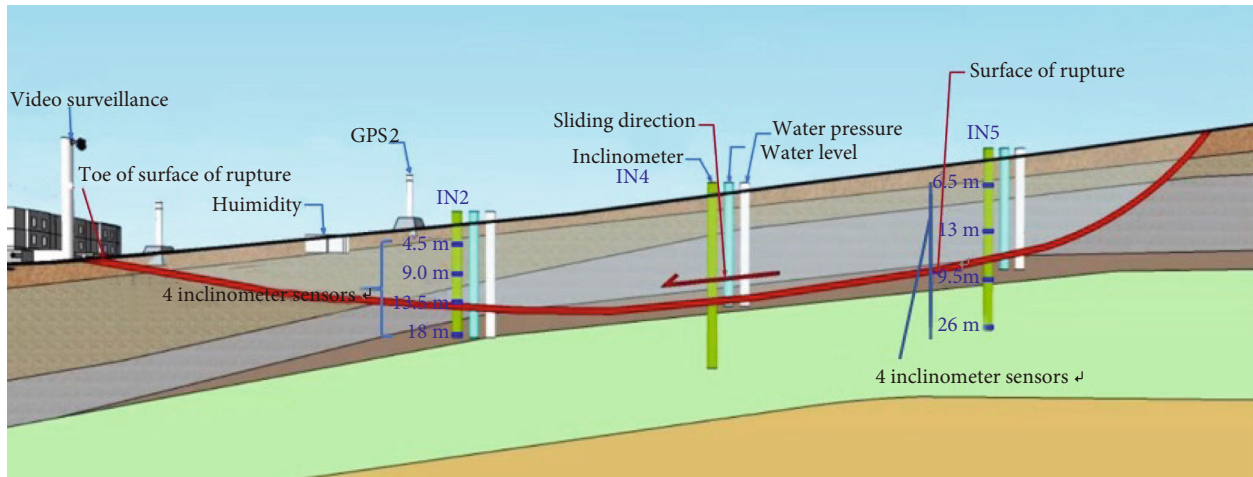
Figure 2: Positions of the monitoring instruments.

Figure 3: Monitoring instruments on the landslide.

each point was installed with four sensors at various depths to detect slope deformation, four water-level monitoring points, three pore water pressure (PWP) monitoring points, one rainfall monitoring point which was installed at the edge of the landslide (Figures 2 and 3), one soil water content monitoring point, and two video monitoring points.

An inclinometer is used for obtaining displacement information of deep sliding mass. As an essential aspect of landslide monitoring, four fixed inclinometers in series are installed in each well log buried at different depths, effectively reflecting the displacement changes of deep sliding mass in real time (Figure 2). Soil moisture sensors are usually used to measure the moisture percentage of the soil. They can calculate the moisture content. Soil moisture sensors are located around the GNSS position and collected the data in real time.

The system was initiated in July 2017, and the data were collected and transferred to the computing center in real time using wireless sensor network technology.

The approach utilized involves the following: (a) GNSS data, inclinometer data, rainfall data, soil water content data, and water pressure data come from the landslide early warning system and (b) data analysis by using the EDA for establishing the correlation between the monitoring rainfall, other monitoring data, outliers, and characteristics of GNSS data.

3. Results and Discussion

3.1. Rainfall and Displacement. In most cases, the primary trigger of landslides is persistent heavy rain. Detailed data from the monitored landslides reveal that numerous landslides have been associated with rainfall [28–30]. Because of the heavy rainfall, the rainwater can seep into the underground and then flows through unsaturated soil. As a result, the water may be located on lower permeability materials or a drainage barrier, such as sandstone, siltstone, marlstone, limestone, soil, and bedrock.

Rainfall has a significant impact on the displacement of the ground surface and underground inclination. On August 15, 2018, the rainfall less than 2 mm caused changes in the surface's horizontal displacement but had a slight effect on the changes in the inclination and elevation. During December 25–27 in 2018, the rainfall was 178 mm, 406 mm, and 313 mm, respectively. These caused dramatic changes in horizontal displacement, vertical displacement, and inclination (Figure 4). The displacement of various inclinometer depths, determined by rainfall, is also different. The surface deformation with a buried depth of 4.5 m surpassed that with a buried depth at 9 m and 13.5 m.

Rainfall has little effect on PWP. The influence of rainfall on soil water content is also comparatively small, only
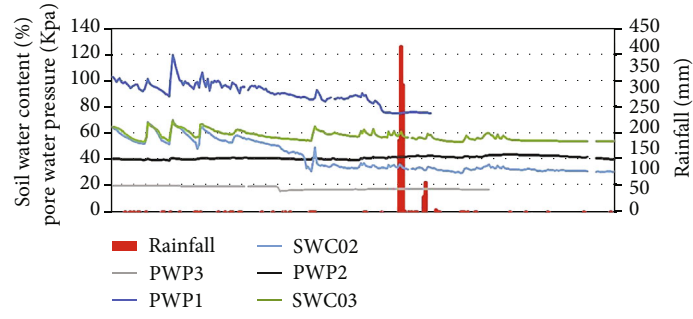
(a) Soil water content, pore water pressure, and rainfall
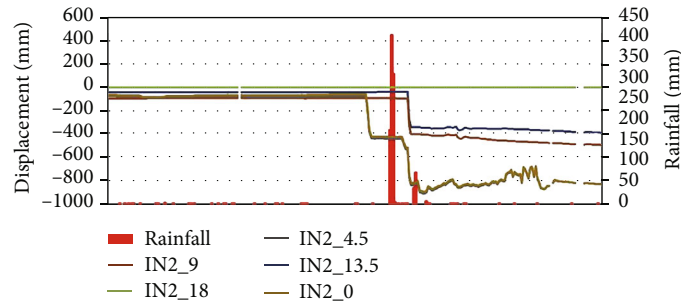
(b) Inclinometer and rainfall
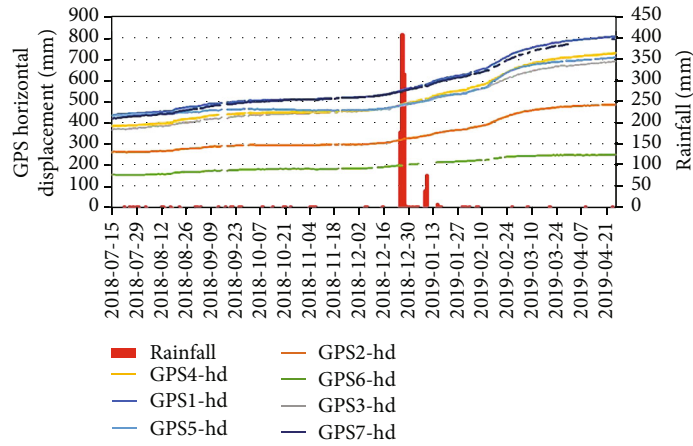
(c) GPS horizontal displacement and rainfall

FIGURE 4: Continued.
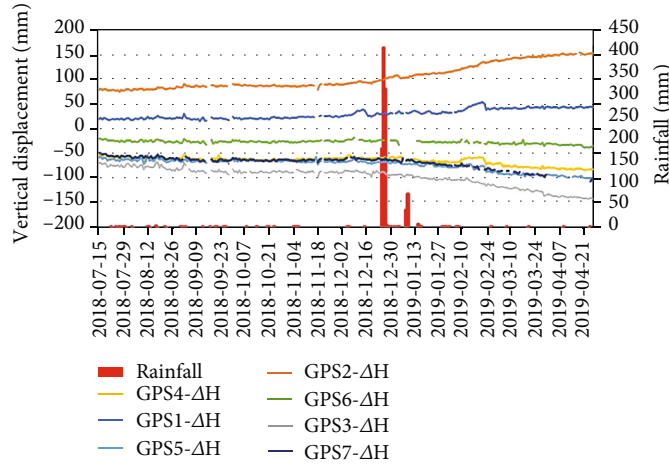
(d) GPS vertical displacement and rainfall

FIGURE 4: Relationship between rainfall and the other monitoring data.
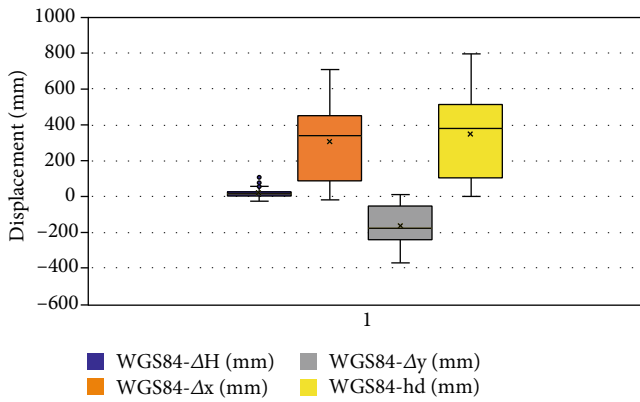
FIGURE 5: Box plots of GPS.

affecting its fluctuation in a small range (Figure 4(a)). Yet the rainfall on December 26, 2018, was 406. These changes are not obvious.

3.2. Outlier Detection in Raw Data.
In GPS data collection and transmission, measurement errors and random noises are inevitable. By establishing the corresponding mathematical model or error processing, the influence of errors and noises on the original data can be reduced. However, an outlier will significantly affect the quality of data determination and modeling of original data. Therefore, the outliers must be identified and removed when a mathematical model is established to reduce the impacts of errors or noises.

Box plots, a statistical diagram that displays a set of data distributions, can be used to detect outliers in raw data. For example, GPS1 (mark 1 of GPS) has an abnormal value in the elevation direction; x, y, and horizontal directions are normal (Figure 5). Therefore, the vertical displacement of GPS1 can be fitted by basic 20 days moving average method. With this method, each observation is replaced by an average (Figure 6). However, some vital information can be concealed. Therefore, the moving average denoising method is suitable [7, 31, 32]. Using this method, we determined the

outliers by the Root Mean Square Error (RMSE) and replaced them with their average values (Figure 7). The other values are still observations because some vital information from the raw data is available.

For the same data, the polynomial fitting model is adopted, and it is found that the correlation coefficient of the second method is better than that of the first method. Thus, the accuracy of the polynomial fitting model is enhanced after the outliers are removed. However, it should be identified whether the measurement error causes the abnormal value. If it is a real deformation value, an alarm is required. This requires careful consideration of various factors to make a comprehensive determination. Since the operation of the landslide monitoring system in 2017, there have been several outliers caused by equipment faults.

3.3. Exploratory Data Analysis (EDA).
The EDA method has been applied to a variety of problems successfully [12]. It refers to a data analysis method that explores structure and raw data through charts, equation fitting, and calculation of characteristic quantities under little prior assumptions for the original data obtained by observation or investigation [33]. From the scattered plots, R squared is greater than or equal to 0.9 (Figures 8 and 9). R squared of GPS3 is the maximum (at 0.970). R squared of GPS1 is the minimum. Some points are far away from the line. On both coordinate axes, the variables are rescaled as standard deviational units. Thus, an observational value exceeding 2 can be designated as outlier (Figure 10(a)) [34]. The regression line is recalculated, and it reflects the slope for monitoring data without the current selection. During updating in the scatter plot (Figure 10(b)), $9R$ squared of GPS1 will increase to 0.911, and T value will increase from 74.031 to 78.324.

Since vertical displacements of GPS1 and GPS2 are upward, and the others are downward, the trend of vertical displacements is either upward or downward, and there is a positive correlation between them. Conversely, if one trend of vertical deformation is upward and another is downward, their relation is negative (Figure 11). The correlation

GPS1-ΔH (mm)

$y=8E\text{-}05x^2+0.0266x\text{-}1.4743$
$R^2=0.9187$

—— GPS1-H
········ Polynomial (GPS1-H)
········ Moving average 20 cycles
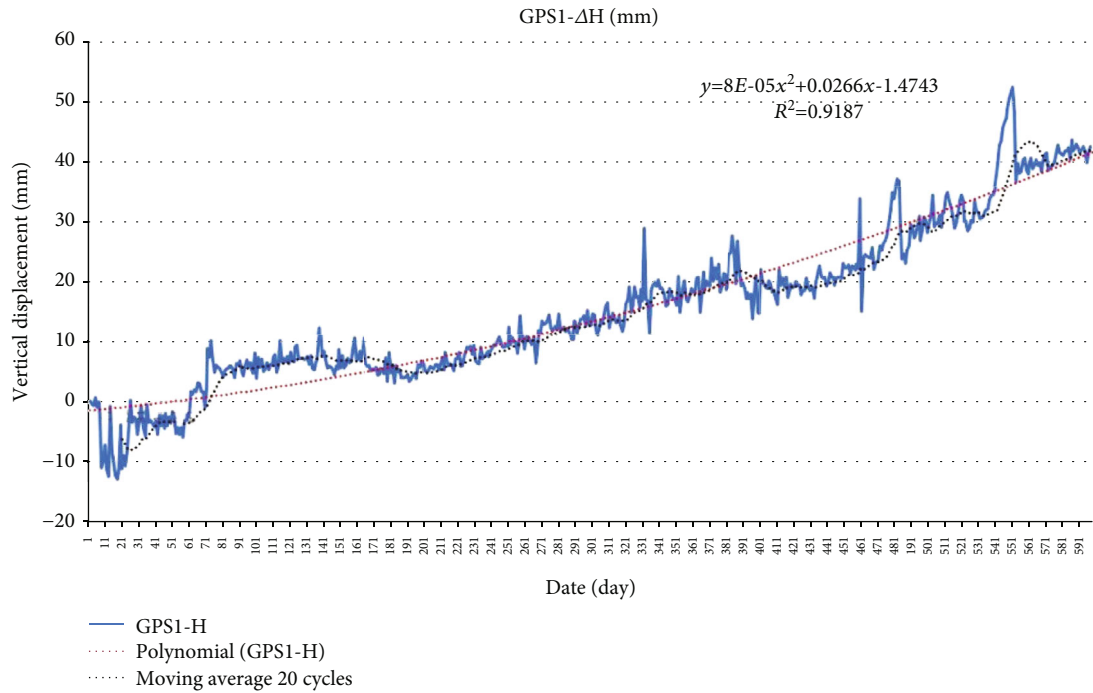
FIGURE 6: Vertical displacement and its fitting.

GPS1-Δh (mm)

$y=7E\text{-}05x^2+0.0286x\text{-}1.6852$
$R^2=0.9357$

—— GPS1-H
—— Moving average denoising
········ Polynomial (GPS1-H)
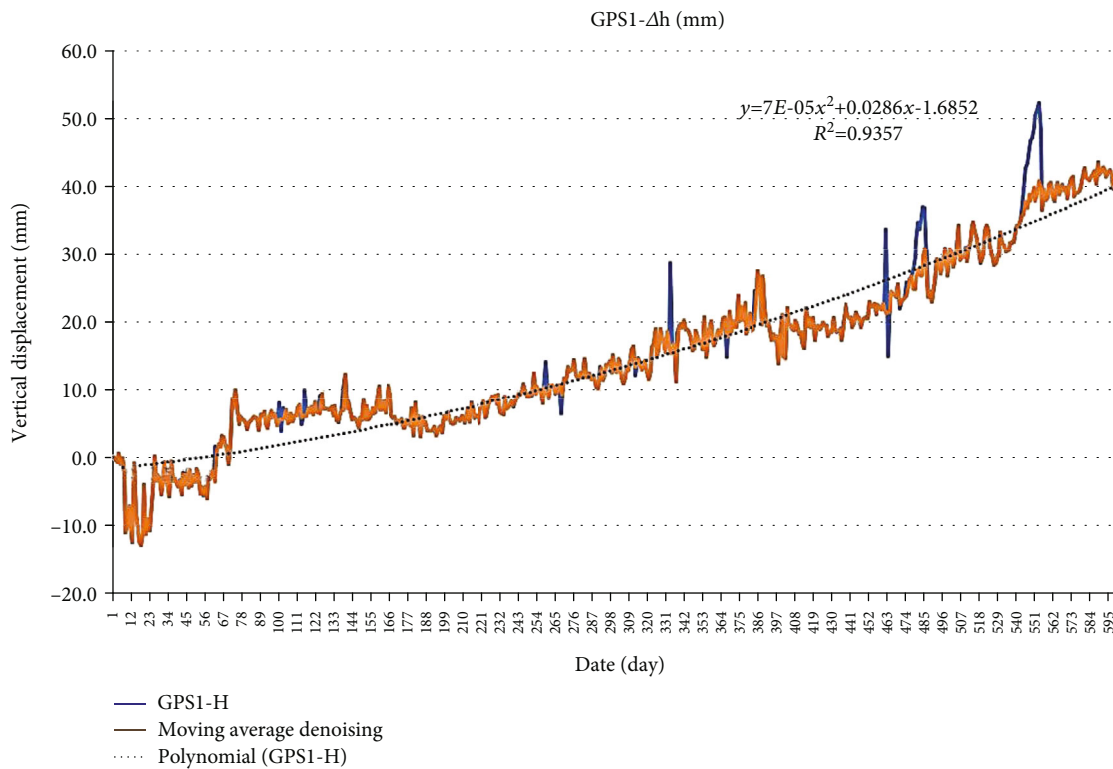
FIGURE 7: Vertical displacement and its fitting.

imitates the deformation characteristics of a rotational land-slide, and it gives information for further research.

3.4. Landslide Surface Displacement. The horizontal displacement direction of the eight GPS stations imitates the sliding tendency of the sliding mass in the horizontal directions. The landslide as a whole is in the northwest direction, and the azimuth angle is around 310° to 330° (Figure 12). The most significant horizontal displacement is GPS1, while GPS8 is the smallest horizontal displacement, and the value

#obs	R^2	Const a	Std-err a	T-stat a	p value a	Slope b	Std-err b	T-stat b	p value b
608	0.900	−7.095	0.358	−19.824	0.000	0.069	0.001	74.031	0

#obs	R^2	Const a	Std-err a	T-stat a	p value a	Slope b	Std-err b	T-stat b
0	0.969	−25.587	0.711	−35.979	0.000	0.253	0.002	136.925
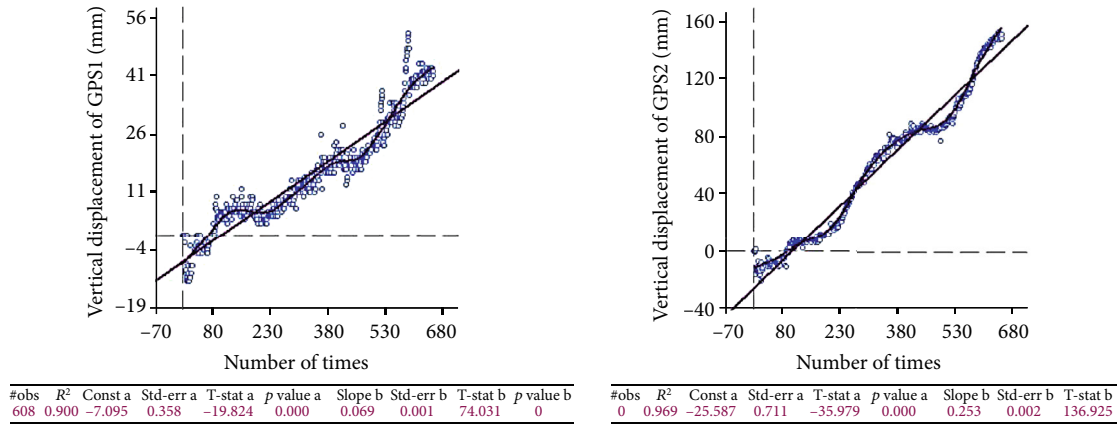
FIGURE 8: Scatter plots of GPS1 and GPS2.

R^2	Const a	Std-err a	T-stat a	p value a	Slope b	Std-err b	T-stat b	p value b
0.970	2.909	0.544	5.343	0.000	0.197	0.001	−139.763	0

R^2	Const a	Std-err a	T-stat a	p value a	Slope b	Std-err b	T-stat b
0.949	−5.095	0.424	−12.016	0.000	−0.117	0.001	−106.563

R^2	Const a	Std-err a	T-stat a	p value a	Slope b	Std-err b	T-stat b	p value b
0.939	4.346	0.621	6.99	0.000	−0.153	0.002	−96.407	0

R^2	Const a	Std-err a	T-stat a	p value a	Slope b	Std-err b	T-stat b
0.941	12.684	0.607	20.905	0	−0.159	0.002	−95.584

FIGURE 9: Scatter plots of GPS3, GPS4, GPS5, and GPS7.

is less than 50 mm, indicating that the point is currently stable or unaffected by the landslide deformation. The reasons are that GPS8 is located far from the landslide. Simultaneously, the displacement of GPS6 is very distinct. The north direction displacement is more significant than that of the west direction; from Figure 1, we can see that the position of GPS6 is located at the edge of the landslide.

The landslide deformation is not just in one direction but in three directions (Figure 13). The deformation at the north is superior to the deformation at the west. Thus, the direction of landslide displacement is transformed into the north. The vertical deformations are rising for the GPS1 and GPS3, and the other monitoring points are the opposite.

The date from July 14, 2017, to April 8, 2019, is selected for this study object on Zhutoushan landslide monitoring. GNSS monitoring data analysis results show that the vertical displacement of other points is larger except GPS6 and GPS8 (Figure 14). The GPS1 deformation monitoring point is the largest horizontal in these eight monitoring points, which is 792 mm. According to the vertical displacement site, the displacement values of GPS1 and GPS2 move up, while the other values move down; also, GPS2 and GPS3 monitoring

#obs	R^2	Const a	Std-err a	T-stat a	p value a	Slope b	Std-err b	T-stat b	p value b
608	0.900	0	0.013	0	1	0.949	0.013	74.031	0

(a) Standardized data of GPS1

#obs	R^2	Const a	Std-err a	T-stat a	p value a	Slope b	Std-err b	T-stat b	p value b
608	0.900	0	0.013	0	1	0.949	0.013	74.031	0
8	0.601	−11.873	4.750	−2.500	0.047	10.659	3.549	3.004	0.024
608	0.911	−0.015	0.012	−1.301	0.194	0.928	0.012	78.324	0

(b) Updating the scatter plot of GPS1
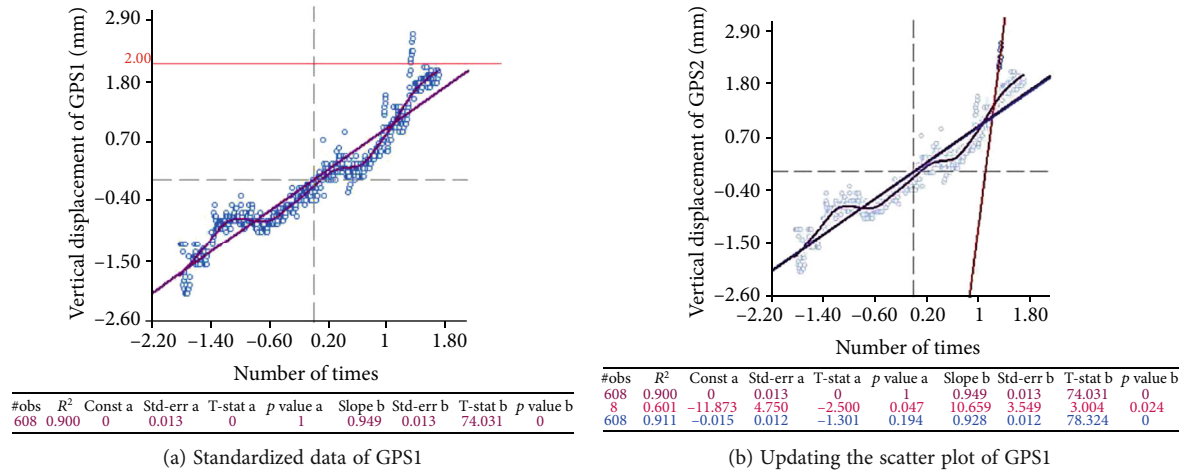
FIGURE 10: Analysis data of GPS1.
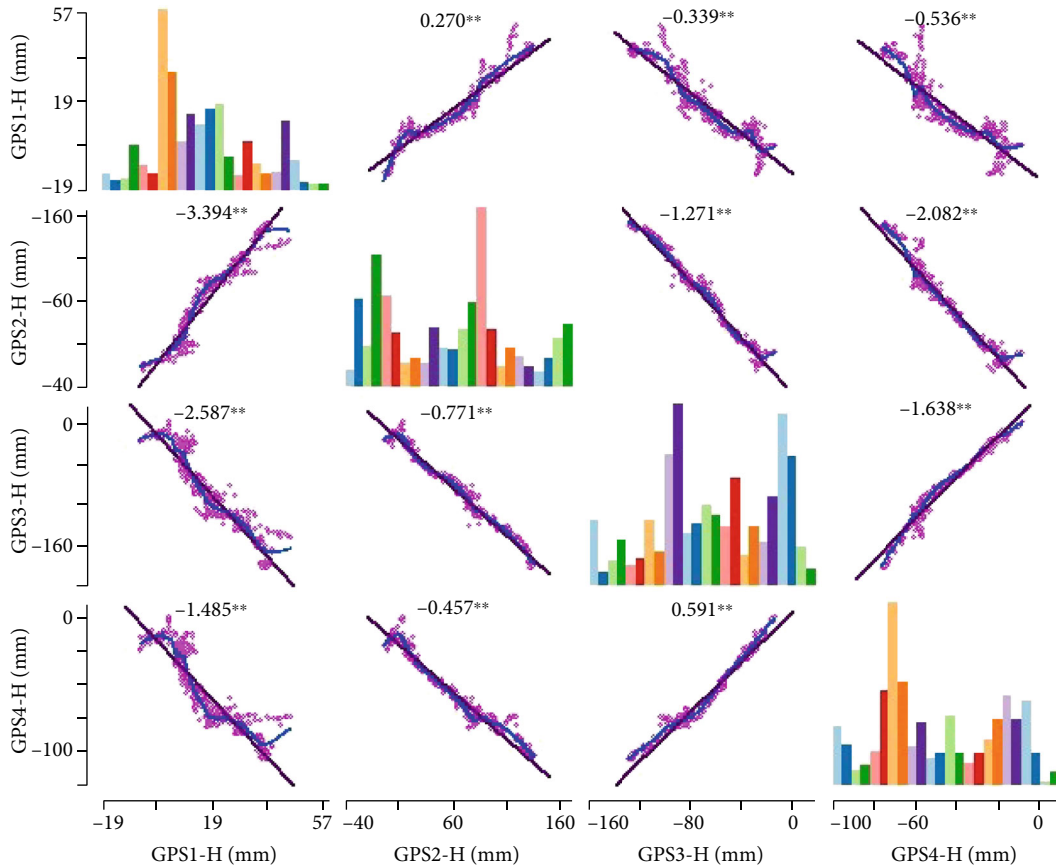
FIGURE 11: Scatter plot matrix between GPS1, GPS2, GPS3, and GPS4.

points are more significant than others. The largest is GPS2, reaching 149.8 mm. From the deformation rate site, the average rate of these eight points is 2 mm per day, which indicates that the Zhutoushan landslide is in a stable stage overall. However, the observation frequency and intensity of GPS1 and GPS2 need to be enhanced, as these two are located in the toes of the landslide and are more affected by the landslide deformation to prevent the possibility of sudden landslide deformation.

According to landslide classifications [35], Zhutoushan is a rotational landslide (Figure 15). Squeezed by the upper landslide, GPS1 and GPS2 that are located in the toe of landslide surface of rupture rise in the vertical direction. Other GPS monitoring points slip down under the influence of gravity.

It is dangerous to overlook outliers in the raw data. Negative results are yielded if outliers are included in the course of processing data and analysis with exclusion. Box plots can
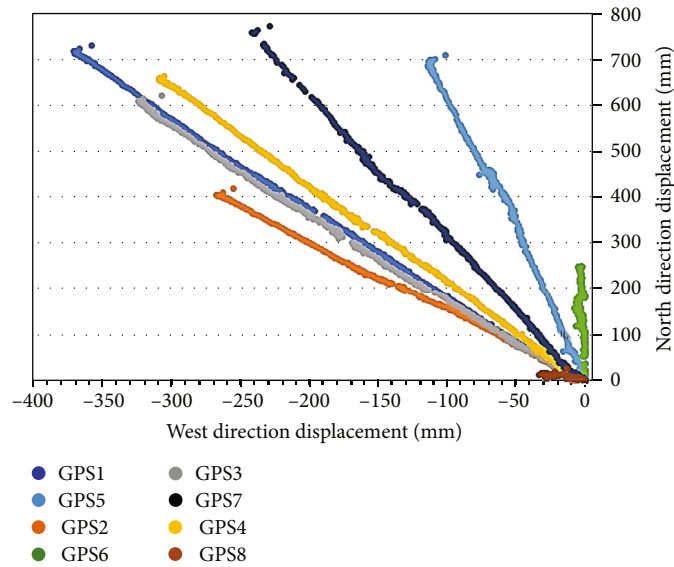
FIGURE 12: GPS displacement from July 14th, 2017, to May 1st, 2019.
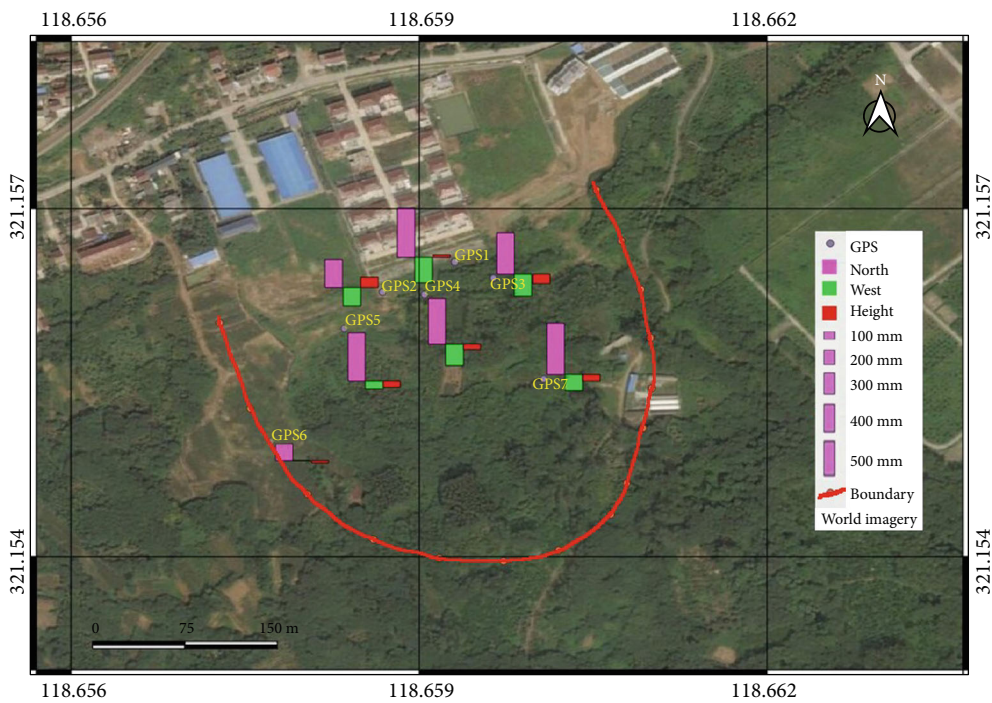
FIGURE 13: Visualization of a surface displacement (2019-04-08).

be implemented for detecting outliers from the raw data. The limitation of a box plot is that accurate measurement of the distortion in data distribution and degree of tail weight are not obtained. In addition, for many data sets, the shape information reflected by the box plot is fuzzier, and there are limitations in using the median to represent the overall average [36–40].

Polynomial fitting models and moving average denoising methods can be used to repair outliers. From the data analysis perspective, the accuracy of the latter is better than the former. The polynomial fitting model is a mathematical model that can be fitted by including outliers and raw data; it will remove some critical information from the raw data and the moving average noise. According to the setting step, the accuracy and retained information will also be different, requiring setting the corresponding step size to the specific project.

Moreover, the authenticity of the data affects the analysis results. One challenge in landslide monitoring is that amid the large amounts of data collected via different monitoring methods, it is hard to identify whether the outliers are caused by external factors or by landslide deformation. This requires a
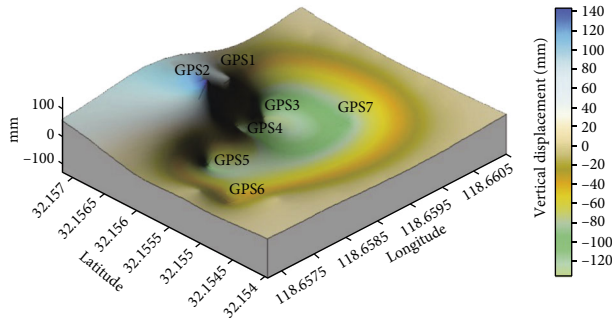
FIGURE 14: 3D graph on April 8th, 2019.
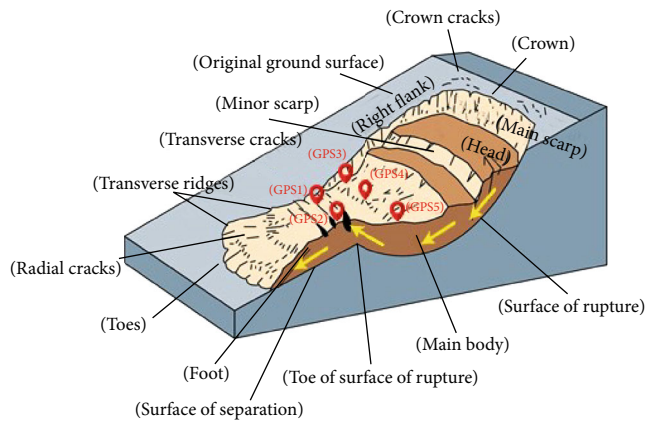
FIGURE 15: Rotational landslide type for Zhoutoushan landslide based on Varnes DJ's paper.

comprehensive determination to avoid misdetermination and threat to people's lives and property damage. If the outliers are caused by the deformation of the landslide and exceed the deformation warning threshold, the system should send an alarm to inform people to take safety measures. Otherwise, the outliers can be removed from the raw data.

EDA can only detect outliers in a data set but cannot recognize the outliers caused by data transmission or deformation of the landslide. Simply removing outliers' value can add further risk of deviation to the analysis. Therefore, EDA needs to improve user engagement through the users' feedback. These are the main challenges in the processing of the raw data.

For GNSS data in landslide monitoring that are data of a single variable, we mainly performed analysis using box plots and scatter plots. To monitor the deformation of the landslide, various means can be used to collect data through various monitoring methods, but it is challenging to describe outliers in multivariable data using the EDA method.

The landslide deformation data can be visualized through many methods. As for the form of expression, it is preferable to distinct the horizontal and vertical deformation data, and it is easier for people to get relevant information from Figures 12 and 14. Though Figure 13 shows the data of North, West, and Height simultaneously, it cannot show the deformation process but only shows the results.

Owing to the landslide's complex geological structure, the landslide's geological characteristics and the all kinds

of types of landslides are related to the deformation of the monitoring points at different locations. The relationship between different monitoring points is positive, consistent with most similar landslide deformations through EDA of surface GNSS monitoring data. After standardizing the data, the outliers can also be detected to improve the quality of the data.

4. Conclusions

The deformation characteristics of a rainfall-induced rotational landslide are analyzed in this paper based on the EDA method, and the Zhutoushan landslide is a rainfall-induced rotational landslide. We get some conclusions that are as follows. First, the box plot can detect outliers from a mass of raw data collected by the instruments located in the Zhutoushan landslide, and the moving average denoising method is better than the polynomial fitting method repairing and fitting the monitoring data. In addition, based on the EDA of GNSS monitoring data, the distribution of GNSS monitoring points has a positive correlation with the deformation characteristics of the rotational landslide, which supports rotational landslide and more helpful information for landslide monitoring. Overall, the EDA method is shown to be interesting and valuable to process massive monitoring data for the rainfall-induced rotational landslide.

Moreover, multiple monitoring methods, which are geological and meteorological monitoring methods, can be used to enhance landslide prediction. The monitoring results of landslides by various monitoring methods can be mutually verified to ensure data correctness and prediction accuracy. With the development of artificial intelligence and deep learning, rapid and effective analysis and determination of monitoring data help us understand and grasp the characteristics of landslide deformation.

With the development of landslide deformation monitoring equipment, data collection, transmission, and storage technology, it is one of the future development directions of landslide monitoring information processing to mine the complex relationship between massive monitoring data and various monitoring data.

Data Availability

The data used to support the findings of the study can be available within the article. Readers can obtain data supporting the research results from the data tables in the paper.

Conflicts of Interest

The authors declare no conflict of interest.

Acknowledgments

References

[1] Y. G. Zhang, Z. Zhang, and S. Xue, "Stability analysis of a typical landslide mass in the Three Gorges Reservoir under varying reservoir water levels," *Environment and Earth Science*, vol. 79, no. 1, 2020.

[2] Y. G. Zhang, J. Tang, Z. Y. He, J. K. Tan, and C. Li, "A novel displacement prediction method using gated recurrent unit model with time series analysis in the Erdaohe landslide," *Natural Hazards*, vol. 105, no. 1, pp. 783–813, 2020.

[3] Y. G. Zhang, J. Tang, R. P. Liao et al., "Application of an enhanced BP neural network model with water cycle algorithm on landslide prediction," *Stochastic Environmental Research and Risk Assessment*, vol. 35, no. 6, pp. 1273–1291, 2021.

[4] E. Monsieurs, O. Dewitte, and A. Demoulin, "A susceptibility-based rainfall threshold approach for landslide occurrence," *Natural Hazards and Earth System Sciences*, vol. 19, no. 4, pp. 775–789, 2019.

[5] R. C. Sidle and T. A. Bogaard, "Dynamic earth system and ecological controls of rainfall-initiated landslides," *Earth Science Reviews*, vol. 159, pp. 275–291, 2016.

[6] B. Koley, A. Nath, S. Saraswati, K. Bandyopadhyay, and B. C. Ray, "Assessment of rainfall thresholds for rain-induced landslide activity in North Sikkim Road Corridor in Sikkim Himalaya, India," *Journal of Geography, Environment and Earth Science International*, vol. 19, no. 3, pp. 1–14, 2019.

[7] L. I. Guangchun, D. A. I. Wujiao, and Z. E. N. G. Fanhe, "Robust moving average and its application in GPS automatic monitoring data processing," *Journal of Geodesy and Geodynamics*, vol. 36, no. 1, pp. 85–88, 2016.

[8] L. Piciullo, M. Calvello, and J. M. Cepeda, "Territorial early warning systems for rainfall-induced landslides," *Earth-Science Reviews*, vol. 179, pp. 228–247, 2018.

[9] K. Koizumi, K. Oda, M. Komatsu, S. Ito, and H. Tsutsumi, "Slope structural health monitoring method against rainfall-induced shallow landslide," *IOP Conference Series: Materials Science and Engineering*, vol. 615, article 012046, 2019.

[10] G. Pecoraro, M. Calvello, and L. Piciullo, "Monitoring strategies for local landslide early warning systems," *Landslides*, vol. 16, pp. 213–231, 2019.

[11] A. Ghosh, M. Nashaat, J. Miller, S. Quader, and C. Marston, "A comprehensive review of tools for exploratory analysis of tabular industrial datasets," *Visual Informatics*, vol. 2, pp. 235–253, 2018.

[12] N. V. Bondarev, "Classification and prediction of sodium and potassium coronates stability in aqueous-organic media by exploratory data analysis methods," *Russian Journal of General Chemistry*, vol. 89, no. 2, pp. 281–291, 2019.

[13] A. Endert, W. Ribarsky, C. Turkay et al., "The state of the art in integrating machine learning into visual analytics," *Computer Graphics Forum*, vol. 36, no. 8, pp. 458–486, 2017.

[14] S. Pabinger, A. Dander, M. Fischer et al., "A survey of tools for variant analysis of next-generation genome sequencing data," *Briefings in Bioinformatics*, vol. 15, no. 2, pp. 256–278, 2014.

[15] Y. G. Zhang, Y. L. Xie, Y. Zhang, J. B. Qiu, and S. X. Wu, "The adoption of deep neural network (DNN) to the prediction of soil liquefaction based on shear wave velocity," *Bulletin of Engineering Geology and the Environment*, vol. 80, no. 6, pp. 5053–5060, 2021.

[16] M. Rautenhaus, M. Böttinger, S. Siemen et al., "Visualization in meteorology-a survey of techniques and tools for data analysis tasks," *IEEE Transactions on Visualization and Computer Graphics*, vol. 24, no. 12, pp. 3268–3296, 2017.

[17] N.-F. Galatoulas, K. N. Genikomsakis, and C. S. Ioakimidis, "Spatio-temporal trends of E-bike sharing system deployment: a review in Europe, North America and Asia," *Sustainability*, vol. 12, no. 11, 2020.

[18] P. Hongxing, Z. Xiangjun, G. Aixia, X. Juntao, and C. Yan, "Color model analysis and recognition for parts of citrus based on exploratory data analysis," *Transactions of the Chinese Society for Agricultural Machinery*, vol. 44, S1, pp. 253–259, 2013.

[19] M. Qarinur, "Landslide runout distance prediction based on mechanism and cause of soil or rock mass movement," *Journal of the Civil Engineering Forum*, vol. 1, no. 1, 2015.

[20] Y. H. Dovoedo and S. Chakraborti, "Boxplot-based outlier detection for the location-scale family," *Boxplot-Based Outlier Detection for the Location-Scale Family.*, vol. 44, no. 6, pp. 1492–1513, 2015.

[21] R. A. Y. SUNIL, *A Comprehensive Guide to Data Exploration*, 2016, https://www.analyticsvidhya.com/blog/2016/01/guide-data-exploration/ January 10,2016.

[22] M. Bounessah and B. P. Atkin, "An application of exploratory data analysis (EDA) as a robust non-parametric technique for geochemical mapping in a semi-arid climate," *Applied Geochemistry*, vol. 18, no. 8, pp. 1185–1195, 2003.

[23] F. Miao, Y. Wu, Y. Xie, and Y. Li, "Prediction of landslide displacement with step-like behavior based on multialgorithm optimization and a support vector regression model," *Landslides*, vol. 15, pp. 475–488, 2018.

[24] X. Zhu, Q. Xu, M. Tang, H. Li, and F. Liu, "A hybrid machine learning and computing model for forecasting displacement of multifactor-induced landslides," *Neural Computing and Applications*, vol. 30, pp. 3825–3835, 2018.

[25] Y. Liu, Z. Chen, B. D. Hu, J. K. Jin, and Z. Wu, "A non-uniform spatiotemporal kriging interpolation algorithm for landslide displacement data," *Bulletin of Engineering Geology and the Environment*, vol. 78, no. 6, pp. 4153–4166, 2019.

[26] Z. Jianjun, S. Yingchun, H. Jun, Z. Bin, and W. Lixin, "Challenges and development of data processing theory in the era of big data in surveying and mapping," *Geomatics and Information Science of Wuhan University*, vol. 46, no. 7, pp. 1025–1031, 2021.

[27] Y. G. Zhang, X. Q. Chen, R. P. Liao et al., "Research on displacement prediction of step-type landslide under the influence of various environmental factors based on intelligent WCA-ELM in the Three Gorges Reservoir area," *Natural Hazards*, vol. 107, no. 2, pp. 1709–1729, 2021.

[28] H. Heyerdahl, C. B. Harbitz, U. Domaas et al., "Rainfall induced lahars in volcanic debris in Nicaragua and El Salvador: practical mitigation," in *Proceedings of International Conference on Fast Slope Movements—Prediction and Prevention for Risk Mitigation, IC-FSM2003*, pp. 275–282, Patron Pub, Naples, 2003.

[29] T. Glade, M. J. Crozier, and P. Smith, "Applying probability determination to refine landslide-triggering rainfall thresholds using an empirical "Antecedent Daily Rainfall Model"," *Pure and Applied Geophysics*, vol. 157, no. 6-8, pp. 1059–1079, 2000.

[30] J. L. Zezere, R. M. Trigo, and I. F. Trig, "Shallow and deep landslides induced by rainfall in the Lisbon region (Portugal): assessment of relationships with the North Atlantic Oscillation," *Natural Hazards and Earth System Sciences*, vol. 5, pp. 331–344, 2005.

[31] J. I. Lianen, Z. O. U. Yinlong, and X. Bing, "Data processing techniques on sensors of smart terminals for 3D navigation," *Journal of Computer Application*, vol. 35, no. 1, pp. 252–256, 2015.

[32] J. I. Jiang, G. A. O. Pengfei, J. I. A. Nannan et al., "Spectral smoothing with adaptive multiscale window average," *Spectroscopy and Spectral Analysis*, vol. 35, no. 5, pp. 1445–1449, 2015.

[33] D. Feng and W. Jie, "Exploratory analysis on air quality monitoring data," *Journal of Anqing Normal University(Natural Science Edition)*, vol. 26, no. 4, pp. 34–40, 2020.

[34] L. Anselin, *Exploring Spatial Data with GeoDa^{TM} : A Workbook*, Center for Spatially Integrated Social Science, 2005.

[35] D. M. Cruden and D. J. Varnes, "Landslide types and processes," *Landslides: Investigation and Mitigation Transportation Research Board Special Report, 247*, A. K. Turner and R. L. Shuster, Eds., National Academy Press, Washington DC, 1996.

[36] N. Bar, M. Kostadinovski, M. Tucker et al., "Rapid and robust slope failure appraisal using aerial photogrammetry and 3D slope stability models," *International Journal of Mining Science and Technology*, vol. 30, no. 5, pp. 651–658, 2020.

[37] D. Shaunik and M. Singh, "Bearing capacity of foundations on rock slopes intersected by non-persistent discontinuity," *International Journal of Mining Science and Technology*, vol. 30, no. 5, pp. 669–674, 2020.

[38] Z. Tao, S. Yu, X. Yang, Y. Peng, Q. Chen, and H. Zhang, "Physical model test study on shear strength characteristics of slope sliding surface in Nanfen open-pit mine," *International Journal of Mining Science and Technology*, vol. 30, no. 3, pp. 421–429, 2020.

[39] A. McQuillan, I. Canbulat, and O. Joung, "Methods applied in Australian industry to evaluate coal mine slope stability," *International Journal of Mining Science and Technology*, vol. 30, no. 2, pp. 151–155, 2020.

[40] D. J. Varnes, "Slope movement types and processes," *Landslides: Analyses and Control Special Report 176*, R. L. Schuster and R. J. Krizek, Eds., National Academy of Sciences, Washington, D.C., 1978.

WILEY | Hindawi

Research Article

Injection Rate-Dependent Deflecting Propagation Rule of Hydraulic Fracture: Insights from the Rate-Dependent Fracture Process Zone of Mixed-Mode (I-II) Fracturing

Yuekun Xing [iD] and Bingxiang Huang [iD]

State Key Laboratory of Coal Resources and Safe Mining, China University of Mining and Technology, Xuzhou 221116, China

Correspondence should be addressed to Bingxiang Huang; huangbingxiang@cumt.edu.cn

Mixed-mode (I-II) fracturing is a prominent mechanical characteristic of hydraulic fracture (HF) deflecting propagation. At present, understanding the effect of injection rates on HF deflecting propagation remains challenging and restricts the control of HF deflecting propagation bearing tensile and shear stresses with fluid injection rates. Our recently published experimental results show that the fracture process zone (FPZ) length of mixed-mode (I-II) fractures in rock-like materials increases with the rising quasistatic loading rate. Both the deformation in FPZ and the generation of real fracture surfaces are tensile. On this basis, the rate-dependent mixed-mode (I-II) cohesive fracture model was proposed under quasistatic loading, and a couple of theoretical outcomes were obtained. Under different injection rates, the deflecting HF propagates step-by-step under mixed-mode (I-II) fracturing, and the HF extension path is supposed to be straight in each step. With the increment of injection rate, the increased (tensile) FPZ length is the stable propagation distance of deflecting HF in each step and besides deteriorates the fracture resistance discontinuity of FPZ developing to be a real tensile fracture. Thus, the mixed-mode (I-II) fracture tends to propagate unstably driven by kinetic energy once FPZ develops completely under fast loading. Moreover, two injection rate-dependent (IRD) HF deflecting propagation modes were determined, i.e., the step-by-step stable-propagation and step-by-step unstable propagation modes. HF deflection occurs in the step alternation of fracture propagation. With the increasing fluid injection rate, the increased FPZ length and kinetic energy (from fracture resistance discontinuity) extend the stable and unstable HF propagation distance along the initial direction in an extension step, respectively. Therefore, fast fluid injection improves the HF deflecting propagation radius; i.e., it inhibits the HF deflecting propagation or promotes HF extension along the initially designed direction. The injection rate-dependent HF deflecting propagation modes (based on the proposed model) were validated by further processing of published true triaxial physical simulation tests of hydraulic fracturing. The ordinal response of Fiber Bragg grating sensors embedded along the fracture propagation path, and the continuous fluctuant injecting pressures validate the step-by-step propagation of the hydraulic fracture. The test-measured deflecting HF trajectory indicates that high fluid injection rates remarkably increase the HF deflecting radius, which is consistent with the theoretical analysis in this work. The above findings can provide theoretical bases for controlling the HF deflecting propagation in the surrounding rock of mines and oil-gas reservoirs.

1. Introduction

In the mine, weakening the hard roof above the coal seam by hydraulic fracturing is a significant technical means to prevent the sudden collapse of the hard roof, avoiding dynamic disasters [1, 2]. For oil/gas exploitation, directional perforation hydraulic fracturing is a practical approach to improve

the permeability and oil drainage area of the oil-gas reservoirs [3, 4]. Due to disturbance stresses caused by excavation in the mine and the directional perforating in oil/gas reservoirs, the designed HF extension direction is always oblique to the principal directions of in situ stresses. Consequently, HF propagates along a deflecting trajectory and presents shape-s (Figure 1). Due to in situ stresses and net pressure
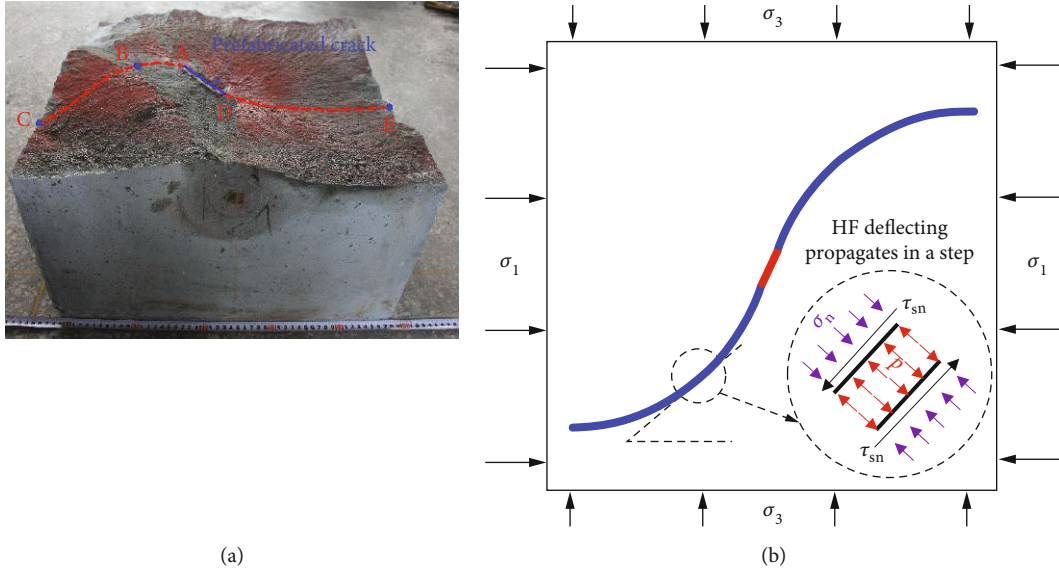
(a)

(b)

FIGURE 1: The photo and diagram of the deflecting hydraulic fracture: (a) photos of the HF deflecting propagation with hydraulic fracturing physical simulation tests (our previous work); (b) the diagram of deflecting HF bearing tensile and shear stresses.

of the hydraulic fluid, the deflecting HF (Figure 1(a)) bears the tensile-shear combined stresses and follows mixed-mode (I-II) fracturing [3] (Figure 1(b)). Therefore, controlling the HF deflecting propagation under mixed-mode (I-II) fracturing conditions is fundamental to enhancing the hard roof weakening in the mine and improving permeabilities in oil-gas reservoirs. Since the fluid injection rate is a significant parameter for controlling HF propagation, the injection rate-dependent deflecting propagation rule of the hydraulic fracture is the theoretical basis for controlling HF in field applications.

To date, investigations of the HF deflecting propagation rules focus on the effects of horizontal in situ stresses differences, fracture initiation azimuth, and disturbance stress on HF deflecting trajectory [3–6]. However, researches on injection rate-dependent (IRD) HF deflecting propagation are relatively limited [7, 8]. The limited studies, conducted by true triaxial physical simulation tests of hydraulic fracturing [8] and extended finite element (XFEM) simulations [7], reveal that the increased injection rates remarkably extend the HF deflecting distance. The above investigation provides references for the effective control of HF deflecting propagation. However, the HF deflecting propagation model was not proposed based on the above hydraulic fracturing experiments; besides, the fracture model employed in the above XFEM simulations is independent of fluid injection rates. Therefore, theoretical characterization of the rate-dependent mixed-mode (I-II) fracturing in rock-like materials is fundamental to revealing the IRD HF deflecting rule.

Mixed-mode (I-II) fracturing is a prominent mechanical characteristic of HF deflecting propagation. As of now, elastic mixed-mode (I-II) fracture models, such as the maximum stress criterion [9], the maximum energy release rate criterion [10], the minimum strain energy density criterion [11], and other modified models [12] of above criteria, were most widely used to characterizing fracture initiation directions.

However, the above mixed-mode (I-II) fracture models are independent of loading rates. Rate-dependent fracturing characteristics of rock-like materials were mainly investigated with fracturing experiments, focus on mode I (tensile) fractures, whereas researches on mixed-mode (I-II) fractures are relatively limited. Most experimental results show both the mode I (tensile) and mixed-mode (I-II) cracks of rock-like materials, such as concrete [13], shale [14], granite [15], and marble [16, 17], have similar rate-dependent fracture behaviors. More specifically, the elastic fracture resistances (fracture toughness or energy release rate) are strengthened with loading rates increasing. The enhanced fracture resistance is attributed to the insufficient development of plastic strains and intergranular cracks under fast loading [13–15, 18]. The above investigations significantly deepen the understanding of the rate-dependent fracture behavior during HF deflecting propagation. Nevertheless, previous investigations still have two limitations. (1) The previous investigations mainly reveal the rate-dependent elastic fracturing characteristics of mixed-mode (I-II) crack in rock-like materials, neglecting the rate-dependent development of fracture process zone (FPZ). Note that FPZ is a nonnegligible microcrack zone ahead of the mixed-mode (I-II) fracture tip, which is the prominent fracture characteristic of rock-like materials [19–23]. Hence, the traditional fracture model cannot delineate the rate-dependent FPZ growth in HF deflecting propagation. (2) The classic elastic mixed-mode fracture model mainly describes the rate-independent elastic fracture initiation and is not well-suited for HF deflecting propagation with FPZ remarkable development [24–27]. Therefore, characterizations of IRD HF deflecting propagation lack the applicable mixed-mode (I-II) fracture model for rock-like materials.

Given that the fluid injection of hydraulic fracturing is usually quasistatic, in our recently published work [28], the quasistatic rate-dependent FPZ development of mixed-
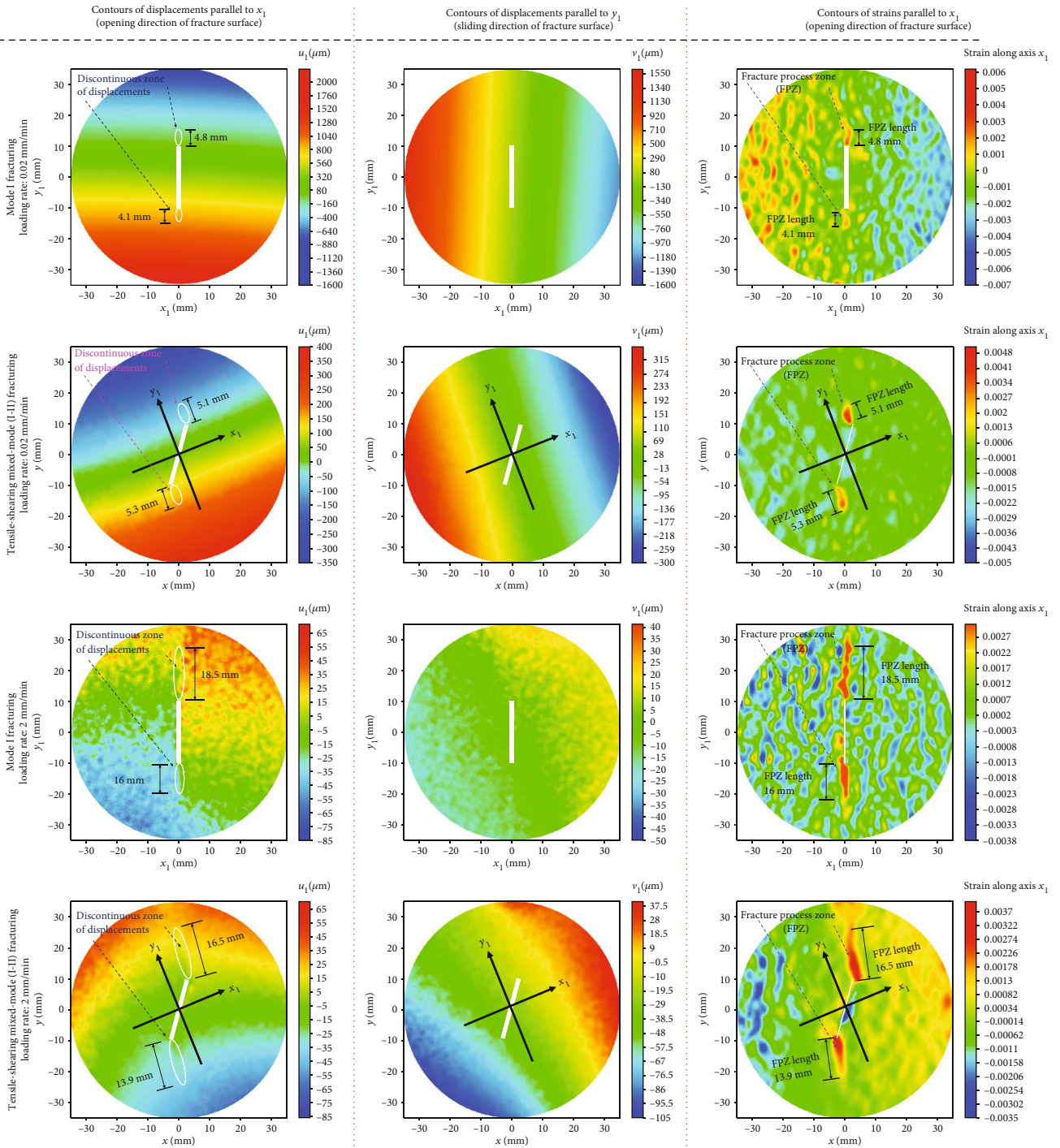
FIGURE 2: DIC-based displacement and strain fields of Mixed-mode (I-II) and pure mode I fracturing at different quasistatic loading rates (replotted based on our recently published work [28]).

mode (I-II) fracturing has been investigated. In detail, we conducted the mixed-mode (I-II) fracturing tests on the centrally cracked Brazilian disk (CCBD) specimens (radius: 50 mm) of artificial rock-like materials to create tensile-shearing mixed-mode (I-II) fractures at different quasistatic displacement loading rates (0.02~2 mm/min). The FPZ development ahead of the mixed-mode fracture tip was characterized with the digital image correlation (DIC) method.

Two main findings were obtained. (1) At different loading rates, in the FPZ ahead of mixed-mode (I-II) fracture tips, the opening displacement perpendicular to the FPZ development direction presents a remarkable discontinuity; in contrast, the sliding displacement parallel to FPZ development direction is continuous (Figure 2). This mixed-mode (I-II) fracturing feature is consistent with the pure mode I fracturing, as shown in Figure 2. Consequently, at different

quasistatic loading rates, the tensile-shearing mixed-mode (I-II) fracturing just represents the fracture bearing tensile-shearing stresses for rock-like materials. Still, at the mixed-mode (I-II) fracture tip, the deformation in FPZ and the generation of the real fracture surface are tensile. (2) The FPZ length and the peak load increase with the rising loading rate (Figure 3) from 0.02 mm/min to 2 mm/min. Note that the increment of FPZ length (Figure 3(b); FPZ length increased by 287%) is much more remarkable than the peak load (Figure 3(a); FPZ increased by 66%). These rate-dependent mixed-mode fracturing characteristics provide significant bases for the theoretical understanding of the injection rate-dependent HF deflecting propagation rule.

In this work, we proposed a rate-dependent mixed-mode (I-II) fracturing model, with insights from the rate-dependent FPZ of mixed-mode (I-II) fracturing (our recently published work [28]). Based on the rate-dependent mixed-mode (I-II) fracture model, we obtained several theoretical outcomes of the injection rate-dependent HF propagation rule, which was validated with the physical simulation tests of HF deflecting propagation.

2. Model Bases of the Injection Rate-Dependent HF Deflecting Propagation

Mixed-mode (I-II) fracturing is a prominent mechanical behavior of HF deflecting propagation. In this section, we will propose a rate-dependent mixed-mode (I-II) fracturing model, with insights from the rate-dependent FPZ of mixed-mode (I-II) fracturing [28], delineating the experiment-measured tensile fracturing characteristic of the mixed-mode (I-II) fracture in rock-like materials. Then, the rate-dependent fracture initiation and deflecting propagation will be theoretically analyzed with the correlation between the fracture driving force and resistance (i.e., the fracture resistance curve). These theoretical investigations are fundamental to revealing the correlation between HF deflecting propagation behavior and fluid injection rates.

2.1. Rate-Dependent Mixed-Mode (I-II) Cohesive Crack Model of the FPZ Development. As mentioned in Section 1, the FPZ deformation ahead of the mixed-mode (I-II) fracture tip has been validated to be tensile, and FPZ length is increased with the rising loading rate (Figures 2 and 3). Therefore, the tensile-shearing mixed-mode (I-II) fracturing in rock-like materials just represents the fracture bearing mixed-mode tensile and shear stresses. Still, at the mixed-mode (I-II) fracture tip, both the deformation in FPZ and the generation of the real fracture surface are tensile. Based on this, the rate-dependent tensile fracturing model and the further theoretical analyses of the mixed-mode (I-II) fracture will be proposed in this section, following three assumptions as below:

(1) The tensile FPZ ahead of the mixed-mode (I-II) fracture can be regarded as a tensile cohesive crack [20–22, 29, 30]

(2) Fracture deflecting propagation follows the step-by-step mixed-mode (I-II) fracturing mode. The proposed model is applicable to each fracture propagation step (Figure 1(b)). In each propagation step, the FPZ (cohesive crack) growth direction follows the maximum tensile (tangential) criteria [9, 31, 32] at the initial mixed-mode fracture tip and the completely developed FPZ tip (cohesive crack tip)

(3) In each propagation step of mixed-mode fracturing, the FPZ growth path and the subsequent real fracture (stable and unstable) propagation trajectory are supposed to be straight, based on the experimental results (Figure 2)

Note that the maximum tensile (tangential) criteria will not be discussed in detail. It is not the goal of this work. The HF deflecting extension trajectory depends on the rate-dependent mixed-mode (I-II) fracture propagation distance in each step, which will be interpreted in Section 3. This model is mainly used to deeply analyze the correlation between the fracture driving force and resistance, providing theoretical bases for revealing the injection rate-dependent deflecting propagation rule of hydraulic fracture.

The tensile FPZ development is seen as the nucleation and coalescence of the microcracks with energy dissipation in the vicinity of a crack tip [21, 27, 33]. At different loading rates, materials softening in FPZ due to the generation of microcracks (Figure 4(a)) can be delineated by the softening opening of cohesive crack ahead of the mixed-mode (I-II) crack tip (Figure 4(b)). Along the cohesive crack, cohesive stress is distributed and tends to close the crack (Figure 4(b)), eliminating the singularity at the cohesive crack tip. Cohesive stress decreases with the softening deteriorating, which can be represented by the relationship between the cohesive stress (σ_c) and the crack opening displacement (COD; w) in a unit area of cohesive crack (Figure 4(c)). Considering the moderate softening in FPZ, the σ_c-w curve of most rock-like materials is supposed to be linear (Figure 4(c)) [22, 34, 35]. At a constant loading rate, the softening function of σ_c-w follows Equation (1).

$$\sigma_c(w) = \sigma_t - \left(\frac{\sigma_t}{w_{cmax}}\right)w, \tag{1}$$

where σ_c is the cohesive stress, w the crack opening displacement (COD), σ_t the cohesive tensile strength, and w_{cmax} the critical COD.

When σ_c on both sides of the FPZ reaches σ_t, the cohesive crack begins to soften, indicating that the FPZ starts to develop (Figure 4(c)). Then, σ_c decreases with the increment of COD. When σ_c vanishes and COD reaches the critical value (w_{cmax}), the real fracture surface of a unit area generates, and FPZ develops completely. The area under the softening curve is the dissipated energy (G_f) (Equation (2)), which is equal to the cohesive fracture energy (G_F) (Equation (3)) when the crack faces are completely separated
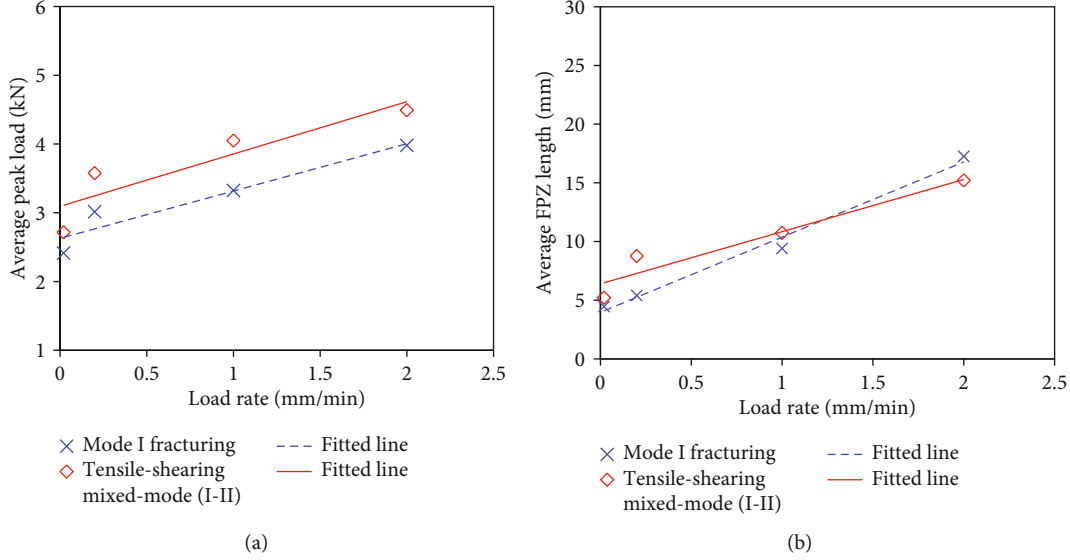
FIGURE 3: The evolution law of FPZ length and peak load with loading rates increasing: (a) peak load vs. loading rates; (b) FPZ length vs. loading rates.

(Figure 4(c)).

$$G_f(y_1) = \int_0^{w(y_1)} \sigma_c(w) dw, \tag{2}$$

$$G_F = \int_0^{w_{cmax}} \sigma_c(w) dw. \tag{3}$$

As shown in Figures 2 and 3, FPZ length is remarkably increased with the rising quasistatic loading rate. The completed development FPZ length (L) is regarded as the prominent rate-dependent parameter [28]. Therefore, distributions of cohesive stress and COD along the FPZ are rate-dependent (Equations (4)–(6)), and the $G_f(y_1)$ in Equation (2) is also rate-dependent. The previous experimental investigations [27, 29, 30, 36] validate that σ_c and w are linearly (Figure 4(d)) distributed along the FPZ (Equations (4) and (5)) and w_{cmax} is linearly (Figure 4(e)) increased with developing FPZ length (l) (Equation (5)).

$$\sigma_c(y_1, r) = \sigma_c(w(y_1, r)) - \left[\frac{\sigma_c(w(y_1, r))}{l}\right] y_1, \tag{4}$$

$$w(y_1, r) = w_c(l, r) - \left[\frac{w_c(l, r)}{l}\right] y_1, \tag{5}$$

$$w_c(l, r) = \left[\frac{w_{cmax}}{L(r)}\right] l, \tag{6}$$

where y_1 is the axis along FPZ develop direction, r the loading rate, l the developing FPZ length, L the length of a completely developed FPZ, and w_c the crack tip opening displacement (CTOD).

In each fracture propagation step, the accumulated dissipated energy (G_d) in FPZ can be obtained by the integration of $G_f(y_1)$ along the FPZ length (Equation (7)). $G_d(l)$ can be

regarded as the fracture resistance during the cohesive crack extending. When the FPZ develops completely; i.e., $l = L$, G_f reaches the critical value, G_D, which is a function of the rate-dependent FPZ length, as presented in Equation (8). G_D indicates the fracture resistance of FPZ completely developing, corresponding to generating the real mixed-mode (I-II) fracture of a unit area at the tip of an initial crack tip without FPZ.

$$G_d(r, l) = \int_0^l G_f(r, y_1) dy_1, \tag{7}$$

$$G_D(r) = \int_0^{L(r)} G_f(r, y_1) dy_1. \tag{8}$$

Substitution of Equations (1)–(6) into Equations (7) and (8) yields

$$G_d(r, l) = \frac{[w_{cmax}\sigma_t(3L(r) - 2l)l^2]}{6L^2(r)}, \tag{9}$$

$$G_D(r) = \frac{[w_{cmax}\sigma_t L(r)]}{6}. \tag{10}$$

As mentioned above, the completed development FPZ length (L) is the prominent rate-dependent parameter [28] of FPZ development during mixed-mode (I-II) fracturing. As presented in Equations (9) and (10), the effect of loading rates on G_d and G_D depends on $L(r)$. Therefore, we can obtain two rate-dependent fracture resistance indexes (including FPZ length) via dividing Equations (9) and (10) by $w_{cmax}\sigma_t$, as listed in Equations (11) and (12).

$$R_d(r, l) = \frac{G_d(r, l)}{(w_{cmax}\sigma_t)} = \frac{[(3L(r) - 2l)l^2]}{[6L^2(r)]}, \tag{11}$$
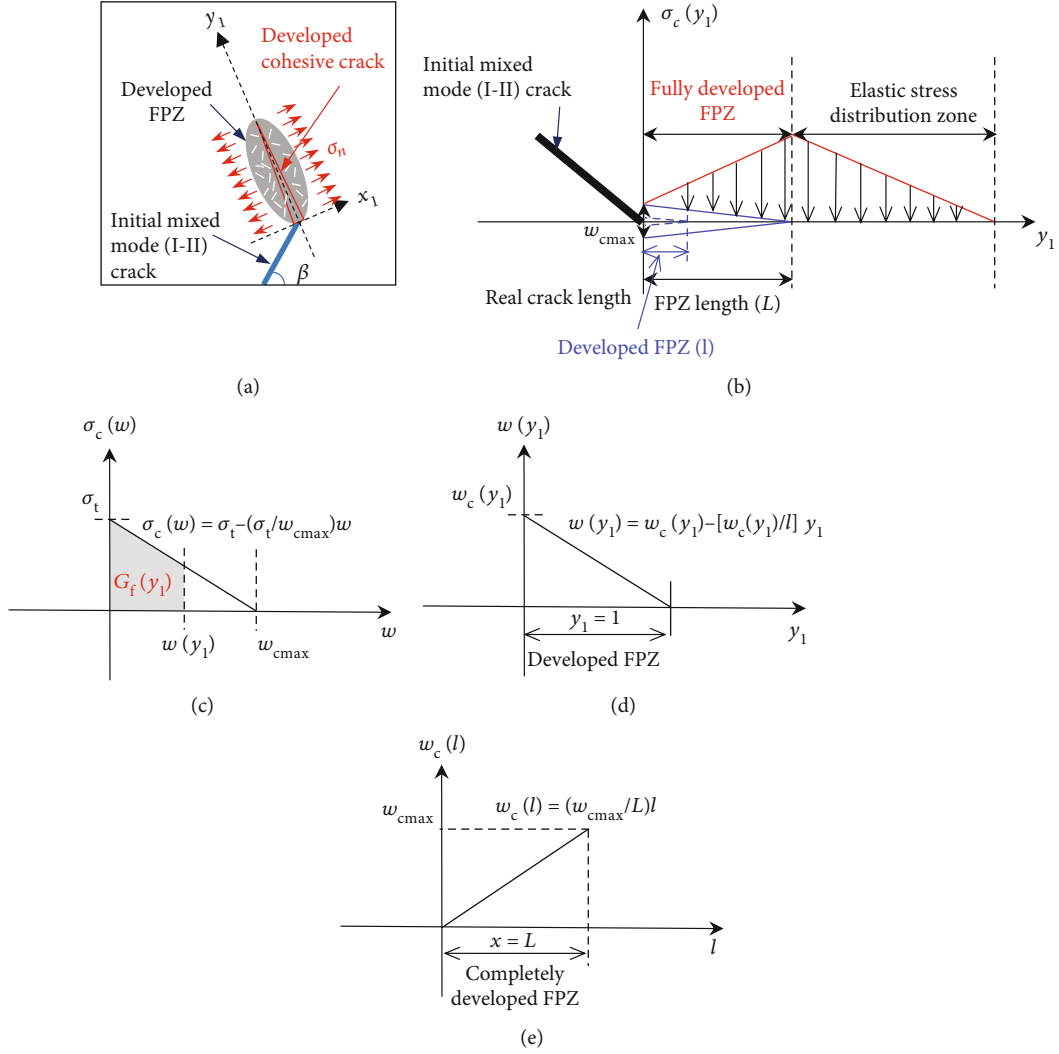
Figure 4: FPZ Development ahead of the mixed-mode (I-II) fracture tip of rock-like materials: (a) schematic diagram of the tensile development of the FPZ under mixed-mode (I-II) stresses; (b) cohesive stresses distributed along the cohesive crack in FPZ, ahead of the mixed-mode (I-II) fracture tip; (c) cohesive stress vs. crack opening displacement; (d) the distribution of crack opening displacement along the cohesive crack (i.e., FPZ); (e) the rising crack tip opening displacement with FPZ development (i.e., the increment of FPZ length).

$$R_D(r, L) = \frac{G_D(r)}{(w_{cmax}\sigma_t)} = \frac{L(r)}{6}, \tag{12}$$

where R_d and R_D are rate-dependent fracture resistance indexes corresponding to the developing and completely developed FPZ length.

Equations (11) and (12) present the fracture resistance during FPZ developing ahead of the real mixed-mode (I-II) fracture tip (i.e., the mixed-mode fracture initiation). The classical rock fracture mechanics indicates that the real fracture generation and extension are supposed to be quasistatic after FPZ completely developing [31, 36–38]. More specifically, once the FPZ develops completely, a new and real fracture surface per unit length will generate in FPZ ahead of the initial fracture tip. Due to the continuous nucleation and coalescence of microcracks in FPZ at the real fracture tip, the completely developed FPZ always locates at the extending real fracture tip. Namely, the real mixed-mode (I-II) fracture

pushes the tensile FPZ to propagate. Therefore, under the condition of stable fracture propagation, G_F is the stable fracture resistance of generating a real fracture surface per unit area after FPZ completely developing. Substituting Equation (1) into Equation (3), the expression of G_F follows

$$G_F = \frac{(w_{cmax}\sigma_t)}{2}. \tag{13}$$

Similar to Equations (11) and (12), the rate-dependent fracture resistance index (R_F) corresponding to G_F follows

$$R_F(r, a) = \frac{G_F}{(w_{cmax}\sigma_t)} = \frac{1}{2}, \tag{14}$$

where a is the real fracture length. Note that R_F is independent of FPZ length and less than R_D, with the unit of mm. Note that the difference between R_F and R_D is rate-

dependent, which significantly correlated to fracture deflecting propagation and will be discussed in detail in Section 2.2.

2.2. Model-Based Rate-Dependent Stable and Unstable Propagation of Mixed-Mode (I-II) Fractures.

The relationship between the fracture driving force (stress or energy driving fracture propagation) and fracture resistance determines the stable and unstable propagation of the mixed-mode (I-II) fracture [31, 32, 37]. Note that the FPZ developing process is stable [22, 34, 35] and the stable or unstable fracture propagation occurs after FPZ developing to be the real fracture surface. In this section, we will analyze the rate-dependent stable and unstable propagation based on the proposed mixed-mode (I-II) fracture model.

2.2.1. Rate-Dependent Stable Propagation of the Mixed-Mode (I-II) Fracture.

The stable fracture propagation follows that the fracture driving force equals fracture resistance [31, 32, 37], as in Equation (15). In each fracture extension step, FPZ ahead of the mixed-mode (I-II) fracture tip is the dominant fracture propagation path, and the real fracture surface stably generates in FPZ. Therefore, FPZ length is the fracture propagation distance in each crack extension step.

$$\begin{cases} D_{\mathrm{F}}(r, l) = R_{\mathrm{d}}(r, l) = \dfrac{\left[(3L(r) - 2l)l^2\right]}{\left[6L^2(r)\right]} \text{ FPZ development,} \\ \\ D_{\mathrm{F}}(r, a) = R_{\mathrm{F}}(r, a) = \dfrac{1}{2} \text{ real fracture propagation,} \end{cases}$$

$$(15)$$

where D_{F} is the driving force. As presented in Equation (15), once the FPZ develops completely, the fracture resistance $R_{\mathrm{d}}(r, l)$ will reduce to $R_{\mathrm{F}}(r, a)$, and the real fracture surface begins to generate in FPZ. Given the above discontinuity of fracture resistance, the driving force should reduce from $D_{\mathrm{F}}(r, l)$ to $D_{\mathrm{F}}(r, a)$ as in Equation (15), keeping the balance between the driving force and the fracture resistance. The overlapped driving force and resistance curve are shown in Figure 5.

As shown in Figure 5, the negative horizontal axis indicates the FPZ development, where the reduction of $l - L$ represents FPZ propagation ahead of the mixed-mode (I-II) fracture. The positive horizontal axis means the real fracture extension (Δa). Under different quasistatic loading rates, Figure 5 shows that only the fracture resistance in FPZ development is rate-dependent; in contrast, the generation of real fracture surfaces after FPZ completely developing is constant. Therefore, the resistance curves at different quasistatic loading rates overlap with the increment of real fracture surfaces.

At different quasistatic loading rates, the stable propagation of the mixed-mode (I-II) fracture divides into four stages. Take the overlapped curves of driving forces and fracture resistances at a loading rate of 2 mm/min as an example. (1) Stage A-B represents the FPZ (FPZ_1) development, where points A and B represent the initial and completed development of the tensile FPZ (FPZ_1) ahead of the mixed-mode (I-II) fracture tip. (2) Stage B-C indicates the transition from FPZ (i.e., cohesive crack) development to the real fracture

generation. More specially, when the fracture resistance reaches point C, the real fracture of a unit area generates, and the fracture resistance sharply decreases. To maintain the fracture propagates stably, the driving force should reduce from point A to point B, consistent with the fracture resistance. Since FPZ_1 grows completely, a new FPZ (FPZ_2) starts to develop at the tip of FPZ_1, i.e., the cohesive crack tip perpendicular to the maximum tensile stress. (3) Stage C-D delineates the stable propagation of a real fracture. When Δa attains to L, FPZ develops to be a real fracture surface, and FPZ_2 grows completely along a new direction. Since the FPZ length is a material property at a constant loading rate, the length of FPZ_1 is equal to FPZ_2.

Note that the deflecting propagation of the mixed-mode fracture will repeat stage C-D once the real fracture length exceeds L. Namely, the stable deflecting propagation follows step-by-step and polyline-mode. The propagation distance in each step is the rate-dependent FPZ length of the mixed-mode (I-II) fracture.

2.2.2. Rate-Dependent Unstable Propagation and Arrest of the Mixed-Mode (I-II) Fracture.

Usually, the increasing real fracture length tends to improve the driving force [38], which will increase the difficulty of keeping the balance between the driving force and the fracture resistance during mixed-mode (I-II) fracturing. Therefore, the fracture tends to propagate unstably once the FPZ develops completely. In this part, the rate-dependent unstable propagation and arrest of the mixed-mode (I-II) fracture will be analyzed.

When the fracture length increases and the driving force has no sufficient time to unload, the driving force will be larger than the fracture resistance, which will lead to the unstable propagation of the mixed-mode (I-II) fracture (Equation (16)). Once the fracture propagates unstably, the kinetic energy (Equation (17)) generates and drives the fracture extension [37], though the driving force is less than fracture resistance (Equation (16) and Equation (18)). Once the fracture resistance depletes the kinetic energy (Equation (19)), the unstable fracture will stop extending (i.e., fracture arrest). Consequently, the kinetic energy (driving force minus resistance, such as the integrated area of S_{BCHE} and S_{GCHF} in Figure 6) of unstable fracture propagation can be regarded as another type of driving force. The above unstable propagation of mixed-mode (I-II) fracture will be illustrated in detail in Figure 6, a simplified schematic diagram of FPZ development, unstable fracture propagation, and fracture arrest at different loading rates.

$$\begin{cases} D_{\mathrm{F}}(r, l) = R_{\mathrm{d}}(r, l) = \dfrac{\left[(3L(r) - 2l)l^2\right]}{\left[6L^2(r)\right]} \text{ stable development of FPZ,} \\ \\ D_{\mathrm{F}}(r, a) > R_{\mathrm{F}}(r, a) = \dfrac{1}{2} \text{ unstable propagation of the real fracture,} \\ \\ D_{\mathrm{F}}(r, a) < R_{\mathrm{F}}(r, a) = \dfrac{1}{2} \text{ fracture arrest,} \end{cases}$$
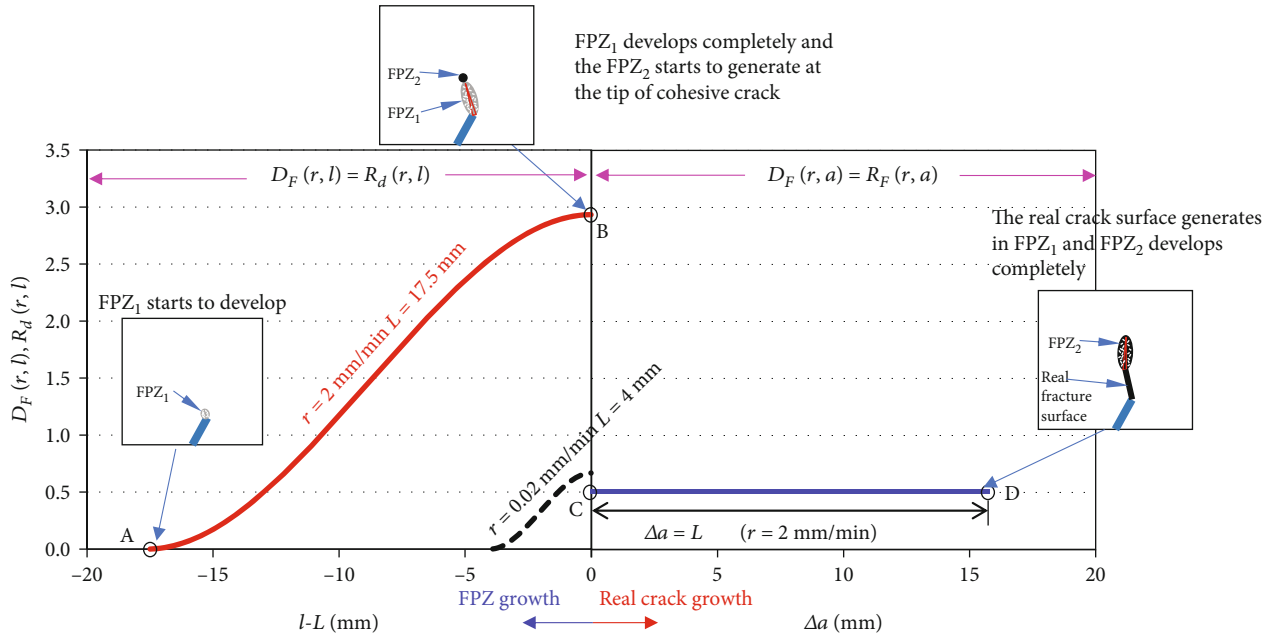
$$(16)$$

FIGURE 5: Schematic diagram of fracture resistance and driving force curves of the stable propagation of mixed-mode cracks at different loading rates.
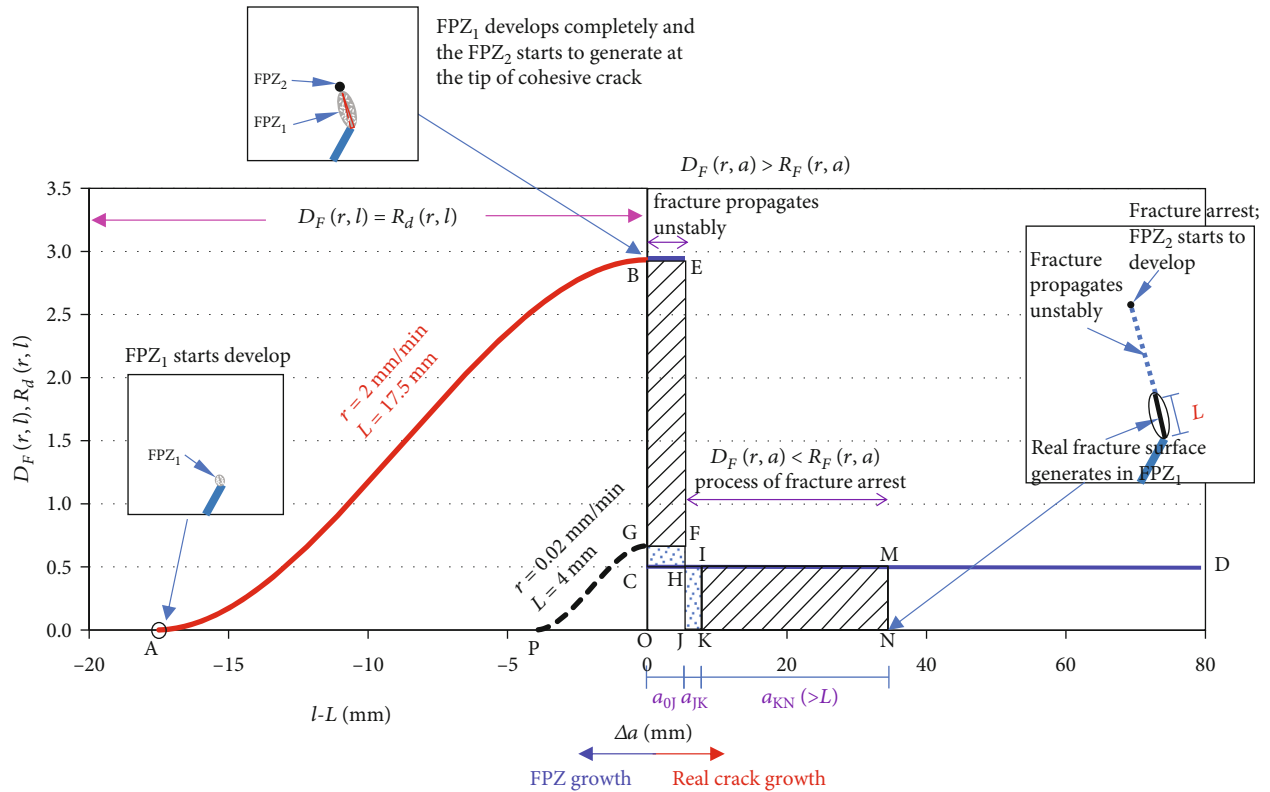

FIGURE 6: Schematic diagram of fracture resistance and driving force curves corresponding to the unstable propagation of mixed-mode cracks at different loading rates.

$$E_{\text{kin}} = \int_{a_0}^{a_0+\Delta a_1} [D_{\text{F}}(r,a) - R_{\text{F}}(r,a)]\mathrm{d}a, \qquad (17)$$

where E_{kin} is the kinetic energy due to unstable fracture propagation, a_0 the initial real fracture length, and Δa_1 the unstable propagation distance of the real fracture under $D_{\text{F}}(r,a) > R_{\text{F}}(r,a)$.

$$E_{\text{arr}} = \int_{a_0+\Delta a_1}^{a_0+\Delta a_1+\Delta a_2} [R_{\text{F}}(r,a) - D_{\text{F}}(r,a)]\mathrm{d}a, \qquad (18)$$

where E_{arr} is the depleting energy of fracture arrest and Δa_2 is the unstable propagation distance of the real fracture under arrest process.

$$E_{\text{kin}} = E_{\text{arr}}. \qquad (19)$$

The unstable propagation and arrest of the mixed-mode (I-II) fracture are mainly due to the fracture resistance discontinuity between the FPZ development and the real fracture generation. More specially, as shown in Figure 6, when the overlapped driving force and fracture resistance reach point B, FPZ develops completely, and the real fracture surface begins to generate. With the increment of loading rates, the fracture resistance discontinuity, such as the segment B-C and the segment G-C, presents more remarkably. Based on this, usually, the driving force is hard to decrease in time and keep balance with the sharply reduced fracture resistance

[37]. Therefore, the mixed-mode (I-II) fracture tends to propagate unstably, which is more remarkable at the high loading rate. Once the balance between the driving force (segment B-E and segment G-F in Figure 6) and the fracture resistance (segment C-H in Figure 6) is broken, the fracture begins to propagate unstably. Then, kinetic energies generate and can be delineated by the integrated area (Equation (20)) of S_{BCHE} and S_{GCHF} (Figure 6). Based on the previous investigation [38], unloading occurs with the sudden generation of real fracture surfaces, and driving forces will decrease less than the fracture resistance. For instance, segments E-J and F-J correspond to the decreased driving fore at loading rates of 2 mm/min and 0.02 mm/min, respectively. The rate-dependent fracture unstable propagation begins to arrest when the driving force is less than fracture resistance. Until E_{arr} depletes E_{kin} (Equations (17)–(19)) at different loading rates, the mixed-mode (I-II) fracture arrests completely. More specifically, as shown in Figure 6, at the loading rate of 0.02 mm/min, when S_{HJKI} (E_{arr}) is equal to S_{GCHF} (E_{kin}), fracture arrests completely. Similarly, at the loading rate of 2 mm/min, the arrest of the unstable propagation of the mixed-mode (I-II) fracture should fulfill $S_{\text{HJNM}} = S_{\text{BCHE}}$. Then, the fracture will propagate along a new direction in the next step, repeating the driving force evolution of segment ABEJKN (at 2 mm/min) and segment PGFJN (at 0.02 mm/min), i.e., the cycle of FPZ development, unstable fracture propagation, and fracture arrest.

$$\begin{cases} E_{\text{kin}} = \int_{0}^{a_{0\text{J}}} [D_{\text{F}}(2,a) - R_{\text{F}}(2,a)]\mathrm{d}a = S_{\text{BCHE}} = E_{\text{res}} = \int_{a_{0\text{J}}}^{a_{\text{JK}}+a_{\text{KN}}} R_{\text{F}}(2,a)\mathrm{d}a = S_{\text{HJNM}} \text{ high loding rate}, \\[4mm] E_{\text{kin}} = \int_{0}^{a_{0\text{J}}} [D_{\text{F}}(0.02,a) - R_{\text{F}}(0.02,a)]\mathrm{d}a = S_{\text{GCHF}} = E_{\text{res}} = \int_{a_{0\text{J}}}^{a_{\text{JK}}} R_{\text{F}}(0.02,a)\mathrm{d}a = S_{\text{HJKI}} \text{ low loading rate}. \end{cases} \qquad (20)$$

The above analyses indicate E_{kin} at the high loading rate is larger than that at the low loading rate. Namely, the increased loading rate will aggravate the unstable fracture propagation. As shown in Figure 6, $(a_{\text{JK}} + a_{\text{KN}})$ at a high loading rate of 2 mm/min is remarkably longer than a_{JK} at a low loading rate of 0.02 mm/min.

2.2.3. Comparison between the Rate-Dependent Stable and Unstable Propagation of the Mixed-Mode (I-II) Fracture. As shown in Figure 7, both the stable and unstable deflecting propagations of the mixed-mode (I-II) fracture follow step-by-step and polyline-mode (HF propagation trajectory presents a polyline shape). With the increment of loading rate, the discontinuity of fracture resistance corresponding to the completed development of FPZ increases significantly, which extends the propagation distance in each extension step of mixed-mode (I-II) fracturing. The velocities (about 0.38 sound velocity at this material) of fracture unstable propagation and arrest are significantly faster than that at quasistatic

propagation conditions [37]. Therefore, the propagation distance of the mixed-mode (I-II) fracture at each extension step is remarkably longer than the FPZ length (i.e., the stable fracture propagation distance in each step), as shown in Figure 7.

Based on the above theoretical analyses, the propagation distance of mixed-mode (I-II) fracture in each extension step will determine the fracture deflecting propagation trajectory, regardless of fracture stable or unstable propagation. The detailed analyses will present in Section 3.

3. Injection Rate-Dependent Deflecting Propagation Rules of the Hydraulic Fracture

The injection of fracturing fluid is the loading approach of hydraulic fracturing. Based on the proposed rate-dependent mixed-mode (I-II) fracture model; in this section, we will propose the injection rate-dependent (IRD) HF deflecting propagation modes.
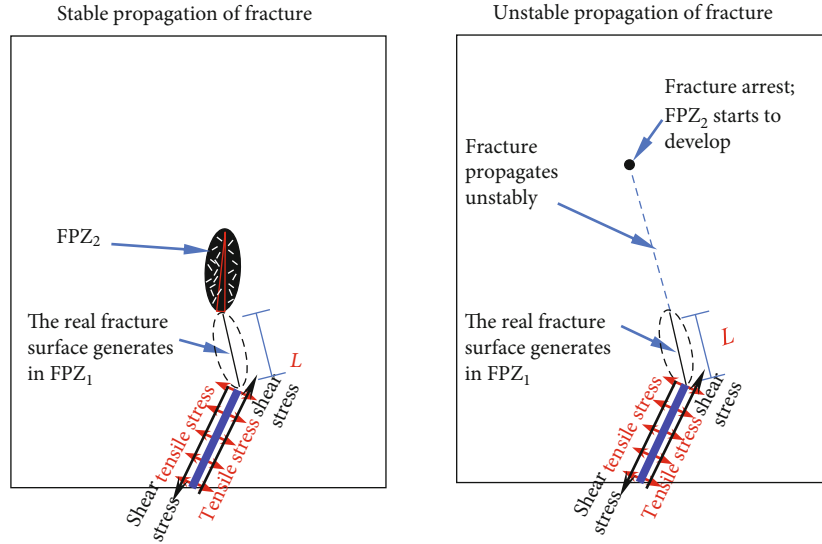
Figure 7: Comparison between stable and unstable propagations of mixed-mode fracturing.

As shown in Figure 1(b), for the microelement of the deflecting HF oblique to the principal stresses, the in situ stresses provide the normal stress (closing the fracture surface) and the shear stress. Once the pressure (p) of fracturing fluid inside the fracture surface offsets the normal closing stress and reaches the critical cohesive tensile strength, the tensile FPZ and real fracture surface propagate in sequence at the mixed-mode (I-II) cohesive crack tip (the tip of a completely developed FPZ in the last extension step). Note that based on the maximum tangential stress criteria [9, 31, 32], the fracture initiation direction depends on the ratio of tensile stress intensity factor to shear stress intensity, i.e., K_{I}/K_{II}, at both the real and nominal crack (such as cohesive crack) tips. Consequently, the fracture propagation direction at each step is independent of the fracture length [3, 9]; i.e., the deflecting angle changes barely at each fracture propagation step. Furthermore, the HF deflecting trajectory is dependent on the fracture propagation distance in each step. The longer the fracture propagation distance in each step is, the larger the HF deflecting radius is. In the next context, we will analyze the injection rate-dependent HF stable and unstable deflecting propagations, respectively. As this research focuses on the rate-dependent mixed-mode (I-II) fracturing behavior of HF deflecting propagation, the flow and seepage characteristics of the fracturing fluid are not the goal of this work.

3.1. Injection Rate-Dependent HF Stable Deflecting Propagation Mode. As shown in Figure 8, β is defined as the angle between the prefabricated fracture (formed by directional slotting or directional perforating) and the direction of minimum in situ stress (σ_3). Considering that the in situ stresses, β and deflecting angle in each step are constant, the overlapped driving force and fracture resistance during stable fracture propagations follow the evolution law as in Figure 5 at different loading rates. The fracture extension distance in each propagation step is consistent with the FPZ length.

Figures 8(a) and 8(b) show that the HF deflecting trajectory or deflecting radius is significantly increased with the rising fluid injection rate, which is due to the extended FPZ length at the fast fluid injection. In detail, under the fracture stable propagation condition, the real fracture stably generates along the FPZ. Thus, the FPZ length is the HF deflecting propagation distance in each step. When the HF deflecting propagation steps are constant, the increased FPZ length at high injection rates will raise the HF deflecting propagation trajectory, i.e., the HF deflecting propagation radius. By analogy, the turning radius of a car depends on the length of the body. To better interpolate the HF stable deflecting propagation rule, the HF stable deflecting propagation trajectory is similar to a car turning. The turning radius is dependent on the car body length, which is corresponding to the FPZ length of HF stable deflecting propagation. In this work, the HF stable deflecting propagation modes at the low and high injection rates are defined as mode 1-1 and mode 1-2, as shown in Figures 8(a) and 8(b).

3.2. Injection Rate-Dependent HF Unstable Deflecting Propagation Mode. As mentioned above, when the mixed-mode (I-II) crack propagates unstably in each step, the extension distance of the real fracture is supposed to be longer than that of stable fracture propagation due to the high velocity [37] of the unstable fracture propagation. Consequently, under the constant loading rate, the HF deflecting extension distance during unstable propagation and arrest in each step (Figures 8(c) and 8(d)) will be much longer than that of stable fracture propagation (Figures 8(a) and 8(b)).

Based on the evolution rule of the unstable fracture propagation and arrest as in Figure 6, the fracture resistance discontinuity of FPZ developing to be a real fracture surface is increased with the rising loading rate, such as the segment BC and segment GC in Figure 6. The increasing resistance discontinuity (from FPZ development to real fracture generation) with a rising loading rate will improve the kinetic energy of HF unstable propagation. Then, the distance of
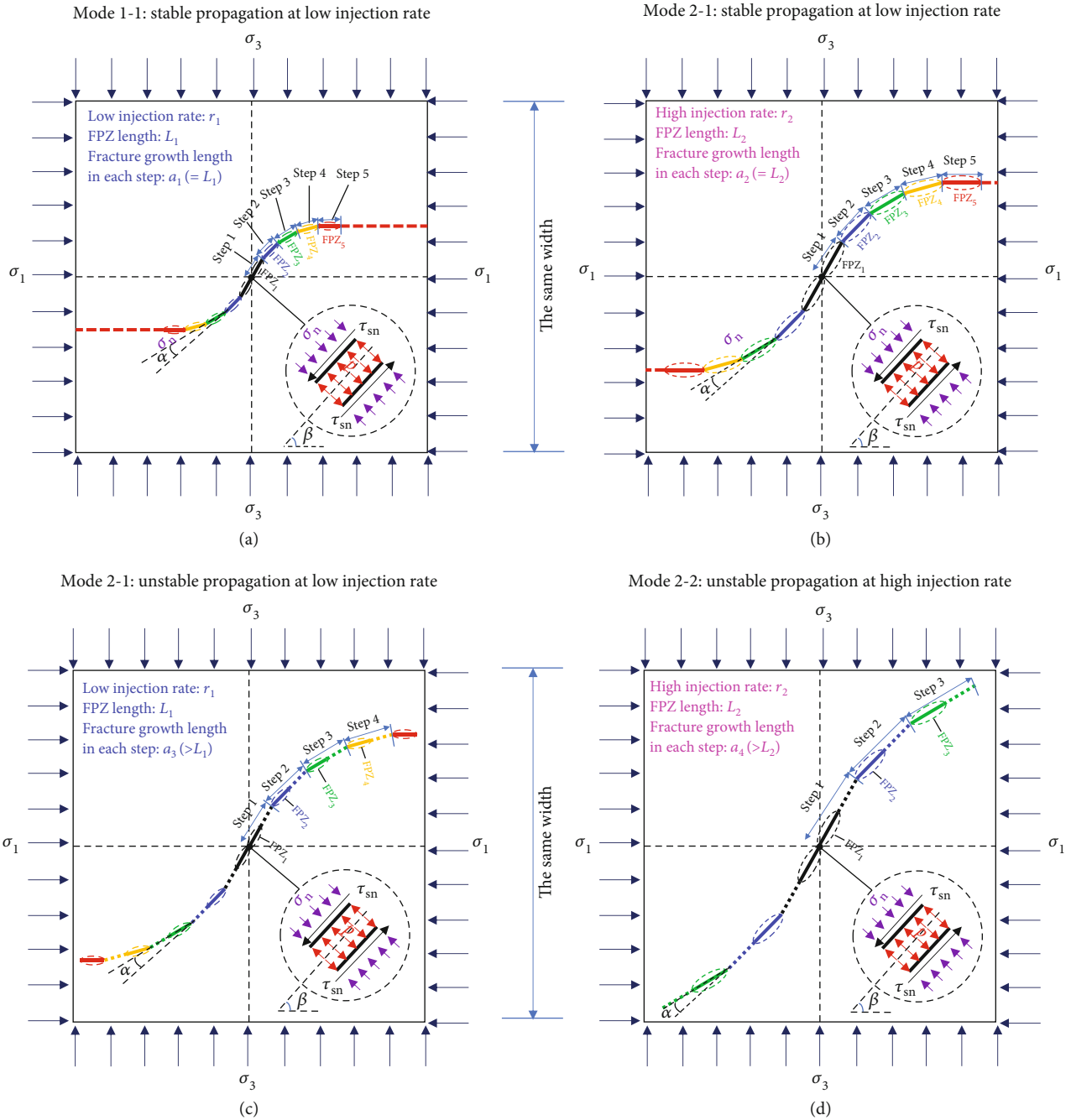
FIGURE 8: Injection rate-dependent deflecting propagation (conceptual) mode of the hydraulic fracture (for r and L, subscripts 1 and 2 correspond to low and high injection rates, respectively; the subscripts of a correspond to the propagation mode, such as modes 1-1, 1-2, 2-1, and 2-2): (a) (mode 1-1) stable propagation at the low injection rate; (b) (mode 1-2) stable propagation at the high injection rate; (c) (mode 2-1) unstable propagation at the low injection rate; (d) (mode 2-2) unstable propagation at the high injection rate.

HF unstable propagation will increase in each deflecting extension step (Figures 8(c) and 8(d)), driven by the increased kinetic energy. Consequently, within the limited extension steps, the deflecting HF will extend over a longer deflecting distance or a larger deflecting radius at a high injection rate. The deflecting HF tends to propagate along the designed initial fracture direction, such as Figure 8(d). At low and high fluid injection rates, the unstable propaga-

tion and arrest of the deflecting HF are defined as mode 2-1 (Figure 8(c)) and mode 2-2 (Figure 8(d)), respectively.

Figure 8 indicates that deflecting HF oblique to the in situ stresses tends to propagate along the initial fracture direction under mode 2-2; i.e., deflecting HF propagates unstably at high fluid injecting rates. In contrast, deflecting HF is hard to maintain the initial fracture direction under stable propagation at a low injection rate, such as mode 1-1.

(a)

(b)

FBG-based strain A -----
FBG-based strain B ·····
FBG-based strain C -----
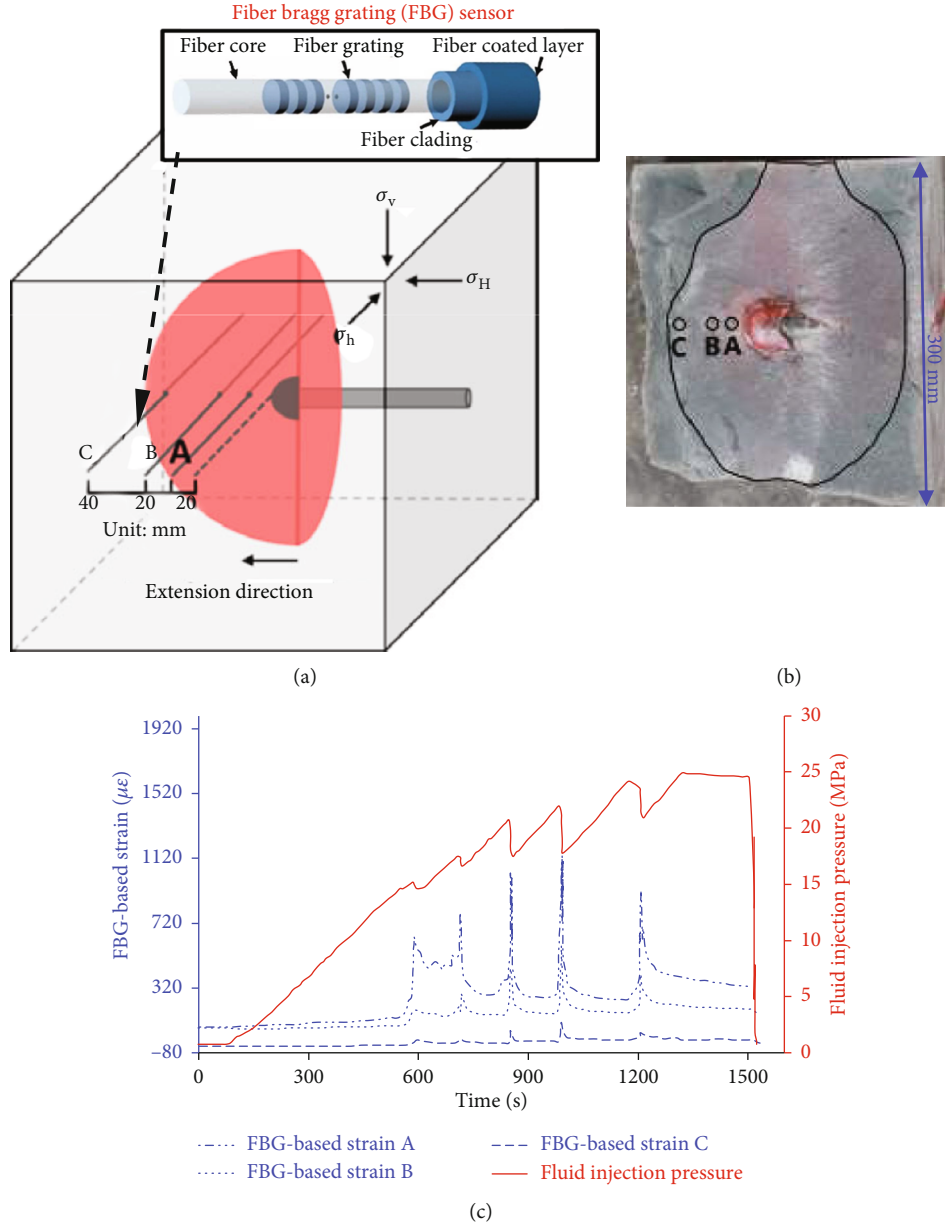Fluid injection pressure ———

(c)

FIGURE 9: Hydraulic fracture propagation characterized by Fiber Bragg Grating (FBG) sensors (replotted based on the experimental results of Yang et al. [39]): (a) the layout of FBG sensors; (b) hydraulic fracture surface; (c) FBG-based strains and injection pressures.

TABLE 1: Experimental programs of deflecting propagation of hydraulic fracture.

Group	Principal stresses (MPa)			The angle between prefabricated crack and σ_h (°)	Fluid injection rate (ml/s)
	σ_v	σ_H	σ_h		
1	10	9	6	45	1.0
2	10	9	6	45	1.5
3	10	9	6	45	5.0

4. Experimental Validations of the Theoretical IRD HF Deflecting Propagation Mode

In this section, the IRD HF deflecting propagation mode mentioned above will be validated by the published physical simulations [8–39] of hydraulic fracturing.

4.1. Validations of the Step-By-Step Propagation of the Hydraulic Fracture. The HF deflecting extension modes in Section 3 are proposed on the premise of the HF step-by-step propagation, whether the mixed-mode (I-II) fracturing is stable or unstable. As mentioned above, the fracture type is tensile ahead of the mixed-mode (I-II) fracture tip at different quasistatic loading rates. In this part, the tensile propagation characteristics (published by Yang et al. 2017 [39]) of the
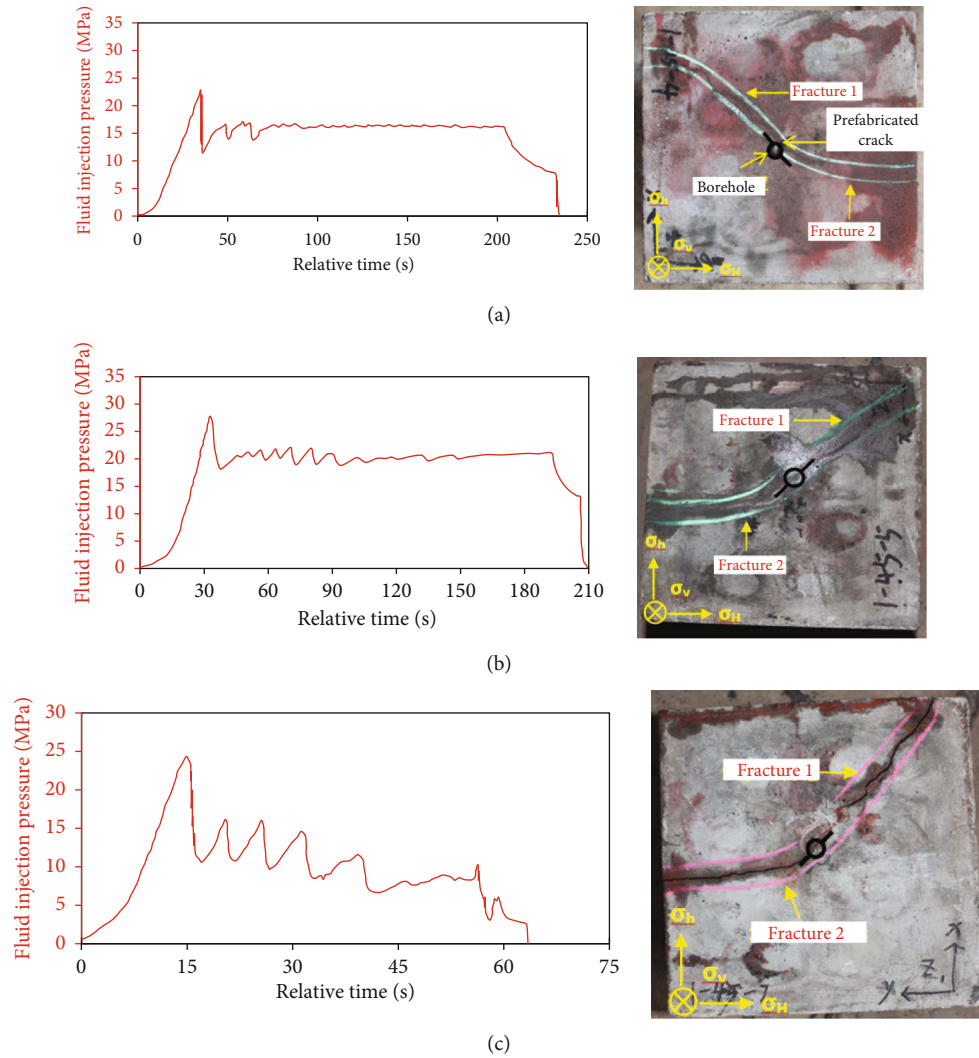
(a)

(b)

(c)

FIGURE 10: Injection pressure curves and deflecting HF geometries at different injection rates (replotted based on the experimental results of Lin et al. [8]): (a) 1.0 ml/s; (b) 1.5 ml/s; (c) 5.0 ml/s.

hydraulic fracture, detected with Fiber Bragg Grating (FBG), are employed to validate the step-by-step extension of the proposed IRD HF propagation mode.

Yang et al. [39] prefabricated three FBG sensors along the hydraulic fracture propagation path in the artificial concrete specimen, as shown in Figures 9(a) and 9(b). FBG sensors were used to identify the opening width (represented by the strain) and propagation rate of the hydraulic fracture in real time. The triaxial confining stress applied to the specimen is 9 MPa (σ_3), 15 MPa (σ_2), and 17 MPa (σ_1). The initial fracturing direction was perpendicular to the minimum principal stress at the center of the sample (Figure 9(b)). The fracturing fluid with a viscosity of 107 mPa·s was injected with a low rate of 2 ml/min, driving the hydraulic fracture propagation. The red dye was added to the fracturing fluid to identify the hydraulic fracture surface (Figure 9(b)). Based on the previous investigations [5, 8, 26], the red dye changes the fracturing fluid very slightly, and adding guar gum is the remarkable and widely used approach for increasing the fracturing fluid viscosity. Since this work mainly investigates the effect of

fluid injection rate on fracture deflecting propagation, the relationship between fracturing fluid properties and hydraulic fracture propagation is not the goal of this work and will not be discussed in detail in this work. The geometry of the hydraulic fracture is approximately elliptical, as shown in Figure 9(b). The responses of injection pressure and FBG-based strain characterize the hydraulic fracture propagation. In detail, the injection pressure gradually rises and fluctuates (Figure 9(c)). Each time the injection pressure reaches the peak, then the injection pressure decreases rapidly, corresponding to the FBG-based strain of quick rising to the peak and then sharp dropping. As the fluid injection pressure can be regarded as the driving force of HF propagation, the sharp decrement of the injection pressure is corresponding to the driving force discontinuity as in Figures 5–6. The fluctuation intensity of the injection pressure curve is consistent with that of the FBG strain, which indicates the sharp fluctuation of injection pressure is supposed to be an index for qualitative characterizing HF extension distance in each step. The sequential responses of FBG sensors A, B, and C indicate
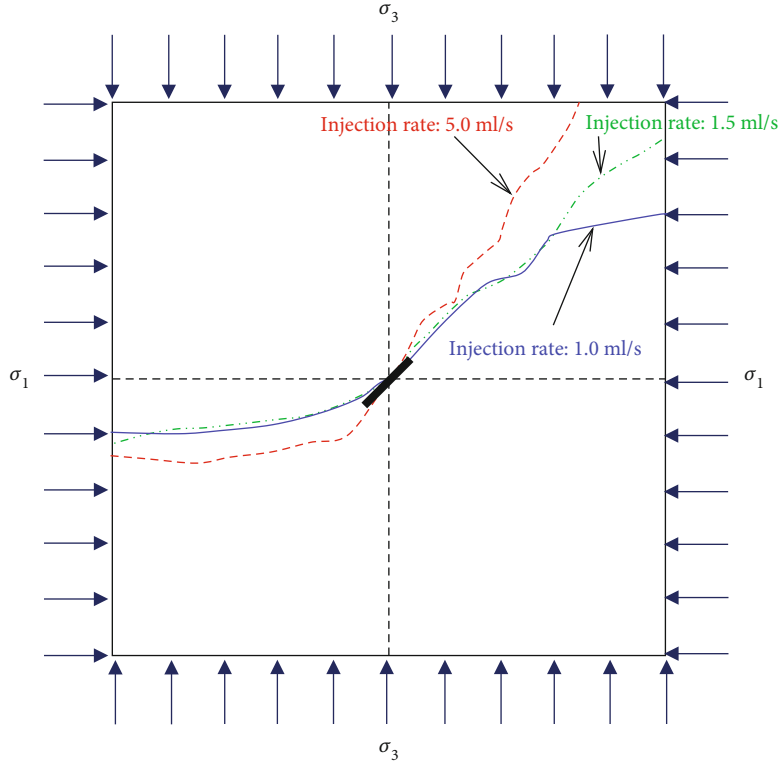
FIGURE 11: The comparison of the HF deflecting propagation trajectories at different loading rates.

the HF extension distance in each step is about 10~20 mm, at an injection rate of 2 ml/min. The above synchronous fluctuations of injection pressures and FBG-based strains validate that the HF propagates step-by-step (i.e., intermittently).

4.2. Validations of the Injection Rate-Dependent HF Deflecting Propagation Modes. In Section 4.1, the step-by-step propagation characteristics of the hydraulic fracture have been validated. On this basis, the injection rate-dependent HF deflecting propagation modes based on the proposed rate-dependent mixed-mode (I-II) fracturing model will be validated in this section, with the HF deflecting propagation tests published by Lin et al. [8].

Lin et al. [8] prepared the cube artificial concrete specimens (dimensions: 300 mm × 300 mm × 300 mm) to conduct hydraulic fracturing tests. At the center of the specimen, the initial crack with a 45° inclination angle to the minimum principal stress was prefabricated to make the hydraulic fracture deflecting propagation. The water with red dye was employed as the fracturing fluid. The red dye changes the fluid viscosity slightly, as indicated by the previous investigations [5, 8, 26]. Since the relationship between fracturing fluid properties and hydraulic fracture propagation is not the goal of this work, the effect of fracturing fluid properties on hydraulic fracture propagation will not be discussed in detail. The fracturing fluid was injected at different loading rates (1.0 ml/s, 1.5 ml/s, and 5.0 ml/s) to drive the deflecting hydraulic fracture extending. The experimental programs are shown in Table 1.

The HF geometries and injection pressures are presented in Figure 10. With the injection rate increasing from 1.0 ml/s to 5.0 ml/s, the fluctuation characteristics of the injection pressure curve present more and more significance. Given the fluctuation consistency of the injection pressures and the FBG-based strain (an index of HF opening width) as in Figure 9(c), the aggravated fluctuation of the injection pressure (Figure 10) is proportional to the HF propagation distance in a step; i.e., deflecting HF tends to unstable propagation and arrest after FPZ develops completely. Therefore, the extension distance of the deflecting HF in each step is increased with the rising injection rate; furthermore, the HF deflecting propagation at the injection rate of 5 ml/s is more in accord with the mode 2-2 as in Figure 9(d).

We compare the HF deflecting propagation trajectories (Figure 10) at different loading rates, as in Figure 11. With the injection rate increasing from 1.0 ml/s to 5.0 ml/s, the HF deflecting extension distance or radius increases significantly; i.e., the deflecting hydraulic fracture tends to propagate along the initially designed direction. Figures 10 and 11 indicate that the deflecting HF propagation mode follows the evolution of mode 1-1→mode 1-2→mode 2-1→mode 2-2 (Figure 8) with the fluid injection rate increasing, and the fast fluid injection tends to drive the deflecting propagating along the initially designed direction.

The above experimental results (Figures 10 and 11) are consistent with the theoretical IRD HF deflecting propagation mode (based on the proposed rate-dependent mixed-mode (I-II) fracture model of rock-like materials).

5. Discussion

This work theoretically investigated the injection rate-dependent deflecting propagation rule of hydraulic fracture, insights from the rate-dependent FPZ of mixed-mode (I-II) fracturing. We can qualitatively determine the key mechanism that the increasing FPZ length and the kinetic energy at high loading rates would improve the deflecting HF propagation distance in each extension step. Then the deflecting trajectory or the deflecting radius of the hydraulic fracture can be increased with the rising injection rate, such as the mode 2-2 in Figure 8. The above theoretical investigations can provide references for field applications in mining and oil-gas reservoir stimulations. (1) For hard roof weakening in mines, increasing the fluid injection rate can improve hydraulic fracture directional propagation along the designed direction, weakening the effect of disturbance stresses on the HF deflecting propagation. Then, the dynamic disaster such as the sudden collapse of the hard roof can be effectively prevented. (2) For oil/gas exploitation, rising injection rate can enhance the HF deflecting radius (i.e., type-S hydraulic fracture trajectory) of directional perforation hydraulic fracturing. Then the reservoir stimulation volume and the permeability can be improved.

The proposed rate-dependent mixed-mode (I-II) fracture model also has limitations. The fluid-solid coupling of hydraulic fracturing was not included in the rate-dependent mixed-mode (I-II) cohesive crack model proposed in this work. Therefore, the proposed model cannot characterize the injection rate-dependent HF deflecting propagation trajectory quantitatively. However, this work can provide references for the deep investigation of the injection rate-dependent hydraulic fracturing model.

6. Conclusions

(1) Given the increased length of the tensile FPZ ahead of the mixed-mode fracture tip at different loading rates, the rate-dependent mixed-mode (I-II) cohesive fracture model was proposed

(2) Based on the proposed model, the model-based rate-dependent stable and unstable propagation of mixed-mode (I-II) fractures were analyzed. Both the stable and unstable fracture deflecting propagations follow step-by-step and polyline-mode. Under stable fracture propagation, the propagation distance in each step is the rate-dependent FPZ length of the mixed-mode (I-II) fracture, and the FPZ length is increased with the increasing quasiloading rate. Under the unstable fracture propagation, the discontinuity of fracture resistance corresponding to the completed development of FPZ increases significantly with the rising loading rate. Due to the above rising discontinuity of fracture resistance at high injection rates, the fracture extension distance of unstable propagation and arrest is improved in each extension step during mixed-mode (I-II) fracturing

(3) The injection rate-dependent HF deflecting propagation modes were proposed. The rising fluid injection rate significantly increases the HF deflecting trajectory or deflecting radius, which is due to the increased HF propagation distance in each step. As the unstable fracture propagation velocity is significantly higher than that of stable propagation, the propagation distance of the deflecting HF in each extension step will be remarkably extended during the unstable propagation and arrest of the mixed-mode fracture. Therefore, the deflecting HF tends to propagate along the initially designed direction under unstable propagation conditions at high loading rates

(4) The model-based injection rate-dependent step-by-step deflecting propagation of the hydraulic fracture was validated by further processing of published true triaxial physical simulation tests of hydraulic fracturing. Furthermore, suggestions for controlling deflecting HF in field applications with the injection rate were discussed. The high injection rate can be employed to increase the deflecting trajectory or the deflecting radius of the hydraulic fracture. On this basis, the injection rate-dependent HF deflecting propagation rule can provide a basis for weakening the hard roof in mines with directional hydraulic fracturing and improving the stimulation volume of the type-S hydraulic fracture in the oil/-gas reservoir

Nomenclature

FPZ:	Fracture process zone
HF:	Hydraulic fracture
IRD:	Injection rate-dependent
XFEM:	Extended finite element method
COD, w:	Crack opening displacement (μm)
CTOD, w_c:	The crack tip opening displacement (μm)
σ_n:	Normal stress for closing HF (MPa)
τ_{sn}:	Shear stress of deflecting HF (MPa)
p:	Fluid injection pressure of hydraulic fracturing (MPa)
σ_c:	Cohesive stress (MPa)
σ_t:	Cohesive tensile strength (MPa)
w_{cmax}:	Critical COD (μm)
G_f:	Dissipated energy (MPa·mm^2)
G_F:	Cohesive fracture energy (MPa·mm^2)
G_d:	Fracture resistance during the cohesive crack extending (MPa·mm^2)
G_D:	Fracture resistance of FPZ developing completely (MPa·mm^2)
L:	The completely developed FPZ length (mm)
l:	The length of a developing FPZ (mm)
y_1:	The axis along FPZ develop direction (mm)
r:	Loading rate (MPa/s, mm/min, etc.)

R_d, R_D:	Rate-dependent fracture resistance indexes corresponding to the developing and completely developed FPZ length (mm)
R_F:	Rate-dependent fracture resistance index corresponding to the real fracture length (mm)
a:	Real fracture length (mm)
D_F:	Driving force corresponding to the FPZ length and the real fracture length (mm)
E_{kin}:	Kinetic energy due to unstable fracture propagation (mm^2; the unit is consistent with the integral area in the fracture resistance curve, as in Figure 6)
E_{arr}:	The depleting energy of fracture arrest (mm^2; the unit is consistent with the integral area in the fracture resistance curve, as in Figure 6)
a_0:	Initial real fracture length (mm)
Δa_1:	The unstable propagation distance of the real fracture (mm)
Δa_2:	The unstable propagation distance of the real fracture under arrest process (mm)
β:	The angle between the prefabricated fracture and the direction of minimum in situ stress (°)
K_I/K_{II}:	The ratio of tensile stress intensity factor to shear stress intensity (unit)
σ_3:	Minimum principal stress (MPa)
σ_2:	Intermediate principal stress (MPa)
σ_1:	Maximum principal stress (MPa)
step-by-step stable propagation mode:	At each fracture propagation step, the fracture extension is stable; i.e., driving force equals fracture resistance.
step-by-step unstable propagation mode:	At each fracture propagation step, the initial fracture propagation state is unstable; i.e., the driving force is higher than the fracture resistance.

Data Availability

The manuscript contains all the original data.

Conflicts of Interest

The authors declare that they have no conflicts of interest.

Acknowledgments

References

[1] B. X. Huang, Y. Z. Wang, and S. Cao, "Cavability control by hydraulic fracturing for top coal caving in hard thick coal seams," *International Journal of Rock Mechanics and Mining Sciences*, vol. 74, pp. 45–57, 2015.

[2] B. Huang, J. Liu, and Q. Zhang, "The reasonable breaking location of overhanging hard roof for directional hydraulic fracturing to control strong strata behaviors of gob-side entry," *International Journal of Rock Mechanics and Mining Sciences*, vol. 103, pp. 1–11, 2018.

[3] G. Q. Zhang and M. Chen, "Dynamic fracture propagation in hydraulic re-fracturing," *Journal of Petroleum Science and Engineering*, vol. 70, no. 3-4, pp. 266–272, 2010.

[4] J. Q. Deng, C. Lin, Q. Yang, Y. R. Liu, Z. F. Tao, and H. F. Duan, "Investigation of directional hydraulic fracturing based on true tri-axial experiment and finite element modeling," *Computers and Geotechnics*, vol. 75, pp. 28–47, 2016.

[5] Z. Y. Liu, Y. Jin, M. Chen, and B. Hou, "Analysis of non-planar multi-fracture propagation from layered-formation inclined-well hydraulic fracturing," *Rock Mechanics and Rock Engineering*, vol. 49, no. 5, pp. 1747–1758, 2016.

[6] Q. Gao, Y. F. Cheng, S. C. Han et al., "Exploration of non-planar hydraulic fracture propagation behaviors influenced by pre-existing fractured and unfractured wells," *Engineering Fracture Mechanics*, vol. 215, pp. 83–98, 2019.

[7] J. X. Li, S. M. Dong, W. Hua, Y. Yang, and X. L. Li, "Numerical simulation on deflecting hydraulic fracture with refracturing using extended finite element method," *Energies*, vol. 12, no. 11, p. 2044, 2019.

[8] J. Lin, C. Xu, and J. W. Yang, "Study on the influence of pump flow rate on the deflection of hydraulic fracturing cracks in longitudinal flume cutting," *Journal of China Coal Society*, vol. 45, no. 8, pp. 118–126, 2019.

[9] F. Erdogan and G. C. Sih, "On the crack extension in plates under plane loading and transverse shear," *Journal of Basic Engineering*, vol. 85, pp. 519–527, 1963.

[10] K. Palaniswamy and W. G. Knauss, "Propagation of a crack under general, in-plane tension," *International Journal of Fracture Mechanics*, vol. 8, no. 1, pp. 114–117, 1972.

[11] G. C. Sih, "Strain-energy-density factor applied to mixed mode crack problems," *International Journal of Fracture*, vol. 10, no. 3, pp. 305–321, 1974.

[12] A. Aminzadeh, A. Fahimifar, and M. Nejati, "On Brazilian disk test for mixed-mode I/II fracture toughness experiments of anisotropic rocks," *Theoretical and Applied Fracture Mechanics*, vol. 102, pp. 222–238, 2019.

[13] Z. P. Bažant and R. Gettu, "Rate effects and load relaxation in static fracture of concrete," *ACI Materials Journal*, vol. 89, no. 5, pp. 456–468, 1992.

[14] B. Mahanta, A. Tripathy, V. Vishal, T. N. Singh, and P. G. Ranjith, "Effects of strain rate on fracture toughness and energy release rate of gas shales," *Engineering Geology*, vol. 218, pp. 39–49, 2017.

[15] X. F. Li, X. Li, H. B. Li, Q. B. Zhang, and J. Zhao, "Dynamic tensile behaviours of heterogeneous rocks: the grain scale fracturing characteristics on strength and fragmentation," *International Journal of Impact Engineering*, vol. 118, pp. 98–118, 2018.

[16] Z. X. Zhang, S. Q. Kou, J. Yu, Y. Yu, L. G. Jiang, and P. A. Lindqvist, "Effects of loading rate on rock fracture," *International*

Journal of Rock Mechanics and Mining Sciences, vol. 36, no. 5, pp. 597–611, 1999.

[17] Q. B. Zhang and J. Zhao, "Effect of loading rate on fracture toughness and failure micromechanisms in marble," *Engineering Fracture Mechanics*, vol. 102, pp. 288–309, 2013.

[18] M. Ju, J. Li, J. Li, and J. Zhao, "Loading rate effects on anisotropy and crack propagation of weak bedding plane-rich rocks," *Engineering Fracture Mechanics*, vol. 230, article 106983, 2020.

[19] G. I. Barenblatt, "The formation of equilibrium cracks during brittle fracture. General ideas and hypotheses. Axially-symmetric cracks," *Journal of Applied Mathematics and Mechanics*, vol. 23, no. 3, pp. 622–636, 1959.

[20] D. S. Dugdale, "Yielding of steel sheets containing slits," *Journal of the Mechanics and Physics of Solids*, vol. 8, no. 2, pp. 100–104, 1960.

[21] K. Otsuka and H. Date, "Fracture process zone in concrete tension specimen," *Engineering Fracture Mechanics*, vol. 65, no. 2, pp. 111–131, 2000.

[22] Z. P. Bažant, "Concrete fracture models: testing and practice," *Engineering Fracture Mechanics*, vol. 69, no. 2, pp. 165–205, 2002.

[23] Q. Lin and J. F. Labuz, "Fracture of sandstone characterized by digital image correlation," *International Journal of Rock Mechanics and Mining Sciences*, vol. 60, pp. 235–245, 2013.

[24] B. Q. Li, B. Gonçalves da Silva, and H. Einstein, "Laboratory hydraulic fracturing of granite: acoustic emission observations and interpretation," *Engineering Fracture Mechanics*, vol. 209, pp. 200–220, 2019.

[25] N. Z. Liu, Y. S. Zou, X. F. Ma, N. Li, and S. Wu, "Study of hydraulic fracture growth behavior in heterogeneous tight sandstone formations using CT scanning and acoustic emission monitoring," *Petroleum Science*, vol. 16, no. 2, pp. 396–408, 2019.

[26] Y. K. Xing, G. Q. Zhang, T. Y. Luo, Y. W. Jiang, and S. W. Ning, "Hydraulic fracturing in high-temperature granite characterized by acoustic emission," *Journal of Petroleum Science and Engineering*, vol. 178, pp. 475–484, 2019.

[27] Y. K. Xing, G. Q. Zhang, B. Wan, and H. Zhao, "Subcritical fracturing of sandstone characterized by the acoustic emission energy," *Rock Mechanics and Rock Engineering*, vol. 52, no. 7, pp. 2459–2469, 2019.

[28] Y. K. Xing, B. X. Huang, E. Q. Ning, L. Zhao, and F. Jin, "Quasi-static loading rate effects on fracture process zone development of mixed-mode (I-II) fractures in rock-like materials," *Engineering Fracture Mechanics*, vol. 240, article 107365, 2020.

[29] J. F. Labuz, S. P. Shah, and C. H. Dowding, "Experimental analysis of crack propagation in granite," *International Journal of Rock Mechanics and Mining Science and Geomechanics Abstracts*, vol. 22, pp. 85–98, 1985.

[30] J. F. Labuz, S. P. Shah, and C. H. Dowding, "The fracture process zone in granite: evidence and effect," *International Journal of Rock Mechanics and Mining Science and Geomechanics Abstracts*, vol. 24, no. 4, pp. 235–246, 1987.

[31] B. K. Atkinson, *Fracture Mechanics of Rock*, Elsevier, 2015.

[32] T. L. Anderson, *Fracture Mechanics: Fundamentals and Applications*, CRC Press, 2017.

[33] E. N. Landis and L. Baillon, "Experiments to relate acoustic emission energy to fracture energy of concrete," *Journal of Engineering Mechanics*, vol. 128, no. 6, pp. 698–702, 2002.

[34] G. Zhang, Y. Xing, and L. Wang, "Comprehensive sandstone fracturing characterization: integration of fiber Bragg grating, digital imaging correlation and acoustic emission measurements," *Engineering Geology*, vol. 246, pp. 45–56, 2018.

[35] Q. Lin, B. Wan, Y. Wang, Y. H. Lu, and J. F. Labuz, "Unifying acoustic emission and digital imaging observations of quasi-brittle fracture," *Theoretical and Applied Fracture Mechanics*, vol. 103, article 102301, 2019.

[36] B. N. Whittaker, R. N. Singh, and G. Sun, *Rock Fracture Mechanics: Principles, Design, and Applications*, Elsevier, Amsterdam, 1992.

[37] D. Broek, *Elementary Engineering Fracture Mechanics*, Springer Science & Business Media, 2012.

[38] Z. P. Bažant and J. Planas, *Fracture and Size Effect in Concrete and Other Quasibrittle Materials*, CRC Press, 1998.

[39] X. Yang, G. Q. Zhang, X. F. Du et al., "Measurement and implications of the dynamic fracture width in hydraulic fracturing using FBG strain sensors," in *51st U.S. Rock Mechanics/Geomechanics Symposium*, American Rock Mechanics Association, San Francisco, 2017.